# Feasibility of Metal Additive Manufacturing for Internal Combustion Engines

By

Jamee Gray

Submitted to the graduate degree program in Mechanical Engineering and the Graduate Faculty of the University of Kansas in partial fulfillment of the requirements for the degree of Master of Science.

Chair: Dr. Christopher Depcik

Dr. Robert Sorem

Dr. Ron Barrett-Gonzalez

Dr. Andelle Kudzal

Date Defended: April 1st, 2020

The thesis committee for Jamee Gray certifies that this is the approved version of the following thesis:

# Feasibility of Metal Additive Manufacturing for Internal Combustion Engines

Chair: Dr. Christopher Depcik

**Date Approved: May 5th, 2020**

## Abstract

As the advancement of metal additive manufacturing (AM) technology persists, so will the expansion of its capabilities and applications. Therefore, automotive and defense industries will need to adapt to these changing trends to remain competitive and sustainable. One potential way of accomplishing this is through the implementation of AM into internal combustion (IC) engines. As a result, the work presented in this thesis aims to expand on this opportunity by demonstrating the process and feasibility of using AM to produce working IC engine components.

Through efforts of reverse engineering, model modifications, parameter selection, build layout optimization, and support structure design, the production of a crankcase and cylinder head from a Saito FG-11 engine was made possible. CT scans were subsequently used to quantify whether defects such as cracks, geometric deviations, and porosity were present/ critical. Once viability of the parts was established, machining and other post-possessing was completed to create fully functional parts. To adequately test engine performance, an entirely new setup and strategy had to be designed and executed, first with a propeller and secondly with an existing dynamometer. Each engine was monitored at the same specific set points during operation for speed, torque, temperatures, pressures, airflow, and mass flow of fuel. The results proved that while the AM engine did have a degraded performance, it was operable and even ran without failure for over 3.5 hours during testing. The major influencers behind the degraded performance were hypothesized to be either variations in assembly, or increased frictions from an insufficient honing procedure. Moreover, there was not enough evidence against the AM process itself for it to be considered a cause, thus deeming this endeavor successful.

## Acknowledgements

Without the seemingly unending patience of my advisor, Dr. Chris Depcik, this work would not have made it this far. It was my sophomore year in his first thermodynamics class that I came to know his dedication and passion for what he does. If he had not recognized my potential during this time, I am not sure I would have pursued graduate degree in the first place, so thank you.

I would also like to express gratitude to the other members of my committee, Dr. Robert Sorem and Dr. Ron Barrett-Gonzalez for their guidance through this process. Moreover, I want to acknowledge Army Research Lab for partnering with these efforts, and everyone who helped me while there, specifically Kyu Cho, Dr. Jennifer Sietins, Dr. Andelle Kudzal, and Ryan Rogers. Additionally, I want to thank my lab mates who aided in my testing efforts, especially Dr. Jon Mattson, Charu Srivasta, Bailey Spickler, and Shah Saud Alam. Furthermore, without the immense help and guidance from Charles Gabel and Ash Shadrick during the manufacturing and test setup process, producing a running engine would have been nearly impossible. With this note, I also wish to acknowledge Jay Myers from Sunnen, who advised me through the honing procedure, lent his mandrel driver, and even made a trip to KU to show me how to use it.

Finally, and arguably most importantly, I want to thank my family and friends for their support and encouragement, which aided in keeping me grounded and sane through this process. Along with this, I want to recognize and thank my Dad for the sacrifices made during his military service, which ultimately allowed an education to be financially possible for me.

# Table of Contents

Abstract ..... iii
Acknowledgements ..... iv
Table of Contents ..... v
Figures ..... viii
Tables ..... xxi
Nomenclature ..... xxiii
Abbreviations & Acronyms ..... xxiii
Variables ..... xxvi
Chapter 1 : Introduction ..... 1
1.1 Introduction to Additive Manufacturing ..... 1
1.2 Thesis Outline ..... 4
Chapter 2 : Use of AM in IC Engines Literature Review ..... 7
2.1 Motivations and Overview ..... 7
2.2 Prototyping ..... 8
2.3 Tooling and Indirect Manufacturing ..... 9
2.4 Remanufacturing and Repair ..... 13
2.5 Design Optimization ..... 14
2.6 AM Part Production for Research ..... 22
2.7 Industry Claims for AM Part Production ..... 29
2.8 Conclusions ..... 30
Chapter 3 : AM Process for Major IC Engine Components ..... 31
3.1 Introduction ..... 31
3.2 Material Determination ..... 32
3.3 Reverse Engineering ..... 36
3.4 Identifying Critical Tolerances ..... 38
3.5 Model Preparation ..... 40
3.6 Machine Choice ..... 41
3.7 Support Design ..... 42
3.8 Build Layout and Parameters ..... 47

3.9 Post AM Results ..... 50
3.9.1. Qualitative Results ..... 50
3.9.2. Nominal Actual Dimensional Analysis ..... 54
3.9.3. Porosity Results ..... 56
3.9.4. Resulting Defects ..... 63
3.10 Post-processing ..... 65
3.10.1. Stress Relieving and Heat Treatments ..... 65
3.10.2. Post Machining ..... 68
3.10.3. Cylinder Honing ..... 84
3.11 Post Machining Results ..... 100
3.11.1. Nominal Actual Dimensional Analysis ..... 100
3.11.2. Porosity Results ..... 102
3.11.3. Resulting Defects ..... 104
3.12 Conclusions ..... 104
Chapter 4 : Experimental Setup, Instrumentation, and Data Acquisition ..... 106
4.1 Engine Test Setup ..... 106
4.1.1. Setup Iteration 1 ..... 106
4.1.2. Setup Iteration 2 ..... 112
4.1.3. Setup Iteration 3 ..... 114
4.1.4. Setup Iteration 4a ..... 117
4.1.5. Setup Iteration 4b ..... 118
4.1.6. Setup Iteration 5a ..... 121
4.1.7. Setup Iteration 5b ..... 126
4.1.8. Setup Iteration 5c ..... 128
4.1.9. Setup Iteration 5d ..... 129
4.1.10. Setup Iteration 5e ..... 130
4.1.11. Setup Iteration 6 (Propeller) ..... 133
4.2 Data Acquisition - Sensors and Hardware ..... 134
4.3 Data Acquisition - LabVIEW Programing ..... 138
4.3.1. Dyno Testing ..... 138
4.3.2. Propeller Testing Modifications ..... 144
4.4 Conclusions ..... 146
Chapter 5 : Test Procedure, Data Post-Processing and Results ..... 147

5.1 Test procedures ..... 147
5.1.1. Propeller ..... 150
5.1.2. Dynamometer ..... 152
5.2 Data Post-processing ..... 153
5.3 Results ..... 159
5.3.1. Propeller ..... 159
5.3.2. Dynamometer ..... 169
5.4 Conclusions ..... 183
Chapter 6 : Conclusion ..... 184
6.1 Summary of Work ..... 184
6.2 Future Work ..... 187
References ..... 188
Appendices ..... 195
Appendix A : Engine Information ..... 195
Appendix B : Surface Roughness and Hardness Data ..... 199
Appendix C : Porosity Data ..... 205
Appendix D : Post-processing Information ..... 218
Appendix E : Tachometer Sampling Frequency Calculation ..... 221
Appendix F : MATLAB Model for Data Post-processing ..... 222
Appendix G : Depcik $AF_s$ Calculation ..... 230
Appendix H : Additional Engine Testing Data ..... 232

# Figures

Figure 1.1: Prediction for AM market growth over the next decade [10] ..... 3

Figure 2.1: Desmosidi engine prototype, manufactured with polycarbonate using FDM [12]. ..... 9

Figure 2.2: AM engine block produced with SLM technology [14] ..... 9

Figure 2.3: Audi bedplate (left) and the AM tool installed on the die (right) [19] ..... 11

Figure 2.4: Using AM in an investment casting process, from left to right: AM master crankcase, silicon mold, wax crankcase, and aluminum cast crankcase [23] ..... 12

Figure 2.5: Cylinder block: Polystyrene AM master (left), and cast aluminum part (right) [24]. 13

Figure 2.6: Comparative illustration of the different optimization strategies [31, 32] ..... 15

Figure 2.7: Before (left) and after (right) topology optimization [33] ..... 16

Figure 2.8: Piston with new components highlighted (pink: oil gallery, blue: lattice structure) [34] ..... 18

Figure 2.9: Optimization steps illustrated on port 1 [35] ..... 19

Figure 2.10: Topology optimization process for diesel engine support [32] ..... 20

Figure 2.11: Compressed air engine original (left) and after optimization (right) [36] ..... 22

Figure 2.12: Fuel distribution produced by three test configurations [39] ..... 24

Figure 2.13: Turbocharger wheels produced through EBM [40] ..... 26

Figure 2.14: Valve configurations and their stress distributions [Pa]: original (left), first valve with added structures (middle), and second valve with added lattice (right) [42]..... 28

Figure 3.1: Nominal actual dimensional analysis of cast parts vs. CAD files for crankcase (left) and cylinder head (right)..... 37

Figure 3.2: Finalized CAD model for crankcase ..... 37

Figure 3.3: Finalized CAD model for cylinder head ..... 38

Figure 3.4: Crankcase drawing section view, units in mm ..... 39

Figure 3.5: Cylinder head drawing section views, units in mm..... 40

Figure 3.6: Model preparation for AM, with gasket faces and bearing surfaces highlighted, crankcase (left) cylinder head (left) ..... 41

Figure 3.7: Crankcase support designs (solid and wall supports are orange and pink respectively) ..... 43

Figure 3.8: Modified crankcase design for AM..... 44

Figure 3.9: Example of an area where support is added (left) and where the support region is modified (right)..... 45

Figure 3.10: Cylinder head support design (solid and wall supports are orange and pink respectively)..... 46

Figure 3.11: Build plate arrangement for crankcase ..... 48

Figure 3.12: Build plate arrangement for cylinder head ..... 49

Figure 3.13: Original crankcase design build results ..... 51

Figure 3.14: Modified crankcase build results ..... 51

Figure 3.15: Cylinder head build plate result ..... 52

Figure 3.16: AM cylinder head results ..... 53

Figure 3.17: AM cylinder heads post support removal, pre-machining ..... 53

Figure 3.18: Nominal actual dimensional analysis of AM parts vs. CAD files for original and modified crankcase designs ..... 55

Figure 3.19: Nominal actual dimensional analysis of AM parts vs. CAD files for cylinder head 56

Figure 3.20: Visual representation of porosity in die cast crankcase ..... 57

Figure 3.21: Visual representation of porosity in AM crankcase 1 (original, left) and crankcase 2 (modified, right) designs ..... 58

Figure 3.22: Image slices, crankcase (left) and solid support (right) ..... 59

Figure 3.23: Visual representation of porosity in cylinder head ..... 60

Figure 3.24: Visual representation of porosity in AM cylinder head 2 ..... 61

Figure 3.25: Crack defect in AM crankcase original design number 1 ..... 64

Figure 3.26: Crack defect in AM cylinder head number 2 ..... 65

Figure 3.27: Graphical representation of the relief of residual stress for Ti-6Al-4V [73]..... 66

Figure 3.28: Graphical representation of Vickers hardness of cast and AM aluminum (a) for step 1-2, (b) step 4-5 [74] ..... 67

Figure 3.29: AlSi12 stress and strain curves for heat treated and as built AM tensile bars [75] .. 68

Figure 3.30: Build plate removal using a bandsaw ..... 68

Figure 3.31: Surface and feature identification for the crankcase: top view, cut section view, and bottom view ..... 69

Figure 3.32: Vice placements for crankcase with (A) used for machining features 1 and 4-10, (B) used for features 16-18 and 22, and (C) used for 15 and 19 ..... 70

Figure 3.33: Vice placement for final squaring step and proceeding boring, reaming, drilling, and tapping steps (features 2, 3, and 11-14 machined with this set up) ..... 72

Figure 3.34: Using a dial indicator on reamed surface to zero x and y axis ..... 73

Figure 3.35: Vice placement using sine block for angled sensor holes (feature 20) ..... 74

Figure 3.36: Final machined crankcase ..... 75

Figure 3.37: Fixturing devices manufactured for cylinder head post machining ..... 76

Figure 3.38: Surface and feature identification for the cylinder head: top view, bottom view, and cut section view..... 76

Figure 3.39: First vice set up to drill the initial four holes (feature 11) in the cylinder head ..... 77

Figure 3.40: Set up for the features that are angled at 20° (features 5-8) on cylinder head ..... 78

Figure 3.41: Set up for 10° angled features (feature 2) on cylinder head ..... 79

Figure 3.42: Setup for rocker flange holes (left), representation of tapping feature 3 though feature 4 (right) ..... 80

Figure 3.43: Setup for intake (left) and exhaust (right) ports ..... 81

Figure 3.44: Setup for drilling sparkplug hole, using a sine block, angle vice, machinist jack, and probe ..... 82

Figure 3.45: Setup to remove left over support material at base of cylinder head ..... 82

Figure 3.46: Setup for boring the cylinder head base and wall ..... 83

Figure 3.47: Exploded view of Sunnen honing mandrel [77] ..... 85

Figure 3.48: Modified Sunnen honing mandrel for blind holes ..... 85

Figure 3.49: Original (top), modified stones for blind hole honing (middle, bottom), and felt replacement for silicon exposure (bottom) ..... 86

Figure 3.50: Modified bronze guide shoes for silicon exposure (top) and blind hole honing (top and bottom) ..... 87

Figure 3.51: Sunnen mandrel driver ..... 89

Figure 3.52: Honing setup with two-piece vice and new fixture ..... 90

Figure 3.53: Example profile (top) and its result from plateau honing (bottom) [79] ..... 90

Figure 3.54: Practice honing: before bronze guide shoes were filed (left), and after (right) ..... 91

Figure 3.55: Using a hydraulic press to yield the cylinder back into a cylindrical shape ..... 92

Figure 3.56: New fixture for honing and boring ..... 93

Figure 3.57: Profilometer measurement set up (left), and fixture for profilometer (right) ..... 94

Figure 3.58: Depiction of measurement locations ..... 97

Figure 3.59: Surface profile of AM cylinder head after boring to +0.003" of final diameter ..... 97

Figure 3.60: Surface profile of AM cylinder head after using the roughing 220 grit stone ..... 98

Figure 3.61: Surface profile of AM cylinder head after using the 400 grit stone ..... 98

Figure 3.62: Surface profile of AM cylinder head after using the polishing stone ..... 98

Figure 3.63: Surface profile of AM cylinder head after exposing the silicon with compound and felt pads ..... 99

Figure 3.64: Surface profile of stock cylinder head liner ..... 99

Figure 3.65: Finished (post honing process) AM cylinder wall ..... 100

Figure 3.66: Nominal actual dimensional analysis of AM modified crankcase 2 vs. original cast part ..... 101

Figure 3.67: Nominal actual dimensional analysis of AM cylinder head 2 vs. original cast part ..... 102

Figure 3.68: Post machined crankcase CT image with the artifact circled in red and its corresponding binary image identifying it as material; hence, causing a false porosity indication..... 103

Figure 3.69: Approximation of time for reverse engineering, AM, and post-processing (days) 105

Figure 4.1: Engine test setup dyno gear connection (left) and engine gear connection (right) .. 108

Figure 4.2: Belt tensioner pulley to prevent belt slippage during operation..... 109

Figure 4.3: Engine test setup iteration #1 ..... 111

Figure 4.4: 3-D printed mount for the servo motor (to control intake)..... 111

Figure 4.5: Engine test setup iteration #2 ..... 113

Figure 4.6: Keyed belt gear with set screw attached to Futek sensor ..... 114

Figure 4.7: Engine test setup iteration #3 (left) and hard geared connection assembly (right) .. 116

Figure 4.8: Damaged brass gear from vibration from engine test setup iteration #3..... 116

Figure 4.9: Additional bracing added to the 80/20 ..... 117

Figure 4.10: Stronger bracketing added to the 2” × 4” T mounting ..... 118

Figure 4.11: Resonating chamber setups: ½ gallon (left) and 5 gallon (right)..... 120

Figure 4.12: Comparative testing of resonating chambers and inlet flow rate ..... 120

Figure 4.13: Engine test setup iteration #5a..... 123

Figure 4.14: Adjustable engine test stand made from 80/20 ..... 124

Figure 4.15: Aluminum hold-downs..... 124

Figure 4.16: Original T-slot nut (left) and modified one (right)..... 125

Figure 4.17: Futek sensor shaft reduction adaptor..... 125

Figure 4.18: Broken shaft coupling ..... 126

Figure 4.19: Failure of the polyurethane spiders in the shaft couplings..... 128

Figure 4.20: Engine failure: broken connecting rod in crankcase (left), and detached piston head (right) ..... 129

Figure 4.21: Finalized dyno engine setup..... 132

Figure 4.22: Propeller test setup ..... 134

Figure 4.23: Sensor and data acquisition hardware wiring diagram..... 135

Figure 4.24: Surface thermocouple placements (left) on cylinder head and (right) on crankcase ..... 136

Figure 4.25: Calibration curve for liquid level height sensor using 20:1 mixture of gasoline and 2-stroke engine oil..... 137

Figure 4.26: cDAQ and Inter-Loc V with myRIO stream GUI ..... 142

Figure 4.27: cDAQ and Inter-Loc V with myRIO stream block diagram ..... 142

Figure 4.28: Flow sensor and servo motor with myRIO stream GUI ..... 143

Figure 4.29: Flow sensor and servo motor with myRIO stream block diagram ..... 143

Figure 4.30: Optimized myRIO VI block diagram with false case structure collecting and displaying data from the flow sensor while also controlling servomotor ..... 145

Figure 4.31: Optimized myRIO VI block diagram with true case structure only collecting data from the Hall effect sensor ..... 145

Figure 5.1: AM cylinder head and crankcase assemblies used during testing ..... 148

Figure 5.2: Depiction of tappet adjustment taken from the Saito FG-11 manual [88] ..... 148

Figure 5.3: Representation of the magnet pass data; each graph is one second inside each of the 20 s segments taken for one test point ..... 155

Figure 5.4: Histogram of the time between magnet passes for one test point with extraneous data with the normal distribution curve displayed (red) ..... 156

Figure 5.5: Histogram of the adjusted time between magnet passes for one test point with the normal distribution curve displayed (red) ..... 156

Figure 5.6: Fuel height senor values (top) and the elimination of the extraneous data (bottom) 158

Figure 5.7: Intake air flow rate results during prop testing ..... 161

Figure 5.8: Fuel consumption results during prop testing ..... 161

Figure 5.9: Engine speed results during prop testing..... 162

Figure 5.10: Exhaust temperature results during prop testing ..... 162

Figure 5.11: Cylinder head temperature results during prop testing ..... 163

Figure 5.12: Crankcase temperature results during prop testing ..... 163

Figure 5.13: Air intake flow rates results during dyno testing ..... 171

Figure 5.14: Fuel consumption results during dyno testing..... 171

Figure 5.15: Exhaust temperatures results during dyno testing..... 172

Figure 5.16: Cylinder head temperatures results during dyno testing ..... 172

Figure 5.17: Crankcase temperatures results during dyno testing ..... 173

Figure 5.18: Engine torques produced results during dyno testing ..... 173

Figure 5.19: Surface profile of AM cylinder head after engine testing (location 2) ..... 180

Figure 5.20: Surface profile of AM cylinder head after engine testing (location 1) ..... 181

Figure A.1: Exploded view of Saito FG-11 engine [88]..... 195

Figure A.2: Solidworks drawing of crankcase..... 196

Figure A.3: Solidworks drawing of cylinder head..... 197

Figure B.1: Cylinder head broken fins used as a test specimen, polished to 1 µm ..... 199

Figure B.2: Vickers hardness test result - printout page 1 ..... 200

Figure B.3: Vickers hardness test result - printout page 2 ..... 201

Figure B.4: SurfTest SJ USB Communication Tool Ver5.007 GUI ..... 202

Figure B.5: Surface profile of un-machined die cast material ..... 203

Figure B.6: Surface profile of un-machined AM Ti64 (crankcase) ..... 203

Figure B.7: Surface profile of un-machined AM AlSi12 (cylinder head) ..... 204

Figure C.1: Porosity area percentage with height of die cast crankcase ..... 205

Figure C.2: Pore size and frequency of die cast crankcase ..... 205

Figure C.3: Porosity area percentage with height of AM crankcase 1 (original design) ..... 206

Figure C.4: Pore size and frequency of AM crankcase 1 (original design) ..... 206

Figure C.5: Porosity area percentage with height of AM crankcase 4 (original design) ..... 207

Figure C.6: Pore size and frequency of AM crankcase 4 (original design) ..... 207

Figure C.7: Porosity area percentage with height of AM crankcase 2 (modified design) ..... 208

Figure C.8: Pore size and frequency of AM crankcase 2 (modified design) ..... 208

Figure C.9: Porosity area percentage with height of AM crankcase 3 (modified design) ..... 209

Figure C.10: Pore size and frequency of AM crankcase 3 (modified design) ..... 209

Figure C.11: Summary of crankcase porosity results, top: original die cast part, bottom: AM parts ..... 210

Figure C.12: Porosity area percentage with height of die cast cylinder head ..... 210

Figure C.13: Porosity area percentage with height of AM cylinder head 1 ..... 211

Figure C.14: Porosity area percentage with height of AM cylinder head 2 ..... 211

Figure C.15: Porosity area percentage with height of AM cylinder head 3 ..... 212

Figure C.16: Pore size and frequency of die cast cylinder head ..... 212

Figure C.17: Pore size and frequency of AM cylinder head 1 ..... 213

Figure C.18: Pore size and frequency of AM cylinder head 2 ..... 213

Figure C.19: Pore size and frequency of AM cylinder head 3 ..... 214

Figure C.20: Summary of cylinder head porosity results, top: original die cast part, bottom: AM parts ..... 214

Figure C.21: Depiction on how the cut off for noise in the CT analysis was found ..... 215

Figure C.22: Porosity area percentage with height of AM crankcase 2 (modified design) for pre and post machined..... 216

Figure C.23: Porosity area percentage with height of AM cylinder head 2 for pre and post machined..... 216

Figure C.24: Pore size and frequency of AM crankcase 2 (modified design) for pre and post machined..... 217

Figure C.25: Pore size and Frequency of AM cylinder head 2 for pre and post machined..... 217

Figure D.1: Vertical mill head controls with labels [93] ..... 218

# Tables

Table 3.1: Support information for cylinder head and crankcase designs ..... 47

Table 3.2: Machine parameters for each component on 3D Systems ProX DMP 320 (Ti64) ..... 49

Table 3.3: Machine parameters for each component on 3D Systems ProX DMP 300 (AlSi12).. 50

Table 3.4: Crankcase porosity results: comparison of cast and AM parts ..... 59

Table 3.5: Cylinder head porosity results: comparison of cast and AM parts ..... 61

Table 3.6: Mitutoyo Profilometer SJ-210 measurement conditions ..... 94

Table 3.7: Roughness value comparisons of cylinder head walls ..... 96

Table 3.8: Cylinder head diameter data in mm for stock cylinder and during honing process (average of three measurements) ..... 97

Table 3.9: Crankcase and cylinder head porosity results after machining ..... 104

Table 4.1: Dyne Systems Dymond Series 12 Specifications ..... 107

Table 4.2: Finalized dyno engine setup label information ..... 132

Table 5.1: Comparison of engine performance parameters during prop testing ..... 164

Table 5.2: Comparison of engines at approximately 5000 rpm during propeller testing ..... 165

Table 5.3: Comparison of engines at approximately 7000 rpm during propeller testing ..... 165

Table 5.4: Comparison of engine performance parameters at 5000 rpm during dyno testing.... 174

Table 5.5: Comparison of engine performance parameters at 6000 rpm during dyno testing.... 174

Table 5.6: Roughness value comparisons of cylinder head walls for pre and post engine testing ..... 180

Table 5.7: Cylinder head diameter data in mm for pre and post engine testing ..... 181

Table A.1: Additive manufacturing vs. die casting ..... 198

Table B.1: Roughness value comparisons of un-machined die cast and AM materials ..... 202

Table D.1: Everything needed to machine parts to final form, list does not include drill bits used when stepping up to the final size ..... 219

Table H.1: Stock engine results for propeller testing ..... 232

Table H.2: AM crankcase engine results for propeller testing ..... 233

Table H.3: AM crankcase and cylinder head engine results for propeller testing ..... 234

Table H.4: Stock engine results for dyno testing ..... 235

Table H.5: AM crankcase engine results for dyno testing ..... 236

Table H.6: AM crankcase and cylinder head engine results for dyno testing ..... 237

# Nomenclature

### Abbreviations & Acronyms

| | |
|---|---|
| *1-D* | One-dimensional |
| *3-D* | Three-dimensional |
| *ACAH* | AM crankcase and AM cylinder head |
| *ACS* | AM crankcase with the stock cylinder head |
| *Al* | Aluminum |
| *AM* | Additive manufacturing |
| *Ar* | Argon |
| *BDC* | Bottom dead center |
| *CAD* | Computer-aided design |
| *cDAQ* | CompactDAQ |
| *cDLVI* | cDAQ and Inter-Loc V (cDLVI) virtual instrument |
| *CFD* | Computational fluid dynamics |
| *CI* | Compression ignition |
| *CNC* | Computer numerical controlling |
| *$CO_2$* | Carbon dioxide |
| *CT* | Computed tomography |
| *Cu* | Copper |
| *DAS* | Data acquisition system |
| *DED* | Directed energy deposition |

| | |
|---|---|
| *Dyno* | Dynamometer |
| *EBM* | Electron beam melting |
| *EVO* | Exhaust valve opening |
| *FDM* | Fused deposition modeling |
| *FEA* | Finite element analysis |
| *GUI* | Graphical user interface |
| *HC* | Hydrocarbon |
| $I^2C$ | Digital inter-integrated circuit |
| *IC* | Internal combustion |
| *ICE* | Internal combustion engine |
| *ID* | Inner diameter |
| *IEM* | Integrated exhaust manifold |
| *LED* | Light emitting diode |
| *LED* | Linear energy density |
| *LMD* | Laser metal deposition |
| *LPBF* | Laser powder bed fusion |
| *Mg* | Magnesium |
| *Mr1* | Peak material ratio |
| *Mr2* | Valley material ratio |
| *NI* | National Instruments |
| $NO_x$ | Nitrogen oxide |
| *OCS* | Operator Control Station |

| | |
|---|---|
| *OD* | Outer diameter |
| *OEM* | Original equipment manufacturer |
| *OT* | Operating temperature |
| *PID* | Proportional-integral-derivative |
| *Prop* | Propeller |
| *PVC* | Polyvinyl chloride |
| *Ra* | Roughness average |
| *Reman* | Remanufactured |
| *Rk* | Core roughness |
| *Rkμ* | Kurtosis (peakedness of profile) |
| *RMS* | Root mean squared |
| *ROI* | Region of interest |
| *Rp* | Maximum profile peak height |
| *Rpk* | Reduced peak height |
| *RPM* | Revolutions per minute |
| *Rq* | RMS roughness |
| *Rsk* | Skewness (asymmetry of profile) |
| *Rt* | Maximum height of the profile |
| *Rv* | Maximum profile valley depth |
| *Rvk* | Reduced valley depth |
| *Rz* | Average maximum height of the profile |
| *SCL* | Serial clock |

| | |
|---|---|
| *SDA* | Serial data |
| *SE* | Stock engine |
| *SF* | Safety factor |
| *Si* | Silicon |
| *SI* | Spark ignition |
| *SLM* | Selective laser melting |
| *SLS* | Selective laser sintering |
| *TDC* | Top dead center |
| *TDCC* | Top dead center combustion |
| *TDCI* | Top dead center at beginning of induction stroke |
| *Ti* | Titanium |
| *Ti64* | Ti-6Al-4V |
| *Top-op* | Topology optimization |
| *UAV* | Unmanned aerial vehicle |
| *URL* | Uniform resource locator |
| *VDC* | Voltage direct current |
| *VED* | Volumetric energy density |
| *VI* | Virtual instrument |

**Variables**

| | |
|---|---|
| *AF* | Air fuel Ratio |
| $AF_s$ | Stoichiometric air fuel ratio |
| $\hat{b}$ | Y-intercept |

| | |
|---|---|
| $m$ | mass |
| $\hat{m}$ | Dataset trendline slope |
| $N$ | Engine speed |
| $n_R$ | Number of crank revolutions per engine cycle |
| $p$ | Pressure |
| $R$ | Universal gas constant |
| $s_m$ | Trendline slope standard deviation |
| $T$ | Temperature |
| $T_{ACAH}$ | Temperature of AM crankcase and AM cylinder head |
| $T_{ACS}$ | Temperature of AM crankcase with the stock cylinder head |
| $T_{SE}$ | Temperature of stock engine |
| $V$ | Volume |
| $\dot{\mathbb{V}}_{air}$ | Average air intake flow rate |
| $\mathbb{V}_{disp}$ | Engine displacement |
| $\dot{\mathbb{V}}_{fuel}$ | Average rate of fuel consumption (mL/min) |
| $\eta_v$ | Volumetric efficiency |
| $\rho_{amb}$ | Density of ambient air |
| $\rho_{fuel}$ | Density of fuel |
| $\phi$ | Equivalence ratio |

# Chapter 1: Introduction

## 1.1 **Introduction to Additive Manufacturing**

Transportation accounts for 28% of the total energy use in the United States and highway vehicles are responsible for 80% of this amount [1, 2]. As a result, it is safe to say that making strides in improving the fuel economy of these vehicles will make a significant impact in reducing emissions and a reliance on fossil fuels. One significant opportunity to accomplish this objective is to reduce vehicle mass. For example, through use of a model, Pagreit et al. showed that there is approximately a 5% increase in fuel economy (i.e., miles per gallon) for every 10% reduction in overall vehicle mass [3]. Moreover, a similar study by Ricardo Inc. demonstrated a 0.33% improvement in fuel economy per % weight reduction for an average passenger vehicle with a gasoline engine [4].

As an estimate, the powertrain makes up 24% of the total weight in Class 8 tractors and 16% of the weight in light-duty passenger vehicles [5, 6]. With respect to this powertrain, the cylinder block (consisting of the cylinder head and crankcase) contributes 20-25% of the overall engine weight [7]. Therefore, focusing on this area for lightening could result in the greatest fuel economy benefit. Previously, efforts have targeted a reduction in weight by directly substituting respectively heavier automotive components with ones made of a lighter material. One significant powertrain example is the shift from iron to aluminum cylinder blocks and more recently magnesium. In fact, by making the switch from cast iron to aluminum or magnesium, it is possible to reduce the weight by 66% and 75%, respectively [8]. However, direct replacement with lighter materials tends to be more expensive, and there is a plateau with respect to notable

weight savings using conventional construction techniques; hence, alternative methodologies for part creation should be considered [9].

One appealing option for part creation is by using additive manufacturing (AM) since it can make lightweight and optimized geometries that would otherwise be impossible to achieve. AM, also referred to as rapid prototyping or three-dimensional (3-D) printing, is a layer-by-layer process in which a part is built using slices of its model geometry, initially generated using a computer-aided design (CAD) program. According to Gibson et al. the major technologies for this include: vat photopolymerization, laser powder bed fusion (LBPF), extrusion-based, material jetting, binder jetting, sheet lamination, directed energy deposition (DED), and direct writing [10]. Of these methods, LBPF and DED are used most often when it comes to metals, making them the most likely technology to be pursued with respect to IC engine components. A report published by SmarTech predicts that AM will continue to grow dramatically within the automotive industry (Figure 1.1) giving further motive to pursue this technology in lightening the powertrain [11].

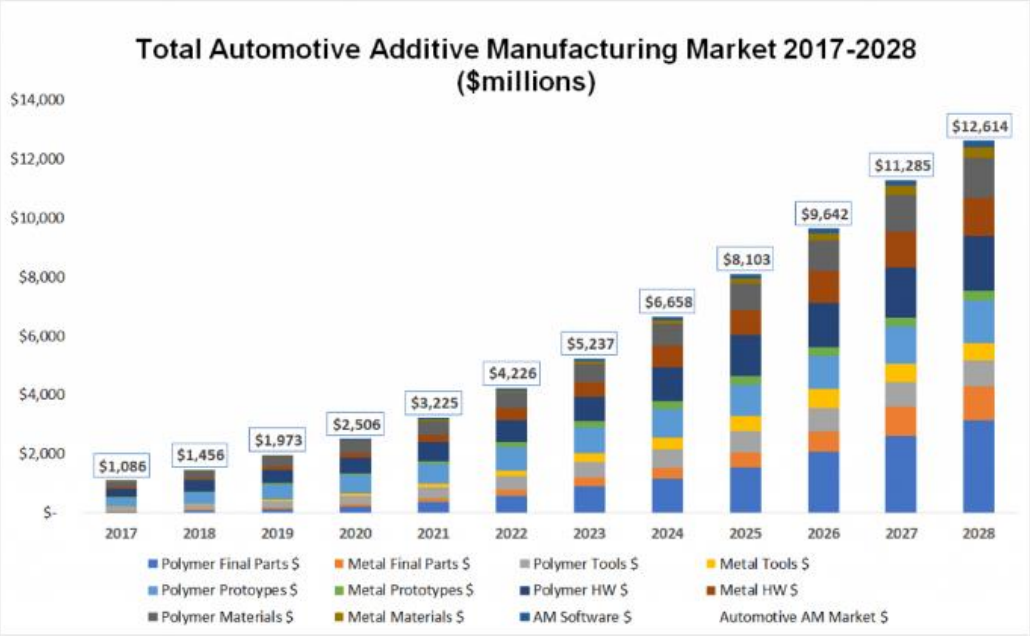


*Figure 1.1: Prediction for AM market growth over the next decade [10]*

In general, AM has less manufacturing constraints when compared to traditional methods, such as casting or machining. This, in conjunction with topology optimization software (finite element analysis on a loop- used to determine where material is and is not needed) allows for the generation of highly optimized designs, subsequently producing parts capable of increased specific strength and/or stiffness. In addition, AM can allow for the reduction of parts (e.g., the elimination of a cylinder liner) that can lead to a greater reliability, further weight reductions, and decreased production costs. Moreover, existing parts can be redesigned for AM to improve performance. For example, fins could be added or modified to provide an increased heat transfer rate, or port swirl can be produced for greater turbulence to facilitate quicker and more thermally efficient combustion inside of the cylinder. Furthermore, the AM process provides better control of heat transfer and the material structure during construction. Achieving

this same level of control in casting requires the creation of expensive molds and dies with complex cooling chambers. In a later chapter, this benefit will be exhibited through a porosity analysis of die cast versus AM engine components. Lastly, higher strength to weight ratios materials that are difficult to cast (e.g., titanium) are AM capable; hence, they can provide another mode of weight loss.

Overall, AM can be used for the production of internal combustion (IC) engines for the consumer market. The use of AM is also highly advantageous for military applications, such as unmanned aerial vehicles (UAV), some of which employ internal combustion engines. In this context, AM would reduce the need for storage of spare parts, molds, and dies in the event that something breaks. This would decrease lead times and create a faster return to the field since these machines are able to manufacture at the point of need. Additionally, military vehicle quantities are relatively low as compared to passenger vehicles, making AM a respectively cheaper alternative to casting. Lastly, the AM process is scalable; therefore, if it can successfully manufacture a functional 10.9 cc cylinder head, then the same machine should be able to manufacture a 600 cc cylinder head given the build envelope is large enough, and with better relative tolerances.

## 1.2 **Thesis Outline**

Due to the potential benefits seen in the use of AM within IC engines, the subsequent chapters of this thesis aim to prove that it is a feasible option using LPBF. These efforts include the full scope of the process involved in designing, manufacturing, and testing two major components (crankcase and cylinder head) of a Saito FG-11 four-stroke 10.9 cc engine. Before

detailing this process, Chapter 2 provides an overview of past research that has been done involving IC engines and AM. This includes everything from prototyping and tooling, to actual component production. However, due to the secrecy within motorsport and luxury vehicle industries, not all information regarding AM's advancement in this area is available.

Chapter 3 provides a detailed explanation of the steps involved in designing and manufacturing a LPBF AM part with the types of critical tolerances needed for engine operation. The chapter starts by selecting the engine to be used, then it provides an in-depth explanation of how the crankcase and cylinder head of the engine are reversed engineered and cross checked with computed topology (CT) scans of the original stock parts. After which, design adjustments for LPBF are made to produce better results. The chapter then gives an overview of the LBPF process itself, which includes material and machine choice, designing support structures, and determining machine parameters. The parts are verified to be useable by quantifying porosity and cracking that occurred through CT analysis. Finally, the extensive post-processing procedure is described, which includes heat treatments, machining, and honing.

Chapter 4 provides an overview of the engine testing setup, instrumentation, and data acquisition system. The testing setup went through multiple iterations until a configuration was found that worked with an existing dynamometer and allowed steady combustion within the engine. A detailed description of the wiring, sensors and LabVIEW programs used to collect data is also provided.

Chapter 5 gives an overview of the testing procedures used along with the targeted data points for each test. There were three major tests performed, the first with both stock cylinder

head and crankcase, the second with the stock cylinder head and AM crankcase, and the third with both AM cylinder head and AM crankcase. Additionally, this chapter presents the results of this testing and data that went along with it.

Finally, Chapter 6 provides a summary of all the work done, from the review of the literature to the reverse engineering, design, manufacturing, analysis and testing of the engine. This chapter also provides insight on what should be improved, and recommendations for future research.

# Chapter 2: Use of AM in IC Engines Literature Review

## 2.1 **Motivations and Overview**

With 22.4% of the total energy consumption in the United States being used in highway vehicles, making strides in improving their fuel economy will positively influence the environmental impact they have [1, 2]. A major way of doing this is by lightening vehicle weight, and because the engine is a major contributor, it is an ideal area to target. In the past, many have tried using alternative materials such as aluminum or magnesium to decrease weight. However, direct replacement of materials has almost entirely been exhausted as a solution at this point. Therefore, additive manufacturing (AM) has become an appealing option to turn towards. Because of its freedom from typical manufacturing constraints, it can produce highly optimized designs, which have the potential to increase reliability, improve performance, decrease production cost, and potentially minimize parts.

AM is a relatively new field in the realm of manufacturing, this is especially true regarding its use within internal combustion (IC) engines. Because of this, it is important to become familiar with the previous work being done in order to make novel advances. In the automotive industry and research, there are five primary areas where AM is being utilized with respect to engines: 1. Prototyping, 2. Tooling and Indirect Manufacturing, 3. Remanufacturing and Repair, 4. Design Optimization, and 5. Production. Currently, most AM in this area is focused on prototyping and tooling, with production of AM components limited to research, motorsport, and luxury vehicle applications. Here, this chapter will cover these areas, along with

providing an overview of the optimization design research for IC engines that necessitates the use of AM.

## 2.2 **Prototyping**

The use of AM has become important within the internal combustion (IC) engine industry due to its ability to create cost effective prototypes faster than its predecessors, which required laborious machining and custom tooling fixtures. As an example, Ducati cut 20 months from their engine development process with their Desmosedici bike by prototyping their entire engine with polycarbonate using fused deposition modeling (FDM) (Figure 2.1). Moreover, the quick turnaround of this model and its physical representation allowed the engineers to quickly recognize flaws and consider design changes that would have ordinarily delayed the project. For instance, they changed the cylinder configuration from two cylinders with oval pistons to four cylinders with round pistons and the entire engine was prototyped once more. This rapid change ultimately ended up helping them to set a new benchmark in the international motorcycle industry [12].

Similar to Ducati, Ford has implemented AM to save millions during their design stage. For example, the engine cover for the Ford Mustang usually takes four months and roughly $500,000 to prototype with traditional methods. However, by using AM, it only took four days and about $3,000 (including multiple iterations) [13]. Other AM engine prototyping efforts can be seen from Haba et al. when demonstrating the design and manufacturing process of an 80 cc four-stroke engine block (Figure 2.2). In this study, they employed selective laser melting (SLM) AM technology which uses metal powder (also referred to as laser powder bed fusion) [14].

Other AM prototyping examples in design development more often involve the use of ceramics and plastics. This includes work by Guarto et al. in developing a flex-fuel rotary engine with variable compression ratio [15], efforts by Han et al. to test their new diesel particulate filter [16], and multiple attempts at the production of a prototype intake manifold design [17, 18].

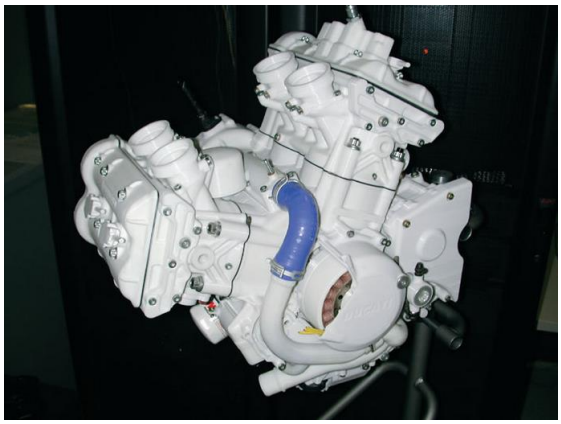

*Figure 2.1: Desmosidi engine prototype, manufactured with polycarbonate using FDM [12].*

*Figure 2.2: AM engine block produced with SLM technology [14]*

## 2.3 **Tooling and Indirect Manufacturing**

Furthermore, AM is a key player in helping to create complex parts indirectly. Specifically, there are two major methodologies where this is accomplished for metal components: tooling (direct and indirect) and indirect manufacturing. These methods are used

when the properties of AM parts are not adequate for the application, but its ability to create intricate geometries is needed. Particularly, direct tooling uses AM to create the actual molds; whereas, indirect tooling uses an AM master part to produce a mold or die. In contrast, indirect manufacturing uses AM pieces to cast a part directly.

One application of direct tooling is within the press hardening manufacturing process. In the automotive industry, press hardening is an emerging technology employed to implement lightweight high strength steel parts for car bodies that is complementary to traditional metal stamping/press forming processes. Through heat treatment during press forming, this process allows sheet metal to have different favorable properties (e.g., higher elongation or strength) in the areas where they are needed the most. Hence, by using direct tooling to create an optimized cooling system, the cycle time of the process can be reduced. For example, Müller et al. numerically simulated the thermal behavior and coolant flow of a traditional tool compared to an AM-optimized one. Due to the optimized system's cooling efficiency, holding time could be shorted by 45%. Subsequent real life testing demonstrated that the AM tool cooled down six times faster than the conventional option; thereby, reducing the cooling time by 50% [19].

With respect to IC engines, there are several components that are traditionally metal stamped: coupling joints, fuel injectors, housings, armatures, fuel rail, fuel pressure regulators, oil pans, etc. Therefore, there is significant potential for AM use in direct tooling these components via press hardening, consequently improving their properties while creating room for optimization.

Relatedly, Audi used direct tooling to add inserts into the mold for their V8-TFSI IC engine (Figure 2.3). This was accomplished because the conventional casting process generated porosity in the bedplate at the oil filter cartridge due to insufficient cooling (circled red in Figure 2.3). As a result, this AM fix demonstrated a reduction of 10% in scrap material rate while decreasing the cycle time by 3% [19].

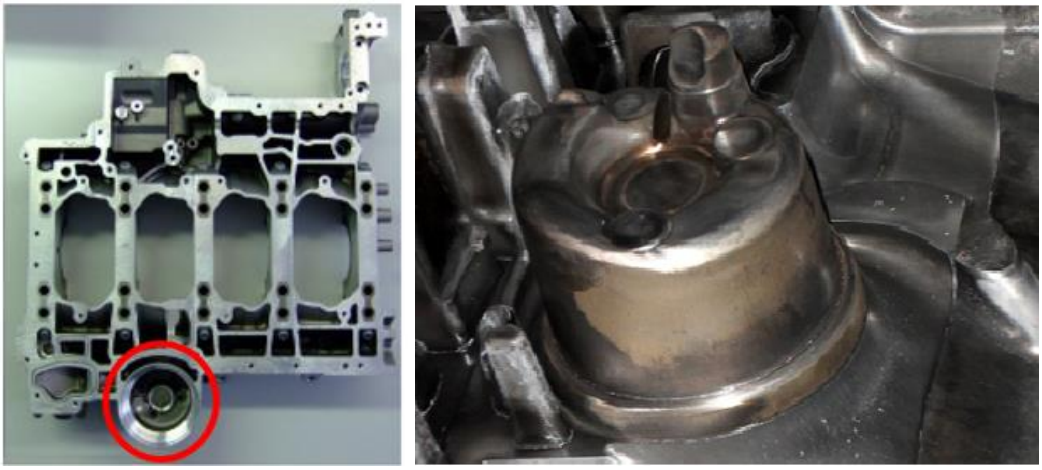

*Figure 2.3: Audi bedplate (left) and the AM tool installed on the die (right) [19]*

Another common use of AM within direct tooling is through the use of binder jet sand cores used to create molds for casting. For example, Ford used this process to create a mold package of interlocking sand cores that aided in their design of lightweight bulkhead inserts allowing for relatively easy and rapid design changes [20]. Analogously, Rochussen et al. developed a research oriented cylinder head for multiple in-cylinder diagnostics using a 3-D printed sand mold [21], and America Makes manufactured a cylinder head water jacket sand core [22].

A major use of indirect tooling can be found in a paper by Agapovichev et al. to cast an IC engine crankcase. To do so, they first modeled the crankcase in CAD software while adding allowance for subsequent machining. Before continuing to manufacture, the casting process was molded using the CAD model with the supply gating system added (entry for cast material). After verification through the simulation, the master model was 3-D printed using a polymer material and an Objet Eden 350 machine (poly jet process). From this 3-D printed part, silicon molds were produced, after which wax was poured to produce a wax crankcase. From here, a lost wax casting process was followed, where the wax was placed in gypsum plaster, which is then hardened, and the wax melted out. Subsequently, the aluminum alloy is poured into the mold and the final crankcase is formed. This entire process is illustrated in Figure 2.4. It showed that using AM with investment casting allowed for the production of high quality castings of thin walled parts quickly with minimal experience [23].

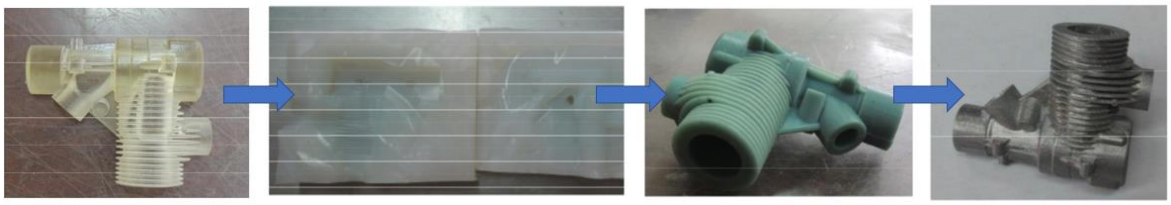

*Figure 2.4: Using AM in an investment casting process, from left to right: AM master crankcase, silicon mold, wax crankcase, and aluminum cast crankcase [23]*

Instead of using the direct manufacturing approach, indirect manufacturing takes an AM part and employs it in an investment casting process. This is based on lost-wax casting, but instead uses an evaporative pattern and the material evaporates as the molten metal is poured. Utilizing this type of casting with AM parts, several engine components have been manufactured including, but not limited to, the cylinder block (Figure 2.5), air intake manifold, exhaust

manifold, and a gear box [24, 25]. In a related effort, Bassoli et al. compared and verified the feasibility and evaluated the dimensional accuracy of a rapid investment casting and rapid direct casting techniques with AM using an automotive part with thin walls as an example. They were able to show that both these manufacturing methods are effective with low costs and tolerances consistent with casting [26].

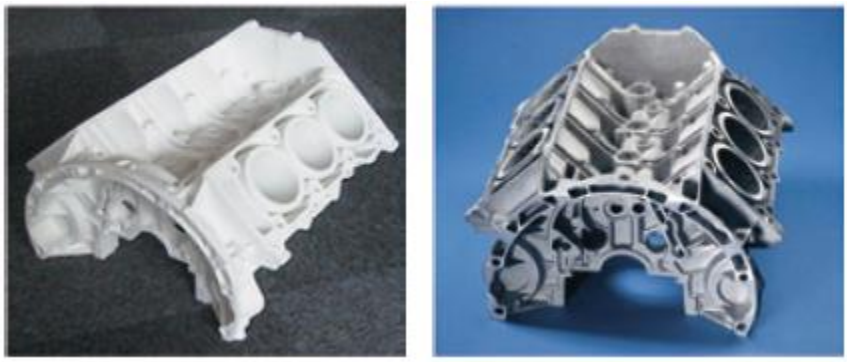

*Figure 2.5: Cylinder block: Polystyrene AM master (left), and cast aluminum part (right) [24]*

## 2.4 **Remanufacturing and Repair**

The use of cold spray AM machines for remanufactured (reman) components is another aspect of AM that is employed within the automotive industry, specifically for IC engines. In fact, cold spray has been used for remanufacturing of Compression Ignition (CI) engines since the 1970s. This technology applies coatings using a high velocity jet of small particles accelerated by a supersonic jet of compressed gas [27]. Because cold spray does not require an inert environment, metal powder can be deposited directly on a damaged part. Today, 40% of the components of a Caterpillar reman engine are new; however, this number can be reduced to 25% through better quality control and by using AM repair techniques to scrap fewer parts. Moreover, AM can be used to repair engine heads and blocks with cracks or similar faults by first milling,

then cold spraying, and lastly grinding and polishing. Overall, a reman engine costs approximately 60% the price of a new engine with reman parts sold at 40% of the original price; hence, there is significant opportunity for profit by the manufacturer [28].

Another AM technology used in the remanufacturing process is DED (also referred to as laser metal deposition (LMD)), and the most popular application of this is for turbine engines [29]. However, these machines can also be used in treating IC engine components. For example, because piston cylinder bores typically become larger due to wear, LMD can be employed to add material back to the piston cylinder walls. This, followed by proper post machining and honing afterwards, will allow the block to achieve its original dimensions [30].

## 2.5 Design Optimization

Since AM facilitates the creation of parts without the constraints of traditional methods, designs can be optimized to produce lightweight parts with organic-like configurations capable of the same strength and/or stiffness values. In this area, there are different optimization methods with the main three being: size, shape, and topology (top-op) as demonstrated in Figure 2.6. Sizing optimization handles the problem of determining the optimal size of a given member within a structure that varies typically with member thickness. Of the three methods mentioned, this is the easiest and earliest approach to improving structural performance. The second option, shape optimization, includes the shape parameters as design variables that change the domain to achieve optimal layout. For example, the location of the nodes on a truss are defined as the design variables. Lastly, topology determines material distribution to satisfy structural and mass requirements. This method is the most challenging opportunity; however, it provides the best

optimization results [31, 32]. In the paragraphs that follow, research is described that uses topology optimization to improve heat transfer characteristics and reduce mass in several IC engine components.

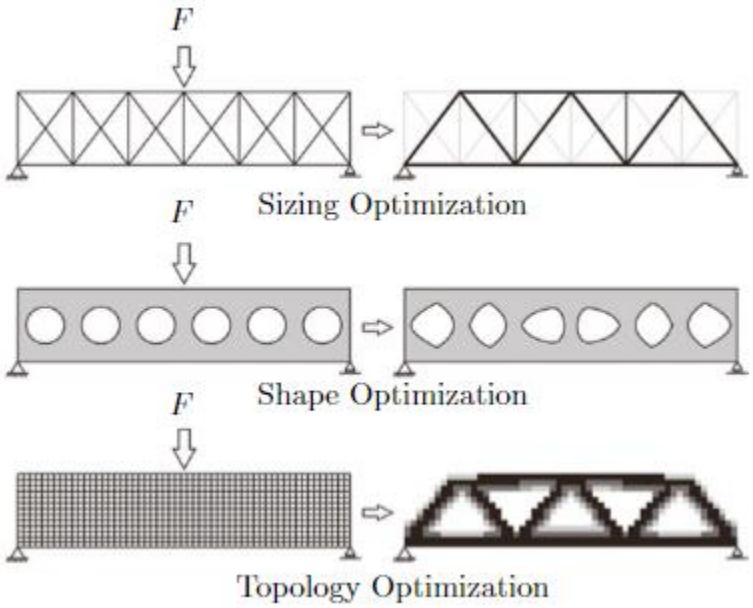


*Figure 2.6: Comparative illustration of the different optimization strategies [31, 32]*

The piston is the main alternating component in an IC engine; hence, minimizing its mass will help reduce inertial forces. Nonetheless, the automotive industry is moving towards boosted, high compression ratio engines using advanced spark timings (for efficiency purposes) that cause greater engine pressures and temperatures. Therefore, continued use of lightweight aluminum may be problematic for future piston components. Instead, employing AM steel given its enhanced density should be considered. Regarding this concept, Marchesi et al. analyzed three significant piston-loading scenarios: top dead center combustion (TDCC), top dead center at the beginning of the induction stroke (TDCI), and maximum piston thrust force. The main structural features that top-op generated for each load case were identified. In particular, the geometries

under the crown and below the pin bosses (from TDCC and TDCI) and the material linking the skirt and pin bosses (form maximum piston thrust force), respectively, by the blue and yellow boxes in Figure 2.7. Then, these geometries were taken and combined in Solidworks. This was followed by a finite element analysis (FEA) that highlighted areas of large stresses subsequently fixed by making the accompanying radii larger. After this optimization process, the steel piston ended up being 9% heavier than the original aluminum version with simulation results showing that the stresses experienced were acceptable. However, a fatigue analysis demonstrated that part of the piston geometry required a more detailed review. Furthermore, a thermal analysis determined that the cooling oil flow rate needed to be increased. Overall, the steel piston did allow larger mechanical and thermal loadings to be reached, but the authors' noted that a wider redesign of the engine is needed to take full advantage of this AM component [33].

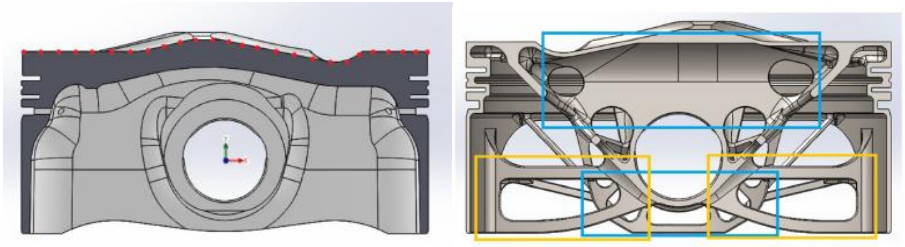

*Figure 2.7: Before (left) and after (right) topology optimization [33]*

Along similar lines, Reyes Belmonte et al. used top-op to improve the characteristics of piston heat transfer while reducing its mass. Previously, piston-cooling techniques included squirting oil under the piston crown, adding internal cooling, or using salt-core galleries. Traditionally, squirting oil under the piston crown has been employed along with internal cooling galleries for CI engines, and aluminum pistons with salt-core galleries for Spark Ignition (SI) engine applications. This is because the temperature reductions observed from oil squirting alone

are not deemed sufficient for high power density engines. Internal cooling galleries are not used for SI engines due to the increased complexity resulting from their smaller size. However, Reyes Belmonte, et al. explored the potential of a liquid cooling gallery for an SI engine using AM as a fabrication method. In their effort, they investigated the peak pressure case with inertia relief at 2000 revolutions per minute (rpm) and a corresponding case at 6500 rpm. Furthermore, temperature fatigue data based on a previous thermal analysis were used to calculate the fatigue safety factor (SF). The results showed that the top-op designed cooling gallery lowered the temperature observed at the piston topland and rings by 33°C. Moreover, the temperature reduction from the cooling gallery allowed the top ring of the piston to be moved closer to the crown. This can reduce the crevice volume between the cylinder wall and piston before the first ring, which is the largest contributor to hydrocarbon (HC) emissions.

Subsequently, an FEA was performed to determine the mechanical stress distribution on the piston due to this ring movement. It showed that the SF increases with the groove moved up because of a larger wall thickness. Furthermore, they speculated that this 2 mm move would reduce HC emissions by approximately 10% based on trends found in other research. In order to build on these outcomes and lighten the piston weight, designs with a lattice structure under the piston head were proposed as shown in Figure 2.8. Again, finite element and thermal analyses were performed with the area first modeled as a void and secondly as a volume with half the material density. Unfortunately, the void option resulted in a piston with a minimum SF of 0.9, which is not acceptable. Comparatively, halving the material density ended up with a 9% lighter piston while incurring a minimum SF of 1.0 [34].

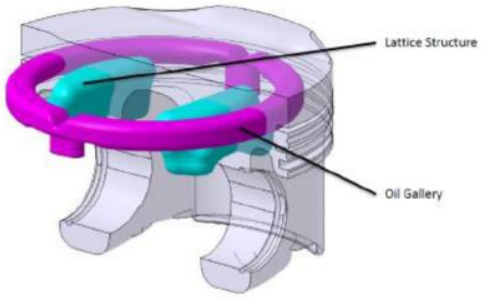


*Figure 2.8: Piston with new components highlighted (pink: oil gallery, blue: lattice structure) [34]*

Not only are IC engines operating with greater temperatures and compression ratios, but modern IC engines require proper gas flow handling in smaller space constraints. Hence, new cylinder head designs are guiding the exhaust gas to the turbocharger system using an integrated exhaust manifold (IEM). This improves weight, cost, and stoichiometric operation of gasoline engines while causing elevated exhaust gas temperatures. Building on this concept, Hopf et al. investigated an advanced boosting concept where two turbochargers are served by two separate exhaust manifolds. Within their design, the outer exhaust ports of the IEM are bent severely within a small space. Furthermore, flow cross-sections are reduced by valve stems, the spark plug, the valve guide, and head bolt cutouts. As a result, this leads to a greater pressure drop through the manifold causing a reduction of volumetric efficiency, higher emissions, and increased fuel consumption. Therefore, to improve this situation, Hopf et al. used a combined optimization strategy based on a computational fluid dynamics (CFD) top-op, followed by CFD shape optimization to maximize the flow through each exhaust port as shown in Figure 2.9. Specifically, the main task was to optimize the port shape to increase the mass flow rate at a given pressure drop. To run the analysis, the design space is first defined as set by the other components. Since it is currently not possible to use top-op with CFD for transient problems, a

steady-state assumption was used. Next, the optimization creates a brick model (sometimes described as a checkerboard), which is smoothed. This resulted in reduced flow velocities around bends with the mass flow rate increasing by more than 4%. Then, the smooth top-op surface is used to set up a shape optimization with pressure drop defined as the objective function. The result was a growth in the mass flow rate by 8% as compared to the baseline configuration. After design finalization, the sixth port flow coefficient was increased by 18% and the entire IEM had an 11% improvement with respect to the flow coefficient and mass flow rate [35].

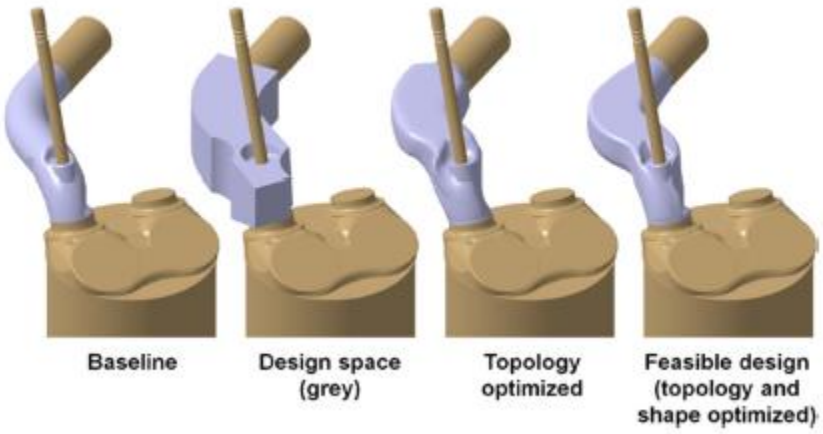


*Figure 2.9: Optimization steps illustrated on port 1 [35]*

Instead of focusing on IC engine components, Marchesi et al. found it advantageous to investigate engine mounts for a CI engine. Here, the goal was to maximize stiffness while satisfying a volume constraint. The first step of their process in Figure 2.10 included defining the design domain definition by setting up boundaries, loads, and outlining space constraints. This associates a pseudo-density to each element within the stiffness matrix, subsequently creating a density distribution. The next step involves starting the optimization loop with the FEA equilibrium equations solved to obtain sensitivities. Then, a filtering technique is applied to

remove the checkerboard-like pattern (previously described as a brick model); hence, creating a smooth surface. Finally, an optimization algorithm is employed, and the process is rerun if a specified convergence is not met. For use within the simulation, engine loads were found using accelerometers while testing a prototype of the vehicle on a track to simulate the worst conditions normally found for this application. Based on the data collected, the free body diagram of the main masses of the engine forces were found along with hub loads (for secondary purpose of mounting). After 40 iterations, the optimization process led to a maximum attainable stiffness with the least amount of material; however, the authors did not provide any comparative stiffness or weight values in their paper [32].

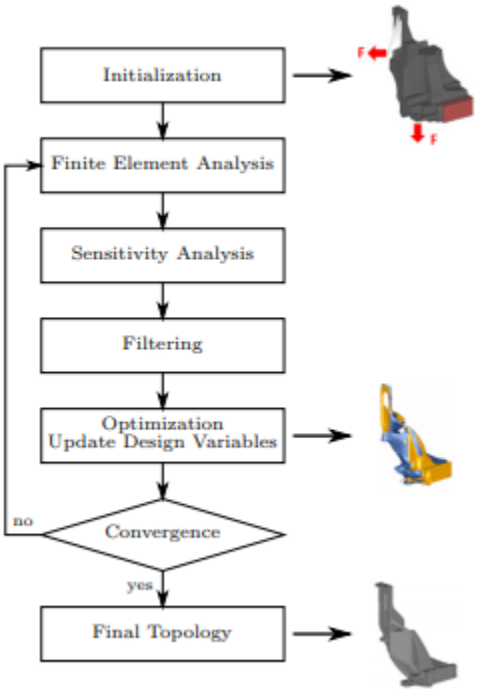


*Figure 2.10: Topology optimization process for diesel engine support [32]*

In another paper, Orquera et al. used top-op in conjunction with a proposed global design methodology for AM to optimize a mechanical system by reducing parts and mass while improving functionality (Figure 2.11). Their case study investigated a compressed air engine consisting of a crankshaft, connecting rod, piston, oscillating cylinder, inlet, and exhaust. All parts were manufactured with AM except the crankshaft and guide shaft. While not specific to an IC engine, the analogous structures (e.g., connecting rod) demonstrate how this process might be applicable for IC engines.

Their optimization strategy consisted of three stages. First, the introduction stage defines the general specifications and an external functional analysis is performed to identify areas of improvement along with how the pertinent variables affect one another. Then, an internal functional analysis is performed on each rigid body or part to define all surface functions and whether or not they have an impact on the system's features. At this point, ideal shapes are proposed, and the design space is defined. The second stage involves optimizing while considering the constraints and opportunities of AM. This stage initially consists of architectural and topology optimizations that finds the optimal locations of features to improve functionality. Moreover, it optimizes for the objective chosen by the designer (e.g., reduced mass or increased stiffness). Consequently, the CAD results and all functions previously stated are analyzed and designed to improve the mechanism while considering AM constraints. Afterwards, each body is checked to respond to the internal functional analysis and the preliminary design is modified accordingly with an FEA performed based on the design changes. Then, CAD findings are used to verify fits and non-interferences. Furthermore, mechanical studies and behavior differences from the first stage are analyzed with respect to expected and obtained results. This brings the

optimization into the final stage that includes preparation for manufacturing, such as choosing the optimal build direction and part orientation. If necessary, manufacturing design changes are made including adding material to machined surfaces and reducing overhangs. Finally, the design is verified by performing a final FEA while investigating machining and assembly forces.

As a result, the engine is optimized via two procedures: First, on a part-by-part basis and second with the methodology described previously. Overall, the first optimization slightly improved performance by decreasing the disruptive mass and inertia, which reduced the pressure drop and friction. The second optimization further improved the design by reducing mass subsequently diminishing friction, thermodynamic losses, leakages, inertial losses, and the pressure drop [36].

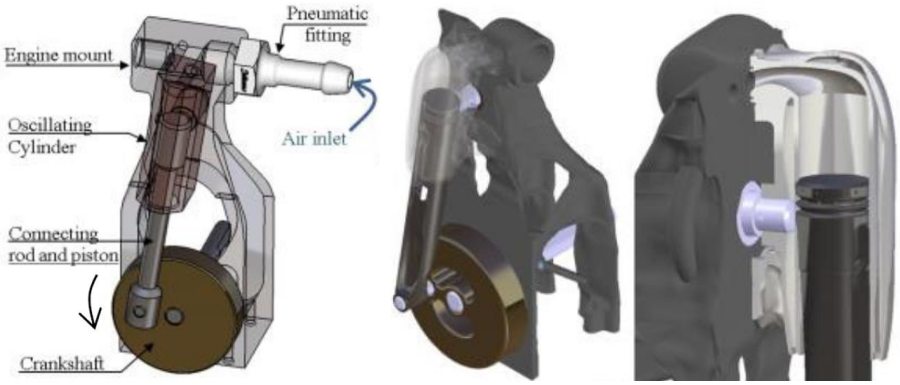


*Figure 2.11: Compressed air engine original (left) and after optimization (right) [36]*

## 2.6 **AM Part Production for Research**

There have been relatively few AM studies accomplished with respect to IC engines. Furthermore, a respectively smaller number of efforts include actual manufacturing of the AM

part and experimental testing for comparative purposes. Here, the first study outlined in this section demonstrates the manufacturing implications of producing a functional AM part. The subsequent studies prove that an AM part is capable of operating effectively within an IC engine powertrain.

A formula SAE team used fused deposition modeling (FDM) with a plastic material to create their intake manifold. When compared to the welded aluminum pieces in the previous design iterations, the FDM manifold had improved pressure losses that increased torque over an extended speed range and provided a more equal charge to each cylinder. This also allowed for a 22% decrease in weight [37]. Similarly, Johnson et el. used AM to prototype three different manifold geometries for a 10 cc, single valve, two-stroke engine while investigating the swirl behavior resulting from each. Because achieving sufficient scavenging at high speed is difficult for these engines, the manifolds are designed to induce enhanced port swirl. In this study, through a combination of experimental and computational approaches, it was shown that the initial configurations substantially reduced performance and that geometric modifications were needed for future testing. In addition, it was determined that improvements made to the flow test rig were necessary for further development of the intake manifolds [38].

In another paper, Schlier et al. explored the possibility of using a 3-D printed macro-cellular silicon-based lattice structure (reactor) to mix air and fuel with the fuel jet injected by a high-pressure valve for nonstationary combustion under piston engine-like conditions. The porous burner combustion technology allows premixed fuel and air to burn within the cavities of a solid porous matrix, the results of which are typically ultra-low exhaust emissions and stable operation. Moreover, specifically because of the low emissions possibility, the authors believed

this effort could be applicable for IC engines. To test this porous structure, a high temperature, high pressure, adiabatic and constant volume combustion chamber was developed. Figure 2.12 shows the diesel fuel distributions by a high-pressure valve produced by the different test configurations inside of this chamber. The results of testing showed that the heat capacity and heat transfer in the reactor made the heat release process faster but did not significantly reduce the temperature while decreasing the pressure peak [39].

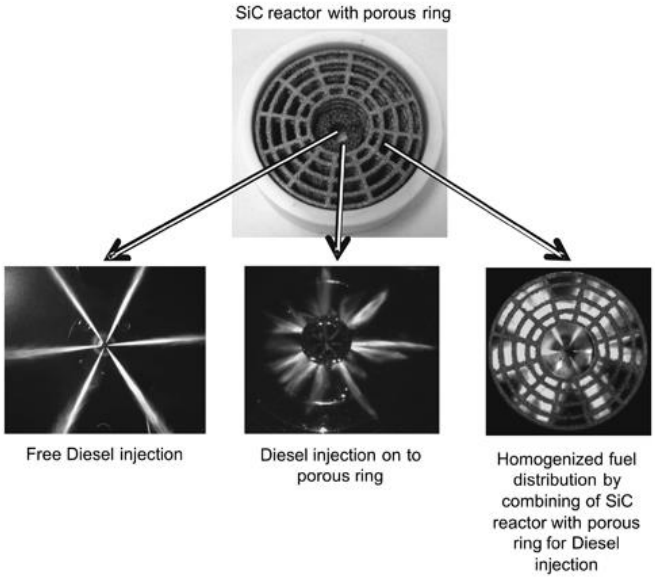


*Figure 2.12: Fuel distribution produced by three test configurations [39]*

With respect to AM, numerous parameters are involved in creating a functional part and the majority come into play during post-processing. For example, a study by Baudana et al. highlights the heat treatment required to obtain a final microstructure capable of being used. In their work, they utilized the electron beam melting (EBM) process of $Ti_{48}Al_2Nb_{0.7}Cr_{0.3}Si$ when constructing a rotor wheel for a turbocharger (Figure 2.13). They found that there was porosity present due to the entrapped argon in the powder particles formed during the gas atomization

process. However, because of their small size, these pores were determined not to influence mechanical properties. Moreover, the EBM process itself did not cause this porosity and the part was considered acceptable without heat treatment from a microstructural standpoint. Nonetheless, full lamellar microstructures are preferable for the high temperature properties (e.g., creep and fatigue resistance) desired in a turbocharger application. In addition, a lamellar microstructure has low room-temperature ductility and strength; hence, it was decided that a near lamellar microstructure with a high percentage of lamellar grains surrounded by equiaxed grains was desired. As a result, a heat treatment of 1360 ºC for 2 hours was employed to achieve this structure, subsequently increasing both part ductility and strength. Furthermore, an average roughness of the EBM specimen was 30-40 μm in terms of Ra, suggesting that post machining and/or adjustment of EBM parameters during construction (e.g., scan pattern or beam strength) is necessary. Overall, it was concluded that the EBM process could produce turbocharger wheels with reduced weight comparable to those traditionally manufactured once the correct post-processing steps were taken [40].

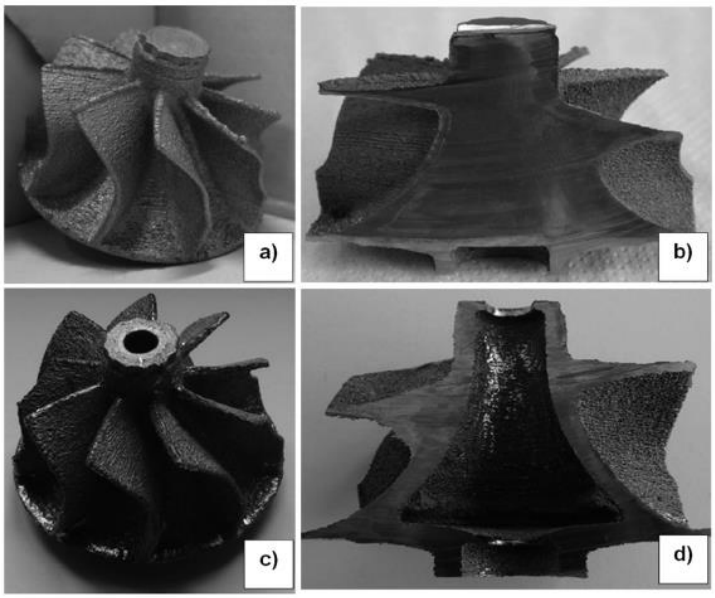


*Figure 2.13: Turbocharger wheels produced through EBM [40]*

In this area, Oak Ridge National Laboratory was the first to conduct AM engine testing. They performed their experiments using a 4 cc, two-stroke, single cylinder, carbureted, glow-ignition engine with no piston rings. Traditionally, this engine is used in applications for Remote Control (RC) airplanes and has an operating speed range between 2,500 and 19,000 rpm. In their efforts, an AM titanium (Ti) cylinder head was fabricated with an added sensor port to measure the in-cylinder pressure during testing. Of note, the original aluminum (Al) head did not have the wall thickness needed to support the pressure sensor. Their results found that engine brake torque was generally similar for both Ti and Al heads. However, at 4000 and 6000 rpm, the maximum brake torque (MBT) was higher for Al; whereas, at 2000 rpm, the Ti head performed better. In addition, the Al cylinder head produced a greater power output and ran more efficiently at higher speeds. However, at lower speeds, the Ti head demonstrated a larger efficiency. Furthermore, the Ti head reached MBT at a leaner mixture than Al because of its reduced level of heat transfer

and greater combustion efficiency. The authors concluded that the reduced power performance of the Ti head might be a result of the disruption in charge motion from the pressure sensor that protrudes into the cylinder, which may negatively affect the two-stroke scavenging process. Another potential reason for reduced performance with the Ti head could be from increased frictional losses. Specifically, the use of Ti with a lower thermal expansion coefficient than Al might lead to higher combustion temperatures (again, a decreased heat transfer rate) and a greater expansion of the piston relative to the cylinder. Overall, the titanium head was used for more than 20 hours of testing without failure [41].

Analogous work by Cooper et al. investigated the benefit of using AM to produce lightweight engine valves. Particularly, lighter valves could help reduce parasitic losses while improving valve response and engine control at the same time enhancing the cooling process with internal liquid sodium. First, an AM valve was reversed engineered by Computed Tomography (CT)-scanning an existing valve, and then generating a CAD virtual valve. Then, two concept valve designs were generated from modeling the forces of combustion including a SF. The first valve was created in Solidworks by adding structural features, and a meshing package was used to generate the internal lattice structure for the second valve. Inconel 718 was chosen as the AM material to match the requirements of the application. Specifically, this includes high yield and ultimate strengths at 600-700 ºC, high wear resistance, and low thermal expansion along with high hardness and weldability (note: Ti's mechanical properties deteriorate rapidly beyond 600 ºC). Furthermore, 0.38 mm was added to all outer surfaces to allow for machining and grinding by a conventional valve manufacturing process to obtain the surface smoothness needed. Moreover, sacrificial material was added to the head for wire Electrical

Discharge Machining (EDM) removal from the build plate. After construction, annealing and age hardening heat treatments were applied to reduce the residual stress, subsequently improving mechanical properties. Then, the powder was removed and inside sealing lids were press fitted to the valve tips and laser welded in place. Once post-processing was complete, the valves were scanned and checked against the production CAD file for internal feature accuracy. After engine testing on a KTM 525 EXC 2006 for a total of 1 hour and 8 minutes, the valves were scanned one additional time to check for fatigue crack formations.

Based on their modeling efforts, significant weight savings were generated; however, there was an appreciable increase in stress. For example, the lattice component provided a 30.7% mass reduction, but the maximum stress it experienced was unfavorable (early fatigue failure). Comparatively, the second design saved 29.4% in mass with a 12% increase in stress (Figure 2.14). All surfaces were found to be within 0.15 mm of the original design, and no defects were found in the AM valve head. However, a number of small spherical voids were observed at the weld site at the top of the shaft [42].

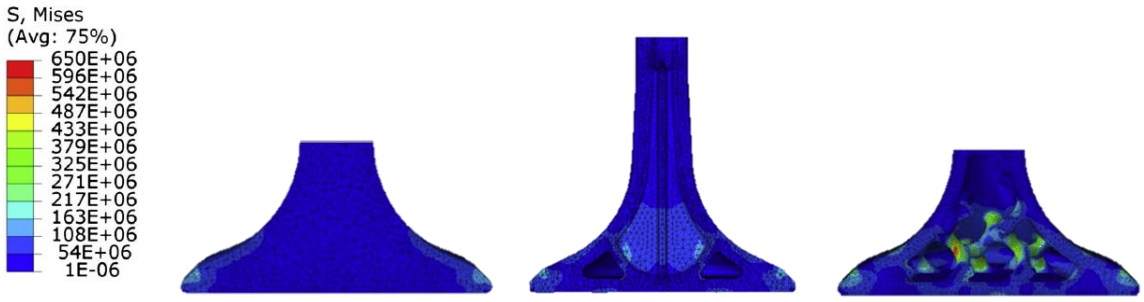


*Figure 2.14: Valve configurations and their stress distributions [Pa]: original (left), first valve with added structures (middle), and second valve with added lattice (right) [42]*

## 2.7 **Industry Claims for AM Part Production**

Since this field is respectively new, various companies are investing in AM to obtain a competitive edge. As a result, many have indicated several advancements in their manufacturing of automotive parts; however, there are no comparative data or publications backing up their claims. For example, Renault stated in a press release that they have reduced the weight and number of components in their engine by 25% each. More impressively, they indicated that they have completed a 600-hour bench test of AM rocker arms and camshaft bearing caps successfully [43]. Similarly, Volkswagen claims to have produced a fully functional AM cylinder block with the cylinder liner coated using an air plasma spray process. Furthermore, they mentioned that the water connectors used for the Audi W12 engine are created by AM [44, 45]. Moreover, Roush has successfully used AM in the construction of a cylinder head with $AlSi_{10}Mg$ helping to illustrate for their customers how make prototypes and develop new technologies more quickly (i.e., days instead of months) [46].

Along similar lines, Koenigsegg produced an AM variable turbocharger for their one:1 car and were able to produce the parts at a lower price than casting (note: low part production) while achieving the necessary geometries without any of the post retrofitting [47]. Another IC engine research and development company, Lumenium, partnered with Desktop Metal, a 3-D printing company to investigate the product development timeline, weight, and cost of machined parts versus AM parts. Their case study was able to show that the production of a saddle carrier, swing arm, and connecting rod was 74% cheaper, 43% faster, and 39% lighter when using AM [48]. Finally, other AM construction efforts can be found online for IC engine parts, including gearboxes, oil pump housings, and other components [49].

## 2.8 **Conclusions**

The field of AM is still relatively new with respect to IC engines, as is evidenced in this chapter. Currently, the major areas of research involve using AM as a steppingstone in the manufacturing and design process. Other areas focus on the theoretical opportunities that AM provides, while mostly failing to implement these ideas into real life application testing. Perhaps, the widest use of AM for IC engines is within motorsport and luxury vehicles, where vast resources are available and production is low compared to the consumer market. However, due to the competitive nature of these industries, there is limited information available on what is being accomplished.

The research in the following chapters will not only extensively review the entire process in designing and additive manufacturing major IC engine components, but it will also attempt to qualify the results of this process by visual inspection, porosity analysis, and real-life testing on an engine dynamometer. It is through this work that AM will hopefully be shown as a more viable option for larger aspects of IC engines.

# Chapter 3: AM Process for Major IC Engine Components

## 3.1 **Introduction**

Additive manufacturing (AM) has numerous potential benefits, especially when considering the production of an internal combustion (IC) engine. Since AM does not have the same constraints that limit traditional methods, such as casting or Computer numerical controlling (CNCing), when used in conjunction with Topology Optimization it allows for the production of lightweight designs with organic-like configurations capable of the same strength and/or stiffness values as their heavier counterparts. Hence, it could be valuable in facilitating the reduction of part weight and quantity, which would result in a lowered cost and better fuel economy along with increased part performance and reliability. Additionally, AM allows for manufacturing at the point of need. This means a decreased necessity for storage of spare parts or dies and reduced lead times, subsequently permitting parts to be returned to use in the field faster.

This chapter will discuss the entire LPBF AM process and difficulties that come with manufacturing IC engine components this way. The engine chosen for this study is a Saito FG-11 engine, most commonly used for remote control airplanes, but its application could be scaled and extended to unmanned aerial vehicles (UAVs). This four-stroke, 10.6 cc, spark-ignition, IC engine uses a 20:1 mixture of regular gasoline and two-stroke oil. An exploded view of all the components can be found in the Appendix (Figure A.1). The complex parts that make up most of the weight are the cylinder head and crankcase, numbers 1 and 15, respectively (Figure A.1). Therefore, these two parts can benefit the most with regards to weight loss from using AM and

are chosen for this analysis. Ultimately, the goal is to compare the stock Saito FG-11 engine to the AM version, with the results demonstrating the differences using an AM process.

First, these parts are reverse engineered by taking measurements, modeling, and verifying the models through dimensional analysis. Next, the materials and machines to be employed are considered. Here, it is important to note that with AM, there is more flexibility in material choice including lightweight materials, such as titanium (Ti) and magnesium (Mg). For the crankcase and cylinder head, Ti-6Al-4V on the 3D Systems ProX DMP 320 and AlSi12 on the 3D Systems ProX DMP 300 are the materials and machines chosen, respectively. In order to achieve the correct tolerances and features, adjustment of the models to allow for post machining of critical geometric features was accomplished. In addition, the models were modified to enable a more successful production process using AM. This included adding fillets to sharp corners and eliminating unnecessary overhanging geometry. Following this, the AM supports are designed, and the parts manufactured. Next, the AM constructed components are checked for porosity and defects, before a final post machining process occurs in order to achieve suitable versions.

### 3.2 **Material Determination**

MIL-HDBK-5 lists four types of mechanical properties for the materials presented, these include: typical, S, B, and A-basis. A-basis materials indicate the highest statistical confidence, with 99% of the population expected to be equal or exceed the mechanical property value with a confidence of 95% [50]. Traditionally, in aerospace applications, fight critical components such as engines and primary structures require designs using A-basis material values. Therefore, due to its high thermal conductivity and its ability to maintain sufficient mechanical properties at typical engine operating temperatures, most of the top performing .20 -.60 size commercial

aircraft engines today are composed primarily of 7075-T6 Al or similar alloys. While Ti-6Al-4V (Ti64) may have more room for optimization because of its higher specific strength, some of the biggest deterrents against it as an engine material are related to its reduced ability to bleed heat (because of relatively low thermal conductivity), manufacturing challenges (difficult to cast and machine), and high bulk material costs. Because of these aforementioned issues, there has not been much research involving its use in engines or with optimizing components for the higher temperatures that would be produced. Moreover, Wu et al. demonstrated that although fatigue averages for Ti64 are acceptable, there is considerable scatter [51]. This platykurtic distribution leads to extremely low A-basis values with respect to many aluminum and steel alloys. This, in turn, would eliminate it as a contender in many aerospace applications.

Here, the stock Saito FG-11 engine is of a die cast aluminum (Al) design and through a Vickers hardness test (Appendix Figure B.1, Figure B.2, and Figure B.3) along with the use of a handheld X-ray fluorescent (XRF) gun (79.39% Al, 17.35% silicon (Si), and 1.81% copper (Cu)), the specific alloy of Al identified is Al 390 [52]. When deciding what materials to use for AM of the cylinder head and crankcase, the choice between Ti64 and AlSi12 had to be made. Given that AM materials do not yet have standards and specifications in place [53], the previous mentioned material considerations did not go into the decision. Moreover, the goal of this specific research is to prove the feasibility of AM in producing a working engine, with the main application being emergency part replacement of Army UAVs. However, in the future when specifications are in place, they should be heavily considered when making any design optimization choices for any UAV engine.

For the crankcase Ti64 was chosen due to its high specific strength (203.16 kN·m/kg) that would allow for future optimization efforts [54]. Since the crankcase is not where most of the heat from the combustion process is contained, this material choice should not greatly influence temperature. Later results confirmed this hypothesis, with the AM crankcase giving values only 10 C higher than the stock engine (Figure 5.12). However, for the cylinder head, the use of Ti64 is more complicated. Investigating thermal expansion and conductivity parameters finds that Ti64 has lower coefficients of thermal expansion and conductivity ($8.6\times10^{-6}$/C and 6.7 W/m·K), respectively, as compared to 21.5-23.6$\times10^{-6}$/C and 130-222 W/m·K for aluminum; hence, operation of the engine could be significantly affected if Ti64 was used for the cylinder head [54]. Specifically, this difference in material properties would require a larger cylinder bore to prevent seizure with the Al piston once components are at their operating temperature (OT). As a result, this would influence the initial combustion event while additionally causing increased blow-by past the piston until the engine has achieved a steady-state OT or even inability to create compression at lower temperatures.

Moreover, if the cylinder head were made of Ti64, the engine would reach higher temperatures, potentially causing other components to fail that were not designed for such temperatures. When considering the engine is fuel cooled, experiencing these higher temperatures will work towards breaking the oil in the gasoline down, rendering it ineffective as a lubrication and cooling agent. This would then put the engine at risk for thermal runaway. These effects could be mitigated through an optimized heat transfer design with the air cooling or perhaps water-cooling designs, however it most likely would not be enough of an effect to overcome the differences caused by the change in material. Additionally, the increased operating

temperatures will cause an increased thermal expansion from the piston and therefore put the engine at heightened risk of seizure. Piston growth can be roughly estimated with Equation (1) (estimation of thermal expansion of a thin circular ring) where $d_1$ and $d_0$ are the post and starting ring diameters, $\Delta T$ is the change in temperature, and $\alpha$ is the coefficient of thermal expansion [55]. Based on this equation, even a 50 °C increase in operating temperature (from 175 °C) would cause the piston to grow an additional 0.03 mm. Relative to the engine size, this is significant, and again, even if the cylinder bore is made larger to accommodate this difference, more blow-by or the inability to create compression will be experienced at lower start-up temperatures.

$$d_1 = d_0 [\Delta T \, \alpha + 1] \tag{1}$$

Finally, Ti is prone to galling (i.e., tearing of material under friction); whereas, the high Si content in the Al powder provides additional wear resistance and allows for the elimination of a cylinder liner; thereby, reducing weight and complexity [56, 57]. In contrast, one benefit of using a Ti64 cylinder head and achieving higher OTs would be a more complete combustion process that could increase efficiencies; however, these greater temperatures would grow the level of dissociation and subsequently produce more nitrogen oxide ($NO_x$) emissions. In addition, if the bore is not made wide enough, these enhanced temperatures could promote the pre-ignition (aka knock) phenomena [58]. When coupled with un-optimized engine components, the complications resulting from using a Ti64 cylinder head are not worth the limited benefits it would provide, therefore AlSi12 is chosen.

## 3.3 **Reverse Engineering**

In many military applications, if a vehicle or aircraft breaks there is not a drawing associated with the broken part (e.g., it has been lost or not filed over the years) and even less likely a corresponding Computer-Aided Design (CAD) file. As a result, being able to reverse engineer these parts in the field is an essential tool. Since Saito is a Japanese company, much of their product information is not readily available or released to the public. Subsequently, this project was started at the same point as many components in the military; i.e., only the information provided by the part itself is available. Therefore, using caliper, telescoping gauge, and micrometer measurements along with inferences based on the bearings and screws used, a CAD model was generated for both parts in SolidWorks.

In order to check the viability of these CAD files, the original cast parts were X-ray computed tomography (CT) scanned with a Zeiss Xradia 520 Versa (micro CT) device. Additionally, a nominal/actual dimensional comparison analysis was performed between the CT scans and the CAD files using Volume Graphics Software (Figure 3.1). The initial analysis found that the CAD files came surprisingly close to the CT scans; however, there were a few areas that were tweaked for better results. The major geometric regions in need of adjustment were those that were difficult to measure; hence, approximations had to be made. For the crankcase, these included the sloped surface on the inside of the crankcase, the location of the drain hole on the bottom, and the angled sensor holes. For the cylinder head, the areas requiring tuning were the angled spark plug surface, the upper internal geometry of the cylinder, and the angled features where the valves are located.

Once the models were adjusted and all critical regions were within acceptable ranges, the CAD files were finalized (Figure 3.2 and Figure 3.3). It should be noted that some outer geometries were out of range, but they were considered of low importance and close enough for this exercise. Throughout this entire process, developing accurate CAD files took a close second to post machining in regards to the amount of time spent. Hence, when adapting this process in the field, having individuals with prior modeling skills would be extremely beneficial.

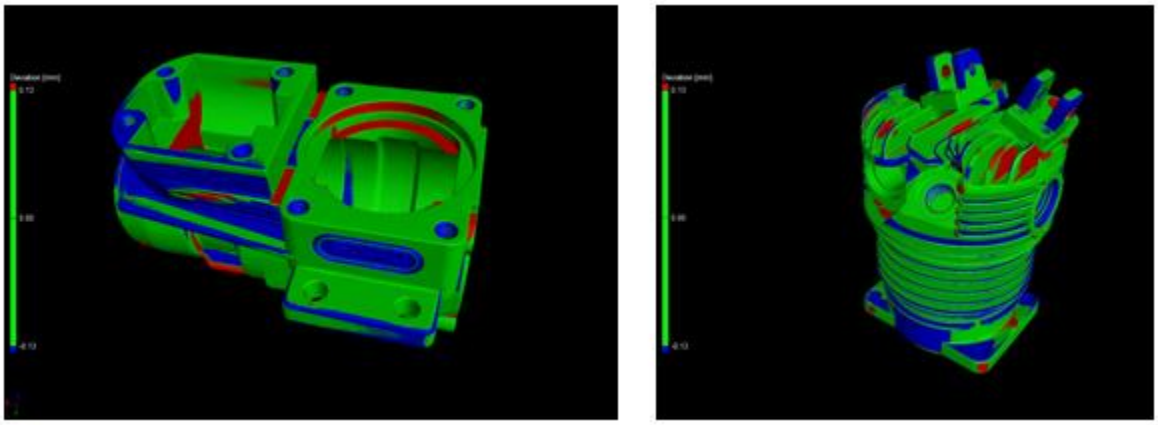

*Figure 3.1: Nominal actual dimensional analysis of cast parts vs. CAD files for crankcase (left) and cylinder head (right)*

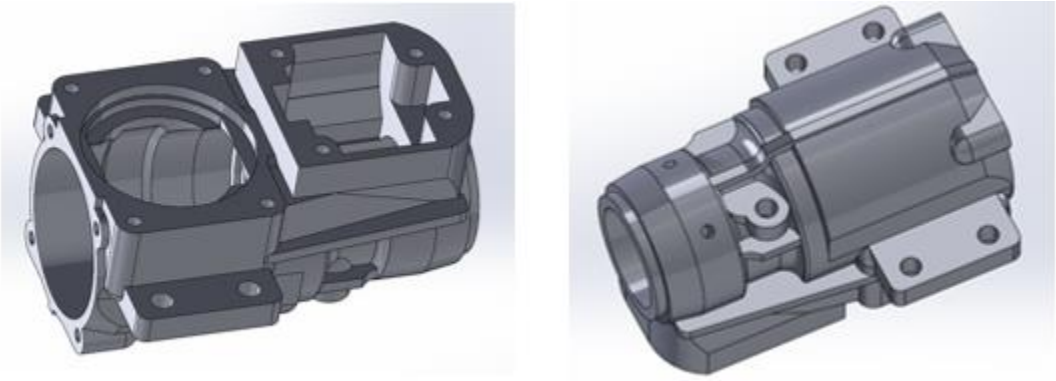

*Figure 3.2: Finalized CAD model for crankcase*

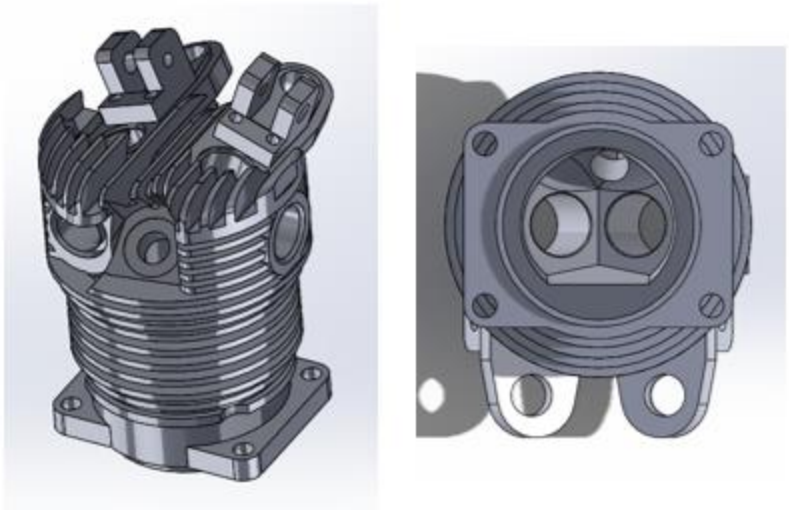

*Figure 3.3: Finalized CAD model for cylinder head*

## 3.4 **Identifying Critical Tolerances**

Typical AM machines are not capable of producing relatively high tolerances. For example, the company 3D Systems claim a minimum accuracy of 0.002″ (50 µm) for their ProX DMP machines. However, as indicated later, this is not always the case due to variations in how the build is setup or supported [59]. After deciding on the material, the next step is to identify the critical tolerance areas for both parts. Specifically, for the crankcase these areas are the two inner bearing surfaces highlighted in Figure 3.4 (a view from the crankcase drawing found in Appendix Figure A.2) , that both require a JS7 fit which equates to a tolerance of ±0.0004″ (±0.011 mm) [35, 58]. Furthermore, keeping these bores concentric is essential for balanced engine operation; otherwise, the vibration induced could destroy the engine. Hence, the runout/alignment/concentricity cannot exceed 0.0003″ (±0.008 mm) [60, 61]. Moreover, meshing of the cam gear and crankshaft along with the alignment of the piston connecting rod and the crankshaft journal is important to ensure the cam gear is rotated so that the valves open

and close appropriately while keeping the crankshaft from experiencing excessive bending forces. Therefore, the heights of the upfacing gasket faces must be within ±0.003″ (±0.08 mm). Additionally, the location (depth) of the larger bearing surface is important to ensure the crankshaft is in the correct location allowing the piston to line up with the cylinder, requiring it also have a ±0.003″ (±0.08 mm) tolerance. It is also important for all threaded holes on these surfaces to be placed correctly so that the cylinder head and cam gear line up with the crankshaft in the *x* and *y* directions. Thus, a ±0.003″ (±0.08 mm) tolerance is placed on those locations. Finally, all other tolerances were kept within ±0.005″ (±0.13 mm) as to not hinder clearances or allow for excessive removal of material, which would lower the safety factor.

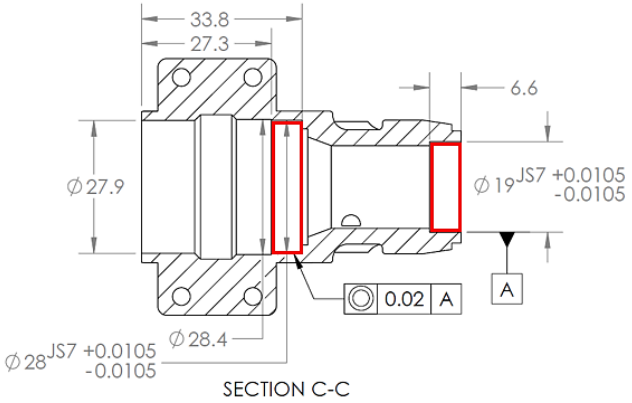


*Figure 3.4: Crankcase drawing section view, units in mm*

For the cylinder head, the cylinder wall requires special attention. Explicitly, the goal is to not use a cylinder liner; thereby, reducing complexity and the number of parts for the engine (an advantage of the AM process). As a result, a complex multi-step honing procedure is required that will be explained further in the post-processing section. Essentially, the silicon in AlSi12 needs to be exposed and a surface finish of 6-10 Ra (roughness parameter) achieved to reduce friction and give an ideal surface for the piston rings to seat [56]. Additionally, the valve

guide bores will need to have a 0.002″ (0.05 mm) interference fit (red circles in Figure 3.5). Once at operating temperature, the aluminum bore will expand more than the brass guide will; hence, an interference fit is required to retain the brass guide. This interference fit also ensures efficient heat transfer from the guide to the cylinder head [62, 63]. Moreover, the chamfer where the valves seat at the top of the cylinder requires consideration to ensure that they sit flat and provide an air tight seal so the cylinder can hold pressure for combustion (right depiction in Figure 3.5). To obtain this feature, a 15 Ra surface finish must be achieved [64]. As previously stated, the holes for the screws to attach the cylinder head to the crankcase must be aligned with a ±0.003″ (±0.08 mm) tolerance, and all other tolerances will be kept within ±0.005″ (±0.13 mm). The complete drawing for the cylinder head can be found in the Appendix Figure A.3.

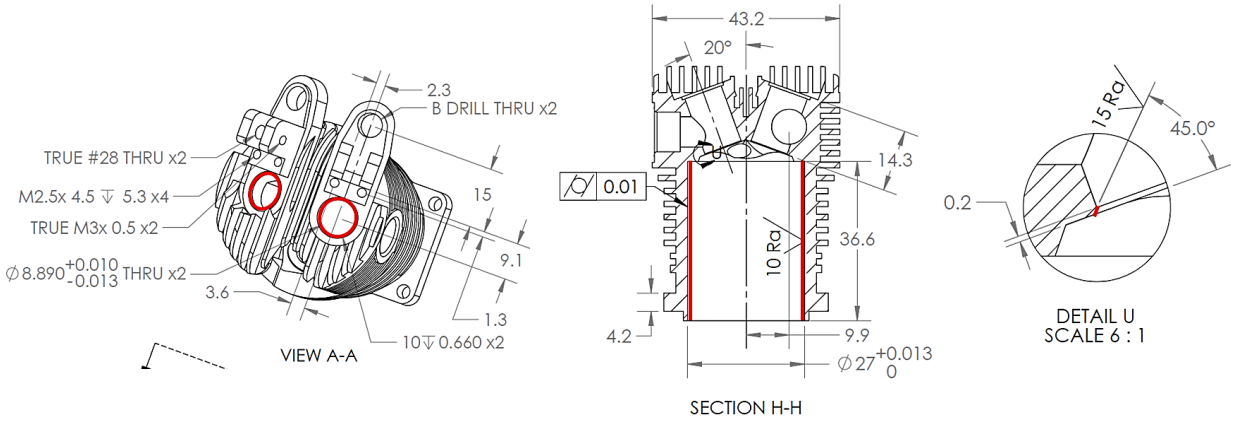


*Figure 3.5: Cylinder head drawing section views, units in mm*

## 3.5 **Model Preparation**

Because AM is reliant on support structures, any overhanging areas are prone to distortion. To prevent this, all holes are filled to a 0.05″ (1.27 mm) diameter; hence, they essentially become pilot holes for later machining. Additionally, since AM cannot achieve the

tolerances and surface finishes necessary for gasket faces and bearing surfaces, 0.03″ (0.76 mm) of material is added for subsequent machining (highlighted in Figure 3.6). Figures of the surface finish profiles and R-values of the un-machined material for both AM parts (Ti64 and AlSi12) and cast parts are provided in the appendix (Table B.1, Figure B.5, Figure B.6, and Figure B.7). Furthermore, for the cylinder head, 0.05″ (1.27 mm) was added to the cylinder walls in case any porosity occurred just below the surface.

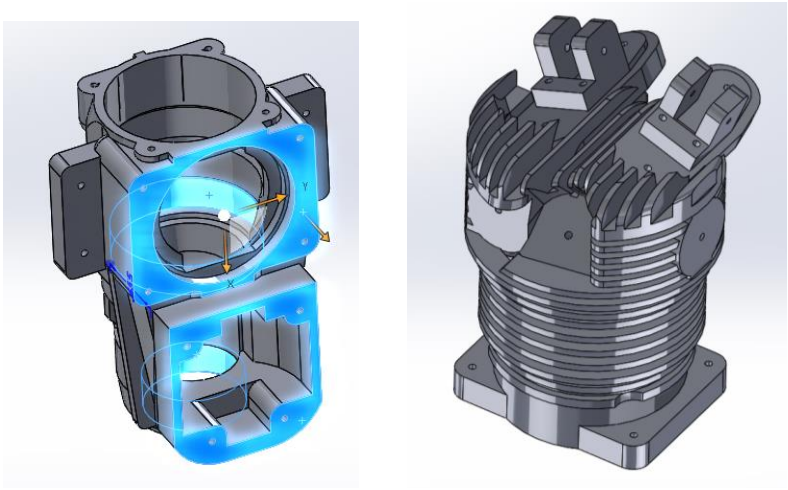

*Figure 3.6: Model preparation for AM, with gasket faces and bearing surfaces highlighted, crankcase (left) cylinder head (left)*

## 3.6 **Machine Choice**

Laser powder bed fusion (LPBF) is an AM process in which, a part is built layer-by-layer onto a build plate by melting powder at each slice into the desired geometry using a laser set to a specific speed and power. Once the current layer is finished being lasered, then the build plate is lowered a set distance (layer thickness) and a new coat of powder is spread evenly across the surface. This is done until the machine has cycled through all slices and the part is completely

encased in powder. The choice of the machine used for both parts was based on availability, material currently in use, and the build envelope. For the crankcase, the 3D Systems ProX 320 was used; this machine has a build volume of 10.82 × 10.82 × 19.96" (275 × 275 × 380 mm) and minimum feature size of 100 µm. In addition, the ProX 320 features a recoater blade that evenly spreads the powder across the build plate by sweeping over it once. The cylinder head was printed on the 3D Systems ProX 300 that has a build volume of 10.82 × 10.82 × 19.96" (275 × 275 × 380 mm) and minimum feature size of $x$ = 100 µm, $y$ = 100 µm, and $z$ = 20 µm. Unlike the ProX 320, the ProX 300 uses a roller recoater that travels across the surface twice between each layer (across and back into position). Because the roller slightly compacts the powder, this machine is less forgiving of fine or poorly supported features. Both these machines have a repeatability of $x$ = 20 µm, $y$ = 20 µm, and $z$ = 20 µm with an accuracy of ± 0.1-0.2% within ± 50 µm minimum and a layer thickness of 10-100 µm. In addition, they both require an inert environment using nitrogen or argon at 6-8 bar [59].

## 3.7 **Support Design**

In metal LPBF AM supports are important for ensuring geometric consistency while preventing movement while printing. Solid supports are especially necessary to provide more structure and to prevent build plate and part delamination. In addition, they act as heat sinks during the AM process, aiding in the reduction of the residual stresses (particularly for Ti64) that build up due to the thermal history. The first step in designing the supports is determining the orientation of the part with respect to the build plate. Usually, this decision is based on minimizing part height to reduce build time and minimizing overhanging areas to reduce the need of supports that can cause poor surface finishes and increased post-processing. Generally,

areas with less than a 45° angle to the build plate and an area ≥ 2 $mm^2$ (0.003 $in^2$) are identified as needing support. Supports for both the crankcase and cylinder head were designed within the 3DXpert software tool.

For the crankcase, critical areas in need of support reduction were the internal features (particularly the bearing surfaces) since they would be difficult to remove and then machine to a smooth surface. Therefore, it was decided to print the part vertically with the propeller end facing down. As a result, this orientation only required one internal support. All outside supports were angled away from the part to allow them to be more readily removable (Figure 3.7).

Additionally, an alternative design modified for AM was created to minimize the need of supports and reduce the amount of post-processing. Specifically, this was accomplished by simplifying the outer geometry and eliminating many overhanging areas (Figure 3.7 and Figure 3.8). Due to these changes, the support volume was reduced from 7.55 $cm^3$ to 5.49 $cm^3$ and the area reduced from 1506.1 $mm^2$ to 1094.5 $mm^2$. However, the volume of the crankcase itself did increase from 30.27 $cm^3$ to 33.08 $cm^3$. Additional information regarding differences in the design process is presented in Table 3.1.

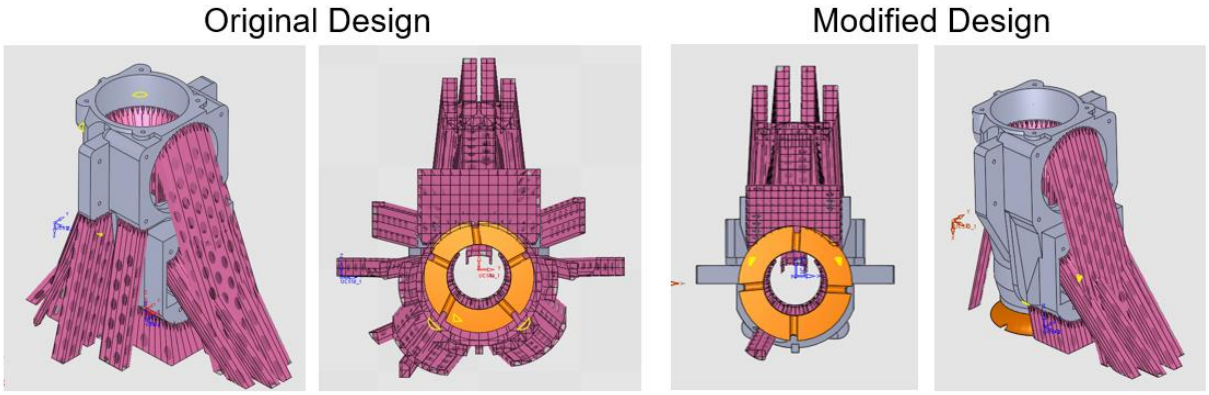


*Figure 3.7: Crankcase support designs (solid and wall supports are orange and pink respectively)*

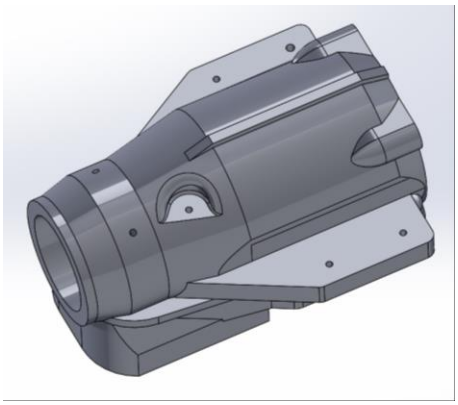

*Figure 3.8: Modified crankcase design for AM*

To design the supports, once the orientation was determined, the software (3DXpert) identified all downward facing areas and outlined them as individual modifiable regions. However, some areas had to be manually adjusted or created. For example, although a surface may not meet the criteria to require a support, it could still start out unattached from the part itself, leaving it completely unsupported. A depiction of this is shown in the left image in Figure 3.9. In addition, other areas needed adjustment because the supports were unable to be angled such that they would not hit other areas of the part before attaching to the build plate. This would make removal difficult and result in poor surface finishes wherever they attached. An example of this is demonstrated in the right image of Figure 3.9. Furthermore, additional support areas where the surface was angled at 45° were removed completely because they were deemed unnecessary or not essential in supporting any critical features.

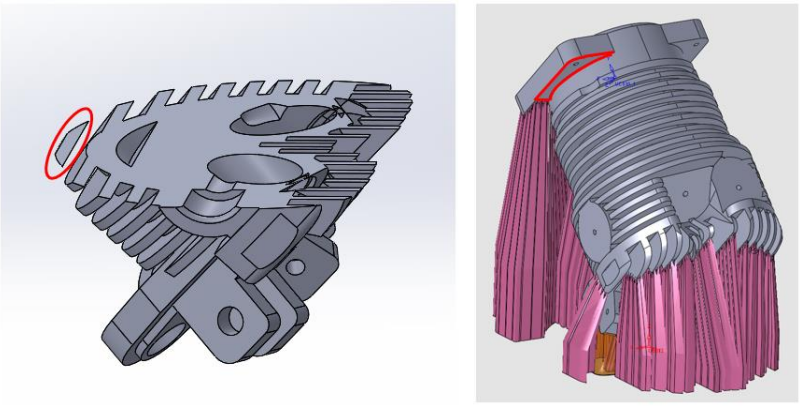

*Figure 3.9: Example of an area where support is added (left) and where the support region is modified (right)*

Next, the designer selects the type of support option they want to employ: wall, solid, lattice, solid wall, cone, manual cone, skirt support, or multi-exposure. Each one of these options required a decision on the additional variables to include, such as the pattern, fragmentation, skirt, texture, thickness, teeth height, cell width, angle, etc. For the crankcase, wall and solid supports were used. For the wall support pattern, a square grid with a 2 mm grid distance was utilized, and the teeth had a base length of 1.5 mm, intersection length of 0.35 mm, a height of 2.5, and a piercing height of 0.25 mm. In comparison, the skirt option was selected for the solid support and drain holes were added to more readily remove excess powder.

For the cylinder head, the internal geometry at the roof of the cylinder made selecting a print orientation difficult. Since these surfaces are complex, post machining is not possible, making the most obvious orientation option upside down. However, this would mean every single fin in the cylinder head would require support. This would increase the temperature of the build process (less heat dissipation), and the supports would become extremely difficult or arguably impossible to machine afterwards. The next option is to lay the cylinder on its side and have supports on the internal wall (not the upper internal geometry); however, this is not ideal

because the support surface finish is relatively rough and would probably require including a cylinder liner. Therefore, the last option was to angle the cylinder head upside down and at 45º where the spark plug surface is not in need of support while also keeping the build symmetric (Figure 3.10). With this slice orientation, the fins would be starting completely unsupported since they would not be connected to the cylinder itself initially. Because of this, a support was added at the underside of every fin (Figure 3.9). This choice resulted in a support volume and area of 10.64 $cm^3$ and 654.84 $mm^2$, respectively.

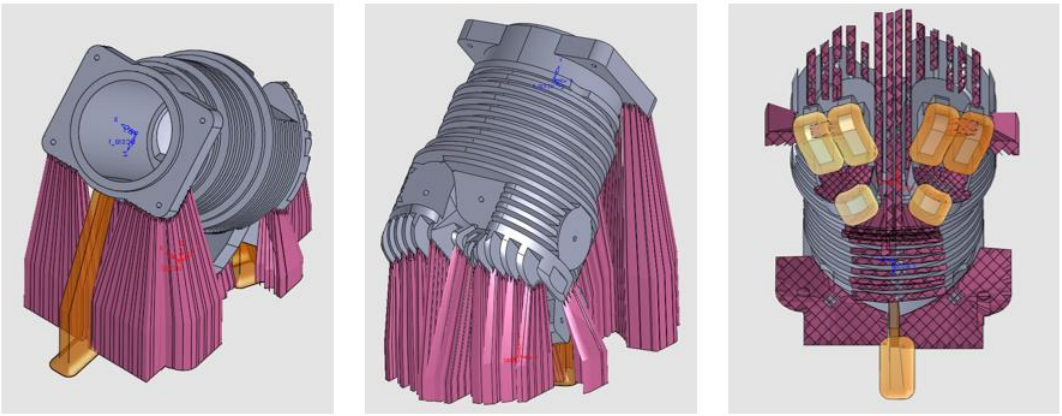

*Figure 3.10: Cylinder head support design (solid and wall supports are orange and pink respectively)*

Overall, the supports for the cylinder were slightly more robust than for the crankcase since this part was manufactured on a slightly less forgiving machine (especially with fine features as discussed in the previous section). In this case, the wall support pattern was still a square grid, but the distance between lines was set to 1 mm and it was decided to not provide a texture for the supports. Other choices included the teeth having a base length of 1 mm, intersection length of 0.35 mm, a height of 1.5, and a piercing height of 0.25 mm. The solid support style remained consistent with that of the crankcase.

*Table 3.1: Support information for cylinder head and crankcase designs*

| | Crankcase Original Design | Crankcase Modified Design | Cylinder Head |
|---|---|---|---|
| Total 2-D Support Area [$mm^2$] | 1506.10 | 1094.50 | 659.84 |
| Total 2-D Unsupported Area [$mm^2$] | 10.41 | 4.32 | 151.49 |
| Average Support Max Angle to Part | 36.57° | 28.49° | 50.29° |
| Average Min Support Height [mm] | 35.53 | 37.97 | 23.26 |
| Support Volume [$cm^3$] | 7.55 | 5.49 | 10.64 |
| Part Volume [$cm^3$] | 30.27 | 33.08 | 38.54 |
| Manufacturing Time for One Part [hr] | 5.23 | 2.42 | 1.75 |

## 3.8 **Build Layout and Parameters**

For the crankcase, a 3D Systems ProX DMP 320A machine was used. Overall, the part was printed in 1220 60 µm layers and was predicted by the software to take a total of 12.78 hours. Two parts of each design are printed (1 & 4 are the original design; 2 & 3 are the modified design in Figure 3.11) to allow for error when machining. Moreover, these parts are arranged in an offset pattern so that the re-coater blade can spread the powder evenly, help with heat dissipation, and to prevent multi-part failure.

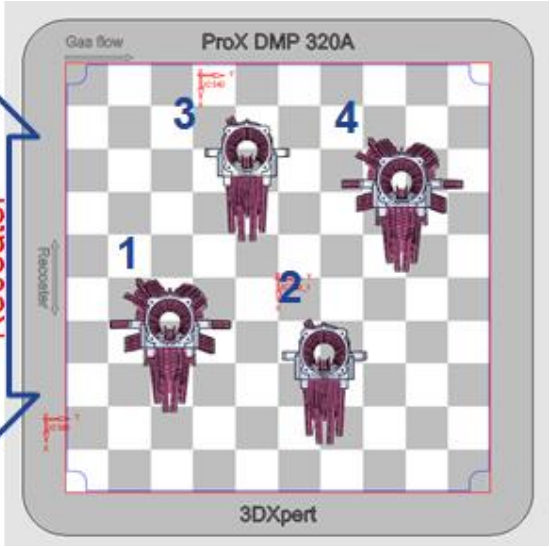


*Figure 3.11: Build plate arrangement for crankcase*

Table 3.2 provides the differing parameters used for each component during construction to speed up the build and allow for easy support removal. Since porosity and tolerances are not of concern for the support structures, less ideal but faster parameters are used. Moreover, understanding the Volumetric and Linear Energy Density (VED and LED, respectively) of every component helps to understand how much power is going into a build:

$$\text{Linear Energy Density} = \frac{\text{power}}{\text{speed} * \text{layer thickness} * \text{hatch spacing}} \tag{2}$$

$$Volmetric\ Energy\ Density = \frac{power}{speed} \tag{3}$$

Specifically, researchers in the AM field are using these metrics to standardize builds between different machines and to aid in prediction of mechanical properties, microstructures, and defects [65, 66]. However, it has been shown that even if the VED is the same, dissimilar parameters can change the results, with laser power having the largest influence [65].

*Table 3.2: Machine parameters for each component on 3D Systems ProX DMP 320 (Ti64)*

| Component | Layer Thickness [µm] | Laser Power [W] | Laser Speed [mm/s] | Hatch Spacing [µm] | VED [J/mm3] | LED [J/mm] |
|---|---|---|---|---|---|---|
| Part (gray) | 60 | 50 | 400 | 82 | 25.41 | 0.1250 |
| Solid Support (orange) | 60 | 340 | 2000 | 100 | 28.33 | 0.1700 |
| Wall Supports (pink) | 60 | 150 | 1600 | 100 | 15.63 | 0.0938 |

For the cylinder head, a 3D Systems ProX 300 Machine was used and the parameters for this machine are listed in Table 3.3. Three cylinders were printed along with test specimens for other research purposes (Figure 3.12). Overall, each cylinder head had a total of 1862 40 µm layers and projected to take 3.68 hours; however, with everything included on the build plate, the manufacturing time was estimated at 44.67 hours.

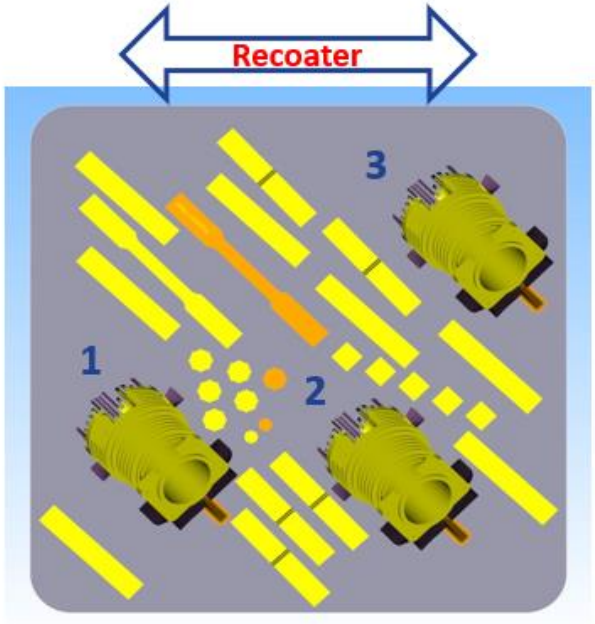


*Figure 3.12: Build plate arrangement for cylinder head*

*Table 3.3: Machine parameters for each component on 3D Systems ProX DMP 300 (AlSi12)*

| Component | Layer Thickness [µm] | Laser Power [W] | Laser Speed [mm/s] | Hatch Spacing [µm] | VED [J/mm3] | LED [J/mm] |
|---|---|---|---|---|---|---|
| Part (gray) | 40 | 225 | 1200 | 70 | 66.96 | 0.1875 |
| Solid Support (orange) | 40 | 400 | 2500 | 70 | 57.14 | 0.1600 |
| Wall Supports (pink) | 40 | 100 | 160 | 70 | 223.21 | 0.6250 |

## 3.9 **Post AM Results**

### 3.9.1. ***Qualitative Results***

Figure 3.13 and Figure 3.14 present the build results of the two crankcase designs and circled in red are the areas where the part delaminated from the support structures. In regards to this outcome, Zaeh et al. demonstrates through simulations using an AM bar that the residual stresses produced between the support and the structure are respectively larger than those in the part or the supports themselves, which is why delamination in this area is more likely [67]. Hence, the circled delamination in the figures likely resulted from the buildup of residual stress in those areas. Moreover, the smaller cross-sectional areas between the upper teeth of the support and where they attach to the part are inherently weaker. When looking at the support areas after removal, it should be noted the modified design had a relatively cleaner resulting surface. In comparison, the original design had significant unconsolidated powder built up in these areas. This build up is most likely due to the additional supports surrounding the part, preventing the heat from dissipating (acting as an insulator) and subsequently producing higher temperatures,

causing the laser to partially melt the layers beneath where the supports and surface met. This poor finish could be a result of increased amounts of ejecta caused by the additional sparking with the larger lasered area (because of the additional supports). In turn, this could have caused substandard material (partially sintered, or larger particles whose morphology or sphericity changed because of proximity to lasering) to be thrown in the central area of the surfaces. Besides these areas, the support structures were removed relatively easily by hand using pliers with the solid supports requiring a milling process.

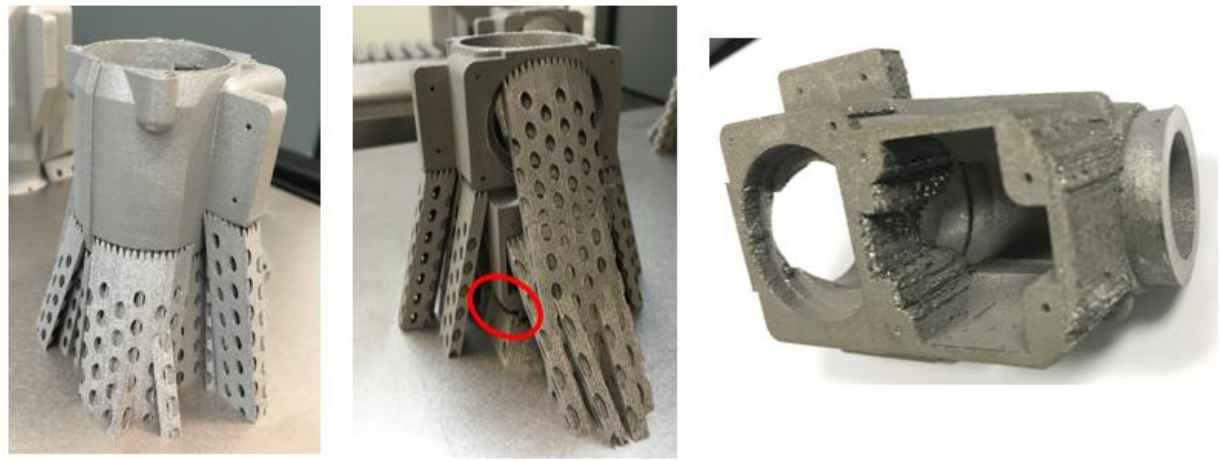

*Figure 3.13: Original crankcase design build results*

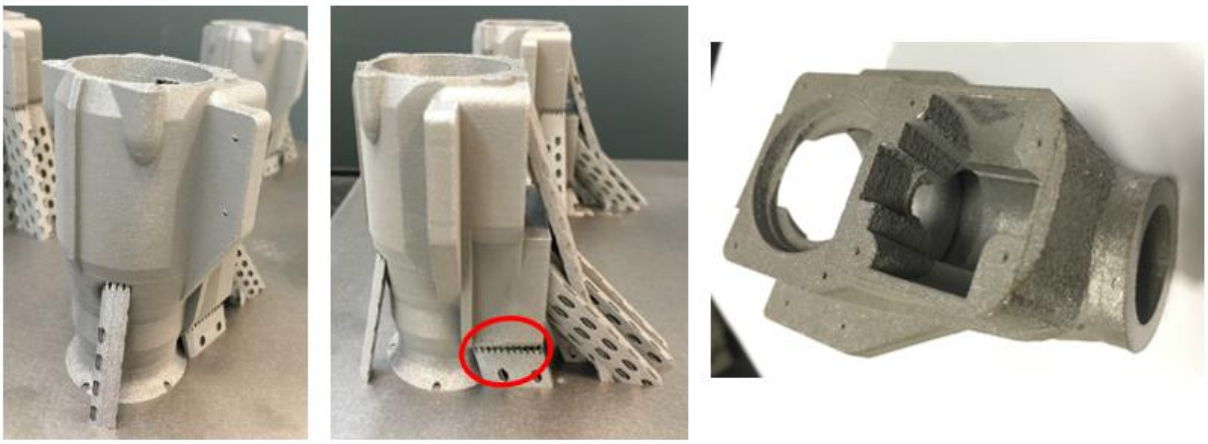

*Figure 3.14: Modified crankcase build results*

Figure 3.15, Figure 3.16, and Figure 3.17 display the results of the cylinder head AM process using the ProX 300 machine. These images show almost no delamination, and they exhibit mostly intact supports. However, the third cylinder head has significant support cracking and damage. This is likely a result of not having the tensile test bars on both sides of the cylinder, subsequently acting as a barrier to prevent the powder or supports from shifting when the roller adds a new layer. It is for this reason that lattice structures and other fine features often have walls printed around them. After removal of the supports it can be observed that this lack of protection had a notable effect on the quality of the upper fins on cylinder head 3.

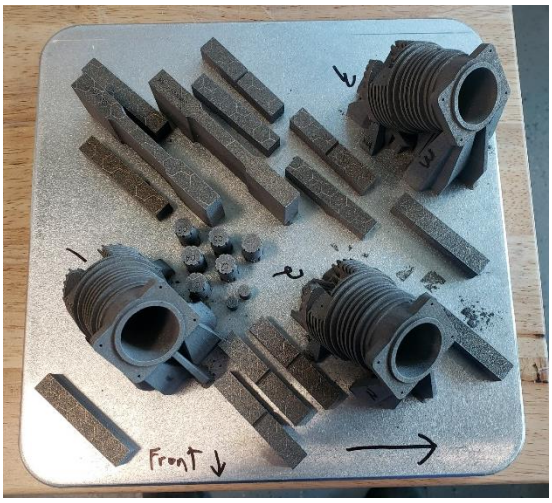


*Figure 3.15: Cylinder head build plate result*

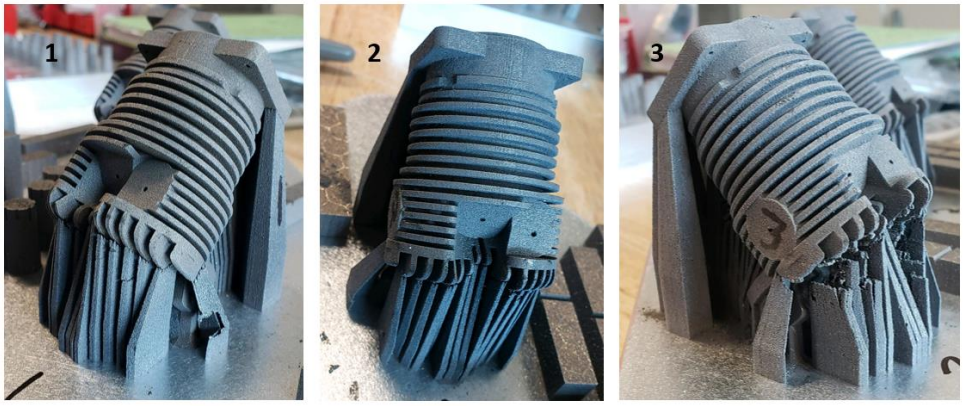


*Figure 3.16: AM cylinder head results*

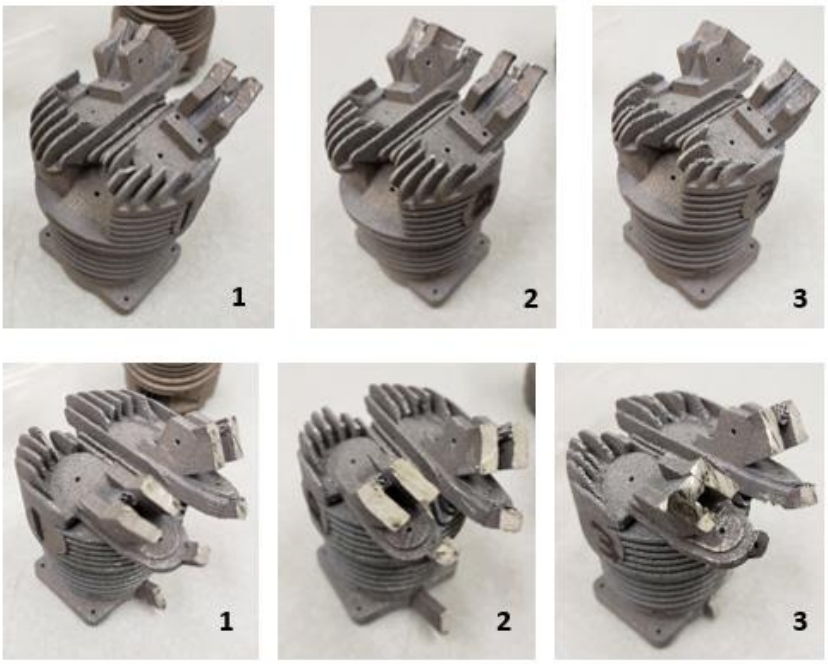


*Figure 3.17: AM cylinder heads post support removal, pre-machining*

### 3.9.2. *Nominal Actual Dimensional Analysis*

To determine whether these parts are useable once manufactured and removed from the build plate, a nominal/actual dimensional analysis was performed (analogous to Figure 3.1) except this time the AM part was compared to the CAD file. The cast parts discussed earlier were scanned with a Zeiss Xradia 520 Versa (micro CT); however, the AM crankcase was scanned using an Northstar X-500 system due to the increased density of the Ti64 that hindered transmission of the X-rays and resulted in unclear images via the Zeiss micro CT. The following nominal/actual dimensional comparison analyses were performed using Volume Graphics Software. Figure 3.18 shows the original and modified designs for the AM crankcases as compared to their CAD models. In this figure, everything in green is within ±0.005″, which is typical milling tolerance [68]. Moreover, the blue areas indicate where material is missing; whereas, the red areas highlight extra material present. In addition, the blue areas on the front of the part are a result of the delamination mentioned previously, which will cause the front thicknesses to be slightly thin after the part is fully machined. Additionally, many of the red areas are caused by the leftover support areas that will be later machined. It is important to note that although there are areas out of tolerance, most of these will either be post machined or they are not of critical importance for successful engine operation. For example, even though the front blue areas will be thinner than intended, this is not a highly loaded area, therefore, it should not hinder lifespan of the part or change the performance. Likewise, almost all internal features will be bored, and any surfaces left untouched are not critical because they still allow for clearance. Lastly, any external areas that are out of tolerance will only affect heat dissipation which is changing due to the material anyways. Overall, these parts are deemed to be within acceptable ranges.

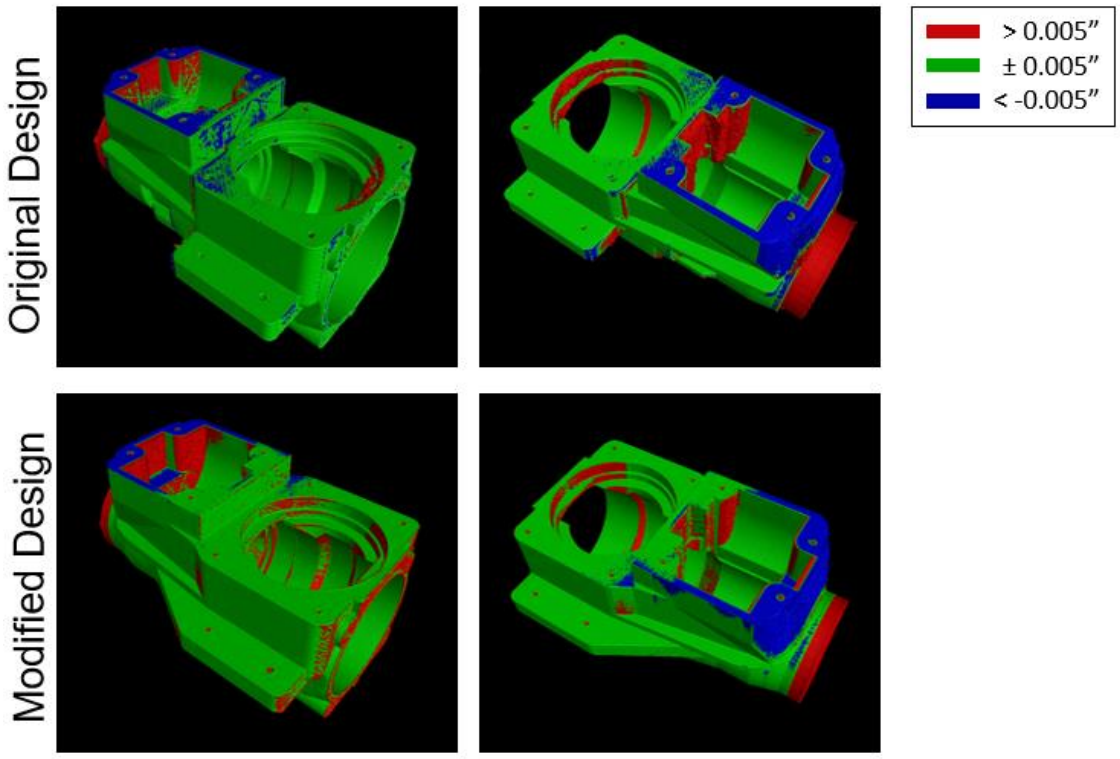


*Figure 3.18: Nominal actual dimensional analysis of AM parts vs. CAD files for original and modified crankcase designs*

As before with the crankcase, the AM cylinder head 2 has a nominal/actual dimensional analysis performed on it comparing the AM part to the CAD file. The areas shown in red here are where material is present where it should not be. In this instance, all of the red areas are a result of left-over support structure and they will be machined away. The blue areas are where material is lacking, but it is determined that none of these areas are critical for engine performance. For example, even though many of the fins are slightly off they will only have a negligible effect on the heat transfer. These blue areas are a result of the AM machine’s achievable tolerance.

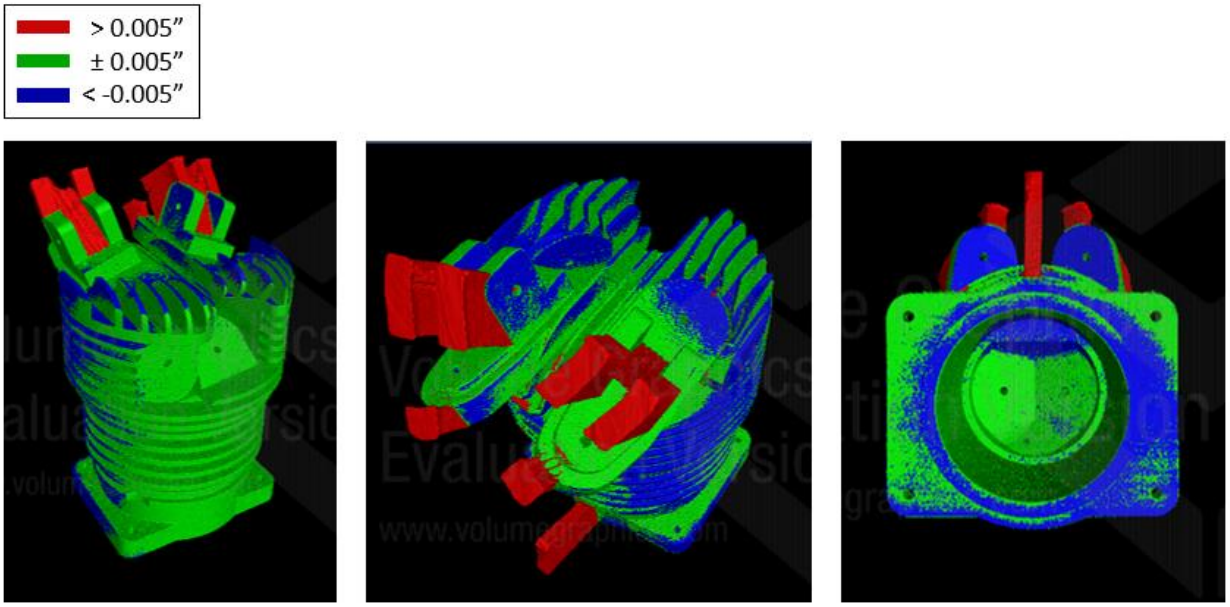


*Figure 3.19: Nominal actual dimensional analysis of AM parts vs. CAD files for cylinder head*

### 3.9.3. ***Porosity Results***

To obtain an understanding of an acceptable porosity level in these engine components, the die cast part CT scans were analyzed using Volume Graphics and CTAn software packages (Figure 3.20) [69]. Appendix Figure C.1 and Figure C.2, along with Table 3.4 display the results for the die cast crankcase with the spikes in porosity percentage (Appendix Figure C.1) directly correlated to material thickness. Furthermore, the main material defect observed in the die cast components is the porosity caused by micro-shrinkage and dissolved gases during solidification. This porosity can stem from hydrogen content and local freezing rate along with the local temperature gradient potentially playing a role. Since the porosity in this case correlates with thickness, it can be assumed that the most likely culprit of this porosity is non-ideal cooling during the casting process [70, 71]. Generally, this is an issue with this process since it is expensive to develop dies with complex cooling channels to ensure a uniform cooling event.

Therefore, in most cases with relatively inexpensive parts, the thicknesses are kept close to the same throughout the part to alleviate any potential porosity issues.

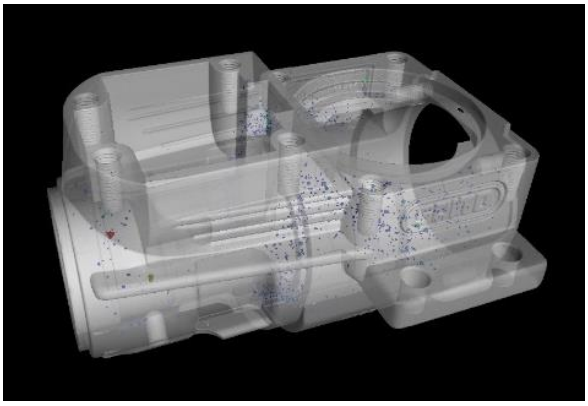

*Figure 3.20: Visual representation of porosity in die cast crankcase*

Once a baseline was determined for the die cast parts, the AM parts were then analyzed as illustrated in Figure 3.21. It should be noted that the area at the front of the crankcases with noticeably more blue porosity is a solid support structure and was not included in the quantitative analysis. As indicated before, Ti64 has a higher density; hence, a larger CT scanner was used, but the voxel sizes of the die cast crankcase and the AM scans are similar, meaning valid comparisons can still be made. Overall, the spikes in porosity are about 0.1% higher in the AM original design parts (#1 and 4), but (like discussed before) these are a result of the leftover support areas and will be machined later. This also explains why in one of the AM original design parts (#1) the largest pore size is almost double the die cast part, but the other AM original design (#4) has a largest pore side that is $1/10^{th}$ of the die cast part. Otherwise, the

porosity stays consistent and has an average percent porosity area of 0.0027%, which is 1/10$^{th}$ the average of the die cast part (Figure C.3, Figure C.4, Figure C.5, and Figure C.6).

Building on this, the modified design results are even better. Specifically, the porosity present is only from support areas, and the rest could be argued to be negligible since the largest average pore size is 1/34$^{th}$ of that in the AM crankcase original design (Figure C.7, Figure C.8, Figure C.9, and Figure C.10). The image slices of the crankcase and the solid support in Figure 3.22 show that this negligible porosity was not a result of the image quality and the scans were still picking up notable porosity in the support structure with direct porosity comparisons presented in Table 3.4. These results appear promising since Mayer et el. demonstrated that 98.5% of fatigue cracks initiate at porosity [70] while Major et el. found the greatest influencer on fatigue life was the largest pore size [71].

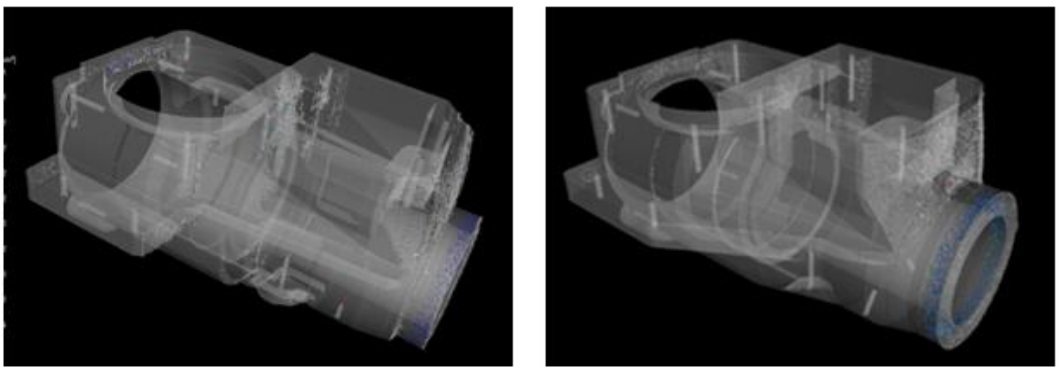

*Figure 3.21: Visual representation of porosity in AM crankcase 1 (original, left) and crankcase 2 (modified, right) designs*

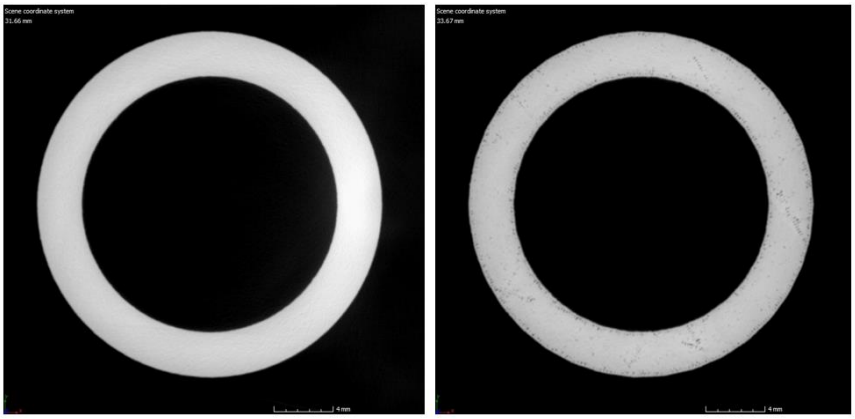

*Figure 3.22: Image slices, crankcase (left) and solid support (right)*

*Table 3.4: Crankcase porosity results: comparison of cast and AM parts*

| | Machine | Voxel Size [µm] | Total Porosity Volume [%] | Largest Pore Size [$mm^3$] |
|---|---|---|---|---|
| Cast Al Crankcase | Zeiss | 57.3622 | 0.0280 | 0.3241 |
| AM Ti64 Crankcase 1 (original) | Northstar | 41.73 | 0.0045 | 0.5182 |
| AM Ti64 Crankcase 2 (modified) | Northstar | 41.73 | 0.0003 | 0.0049 |
| AM Ti64 Crankcase 3 (modified) | Northstar | 41.73 | 0.0002 | 0.0114 |
| AM Ti64 Crankcase 4 (original) | Northstar | 41.73 | 0.0008 | 0.0375 |
| *AM Ti64 Crankcase Original Average* | Northstar | *41.73* | *0.0027* | *0.2779* |
| *AM Ti64 Crankcase Modified Average* | Northstar | *41.73* | *0.0003* | *0.0082* |

For the cylinder head, the same porosity analysis procedure was followed. Unsurprisingly, the die cast cylinder head had a relatively higher porosity (see in Figure 3.23) than the die cast crankcase because of its thicker material areas at the top of the cylinder. Specifically, the red, green, and yellow areas are a result of the large pores found. Overall, the cylinder head's largest pore size and total porosity percentages were roughly 30× and 5× greater than the cast crankcase, respectively (Table 3.4 and Table 3.5).

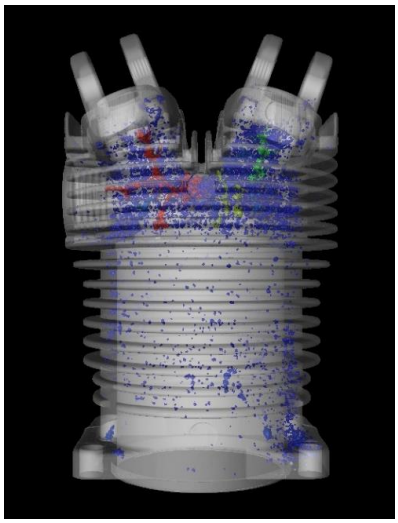

*Figure 3.23: Visual representation of porosity in cylinder head*

In general, the porosities of the AM cylinder heads are 0.0253-0.0229% higher than the AM crankcase designs. However, comparing the die cast cylinder head and the AM version still indicates a positive trend with the AM cylinder heads having an average porosity area percentage of 0.0256 as compared to 0.1571 for the cast part (Figure C.12, Figure C.13, Figure C.14, and Figure C.15). Additionally, the cast cylinder head had large pores that were about 150× greater than the AM parts, resulting in the bigger porosity area percentage (Table 3.5). Nevertheless, when observing the pore volume distribution in Figure C.16, Figure C.17, Figure C.18, and Figure C.19, the AM parts had considerably more pores that were smaller than 0.001 $mm^3$ (roughly 3300 and 1350 for the AM and die cast, respectively). Of importance, this increase in small pores could influence the surface finish; thereby, making the use of a cylinder liner necessary. It can also be observed that these small pores are more prevalent on the backside of the cylinder head (Figure 3.24) since this side was downfacing during the build process.

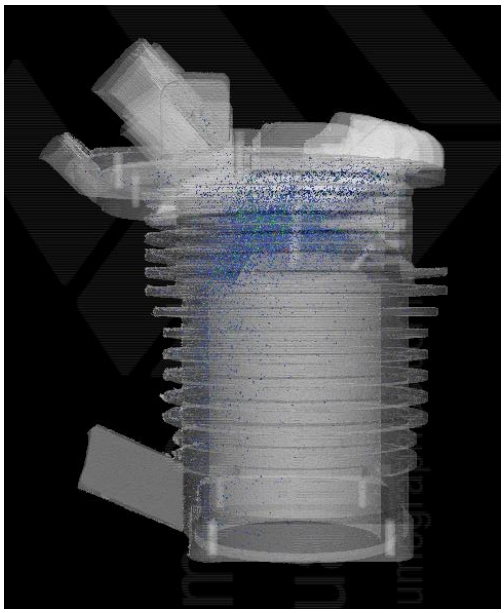

*Figure 3.24: Visual representation of porosity in AM cylinder head 2*

*Table 3.5: Cylinder head porosity results: comparison of cast and AM parts*

| | Machine | Voxel Size [µm] | Total Porosity Volume [%] | Largest Pore Size [$mm^3$] |
|---|---|---|---|---|
| Cast Al Cylinder Head | Zeiss | 57.36 | 0.1571 | 9.073 |
| AM Al Cylinder Head 1 | Zeiss | 41.80 | 0.0127 | 0.0191 |
| AM Al Cylinder Head 2 | Zeiss | 41.76 | 0.0292 | 0.0393 |
| AM Al Cylinder Head 3 | Zeiss | 41.80 | 0.0349 | 0.1194 |
| AM Al Cylinder Head averages | - | 41.79 | 0.0256 | 0.0593 |

For this CT analysis, the following image processing task list macro was developed following the efforts of Sietins [69]:

1. Reload – Image:

   The images are reloaded to remove any previous analysis.

2. Reload – Region of Interest (ROI):

Similar to step 1, the ROIs are reloaded to remove any previous analysis.

3. Threshold – Global, input threshold number:

   Thresholding takes a raw image and transforms it into a binary image for an easier analysis (less computationally intensive). White areas are identified as objects and black areas are considered empty space. For this step, the threshold was determined visually by switching back and forth between the raw image and the binary image while looking at the edges and pores identified. The upper threshold number found through this process is input into the program during this step.

4. ROI Shrink Wrap – 2-D space:

   This sets the ROI to the outside edges of the sample so the air around the object is not considered in the analysis as part of the porosity percentage. In this case, it is done for each 2-D image and it is set to not stretch over holes.

5. Despeckle – 3-D space, out of range of 2-100000 voxels, apply to image:

   This step cleans up the image and can remove some noise in these data. For this analysis, the upper range is needed to prevent the program from identifying threads and hole features as pores. In order to do this successfully, the program had to look at the 3-D space instead of the 2-D images.

6. Bitwise operations - Image NOT image:

   This effectively swaps the black and white regions so that when the individual object analysis is done, it will analyze the pores themselves instead of the sample.

Before employing this macro, it was first tested on a small number of images due to the respectively long analysis time. After finalizing, the only adjustment needed between analyzing each individual part image stack is the threshold number and the pixel size.

It should be noted that thresholds were set visually; thus, leaving some room for user bias, and all volumes < 0.0002 $mm^3$ are classified as noise. This was determined by taking individual object analysis data (that lists information about every pore found) and ordering the pore sizes from largest to smallest. Then, after plotting, a cut-off was found by determining where data stops stepping up. For the scans performed on the Zeiss, this occurred around 0.0002 $mm^3$ (Figure C.21); hence, this was also used as the cut-off for the Northstar in efforts to keep these data consistent [69].

### 3.9.4. ***Resulting Defects***

A weakness of the AM process is in its ability to create clean features, especially sharp corners. When combined with a residual stress build up, corners are prone to produce localized stress concentrations and cracking is more likely to happen [72, 73]. For instance, Figure 3.25 illustrates a crack that occurred along a corner feature on this part with this defect occurring in the first and third crankcases. Investigating, crankcase 1 had a crack depth of 1.47 mm and length of 15.05 mm; whereas, crankcase 3 had a crack depth of 1.89 mm and length of 12.20 mm. These defects are concerning due their proximity to one of the major cyclical loading areas induced by the bearing during engine operation when the piston is at top dead center (TDC) and bottom dead center (BDC). Because of this, crankcases without this defect were used going forward in the machining and testing processes. In addition, Figure 3.25 provides a closer look at

the unconsolidated powder experienced in the original crankcase designs. Here, the wavy structure on the surface is the leftover support and the darker gray is the unconsolidated powder.

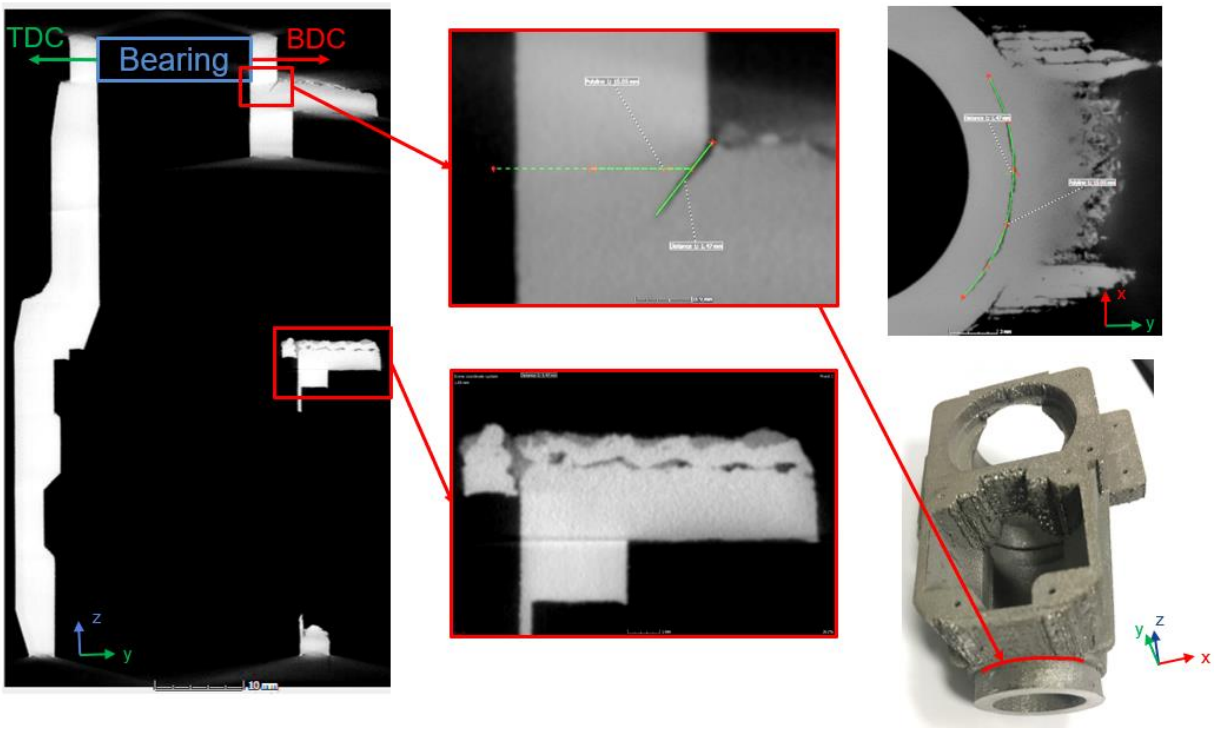


*Figure 3.25: Crack defect in AM crankcase original design number 1*

In addition, the AM cylinder heads had a small defect resulting from the geometry, creating a localized stress concentration. The material thickness in this area was low and there were two corners close to each other making this flaw possible. This defect was seen in all three of the manufactured cylinder heads (Figure 3.26) with the following dimensions: cylinder head #1 - 2.78 mm long, 0.54 mm thick; cylinder head #2 - 2.48 mm long, 0.51 mm thick; and cylinder head #3 - 2.87 mm long, 0.45 mm thick. As a result, when choosing the cylinder head

that would be used going forward for machining and testing, the quality of the fins and features were investigated and cylinder head 2 was determined to be the best.

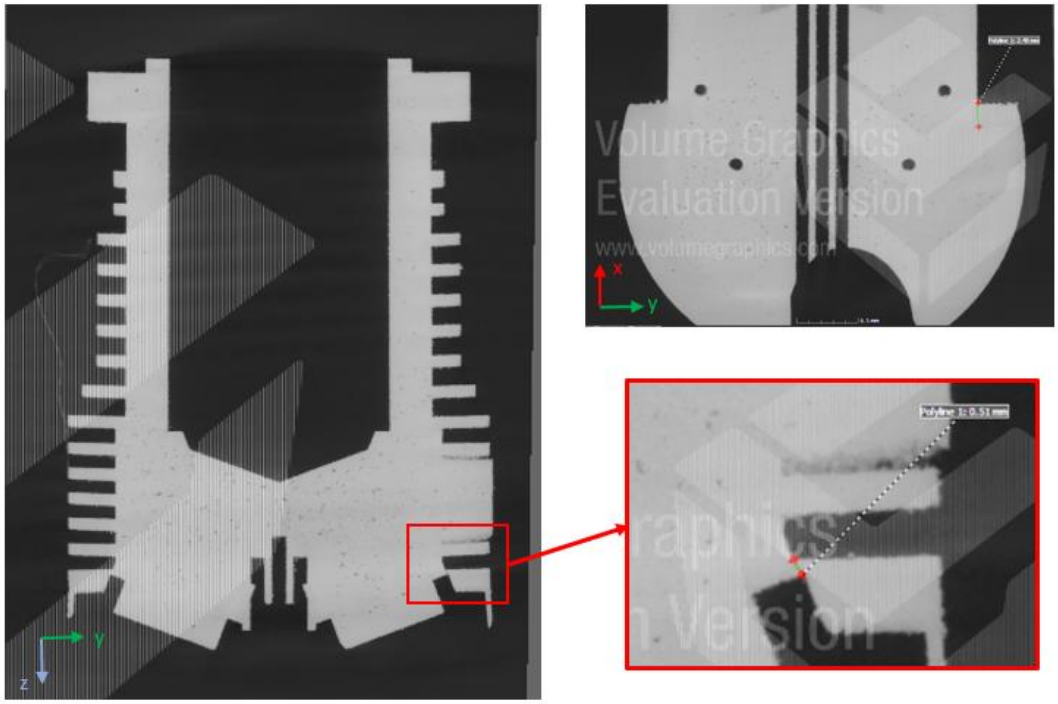


*Figure 3.26: Crack defect in AM cylinder head number 2*

## 3.10 **Post-processing**

### 3.10.1. ***Stress Relieving and Heat Treatments***

Residual stresses are caused by non-uniform cooling and can result in unfavorable conditions such as cracking, or loss of compressive yield strength. Therefore, it is important to remove these stresses using a heat treatment process. With respect to Ti64, these residual stresses are especially detrimental due to its poor heat dissipation. Generally, the process for Ti64 is as follows and must occur in an inert environment (either under vacuum or argon (Ar), with Ar chosen for the crankcase):

1. Raise temperature to 600ºC in 1 hr.
2. Dwell for 4 hours
3. Cool at 6ºC/min for 1 hr. 40 min.
4. Remove part

Overall, the results of this stress relief process should follow the trend as shown in Figure 3.27 [74].

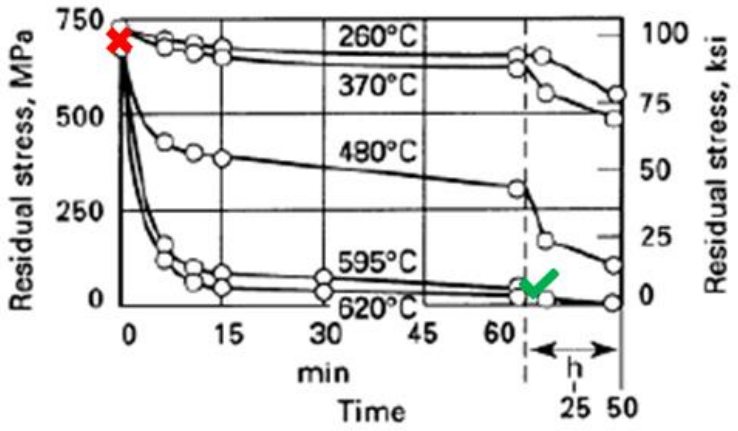


*Figure 3.27: Graphical representation of the relief of residual stress for Ti-6Al-4V [75]*

Similarly, heat treatment was investigated for the cylinder head in order to obtain a comparable hardness and yield strength to cast Al. Here, Zhou et el. identified the following as producing the best results under ultra-high purity Ar with the graphical representation shown in Figure 3.28 [76]:

1. Heat oven to 520°C
2. Place part in oven for 2 hours
3. Water quench sample to room temperature

4. Heat oven to 160°C
5. Place part in oven for 10 hours
6. Air cool

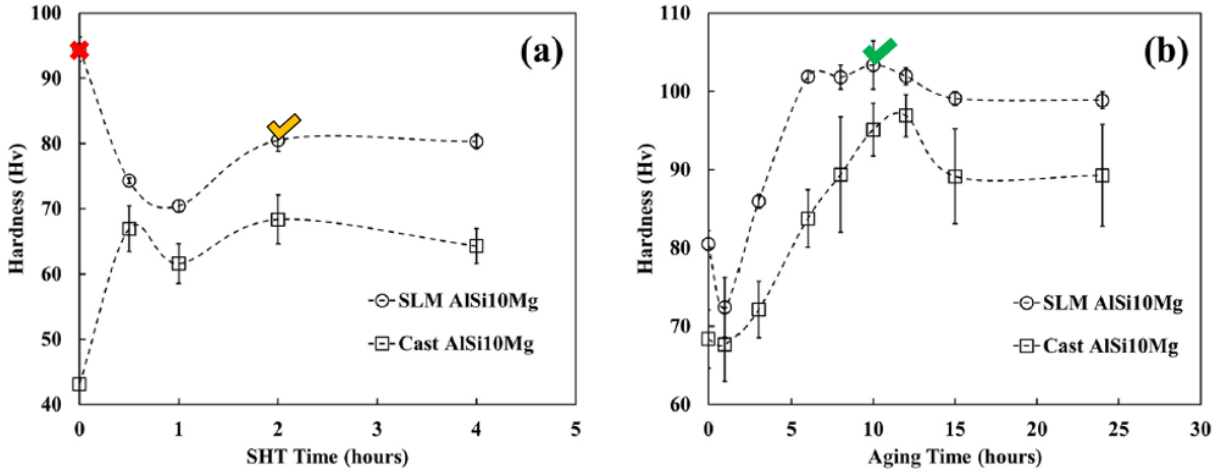


*Figure 3.28: Graphical representation of Vickers hardness of cast and AM aluminum (a) for step 1-2, (b) step 4-5 [76]*

However, these findings were generated for another commonly used additive manufactured aluminum, AlSi10Mg. Instead, the cylinder head here was printed with AlSi12. Therefore, the absence of Mg results in the elimination of any phases to precipitate out for strengthening. Therefore, heat-treating can degrade the properties as indicated by the U.S. Army Research Lab (Figure 3.29). As a result, the choice to use the AM cylinder head as built was made.

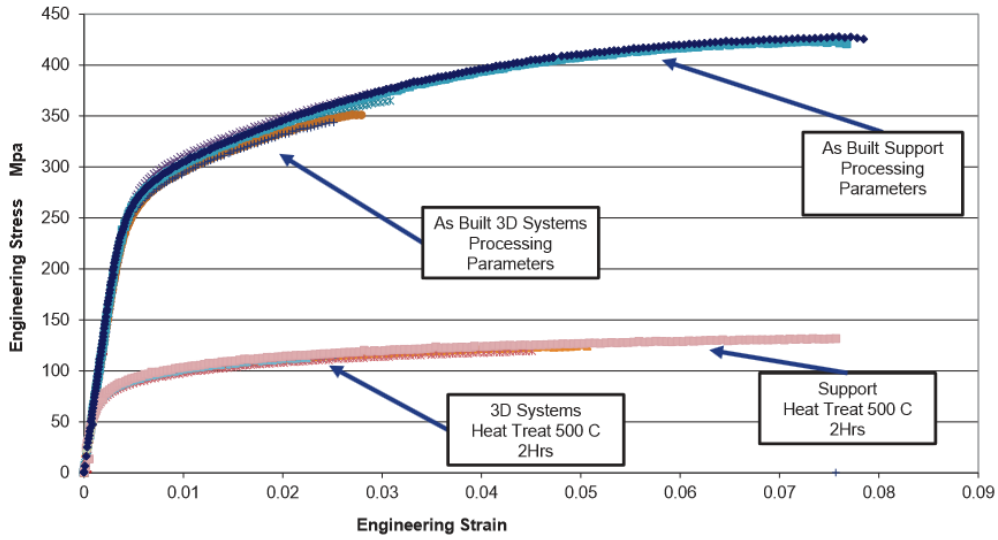


*Figure 3.29: AlSi12 stress and strain curves for heat treated and as built AM tensile bars [77]*

### 3.10.2. ***Post Machining***

After going through the heat treatment processes, the wall support structures are removed manually using pliers. Then, a band saw is used to detach each part from the build plate (this can also be done with a handsaw) by sawing through the solid support structures (Figure 3.30).

*Figure 3.30: Build plate removal using a bandsaw*

Lastly, the parts undergo a required post machining; however, this will not occur until they are first CT scanned and checked for distortions, porosity, and cracking to ensure they are usable as discussed previously. Figure 3.31 outlines all surfaces and features that are machined to achieve the final form of the crankcase; hence, these numbers will be referenced going forward when describing the process. For titanium, slower speeds, feed rates, smaller depths, harder tools, and more coolant is used than with aluminum since it is a more difficult material to machine. Moreover, it should be noted the *x* and *y* axes were locked whenever appropriate to prevent the mill from coming out of alignment after zeroing. In addition, the vice was always cleared of any chips and the part deburred to keep everything as square as possible. All tools and equipment needed to machine the crankcase are listed in Table D.1 in Appendix. Additionally, a labeled figure of a vertical mill is provided in the Appendix (Figure D.1) to assist with vocabulary.

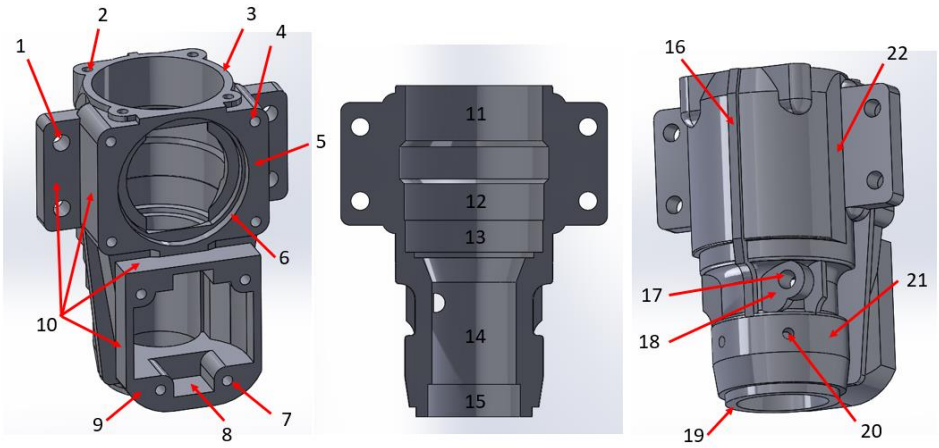


*Figure 3.31: Surface and feature identification for the crankcase: top view, cut section view, and bottom view*

Beginning with the manufacturing process of any part, the stock must first be squared. Here, this meant taking all square features on the part and facing them before proceeding with any major machining operations. To accomplish this, the crankcase was first placed in the vice as shown in Figure 3.32; specifically, orientation A where surfaces 5, 9, and 10 are faced, then placed in orientation B where surface 16 was faced, and lastly orientation C where surface 19 was faced. To insure the crankcase stayed square during these processes, it is important that the part is firmly held in place while clamping the vice, followed by lightly tapping it with the raw hide hammer to ensure it is completely flat against the vice, and finally deburring before each repositioning. For these steps, the vertical mill spindle is set to a low speed of 300 revolutions per minute (rpm) and a 3/8" carbide square-end end mill was used.

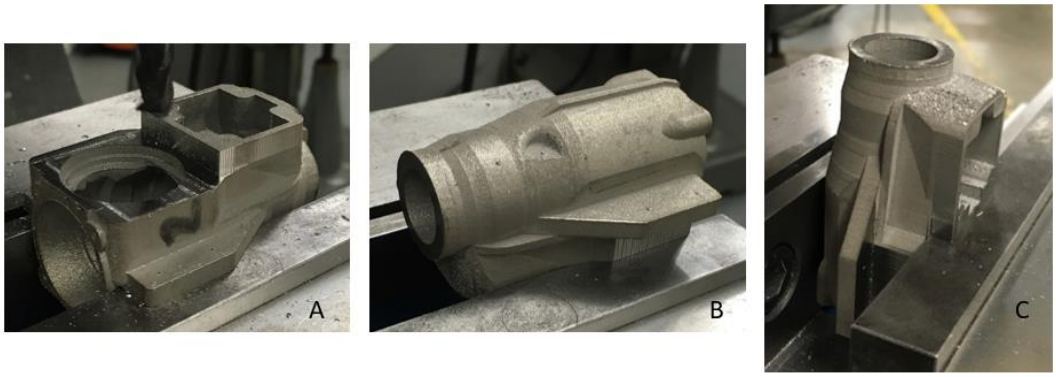


*Figure 3.32: Vice placements for crankcase with (A) used for machining features 1 and 4-10, (B) used for features 16-18 and 22, and (C) used for 15 and 19*

To finish squaring the crankcase, it was placed in the vice as shown in Figure 3.33 and surface 3 was faced. It should be noted that the crankcase is sitting on a parallel bar that is removed after the vice is clamped. The importance of doing so will become apparent in later steps. After facing, the *x*- and *y*-axes of the mill are zeroed to the center of the circle created by surface 11. This is done by first using an edge finder for an approximate location and then a dial

indicator for a more precise zeroing. However, because the surface was relatively rough, it was difficult to obtain exact readings with the indicator; hence, a slight estimation was made.

The next step was to insert the boring bar tool into the mill and to zero the *z*-axis. For this zeroing process, a parallel bar was placed on top of surface 3 and the quill lowered (the amount lowered should exceed the depth of the cut) until the carbide tool touched the bar. Then, the quill was locked using the quill clamp and the control for the micrometer depth was set flush against the quill depth stop. Next, the *z*-axis is raised to the thickness of the parallel bar to set it as zero on the top surface. To allow the quill to move down to the desired depth, the *z*-axis is then raised again, equivalent to the amount it should progress downwards for the bore.

The first surface to be bored is 13 (a bearing surface with a ±0.0004" tolerance), after which the *z*-axis will need to re-zeroed and lowered to the required depth for surface 12, then surfaces 11 and 12 are bored. To provide a uniform finish during the boring process, the auto quill feed is engaged with the feed rate set to 0.0015"/spindle revolution. Here, this feed rate is used when the quill is progressing downwards; however, the quill is manually pushed back up. For the best results, each bored surface should be measured after every intermediate material removal with telescoping gauges and a micrometer, and no more than 0.005" should be removed from the diameter each time.

After the boring process has finished, surface 14 is reamed using an $11/16^{th}$ size reamer. This is to provide a surface on which to perform a dial indication process (Figure 3.34) when the crankcase is flipped to orientation C in Figure 3.32 in order to bore the second bearing surface (surface 15) later. Otherwise, there is no way of assuring concentricity of the two bearing surfaces. Moreover, the parallel bar that elevated the crankcase provides the needed clearance for

the reamer to traverse the entirety of part; thus, eliminating the risk of hitting the vice (Figure 3.33).

Lastly, while in this vice position, the rear cover holes (feature 2) are drilled and tapped with the spindle speed set to 600 rpm. In order to accomplish this facet, a larger pilot was drilled using a small center drill, employing the traditional drill chuck followed by a #39 drill bit. The use of coolant during this step is important to extend tooling life and prevent it from breaking off in the hole. The approximate depths were reached by using tape to indicate where the drill bit should stop. Finally, the holes were threaded using an M3 × 0.5 tap by placing the tap in the drill chuck with the spindle set to "neutral" allowing the tap to spin freely. Then, the quill is lowered and the spindle is turned by hand, backing out slightly after every rotation prevent chip buildup on the tap (giving a cleaner thread finish). After the tap is firmly in the hole, the drill chuck is loosened and pushed back up, leaving the tap in the part. Finally, the hole is hand tapped the rest of the depth. Of importance, cutting oil must be used when tapping titanium.

*Figure 3.33: Vice placement for final squaring step and proceeding boring, reaming, drilling, and tapping steps (features 2, 3, and 11-14 machined with this set up)*

For the next step, the crankcase is placed in the vice exactly like Figure 3.32 C. The rest of the support material is removed, and it is milled down (using the same end-mill as before) to the depth that will produce the correct overall part length. The same *x* and *y* zeroing process is used from before with the edge finder and indicator (along the reamed surface, Figure 3.34). The boring bar is then inserted again, and the *z*-axis is zeroed and lowered to desired depth. Then, material is cautiously removed until the bore is within tolerance (±0.0004").

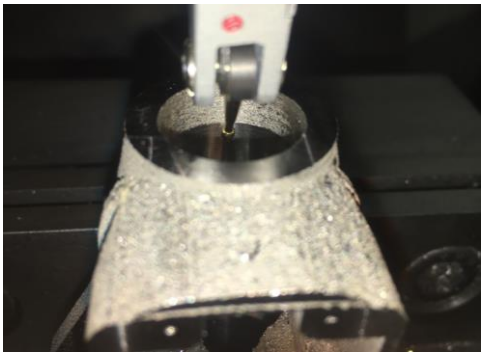

*Figure 3.34: Using a dial indicator on reamed surface to zero x and y axis*

Next, the side flange holes are drilled (feature 1) with the crankcase oriented like Figure 3.32 B. The *x* and *y*-axes are zeroed using surface 19, 22, and 22's symmetric equivalent. For this process, the spindle speed is set to low at 400 rpm and a standard center drill, followed by a #26 drill bit is used. Next, feature 17 is drilled and tapped using the same center drill along with a #19 drill bit and a M5 × 0.8 tap. Finally, a ¼" square-end end mill is used to face the surface.

To drill the angled sensor placement holes (feature 20), the employment of a 2.5" sine block was required (Figure 3.35). The standard 5" sine block could not be used since it would not allow enough material to be gripped by the vice (i.e., the sine block is too tall). Here, a parallel bar had to be used to provide a flat surface for the sine block. To locate the holes, the mill was zeroed using an edge finder on surface 19 and on both sides of surface 21 at the same *y*

and *z* locations. The hole was drilled and tapped using the small center drill and the #39 drill bit followed by the M3 × 0.5 tap. To drill the second angle hole, this process was repeated with the sine block sloped in the other direction.

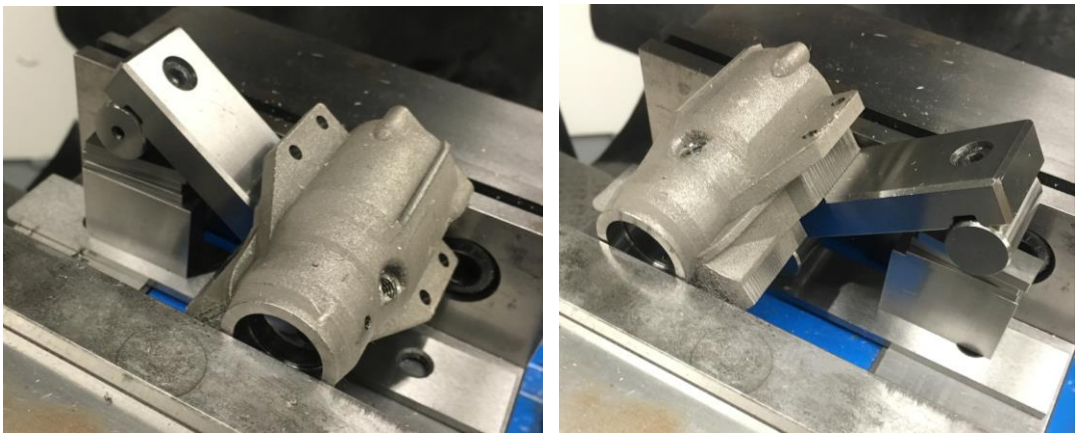

*Figure 3.35: Vice placement using sine block for angled sensor holes (feature 20)*

Afterwards, the crankcase is placed in the vice again like Figure 3.32 A in order to mill the gasket faces (surfaces 5 and 9) to their final heights using the same 3/8" carbide square-end end mill. To ensure proper surface height, the distance between the bore surface and the gasket face was measured. After the faces have achieved their final heights, surface 6 is bored to remove the left-over support material so that the cylinder head would fit concentrically. A similar zeroing process is used as before with the edge finder and indicator gage, making sure to only use the clean parts of the surface (i.e., no support remnant). After this allowed the cylinder head to fit, all of the gasket face holes are drilled and tapped (features 4 and 7) using the small center drill, the #39 drill bit, and the M3 × 0.5 tap with the mill still zeroed on the hole. Lastly, due to material delamination from the AM-production process (as discussed in the Post AM Results section), surface 8 had to be milled using a 3/32" square-end end mill to provide clearance for the cam gear cover. Overall, Figure 3.36 shows the finished crankcase.

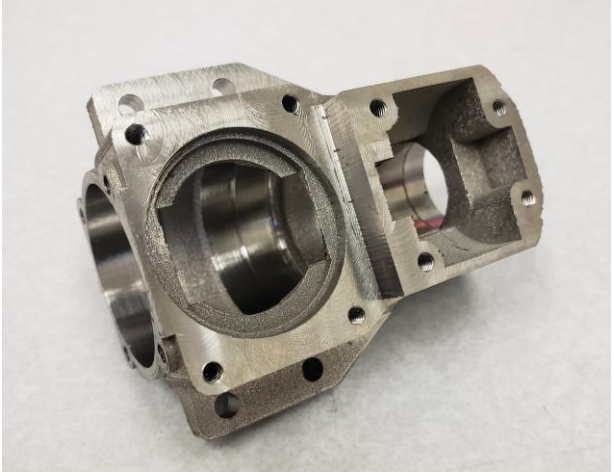

*Figure 3.36: Final machined crankcase*

Because the cylinder head is composed of aluminum, it can handle higher machining speeds and rates due to its material properties as mentioned earlier. For example, its relatively high thermal conductivity keeps the part and tools from heating up as they would with titanium, which causes tools to wear faster. In addition, because aluminum has a lower hardness, it makes material removal easier. Due to these factors, unless stated otherwise, the spindle speed was set at 1200 rpm. Moreover, because of its geometry, special care was taken during the fixturing process as to not crush the cylinder that would cause the inside walls to lose cylindricity and/or potentially damage the fins. As a result, two fixturing aids were developed and machined to help with this process as shown in Figure 3.37. Moreover, Figure 3.38 labels all the surfaces and features that were machined or used when machining to achieve the final form of the cylinder head; hence, these numbers will be referenced moving forward when describing the processes. All required tools for this effort are indicated in Table D. in the Appendix.

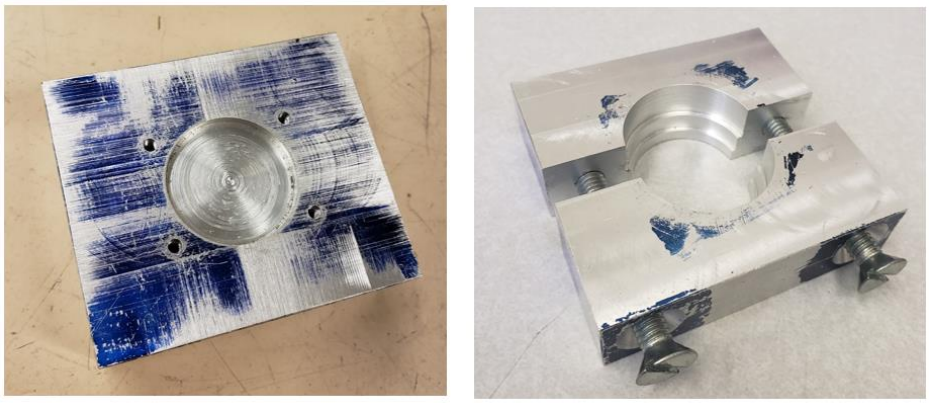

*Figure 3.37: Fixturing devices manufactured for cylinder head post machining*

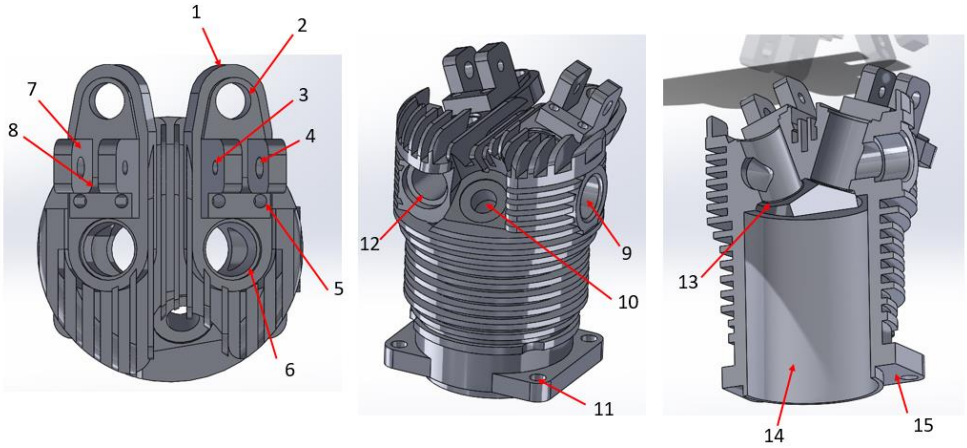


*Figure 3.38: Surface and feature identification for the cylinder head: top view, bottom view, and cut section view*

Unfortunately, the first step of this process required the cylinder head to be clamped in the vice. However, since the cylinder walls had 0.050" material added and the top of the cylinder was still respectively solid (i.e., no holes drilled yet) it was deemed acceptable to proceed (Figure 3.39). Therefore, after zeroing the *x*- and *y*-axes using a dial indicator (Figure 3.39), the four through holes at the base were located and drilled (feature 11) using a center drill followed by a 3.4 mm drill bit.

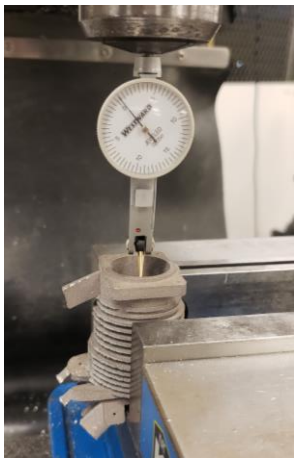

*Figure 3.39: First vice set up to drill the initial four holes (feature 11) in the cylinder head*

After drilling the base holes, the cylinder was then attached to the first fixturing aid using the screws from the engine assembly. Then, by employing a 2.5" sine block set on a parallel bar (note: as before, a parallel bar was used because the 2.5" sine block is too short to bridge the gap in the vice, but too long to fit on one side), the cylinder head was angled at 20° so that features 5, 6, 7, and 8 can be machined (right and middle pictures in Figure 3.40). In order to accomplish this, first the supports are machined using a 3/8$^{th}$ square-end end mill to make the top and back side of the rocker flanges flat (feature 7). Then, a 1/8$^{th}$ ball-end end mill is used to remove the support between the rocker flanges. In addition, the inside surfaces (surface 7) are machined with the ball-end end mill to provide the correct clearance for the rocker arm.

Next, the valve guide hole is drilled (feature 6), with the flanges used as a reference to zero the *x*- and *y*-axes on the mill. Here, the hole is first center drilled. Then, using multiple drill bits, the hole is stepped up while reducing the speed until an 11/32 drill bit is used at 800 rpm. After which, a 0.35" reamer is used with cutting oil at 240 rpm to bring the hole to its final dimensions within the necessary tolerance. Lastly, the 10 mm square-end end mill is used to create the 0.026" deep counterbore. Finally, the rocker cover screw holes (feature 5) are drilled

and tapped using #46 drill bit to a depth of approximately 0.209” at 1600 rpm followed by a M2.5 × 4.5 tap with wax applied. This process is then repeated for the left side of the cylinder head after angling the sine block 20° in the opposite direction (right picture Figure 3.40).

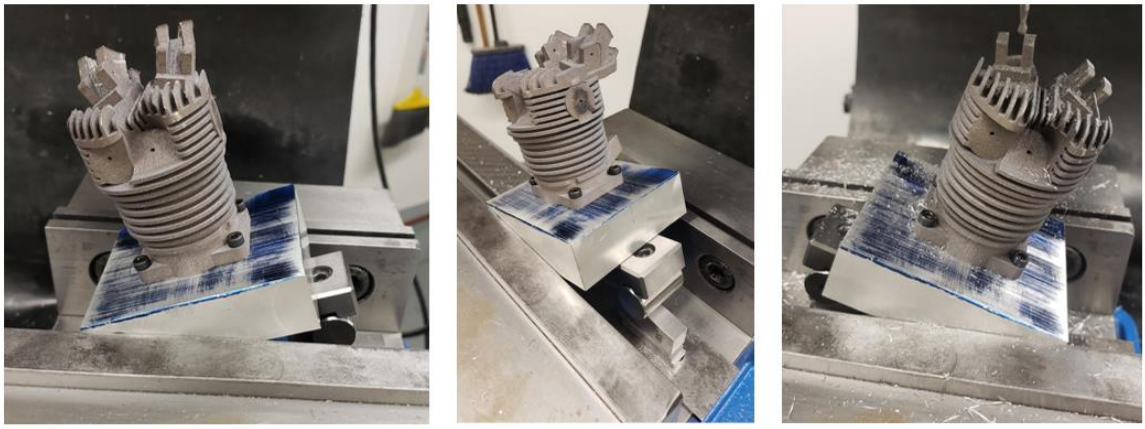

*Figure 3.40: Set up for the features that are angled at 20° (features 5-8) on cylinder head*

Next, the cylinder is positioned similarly to previous steps, but now at 10° so that the pushrod holes (feature 2) can be drilled (Figure 3.41). Since the geometry of the cylinder head does not provide any surfaces for zeroing, a #58 drill bit (0.008” smaller than the AM pilot hole size) is used to line up the axes by making sure it goes through the pilot hole with an example of this process shown in Figure 3.41. This effort requires a stiff tool to prevent it from slipping when starting the hole since it is being drilled on an angled surface. Therefore, a center drill followed by carbide drill bit is used for the smaller initial hole. Finally, a B drill bit with a speed of 1000 rpm is used to obtain the final diameter. Like before, this process is repeated for the other side by tilting the head in the opposite direction.

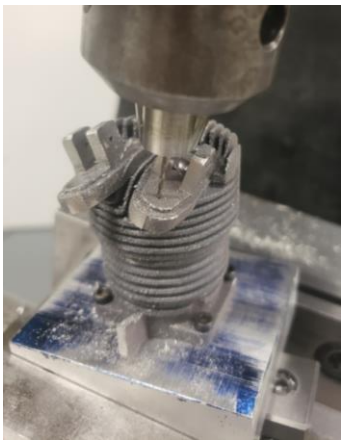

*Figure 3.41: Set up for 10° angled features (feature 2) on cylinder head*

Subsequently, the cylinder had to be positioned such that the vice was not grasping a significant amount of material and the part was not self-supporting. Therefore, a 5" sine block as shown in Figure 3.42 was used because it has a larger lip at the end for squaring. Moreover, this configuration required the sine block to be set at 20° in order to make the rocker flanges level (normal to the drill bit), allowing features 3 and 4 to be machined. To zero the axes on the hole, the prior technique using a small drill bit to align the axes with the AM pilot holes was similarly used. Of importance, this zeroing process was utilized for all hole features. Then, features 3 and 4 were drilled through, employing a #39 drill bit, with a subsequent drilling of feature 4 using a #28 drill bit. Lastly, feature 3 was tapped by letting the tap move through the feature 4 hole as shown in the right picture in Figure 3.42. This entire process was repeated after flipping the cylinder to the other side.

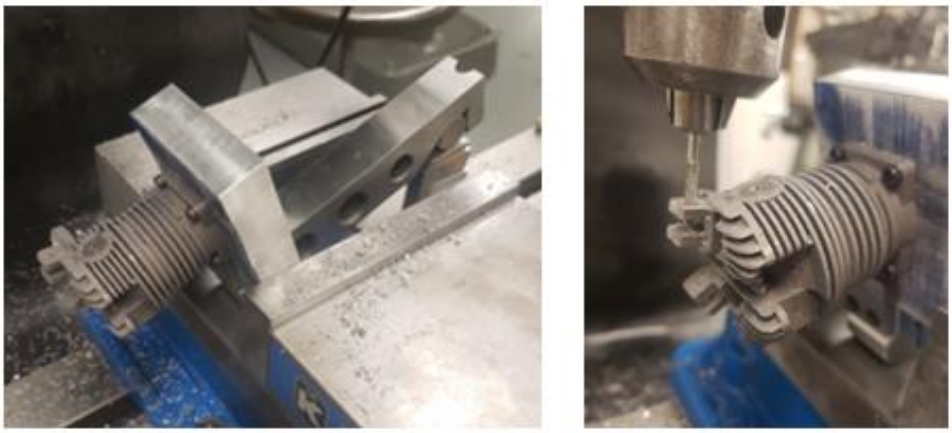

*Figure 3.42: Setup for rocker flange holes (left), representation of tapping feature 3 though feature 4 (right)*

Consequently, the air intake port (feature 12) is drilled. To accomplish this procedure, the cylinder head is placed in the vice as shown in Figure 3.43 (left). The pilot hole is first made larger using a center drill, then the drill bit size is stepped up while decreasing the spindle speed until it is finally drilled with an O drill bit to a depth of 0.75" at a speed of 1000 rpm. With each drill bit change, the *z*-axis is zeroed using the same process to the bearing bores for the crankcase; however, instead of using a parallel bar, a gauge block is used since the surface area is relatively small. Lastly, a 10.5 mm square end mill is used to create a 0.077" deep counterbore.

Next, the exhaust port must be drilled and tapped while in the configuration shown in Figure 3.43 (right). Since this is a through hole into the valve guide bore, the *z*-axis does not require zeroing. Again, the drill bit sizes and spindle speeds are stepped up and down, respectively, as they were before until a J drill bit is used at a speed of 1000 rpm for the final cut. A 9 mm square end mill is then used to excavate the counterbore to a depth of 0.235" after which

the same depth is threaded using a M10 × 1 tap, followed by a deburrer to create a rounded finish from the top flat original surface to the threads.

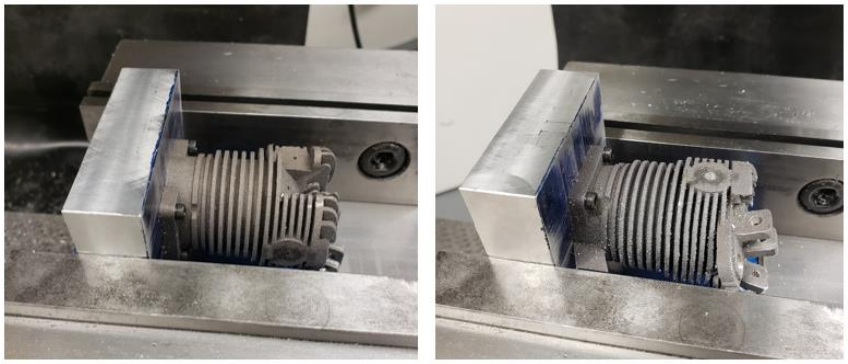

*Figure 3.43: Setup for intake (left) and exhaust (right) ports*

For the spark plug hole (feature 10), extra care was taken to ensure that the part was fixed correctly. Since the surface of this hole is at a plane angled 9.6° from the *x*-axis and -40.5° from the *z*-axis, the combination of an angled vice and a sine block had to be used as shown in Figure 3.44. Note, if another fixturing device was made with an angled surface on it, an angled vice might not have been needed. Here, the sine block was angled at 40.5° and the angle vice turned 9.6°. Then, using a machinist jack and a probe, the third angle was set. After this, the hole was drilled through by stepping up drill bits until employing a final 7/32 drill bit. Next, a 0.013" counterbore was drilled using a 10 mm square-end end mill and finally the hole was threaded using ¼-32 tap.

*Figure 3.44: Setup for drilling sparkplug hole, using a sine block, angle vice, machinist jack, and probe*

Before taking the cylinder head off the fixture device, the rest of the support material was removed from the base using the set up in Figure 3.45. This was accomplished by using a square-end end mill to machine the head down to the surface. However, the push rod guide supports (feature 1) only required sanding via a belt sander.

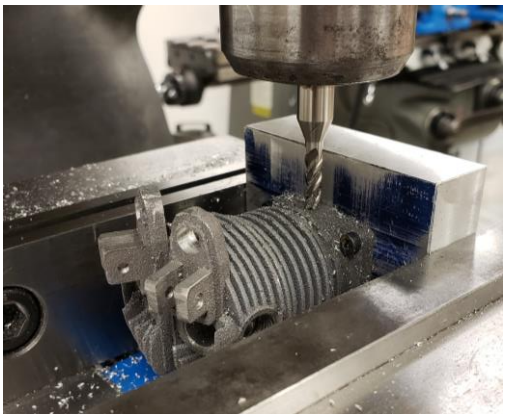

*Figure 3.45: Setup to remove left over support material at base of cylinder head*

For the last vice setup, a second fixture device was used to machine the base of the cylinder head and also bore the cylinder walls. This device lets the cylinder sit flat upside down while elevating it for clamping purposes. It should be noted that the device is clamped in the vice on the sides that are not already stressed by the bolts; hence, this allows the clamping load to be evenly distributed on the cylinder, subsequently preventing any distortion of the inner walls (Figure 3.46). Then, the *x*- and *y*-axes are zeroed using a dial indicator on the inside surface of the cylinder. Next, using a boring bar at a speed of 200 rpm, the bottom surface is machined to take away the extra 0.030" of material added during the manufacturing process. This is followed by boring the cylinder walls at a speed of 280 rpm and using the auto quill feed at rate set to 0.0015". Afterwards, the *z*-axis was zeroed using the same process as the crankcase bearing surfaces. Note that while boring, WD40 was sprayed into the cylinder frequently and the quill feed was used for both upwards and downwards motions. Like before, the bore is measured repeatedly between cuts using a telescoping gauge and micrometer, and the diameter is taken down to just 0.003" over the final dimension.

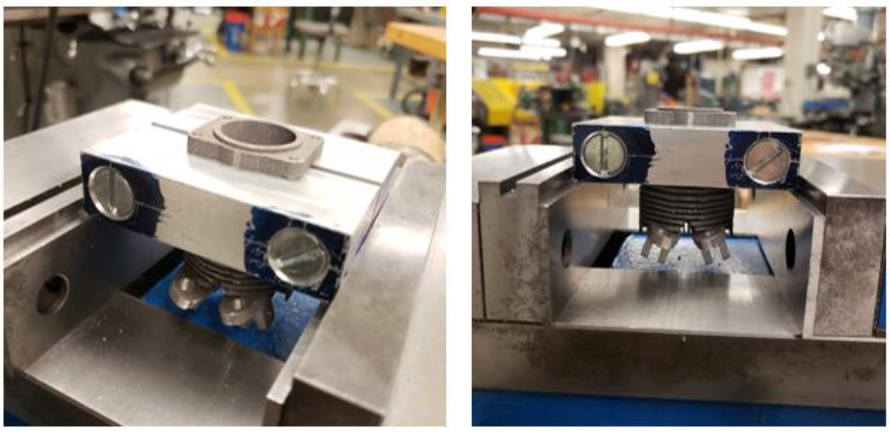

*Figure 3.46: Setup for boring the cylinder head base and wall*

Finally, before honing the cylinder, the valve seats must be created. To do this, the following process was applied: a 45° chamfer tool is used to cut the approximate geometry, then to smooth the surface perfectly, the valves themselves along with fine sandpaper pressed against the seat by inserting the stem into the guide and rotating the stem outside of the cylinder using a hand drill, for the final passes, this same process was followed again but with an abrasive agent for lapping instead of sandpaper. The integrity of the seal is checked afterwards by listening for leaks as the piston is pushed into the bore.

### 3.10.3. ***Cylinder Honing***

As discussed earlier, due to the high silicon content of the AM cylinder head, a cylinder liner is unnecessary and the cylinder could instead be honed according to the hypereutectic aluminum boring process described by both Engine Builder Magazine and Sunnen [56, 66]. The goal of this process is to achieve a smooth finish with a crosshatch pattern for oil lubrication, and a 19 μin silicon exposure height. An advantage of exposing this silicon is that it provides a harder surface for the piston rings to ride on, preventing wear on the aluminum. Before honing, the Sunnen honing mandrel (Y32-1062PB), stones (Y32J54, Y32J84, Y32-C03-31), bronze guide shoes (PBB), and felt pads had to be modified for use in a blind hole (C30F85). All of these could have been special ordered, but to make this process more economical, all changes were made in KU's machine shop instead.

The honing mandrel was modified so that the stones and guide shoes were able to reach the bottom of the bore, the original design is depicted in Figure 3.47 and the modified mandrel is shown in Figure 3.48. To do this, the bottom 0.8" of the mandrel was cut off using a hand saw

and a new hole was drilled to insert a smaller tension rod. Furthermore, new holes were drilled and tapped for 4-40 machine screws to hold the bronze guide shoes in place on the bottom since the shoe clamps had to be taken off.

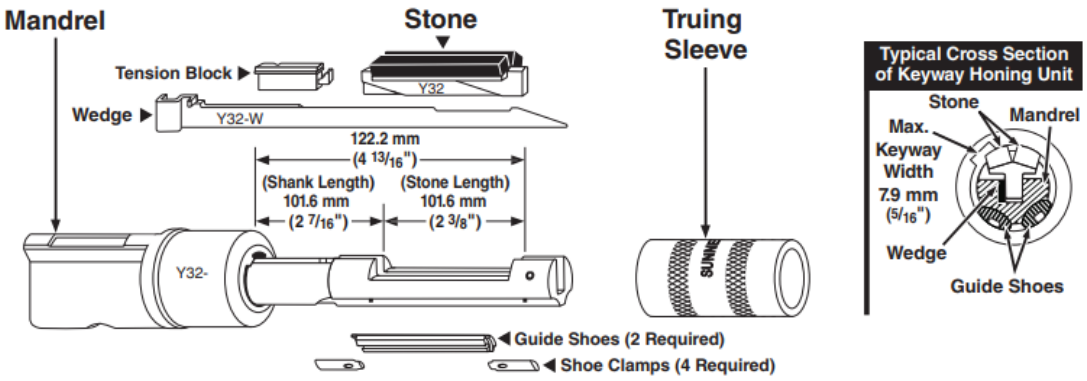


*Figure 3.47: Exploded view of Sunnen honing mandrel [78]*

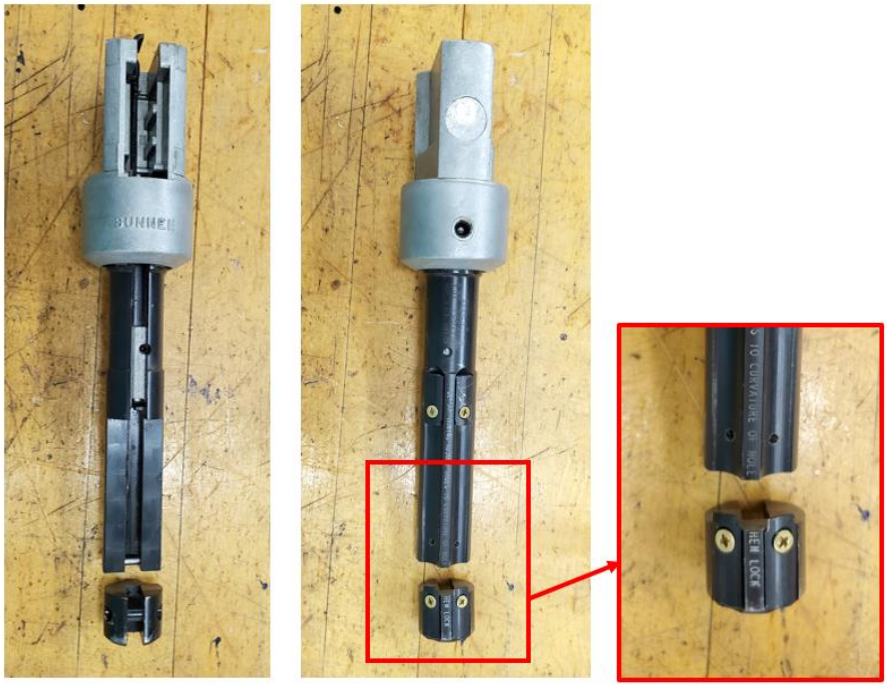

*Figure 3.48: Modified Sunnen honing mandrel for blind holes*

The modifications of the stones were made according to the Technical Data section of the Sunnen Precision Honing Supplies catalogue [78]. Accordingly, the new stone and guide shoe length should be between ½ and 2/3 of the bore length and in this case it put the stone length at ~0.95". The stones were shortened by hand sawing at the cut off line and chiseling the excess away. Figure 3.49 shows the shortening of the stone (middle) compared to the original untouched stone (top), and the replacement of the stone with felt attached with J-B Weld two-part epoxy (bottom). Additionally, Figure 3.50 shows the addition of the felt pad on the machined flat surface (top) and the bronze guide shoe shortened by milling down the top (bottom). All of the felt pads had to be shaved down prior to the final honing step to get them to fit snuggly in the bore without putting too much pressure on the cylinder walls.

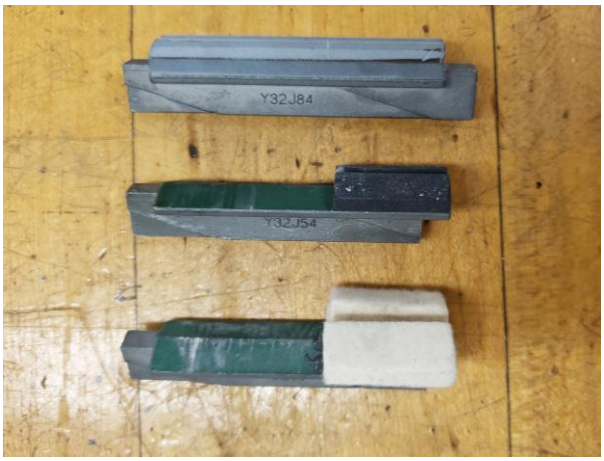


*Figure 3.49: Original (top), modified stones for blind hole honing (middle, bottom), and felt replacement for silicon exposure (bottom)*

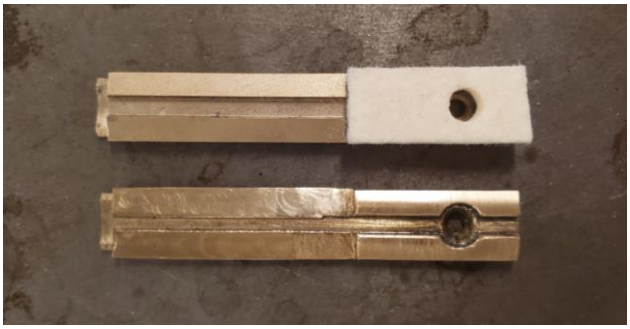

*Figure 3.50: Modified bronze guide shoes for silicon exposure (top) and blind hole honing (top and bottom)*

Further modifications can be seen in Figure 3.49 and Figure 3.50 to accommodate the blind hole. For the stones, this includes milling of the step into the steel backing making the shortened length 2.55” so they could sit on the new tension rod and stay in place. Moreover, the bottom lip on the brass guide shoes was milled away, and a screw hole with a counter sink is drilled. These are made so the stones and the shoes are able to go all the way to the bottom of the bore.

The setup of the honing mandrel, stones, and guide shoes are depicted in Figure 3.47. To use this tool on a vertical mill, the entire assembly must be inserted into a mandrel driver (pictured in Figure 3.51). Once everything is in place with the quick release lever down, and the mandrel not in the work piece, the cutting pressure dial is set to 4. The quick release lever is then pulled up and the tool inserted into the bore, after which the quick release lever can be pushed back down. Lastly, the stone feed-up knob is rotated clockwise until the quick release lever can be pulled back halfway without force and without retracting the stones. The quill speed on the mill was set to 260 rpm and the stones were stroked at about 60 strokes/minute to get a roughly 45° crosshatch pattern. The micrometer depth control was set so the quill would stop just before

the stones hit the bottom of the bore. A clamping device was also used to prevent the honing mandrel from coming too far up and out of the bore, otherwise the universal joint would allow it spin outwards in a dangerous manner. Moreover, the standard vice had to be replaced with a two-piece vice so that the cylinder could sit low enough for the honing mandrel to be above it with the mill at its lowest *z* position. Figure 3.52 shows the honing setup used for the cylinder and as can be seen, there was just barely enough room. For all the stone honing steps, an ample and steady flow of Sunnen honing oil should be used, but for the felt pads only the Sunnen AN30 silicon compound should be used to coat the cylinder walls and cover the pads. The following process was used to achieve a plateau finish (i.e., Figure 3.53) with exposed silicon [66, 73]:

1. Bore the cylinder to within -0.003" of the final diameter.
2. Use the roughing stone to put in a crosshatch pattern. This pattern is critical for oil lubrication of the cylinder walls during operation. This is done with the Sunnen 220 Grit stone (Y32J54). Roughly 0.002" of material should be removed from the diameter during this step.
3. Take off the peaks of the surface profile using the Sunnen 400 grit stone (Y32J84). After this step the surface should have ≤ 19 μin Ra finish. Only 0.0005" of material should be removed from the diameter during this step.
4. Further smooth out the peaks using a polishing stone (Y32-C03-31). This step should produce a ≤ 3.9 μin Ra finish and only remove 0.0001" of material from the diameter.
5. The final step is to expose the silicon using the AN30 compound and felt pads. For this step, pressure should be low, and it should last 1-1.5 minutes to achieve a 19 μin exposure height for the silicon.

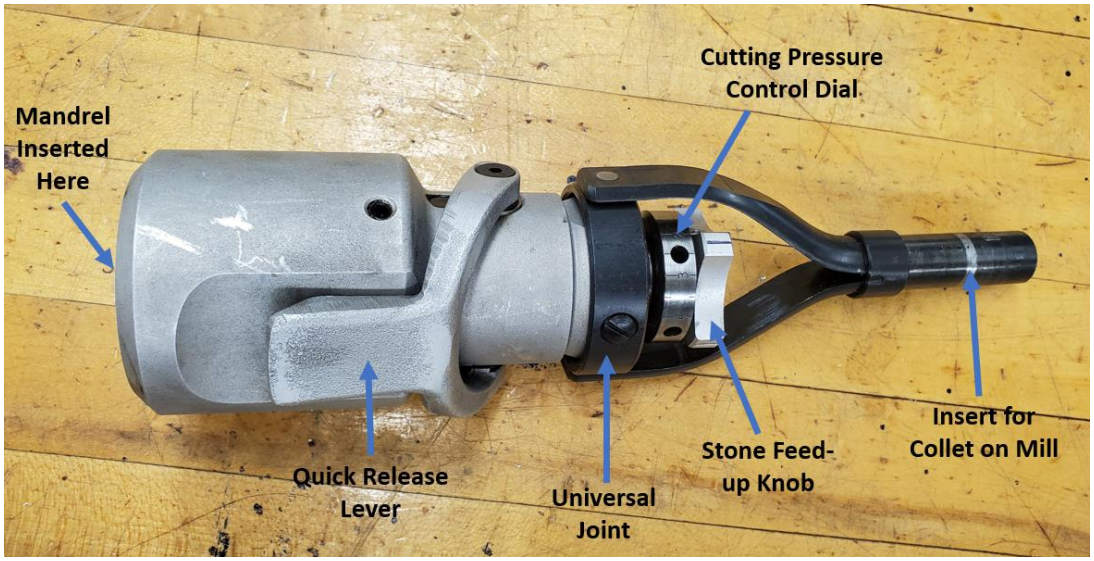


*Figure 3.51: Sunnen mandrel driver*

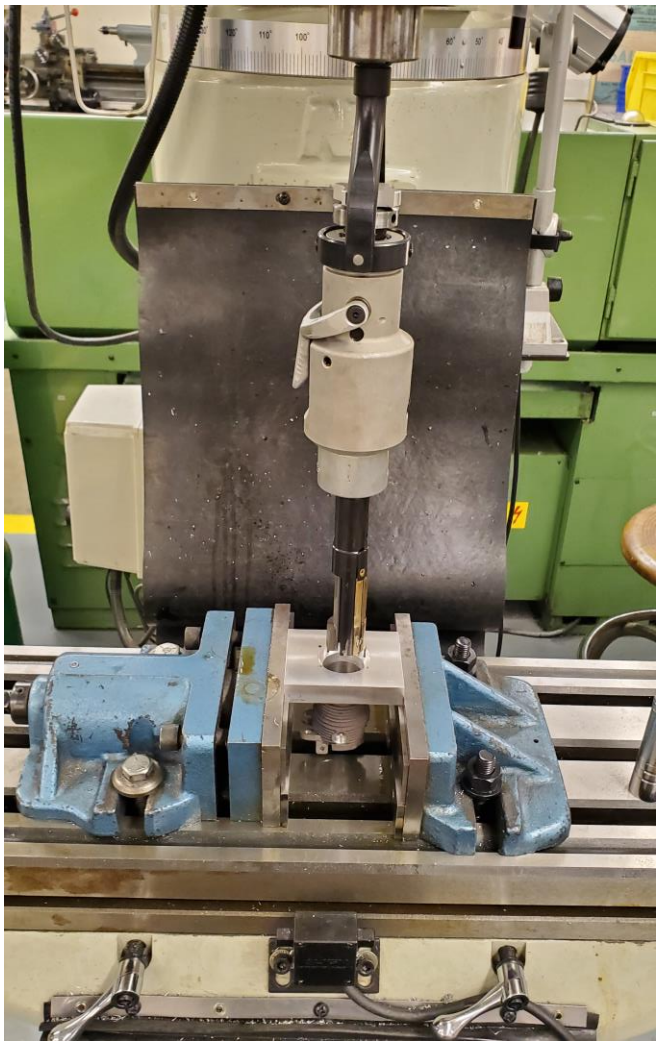

*Figure 3.52: Honing setup with two-piece vice and new fixture*

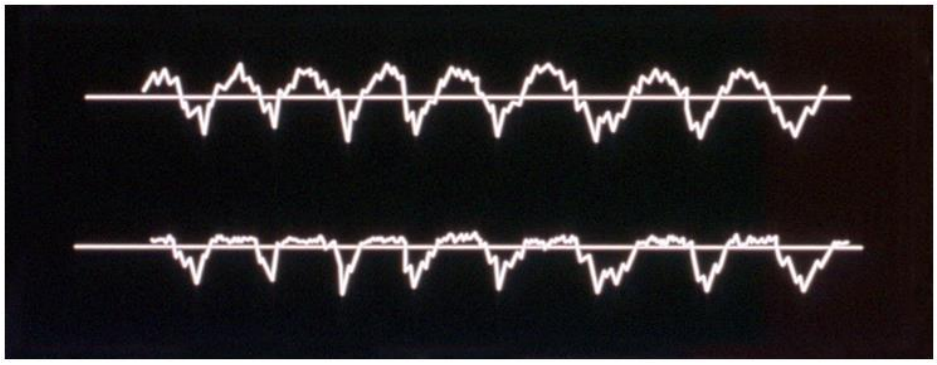

*Figure 3.53: Example profile (top) and its result from plateau honing (bottom) [72]*

Before honing the actual AM cylinder, testing occurred using two pieces of aluminum scrap and during this process it was discovered that the bronze guide shoe edges were too sharp and consequently taking material off themselves instead of just keeping the mandrel in place. To alleviate this issue, all sharp edges and burrs were filed on the shoes. The result of this fix can be seen in Figure 3.54.

*Figure 3.54: Practice honing: before bronze guide shoes were filed (left), and after (right)*

Next, one of the extra AM cylinders was used for practice in case anything was different with the AM material (such as a greater porosity causing issues). After which, it was discovered that the fixture mentioned earlier in Figure 3.37 (right picture) did not do a sufficient job in distributing the clamping force throughout the cylinder. In fact, the diameter of walls clamped by the screws were 0.006" bigger than the walls clamped by the vice. After this discovery, the actual AM cylinder dimensions were checked and they were off by ~0.007", with parts of the cylinder being 0.002" greater than the desired final diameter. In an attempt to fix this, the cylinder was placed back into the jig and a hydraulic press was used to yield the cylinder back into a cylindrical shape (Figure 3.55). To make sure this was not overdone, the cylinder was

pressed into smaller diameters, the pressure was removed, and the relieved diameter was checked. This was done with consecutively smaller diameters under pressure until the relieved diameter measured 0.001” under tolerance, giving room for material to be removed during honing. A new jig was developed to more effectively simulate the force of securing the cylinder head to the crankcase (Figure 3.56). This was unable to be used previously since the standard vice employed was not tall enough. A larger diameter step was also machined into the fixture to give room and provide a platform for surface roughness measurements.

*Figure 3.55: Using a hydraulic press to yield the cylinder back into a cylindrical shape*

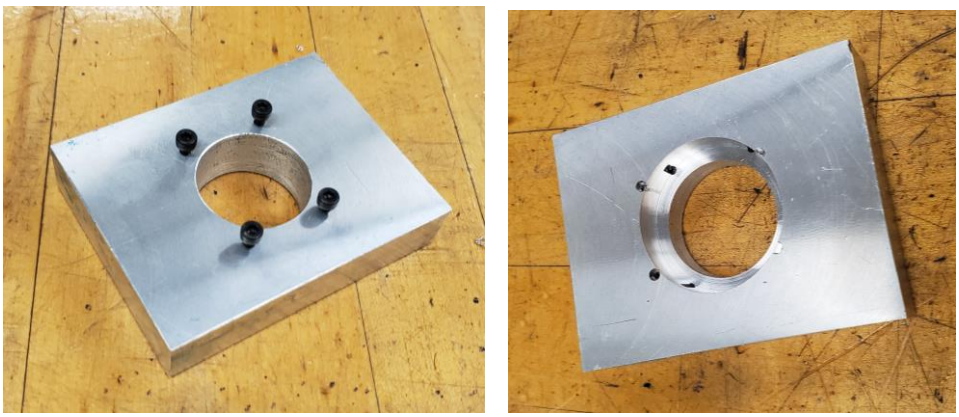

*Figure 3.56: New fixture for honing and boring*

In order to make sure the honing process was being done correctly, a Mitutoyo Profilometer SJ-210 was implemented to take intermittent surface roughness measurements between steps. Each time the drive unit and stylus were reattached, the profilometer was recalibrated using the Precision Reference Specimen provided by Mitutoyo. The surface profiles were taken utilizing the parameters provided in Table 3.6. Moreover, a clamping device with a nylon screw (to prevent scratching) was developed and used to secure the profilometer and ensure it was measuring at a consistent angle and depth (Figure 3.57). Additionally, to extract the data collected by the device, a free software provided by Mitutoyo was used (SurfTest SJ USP Communication Tool Ver5.007), a depiction of this interface can be found in the appendix (Figure B.4). After measuring a surface with the profilometer connected to the computer via USB, the “Meas. Data” button on would load the data to the program, then the “Export” button was used to save everything to an external Excel file.

*Table 3.6: Mitutoyo Profilometer SJ-210 measurement conditions*

| | |
|---|---|
| **Standard** | ISO 1997 |
| **Profile** | R |
| **λs** | 320 µin |
| **N** | 5 |
| **Cut-Off** | 0.1 in |
| **Filter** | GAUSS |

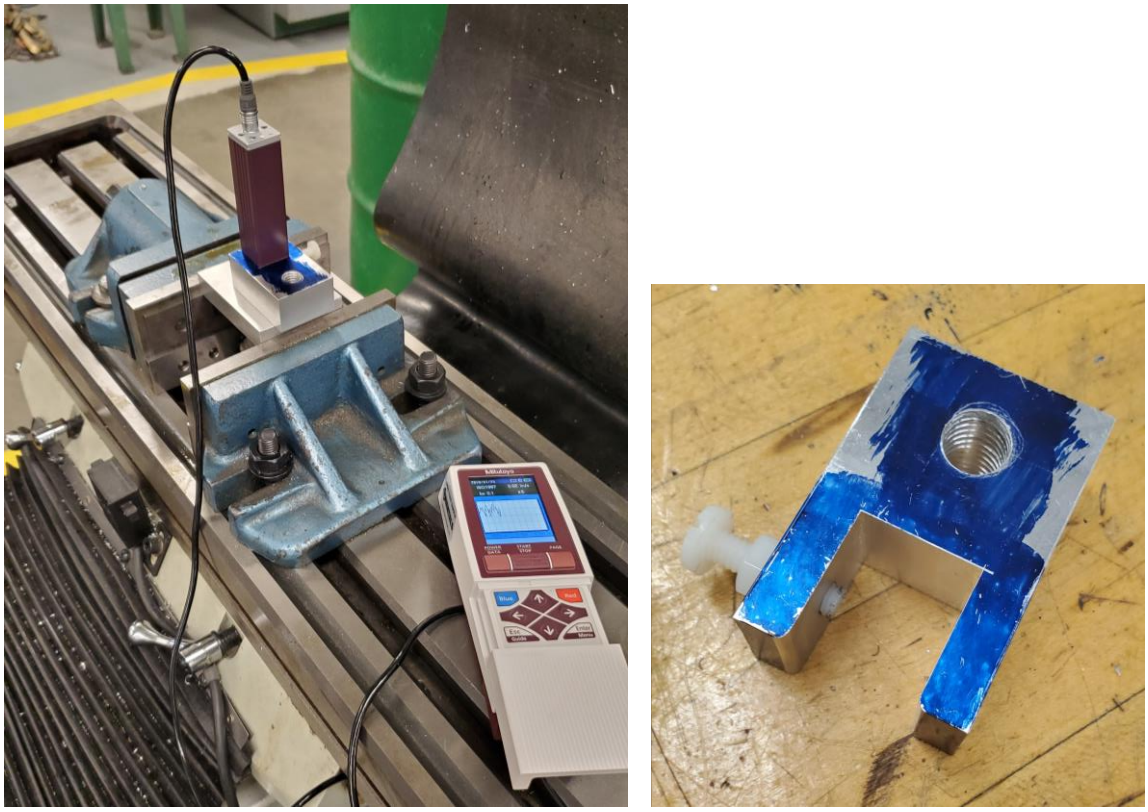

*Figure 3.57: Profilometer measurement set up (left), and fixture for profilometer (right)*

Table 3.7 shows the surface R-values of the stock cylinder head, and between all steps while honing the AM cylinder head. Each of these values is an average of the four measurements taken, the locations of which are designated by the red numbering in Figure 3.58. Furthermore,

Table 3.8 displays diameter measurements (average of three) taken between honing steps using a telescoping gauge and a 1-2” micrometer to characterize how much material was being removed. These data show that the honing process removed less material from the bottom of the cylinder as compared to the rest of the part; however, this should be acceptable since the piston will not traverse that far up the wall. Additionally, Sunnen provided approximate numbers for where R-values should fall for a “Performance Finish” including: Ra = 6-10 µin, Rpk = 8-13 µin, Rk = 16-24 µin, Rvk = 15-23 µin, Mr1 ≥ 6%, Mr2 ≥ 83%, Rz = 10×Ra µin [72]. According to these values, the AM cylinder honing was done properly. The only value that fell outside is Rvk which is still relatively close. Overall, Figure 3.59 through Figure 3.63 show the surface profiles that correspond to each of these steps. As can be seen, these profiles are exactly what was expected: i.e., the roughing stone created peaks and valleys more consistently than boring did, the 400 grit cut off some of the peaks, the polishing stone smoothed these peaks further, and the exposure step produced silicon protrusions roughly 19 µin above the surface. Moreover, when comparing the results of this honing process (Figure 3.63) to the stock cylinder liner (Figure 3.64), the AM cylinder has a more apparent plateau finish with deep valleys for oil lubrication, meaning that the AM cylinder could potentially perform better than the stock option. However, there was some slight visible porosity in the AM cylinder wall which could potentially cause issues during operation (Figure 3.65).

*Table 3.7: Roughness value comparisons of cylinder head walls*

| Value | Description | Unit | Stock Cast Part | After Boring | After 220 Grit | After 400 Grit | After Polishing | After Silicon Exposure |
|---|---|---|---|---|---|---|---|---|
| **Ra** | Roughness Average | µin | 6.81 | 75.22 | 40.06 | 11.34 | 7.80 | 9.12 |
| **Rq** | RMS Roughness | µin | 8.74 | 93.09 | 50.92 | 15.8225 | 10.13 | 12.99 |
| **Rz** | Average Max. Height of the Profile | µin | 52.82 | 463.89 | 308.85 | 137.82 | 67.47 | 92.04 |
| **Rp** | Maximum Profile Peak Height | µin | 19.75 | 209.06 | 103.66 | 36.49 | 24.86 | 21.47 |
| **Rv** | Maximum Profile Valley Depth | µin | 33.07 | 254.82 | 205.19 | 101.34 | 42.60 | 70.57 |
| **Rsk** | Skewness (Profile Asymmetry) | | -0.63 | -0.07 | -0.75 | -1.75 | -1.12 | -1.66 |
| **Rkµ** | Kurtosis (Profile Peakedness) | | 3.83 | 2.79 | 3.86 | 10.12 | 6.51 | 8.20 |
| **Rt** | Maximum Height of the Profile | µin | 78.19 | 600.43 | 378.62 | 203.19 | 110.67 | 129.31 |
| **Rk** | Core Roughness | µin | 19.05 | 239.98 | 121.38 | 31.31 | 15.05 | 22.21 |
| **Rpk** | Reduced Peak Height | µin | 9.96 | 95.68 | 36.57 | 11.84 | 21.73 | 10.16 |
| **Rvk** | Reduced Valley Depth | µin | 17.41 | 101.72 | 78.11 | 30.66 | 25.41 | 28.57 |
| **Mr1** | Peak Material Ratio | % | 7.39 | 9.40 | 5.29 | 4.94 | 11.57 | 8.47 |
| **Mr2** | Valley Material Ratio | % | 85.95 | 89.33 | 85.39 | 84.11 | 80.18 | 83.46 |

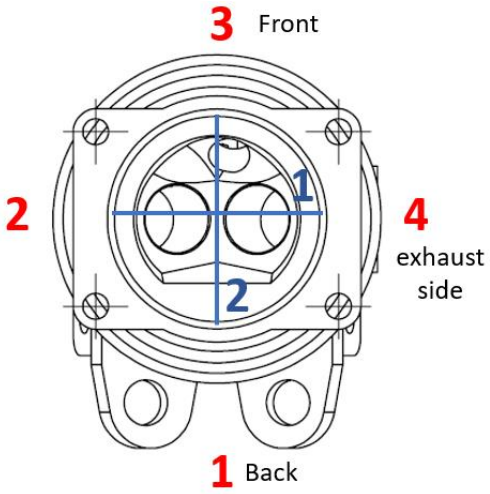


*Figure 3.58: Depiction of measurement locations*

*Table 3.8: Cylinder head diameter data in mm for stock cylinder and during honing process (average of three measurements)*

| | Stock Cylinder | After Boring | After 200 Grit | After 400 Grit (Final) |
|---|---|---|---|---|
| 1 Top | 1.0627 | 1.0608 | 1.0618 | 1.0619 |
| 2 Top | 1.0628 | 1.0610 | 1.0617 | 1.0617 |
| 1 Middle | 1.0630 | 1.0607 | 1.0629 | 1.0635 |
| 2 Middle | 1.0630 | 1.0613 | 1.0627 | 1.0633 |
| 1 Bottom | 1.0633 | 1.0614 | 1.0633 | 1.0639 |
| 2 Bottom | 1.0630 | 1.0623 | 1.0634 | 1.0635 |

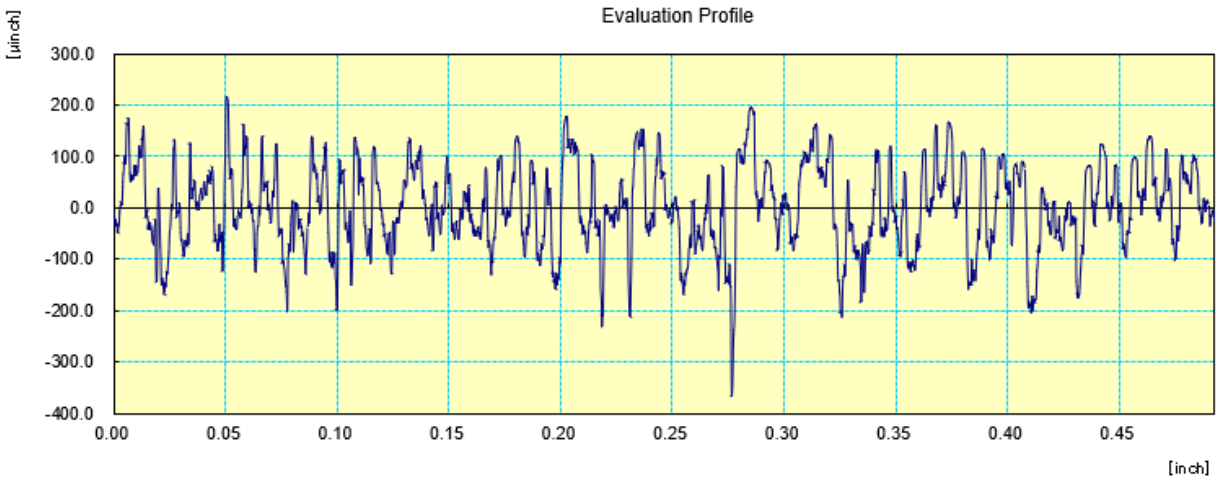


*Figure 3.59: Surface profile of AM cylinder head after boring to +0.003" of final diameter*

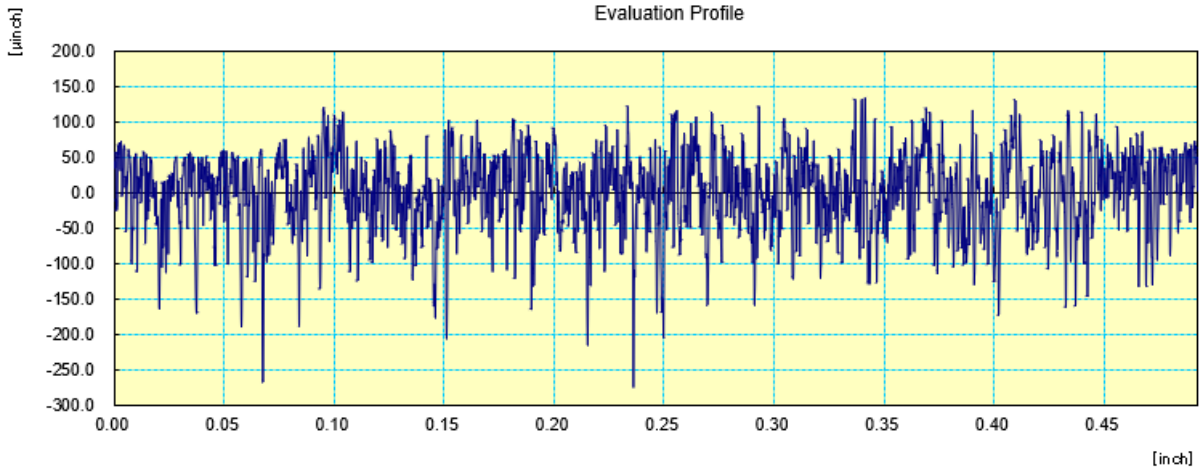


*Figure 3.60: Surface profile of AM cylinder head after using the roughing 220 grit stone*

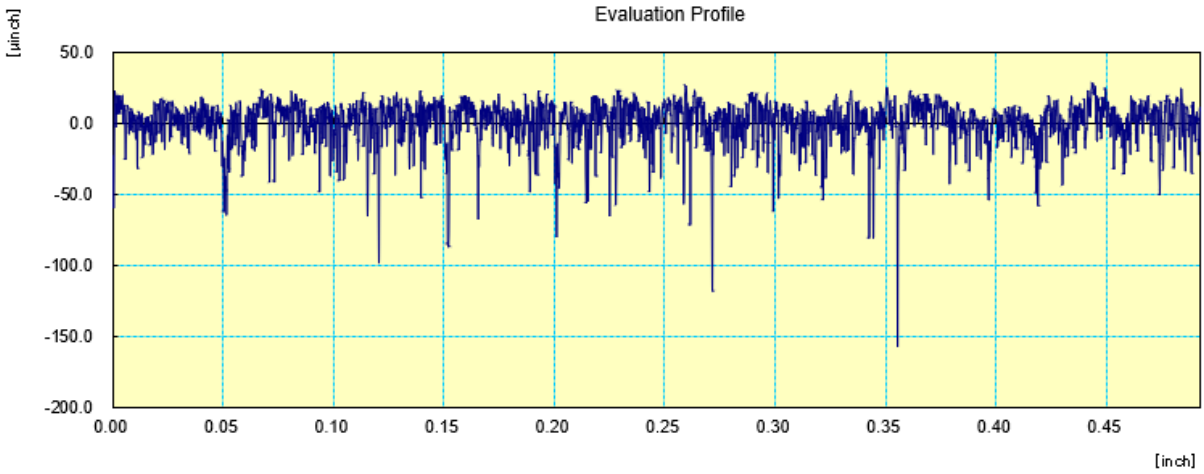


*Figure 3.61: Surface profile of AM cylinder head after using the 400 grit stone*

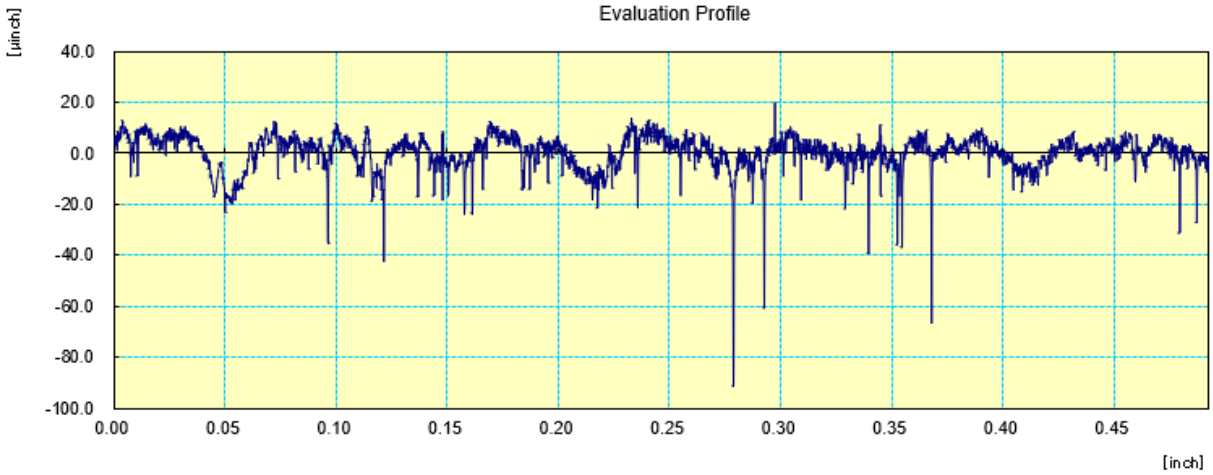


*Figure 3.62: Surface profile of AM cylinder head after using the polishing stone*

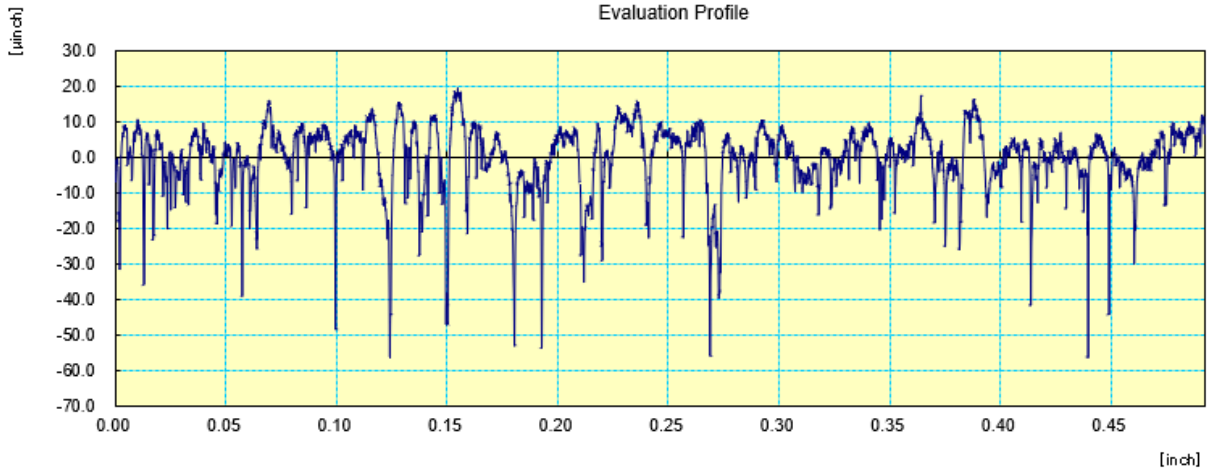


*Figure 3.63: Surface profile of AM cylinder head after exposing the silicon with compound and felt pads*

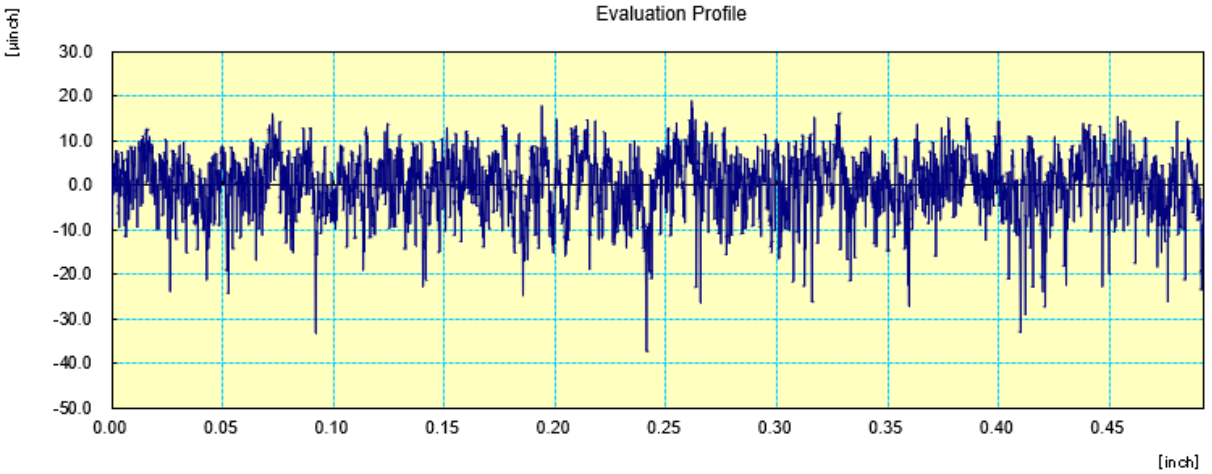


*Figure 3.64: Surface profile of stock cylinder head liner*

*Figure 3.65: Finished (post honing process) AM cylinder wall*

## 3.11 **Post Machining Results**

After machining these components, one final CT scan was performed to check for any cracking or defects that vibration from machining may have caused. In addition, this allowed for a comparison of the finalized part to the original cast part to see how close the AM method was able to come to the initial design.

### 3.11.1. ***Nominal Actual Dimensional Analysis***

Comparing AM parts to the cast parts was the best way to illustrate how close this entire process can get to replicating and replacing original equipment manufacturer (OEM) parts. It should be noted that even if a casting process was used to reproduce these parts, there would still be some differences due to initial variances in the CAD models. From examining Figure 3.66 and Figure 3.67, almost all critical features including bearing surfaces, screw, holes, and gasket

faces are within ± 0.005”. The areas of concern are mostly within the cylinder head, where the internal geometry is slightly off and where the gasket face has a bit too much material on it. However, despite these differences, the geometry appears close enough to where engine operation should not be drastically influenced. If major issues are identified while reassembling, there may be further adjustments made to these parts to generate the best results.

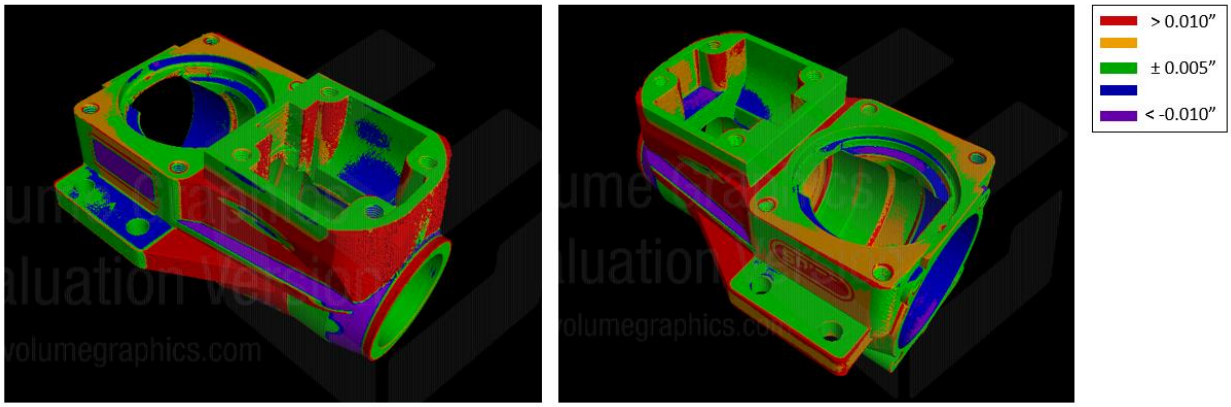


*Figure 3.66: Nominal actual dimensional analysis of AM modified crankcase 2 vs. original cast part*

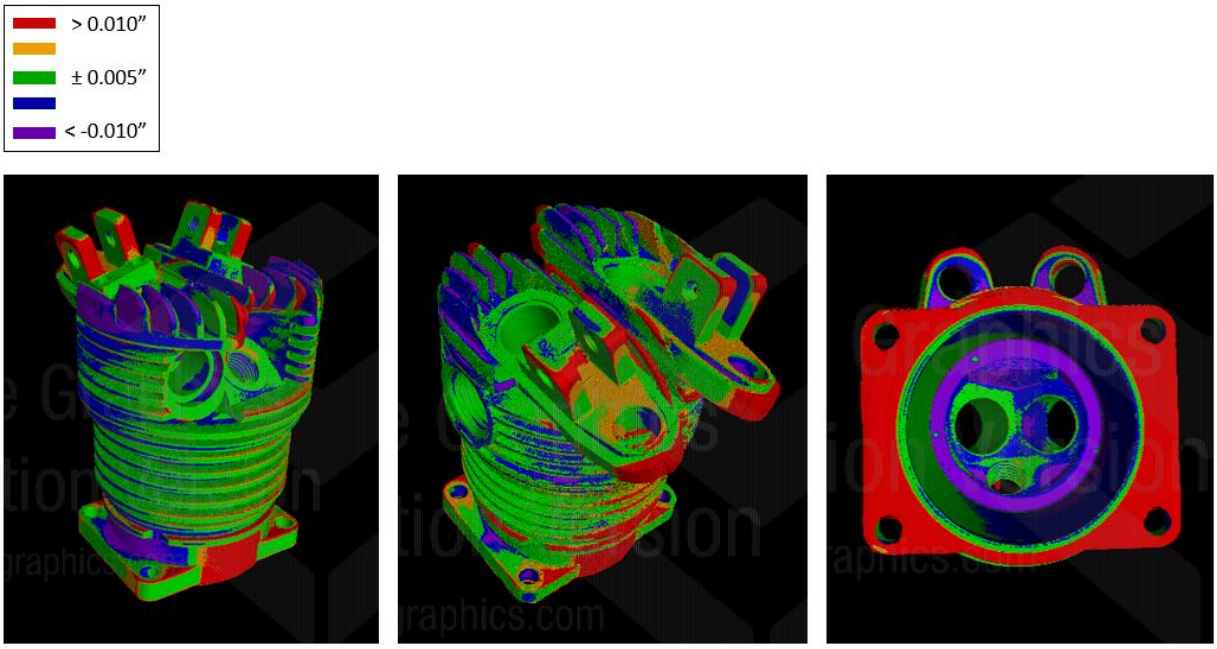


*Figure 3.67: Nominal actual dimensional analysis of AM cylinder head 2 vs. original cast part*

### 3.11.2. ***Porosity Results***

As expected, the porosity percentage of the parts decreased after machining due to the removal of the support ruminants, the pilot holes being drilled, and by machining the bulk material in the top of the cylinder head. In specific, the crankcase porosity volume percentage was reduced by 1/3 and the machined cylinder head has 1/5 the porosity volume percentage of the pre-machined part (Figure C.22, Figure C.23, and Table 3.9). For the crankcase, the largest pore size stayed relatively the same; whereas, the cylinder head's largest pore is 1/3 of the pre-machined part (Table 3.9). In Figure C.24 and Figure C.25, the porosity distribution between the pore sizes stayed consistent for the cylinder head albeit with lower values. Furthermore, the

crankcase also stayed constant, except for the reduction in the larger pores detected. This is most likely due to the elimination of the piolet holes from being drilled and tapped.

Of note, there were some issues with scan artifacts in the CT images of the crankcase, subsequently causing the CTAn software program to identify large areas of porosity (demonstrated in Figure 3.68) that did not actually exist at the front of the crankcase. To resolve this issue, porosity data for these image slices were replaced by data from the previous scan of the pre-machined crankcase. Here, since this area was not touched while machining, the porosity should not have changed; hence, this makes this replacement justifiable. In addition, it should be noted that the heights for the pre and post machined parts do not line up exactly. This is most likely because they were not perfectly vertical during the scanning process.

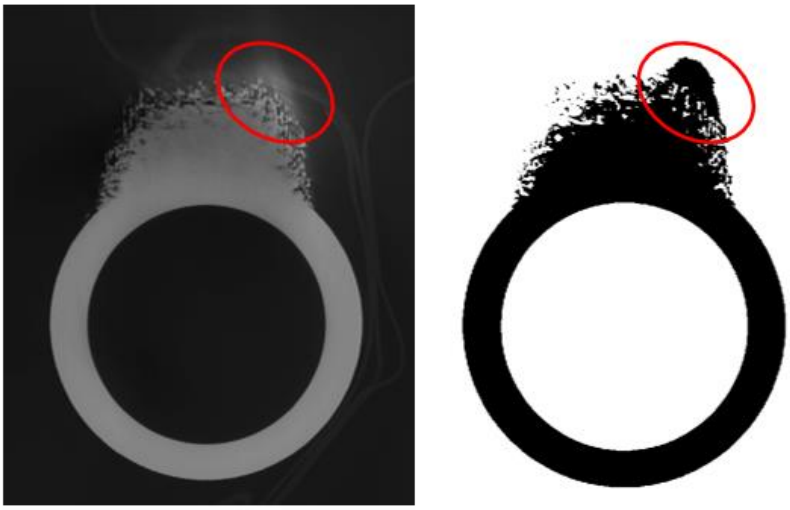

*Figure 3.68: Post machined crankcase CT image with the artifact circled in red and its corresponding binary image identifying it as material; hence, causing a false porosity indication*

*Table 3.9: Crankcase and cylinder head porosity results after machining*

| Component | Machine | Voxel Size [µm] | Total Porosity Volume [%] | Largest Pore Size [$mm^3$] |
|---|---|---|---|---|
| AM Ti64 Crankcase 2 (Modified) | Northstar | 41.30 | 0.0002 | 0.0040 |
| AM Al Cylinder Head 2 | Northstar | 41.30 | 0.0061 | 0.0096 |

### 3.11.3. ***Resulting Defects***

There were no additional defects caused by the machining process. Therefore, the post machining process appears to be effective and appropriate for these AM parts. As a result, it was determined that these parts would be acceptable going forward into engine testing.

## 3.12 **Conclusions**

In this chapter, the entire AM process and its associated difficulties are discussed for major IC engine components (i.e., crankcase and cylinder head). First, these parts were reverse engineered by taking measurements, modeling, and verifying the models through dimensional analysis. Next, the materials and machines to be employed are considered. Subsequently, the models were modified for AM construction while adding the needed support structures. After manufacturing, the AM constructed components were checked for porosity and defects, before finally post machining. While this process presented many challenges, post-processing of the AM parts determined that they appear to reasonably approximate their corresponding cast versions (i.e., no major discrepancies) and are functional for engine test cell operation.

When presented to a skilled modeler and machinist, this entire procedure should be able to be completed in roughly a month with the step-by-step approximate timeline given in Figure 3.69. This relatively short process illustrates its viability for the Army to use in field applications should an engine be damaged. Moving forward, the next chapter will discuss the engine setup, data acquisition, and the results of the comparative testing between the stock and AM constructed engines. These results will be the true test as to whether all the prior mentioned processes were indeed successful.

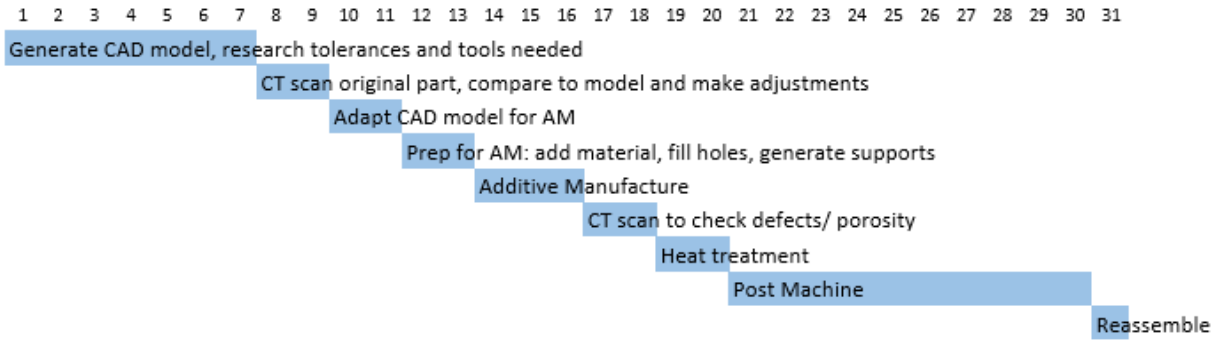


*Figure 3.69: Approximation of time for reverse engineering, AM, and post-processing (days)*

# Chapter 4: Experimental Setup, Instrumentation, and Data Acquisition

The previous chapter discussed the entire process involved in using additive manufacturing (AM) to produce internal combustion (IC) engine cylinder head and crankcase components. The results showed that the parts were similar enough geometrically and structurally to validate the assumption that they will perform the same as the die cast originals. To test this hypothesis further, an experimental setup was created by attaching stock and AM part variants of the same engine to a dynamometer or propeller while using sensors to measure several parameters during operation. It is through these efforts that a determination of AM's effectiveness in engine components is possible**.**

## 4.1 **Engine Test Setup**

### 4.1.1. ***Setup Iteration 1***

In order to gather consistent engine data, the use of a dynamometer (dyno) is necessary to accurately and repeatedly load the engine. In this case, a Dyne Systems, Inc. Dymond Series 12 Alternating Current dyno was implemented, with its specifications listed in Table 4.1. The dyno is controlled using the Dyne systems, Inter-Loc V Operator Control Station (OCS), with the proportional-integral-derivative (PID) controls set to 10, 3.0, and 0.1 for P, I, and D, respectively. Before initial tests were performed, the dyno was decoupled from a Yanmar single-cylinder engine connected on the other side to reduce friction and inertia in the system. Then, a metal plate was attached to the Yanmar-geared lovejoy coupling to prevent any interference between the connections while testing.

*Table 4.1: Dyne Systems Dymond Series 12 Specifications*

| | |
|---|---|
| Manufacturer and Model | Dyne Systems, Inc.<br>Dymond Series 12 |
| Continuous Torque | 21.1 ft-lbs |
| Continuous Power | 12 hp |
| Speed Range | 0-7500 rpm |
| Voltage | 480 VAC |
| Phase | Three-phase |
| Frequency | 60 Hz |
| Controller | Dyne Systems, Inc.<br>Inter-Loc V OCS |

The dyno is limited to a maximum speed of 7500 revolutions per minute (rpm), however due to hardware limitations, it is only able to achieve speeds of up to 6000 rpm. This is because the standard firmware package loaded in the ABB drive's memory that limits the frequency output to 300 Hz (opposed to the max of 400 Hz). The engine has a speed range from 2000-9500 rpm; hence, this required integration of a gear ratio when connecting to the dyno. Using an MXL series timing belt (McMaster-Carr 1679K673) and two timing belt gears, a reduction from 0.79" to 1.26" was achieved; thus, allowing the dyno to operate within the engine's speed range. The 1.26" outer diameter (OD) timing belt gear (McMaster-Carr 1375K56) was attached to the dyno by screwing in a M12 × 1.75 threaded rod into the female threaded shaft of the dyno and then attaching the female threaded belt gear to the rod and tightening the set screws (Figure 4.1, left). Since the threaded rod could not be secured or tightened into the dyno shaft, the engine had to be positioned so that it would rotate the attached belt in a way that would allow the shaft to be self-locking. The 0.79" OD timing belt gear (McMaster-Carr 1375K45) was similarly attached and secured with set screws onto the end of the M7 × 1.0 threaded crankshaft of the engine (Figure 4.1, right). Both gears had to be drilled and tapped for this purpose. A belt tensioner was

necessary to make sure the belt maintained a tight connection with the belt gears, subsequently preventing slippage during operation. This belt tensioner pulley was employed by using the device pictured in Figure 4.2. This was constructed from three steel pieces welded together with slots milled in the two sidepieces to allow the pulley (McMaster-Carr 6235K64) to be adjusted vertically when setting the tension of the belt. The bottom piece had a ¾" hole drilled in it so that it could be secured to the T-slot skid that the engine and dyno both sit on. Additionally, a rod with threaded ends was manufactured that ensured a press fit of the bearing in the belt tensioner pulley. The threads are used along with butterfly screws to tightly secure the position of the pulley in the slots.

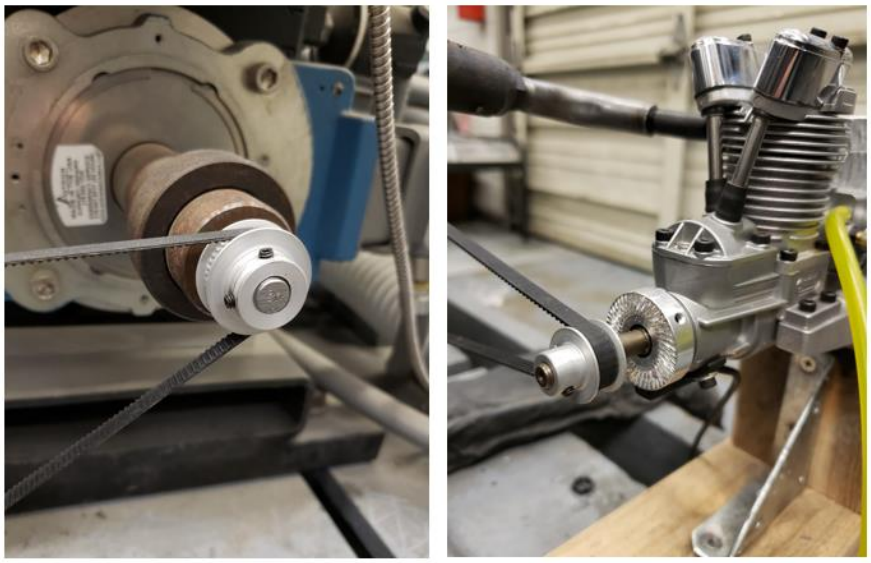

*Figure 4.1: Engine test setup dyno gear connection (left) and engine gear connection (right)*

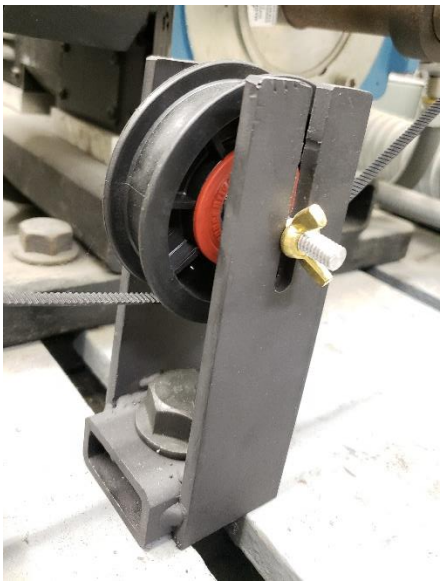

*Figure 4.2: Belt tensioner pulley to prevent belt slippage during operation*

The engine is fixed in place by using the aluminum mount that came with it along with two wooden 2” × 4”s screwed together in a T-shape with metal bracketing added for extra stability, as recommended in the manual [79]. Two ¾” holes were drilled in the bottom 2” × 4” to secure it to the T-slot skid with bolts. To keep the gears and tensioner pulley in line, the engine stand had to hang slightly hang off the skid (see Figure 4.3). The backside is secured with a C-clamp attached to the bottom of the skid. Furthermore, the wood was coated with Flamex PF-2 Exterior Fire-Retardant Spray, and the area where the engine attached to the wood was covered with thermal tape.

To monitor the exhaust temperature, pressure, and carbon dioxide ($CO_2$), the muffler was taken off the engine and replaced with a standard ½ size steel pipe with three holes drilled 2” apart and three 1/4 NPT female steel tee outlets (McMaster-Carr 4587K21) were welded on. This provided secure and leak-proof placements for the sensors. A ½-20 nut was also welded to one

end of the pipe. All welded surfaces were sandblasted beforehand to ensure the absence of contaminants, making the welds more secure. This pipe was attached to the engine using ½" OD steel tubing bent to 90 degrees with M10 × 1 female threads on one end and ½-20 male threads on the other. This allowed the tubing to screw onto the existing exhaust manifold and the sensor pipe to be threaded onto the other end. Moreover, all threads are sealed for testing with PTFE thread seal tape for gasoline lines and thermal tape. Additionally, the exhaust is wrapped with ceramic fiber blanket material and covered with thermal tape to minimize heat loss.

Since the intake of this engine has a conical shape, a high temperature rubber hose with a ½" inner diameter (ID) was used (McMaster-Carr 5301K11). The ID was sized slightly smaller than the intake to ensure an airtight fit. Subsequently, the hose was attached to another sensor pipe, this time with two holes drilled 2" apart and two 1/4 NPT female steel tee outlets were welded on these holes similar to the exhaust. A steel barbed hose fitting for a ½" hose (McMaster-Carr 5361K42) was welded to one end for the rubber hose to attach. Finally, a polyvinyl chloride (PVC) compression clamp for 0.84" OD pipes (McMaster-Carr 4562K131) was used to attach the air flow sensor to the other side of the sensor pipe. A mount for the servomotor (to control intake) was 3-D printed and secured to the side of the 2" × 4" T mount connected to the engine (Figure 4.4). Furthermore, a SEOH 250 mL graduated cylinder (5255-5LC, accuracy ± 2 mL) was used for pressure measurements of the fuel for calculating the mass flow rate (this process will be explained later). This was done by drilling a hole at the bottom of the cylinder and attaching a chemical resistant tubing with 1/16" ID (McMaster-Carr 6519T16) using pressure fitting with PTFE thread seal tape for gasoline in Figure 4.3 shows the full test setup of the engine coupled to the dyno.

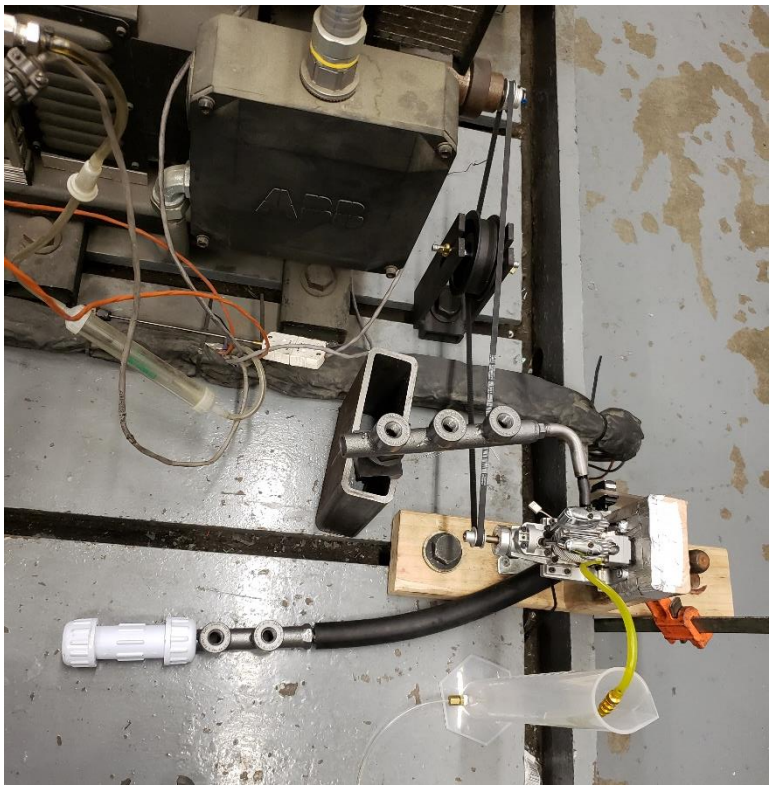

*Figure 4.3: Engine test setup iteration #1*

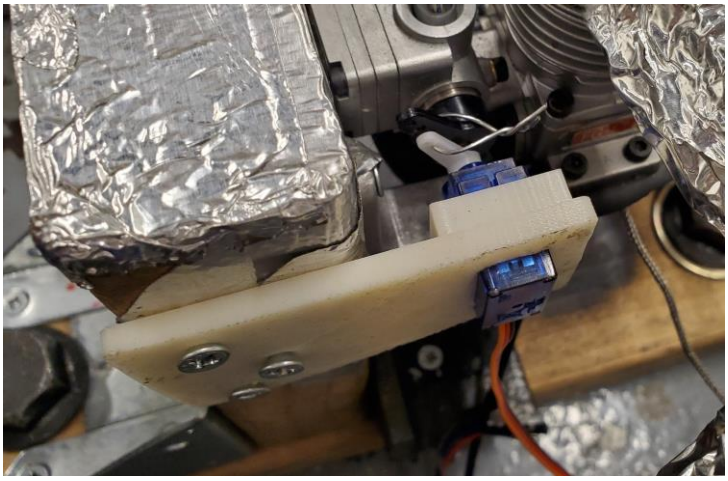

*Figure 4.4: 3-D printed mount for the servo motor (to control intake)*

Once the initial setup was in place, it was realized that although the engine was positioned to self-lock the threaded gear insert on the dyno, when the engine becomes the driver during testing (i.e., produces positive torque) the gear insert would unscrew itself. Additionally, it was discovered that the dyno is unable to rotate in the opposite direction, meaning the engine would have to be turned around. Lastly, it was revealed that the dyno does not have an internal torque reading, also necessitating the attachment of the engine to the Yanmar side of the dyno since a Futek torque transducer is mounted on that side. Therefore, the setup had to be changed to fix these issues.

### 4.1.2. ***Setup Iteration 2***

Setup iteration 2 is shown in in Figure 4.5, the following changes were made between the first and second iteration to achieve this:

- The engine was moved on the skid to the other side of the dyno. To accomplish this, the 2” × 4” mounting had to be shortened on the backside to prevent interference with existing systems. Additionally, the Lovejoy connectors had to be removed from the Yanmar and Futek sensor shafts to provide room for the keyed belt gear.
- The engine was rotated to face the opposite direction.
- The dyno belt gear was replaced by an XL series 2.125” OD gear (McMaster-Carr 1277N54) because the connection on the other side of the dyno was different and required a larger ID. Moreover, this gear was modified to have a keyed connection (Figure 4.6).

- The belt gear on the engine was also replaced by an XL series 1.625” OD (McMaster-Carr 1277N5) to maintain the proper ratio between the two gears.
- The belt tensioner pulley mount was modified by drilling and tapping two ¼ × 20 holes in the sides so that it could be attached to the existing 80/20, formerly used to create an enclosure around the coupling system between the Yanmar engine, Futek sensor, and the dyno.

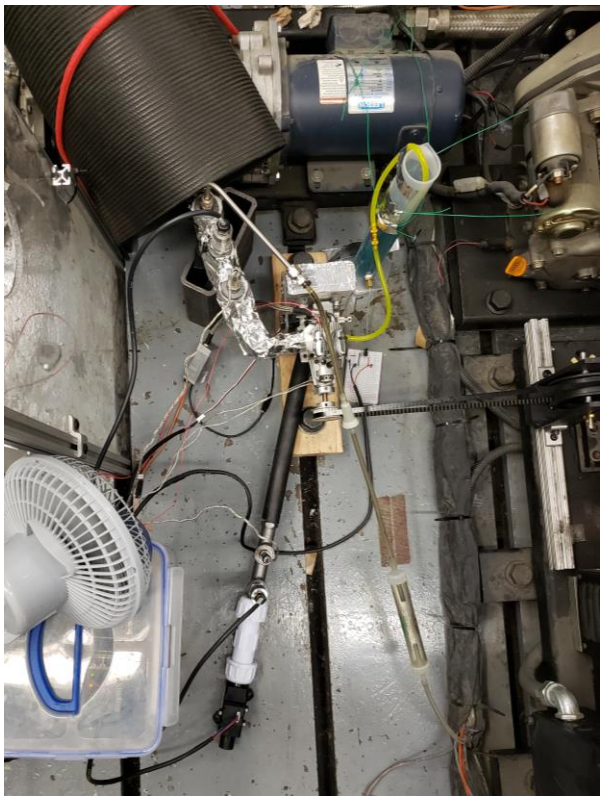

*Figure 4.5: Engine test setup iteration #2*

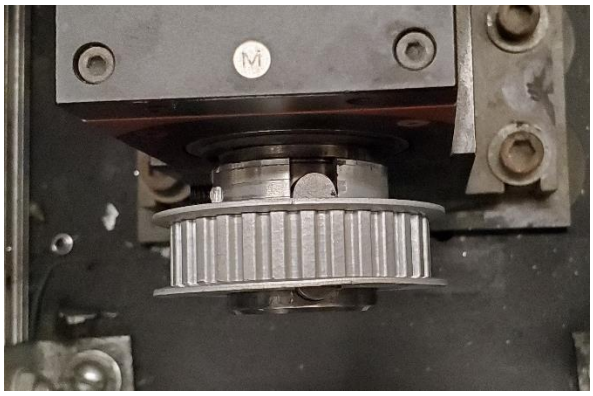

*Figure 4.6: Keyed belt gear with set screw attached to Futek sensor*

Upon initial testing, it was found that due to excessive vibration, the belt produced an unacceptable amount of gear slip that hindered combustion from happening; i.e., a constant engine speed could not be maintained. To mitigate this issue, it was believed that a hard-geared connection could provide the solution, this is discussed next.

### 4.1.3. ***Setup Iteration 3***

The following changes were made for the third iterative setup as shown in the left image of Figure 4.7:

- A 32 pitch steel gear with 20 teeth (McMaster-Carr 6832K52) was threaded and attached to the engine shaft using set screws.
- A hard-geared connection between the engine and the belt was manufactured (shown on the right of Figure 4.7). This assembly was formed by modifying the 1.625” OD belt gear so that it could be attached with the existing (shortened) set screws to a brass 32 pitch, 36 teeth brass gear (McMaster-Carr 7880K34) to mesh with the new gear on the engine.

Furthermore, the free sides of the belt gear and the brass gear were both bored to press fit 0.5” bearings (McMaster-Carr 60355K861). Then, the gear combo was mounted on a 3/16” shaft and set in place by tightening shaft collars on each side. Here, the positioning along the shaft was adjustable to ensure that it lined up with the engine gear. The steel structure was created by drilling a 1” hole in a steel plate and welding two 90° steel angles to it. The 1” hole was slightly extended to provide adjustment in the direction perpendicular to the shaft so that it could mesh with the engine gear. The 90° steel angles had holes drilled for the 3/16” shaft with a shaft collar welded on one end to secure it in place.

- Rubber gaskets were placed between the engine and the aluminum engine mount to damp out some vibrations.
- A rubber piece was used for the exhaust to rest on and to further reduce vibration.
- The engine was rotated once more to face the opposite direction since the introduction of another gear reversed the rotational direction of the shaft.

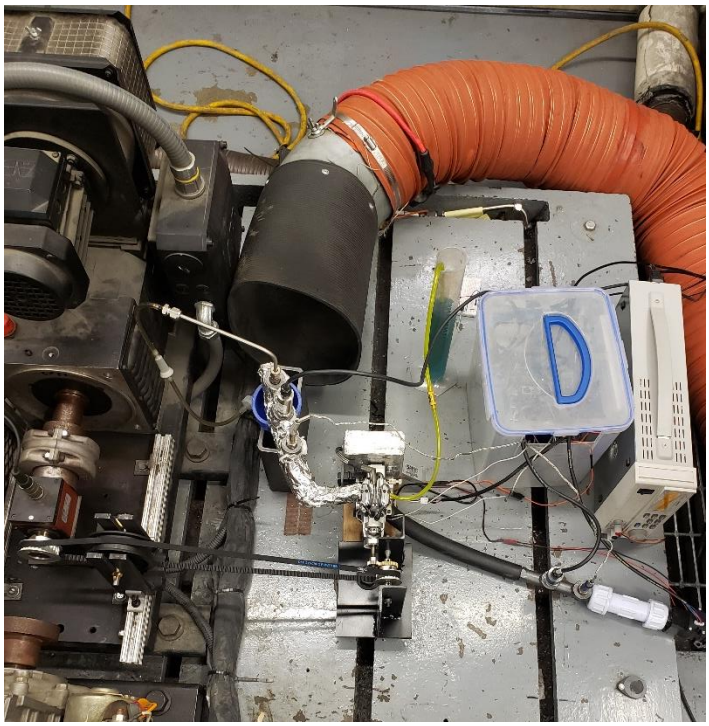

*Figure 4.7: Engine test setup iteration #3 (left) and hard geared connection assembly (right)*

Unfortunately, this setup additionally had problems with vibration and damage to the brass gear due to this vibration and gear slip can be seen in Figure 4.8. However, this setup did identify the source of the vibration problem as coming from twisting in the 2” × 4” T mount and rocking in the belt tensioner pulley, this is addressed in the next iteration of the setup.

*Figure 4.8: Damaged brass gear from vibration from engine test setup iteration #3*

### 4.1.4. ***Setup Iteration 4a***

To alleviate excess vibration the following changes were made:

- The hard-geared connection was abandoned, and the engine was setup similar to iteration 2 with the engine turned back around.
- Additional bracing was added to the 80/20 to reduce compliance making the belt tensioner pulley more stable (Figure 4.9).
- More bracketing was added to the 2” × 4” T mounting to add stiffness and prevent any twisting (Figure 4.10).

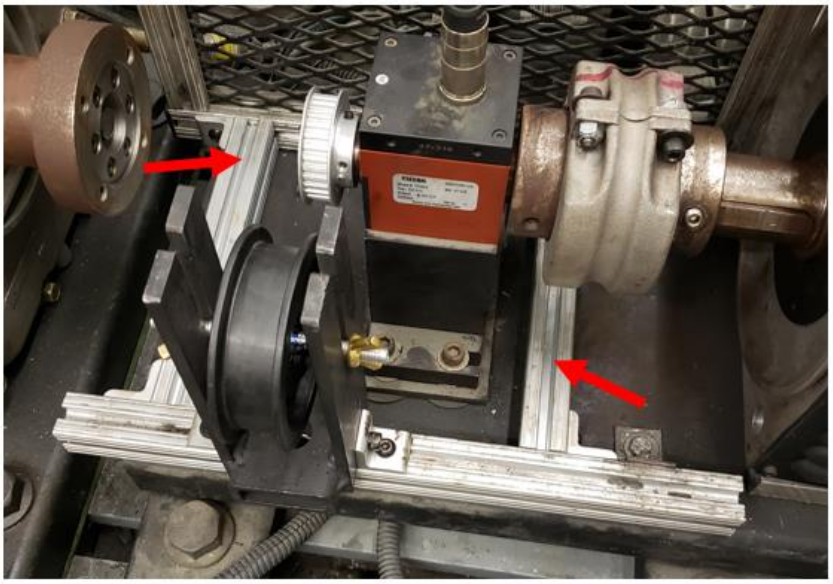

*Figure 4.9: Additional bracing added to the 80/20*

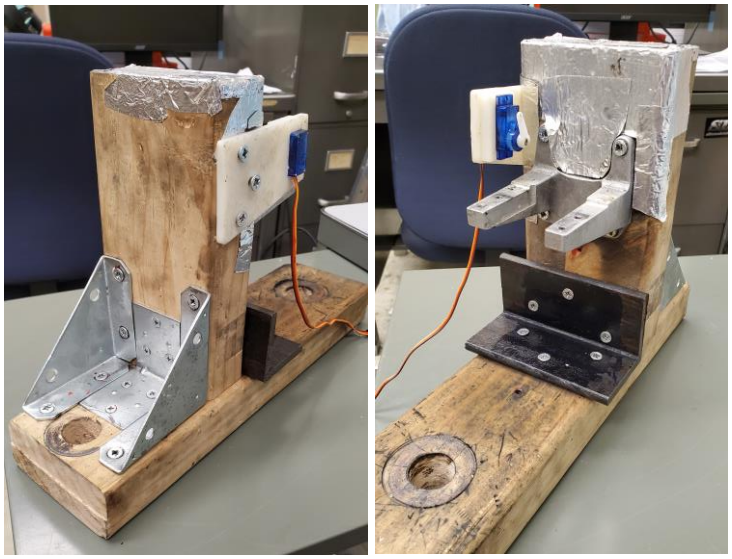

*Figure 4.10: Stronger bracketing added to the 2" ×4" T mounting*

Finally, these changes allowed combustion to be achieved when starting the dyno. However, the intake flow rate was sporadic and going past the sensors negative range (-10 slpm). These unsteady pulsations are caused because this is a single-cylinder engine (opposed to multiple cylinders); hence, it only pulls air during the intake stroke. Once the intake valve closes, it creates a negative pressure pulse making the air flow backwards. In addition, the belt gear on the engine would unscrew after speeding up the dyno every couple of times, even with the set screws tightened fully.

### 4.1.5. ***Setup Iteration 4b***

To alleviate the unscrewing of the belt gear and the unsteady air intake, the following changes were made:

- Blue Loctite was added to the threads on the engine shaft to further secure the belt gear. However, removal should still be relatively straightforward when the stock crankcase is replaced with the AM version.
- A resonator chamber was used between the flow sensor and the intake, similar to the one created for the Yanmar single-cylinder engine [80]. First, a thin walled half-gallon chamber (milk jug) was used by taping the opening to the compression clamp, cutting a hole in the side, and sealing the flow sensor to it (Figure 4.11, left). This showed an improvement in data, but the results were still not consistent enough for testing purposes. Hence, the chamber was sized up by using a thicker walled 5-gallon chamber (paint bucket) instead. Two holes were drilled in the bucket lid and plastic conduit was attached to each one using a rubber ring and a locknut. Then, the flow sensor and the sensor pipe were inserted into the conduit using a gasket (Figure 4.11, right). Again, the flow rate demonstrated improved behavior, and this time within a perceived acceptable range given the available space for the setup with Figure 4.12 displaying the comparative data for the intake flow between the three chamber setups. For this effort, the engine was tested with the dyno set to 1500 rpm (2045 engine rpm) and wide-open throttle. At this engine speed, the theoretical flow rate, assuming 80% volumetric efficiency should be roughly 8.916 slpm. Moreover, the average inlet flow over 30 seconds with the 5-gallon bucket, the ½-gallon jug, and no chamber are 8.689±1.181, 4.190±2.399 and 5.882±13.536 slpm, respectively, further proving that the larger resonance chamber is necessary for providing data that are more reliable.

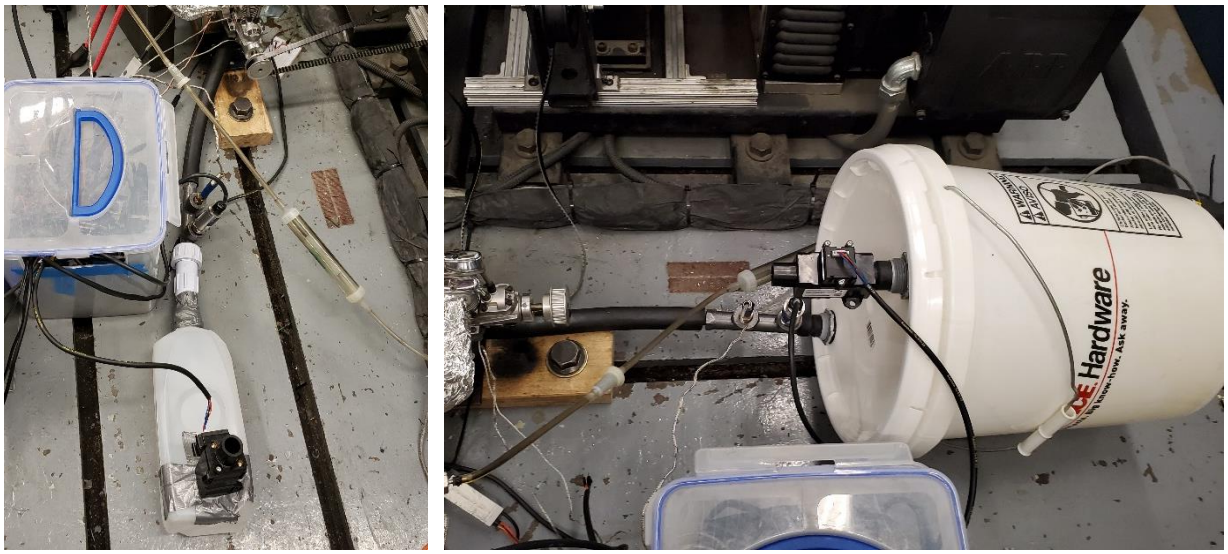


*Figure 4.11: Resonating chamber setups: ½ gallon (left) and 5 gallon (right)*

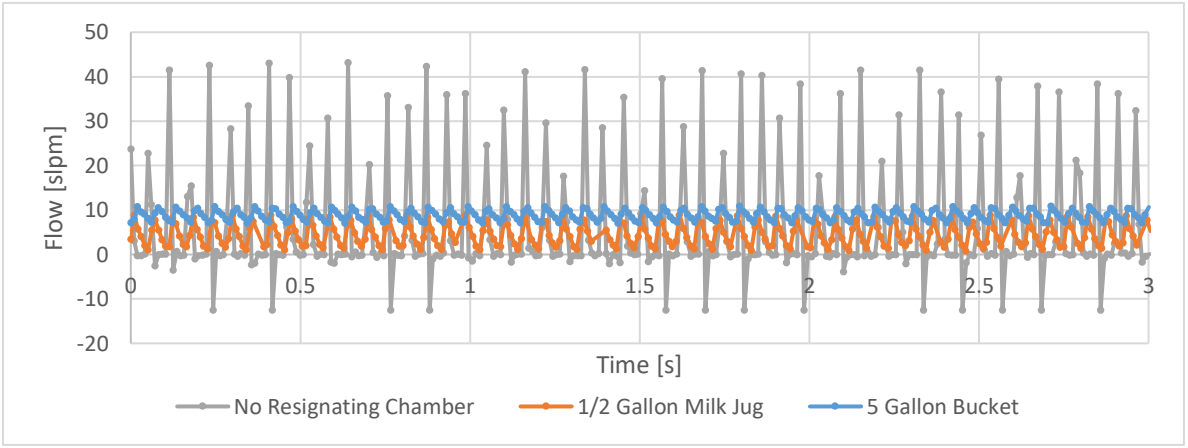


*Figure 4.12: Comparative testing of resonating chambers and inlet flow rate*

After extensive testing in the latest setup, it was determined that not only did the belt make the system unreliable concerning torque readings, it also snapped frequently enough that consistent data, especially at steady state, were difficult to obtain. It is believed that once the engine was running, the belt would heat slightly; hence, changing its properties and causing it to stretch that would reduce some of the torque placed on the transducer. Furthermore, when the

engine operated at speeds faster than 4000 rpm, steady combustion was hard to sustain, most likely due to the increased vibrations making the load from the belt on the engine intermittent.

### 4.1.6. ***Setup Iteration 5a***

Due to inconsistencies involving setup iteration 4 and its inability to reach speeds above 4000 rpm, it was decided that the gear ratio would be abandoned and a direct connection to the dyno would be implemented instead. Therefore, the setup had to be entirely redesigned as shown in Figure 4.13. The following changes were made to achieve this:

- A new engine stand was designed out of 80/20 to allow for adjustment in the *x*, *y*, and *z* planes along with rotational adjustment in the *z*-direction (Figure 4.14). To create this stand, several 80/20 pieces had to be cut to size, a small piece was used towards the top to add stability, and four corner pieces were used at the bottom to reduce any vibrations and twisting. Two aluminum square tube pieces were cut to size to further aid in stability while keeping the connections square by linking the corner pieces on the backside of the stand.
- Two aluminum pieces were machined to provide a surface to tighten the T-slot bolts. These pieces had a 1” hole drilled for the bolt and a 3” slot milled on the underside so they would sit squarely on the 80/20 when securing the stand.
- A wood piece was used as the mounting between the engine and the 80/20. Here, four holes were drilled all the way through, followed by larger ones on the backside so that wood T-nuts could be used (the wood is too thick for the bolts to reach otherwise). In addition, there were four holes drilled through so that ¼-20 bolts and slide-in T-nuts

could be used to secure the wood to the 80/20. Additionally, this wood was coated with the Flamex PF-2 Exterior Fire Retardant Spray, and coated with Rust-Oleum Engine Enamel once dry (rated to resist heat up to 500°F). Then, the wood had thermal tape placed on it before the engine mount was secured.

- Two skit T-slot nuts were modified so that they could be placed directly in the slots since it would have been impossible to slide them all the way through from the end due to dyno stand bolts and T-nuts blocking the way (Figure 4.16).
- The stand was secured to the skid with a sheet of rubber underneath to damp out vibrations that may occur.
- The servomotor to control air intake was mounted to an 80/20 cross bar coming off the stand by using zip ties, this is shown in Figure 4.14.
- An 80/20 cross bar was used to give the exhaust a secure place to rest and prevent any twisting or strain on the material.
- An adapter was machined to reduce the shaft size of the Futek sensor and allow the engine to connect readily to it; this is pictured in Figure 4.17. In order to keep a high precision concentricity, this part was created from one piece and split after the 0.5" shaft was lathed and four holes were drilled. Additionally, the shaft piece had a 1.1" diameter protrusion lathed in the backside so it could be press fit into the other once the hole was bored and the keyway added.
- A clamping precision flexible shaft coupling from McMaster-Carr (6208K595) was used to connect the engine to the dyno. This coupling allowed for 0.015", 5°, and 0.01" parallel, angular, and axial misalignment, respectively. It was also rated for 10,000 rpm and 13 N-m of torque.

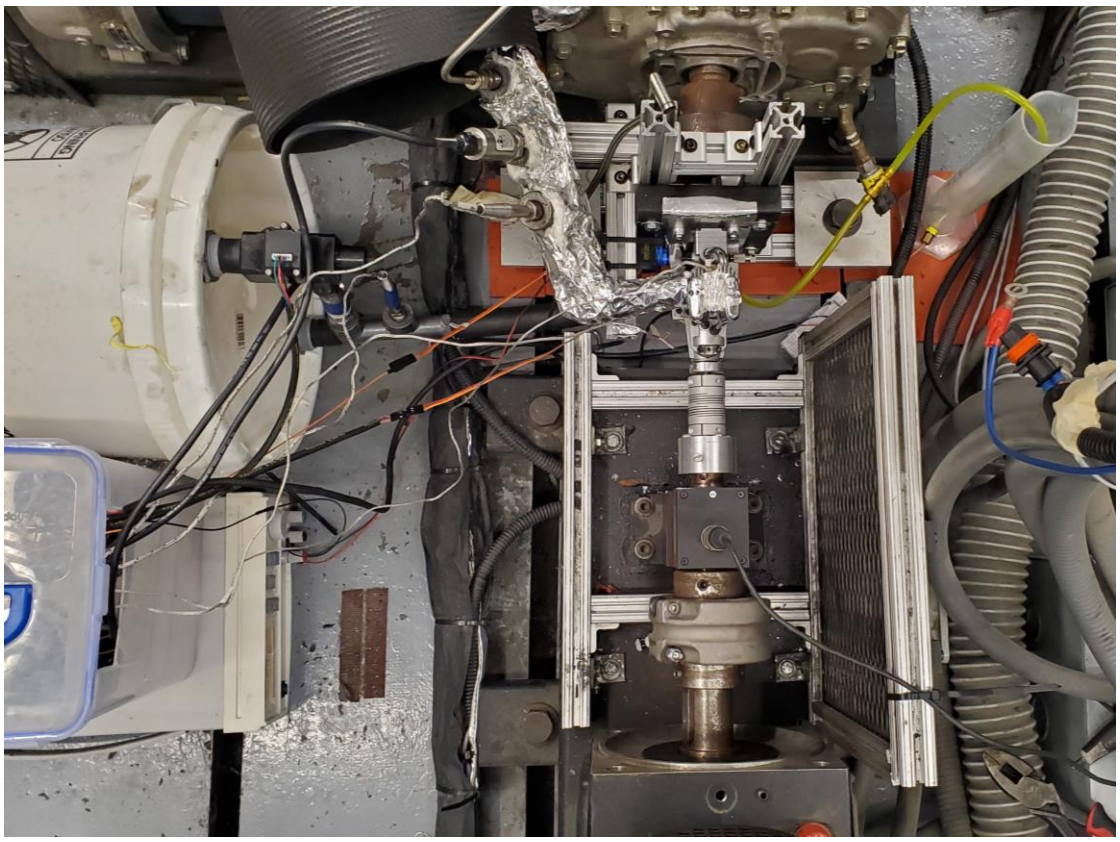

*Figure 4.13: Engine test setup iteration #5a*

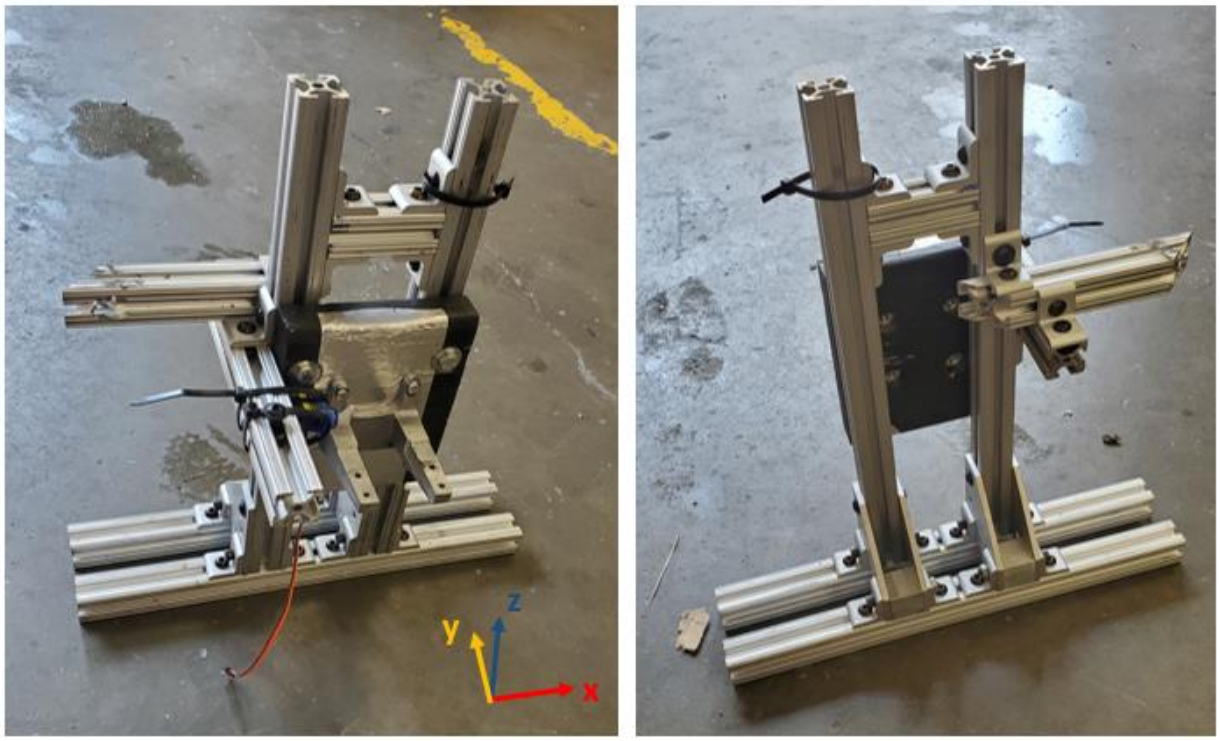


*Figure 4.14: Adjustable engine test stand made from 80/20*

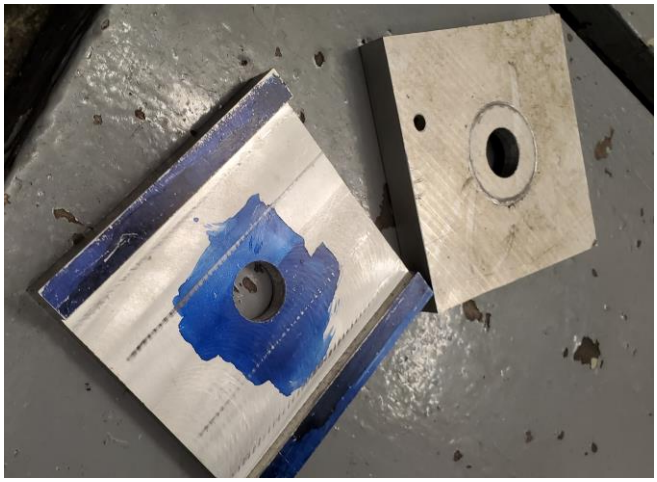

*Figure 4.15: Aluminum hold-downs*

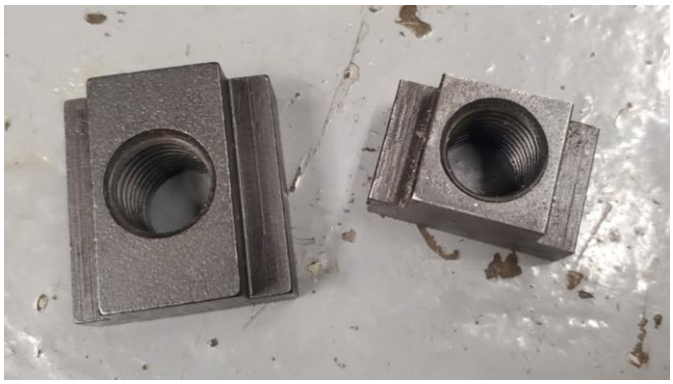

*Figure 4.16: Original T-slot nut (left) and modified one (right)*

*Figure 4.17: Futek sensor shaft reduction adaptor*

Unfortunately, this setup resulted in the coupling breaking in half once the engine was combusting (Figure 4.18). This was most likely due to small vibrations caused by combustion making the engine come out of alignment with the dyno shaft past the limitations of the coupling, causing it to snap.

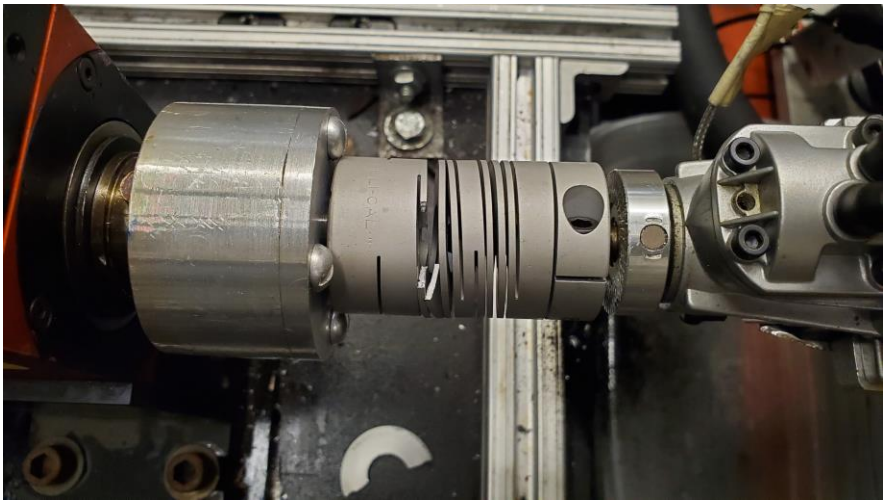

*Figure 4.18: Broken shaft coupling*

### 4.1.7. ***Setup Iteration 5b***

In efforts to alleviate the issues experienced in the previous setup, it was believed that reducing vibration and keeping the crankshaft in line with the dyno would help; therefore, the following changes were made:

- A more rigid coupling was used to keep the crankshaft in line with the dyno and the wood mounting was employed to damp the transverse movement of the engine. For this, two shaft-coupling hubs and a polyurethane spider were used (McMaster-Carr 2401K15, 2401K15, and 2401K87). This coupling was rated for 12,700 rpm, 15 N-m, and 160° F along with 0.004” and 1° of parallel and angular misalignment, respectively. The piece on the engine side had to be threaded because it was not long enough to clamp on the shaft unlike the previous coupling (the engine shaft would run into the dyno adapter 0.5” diameter shaft). It was secured by the unthreaded part of the crankshaft and forward

movement was hindered by the coupling on the other side. In addition, blue Loctite was used to give another mode of security.

- The rubber underneath the 80/20 stand was removed and small pieces were placed between the crankcase flanges and the engine mount. This was believed to create a smaller vibrational moment that would hopefully decrease the amount of movement at the crankshaft.
- The graduated cylinder used for fuel was placed on a piece of rubber to reduce the noise caused by vibration in fuel height pressure sensor readings.

These changes did result in stable combustion at low speeds, with torque readings that at first appeared sensible. However, the spider coupling was unable to withstand speeds higher than 3000 rpm for multiple test points. This is most likely due to the vibration and heat transferred from the crankshaft caused by combustion. Furthermore, while the engine was running, the torque decreased at a constant rate that seemed to be similar for each speed. One explanation of this could be that even though only the end of the crankshaft is touching the polyurethane spider, it may be conducting enough heat that it is going past the material's 160° F range. This would explain why the torque starts around 0.35 N-m for each test and gradually decreases as the engine gets hotter. Here, the crankcase surface thermocouple measured temperatures of up to 210° F towards the end of each two-minute test. Hence, it is entirely possible that enough heat was conducting through to the end of the crankshaft to affect the spider's properties, rendering it ineffective in transmitting torque. As shown in Figure 4.19, the failure and resulting damage of the spiders indicates that the dyno was driving the engine at the end meaning it was not combusting consistently enough to keep up.

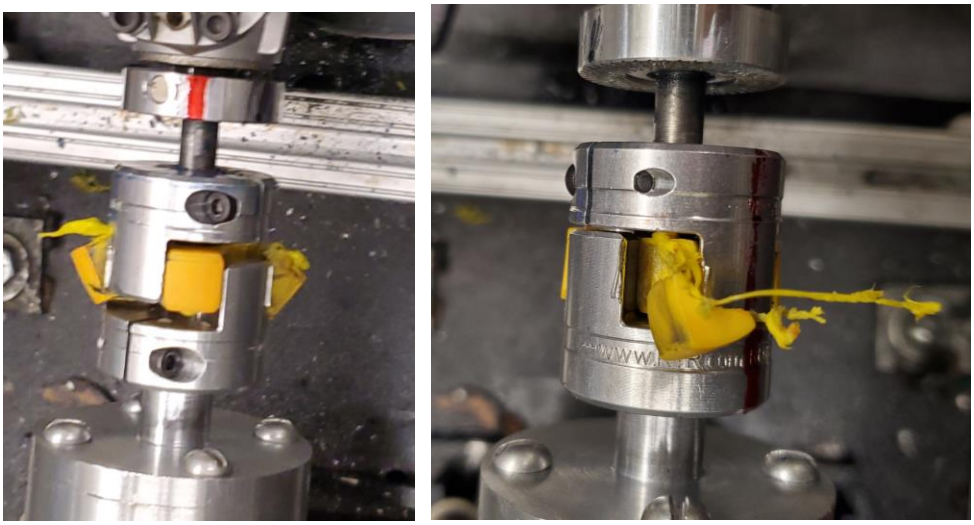

*Figure 4.19: Failure of the polyurethane spiders in the shaft couplings*

### 4.1.8. ***Setup Iteration 5c***

To resolve the previous issues, the following changes were made:

- The polyurethane spider was replaced with a hytrel rubber spider (McMaster-Carr 2401K88) that is a harder material with slightly tighter tolerances and a temperature rating of 245° F (105° F higher than the polyurethane spider).
- During testing, it was discovered that the orange rubber used for damping vibrations became more pliable with the heat from the engine. This could have increased the level of engine vibration causing it to become less secure. Therefore, the rubber was taken out from between the flanges and mount and placed again back under the stand.

These changes fixed all prior problems experienced, there was almost negligible vibration from the engine, and the spider remained completely undamaged at high speeds. However, the engine itself had a connecting rod failure at 4500 rpm (Figure 4.20). There are three major

reasons this could have happened: compounded abuse from testing with the engine not operated optimally, vibration damaging the internals of the engine from the shaft being held in place, or the temperature was too high. The temperature is the most likely culprit because when running the engine with a propeller, the cylinder head temperature never went much past ~180° C. However, for this round of tests it went up to ~380° C. Moreover, the yield strength for aluminum 390 at ~315° C is roughly 2/3 yield at ~260° C [81]. In addition, this engine is meant to be air-cooled during flight; hence, the cylinder head has numerous fins. However, in the test cell there was not sufficient ventilation to cool it down. Finally, these elevated temperatures could have rendered the lubrication from the oil inside of the cylinder ineffective due to a reduced viscosity.

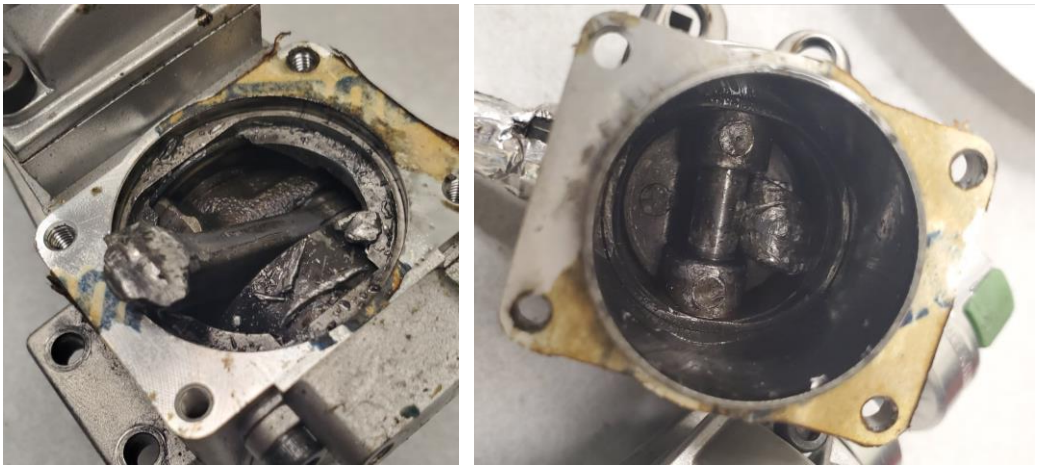

*Figure 4.20: Engine failure: broken connecting rod in crankcase (left), and detached piston head (right)*

### 4.1.9. ***Setup Iteration 5d***

Because inadequate cooling was the most likely culprit for the failure of the engine, the following change was made after obtaining another Saito FG-11 engine:

- A Dayton fume exhauster (model 1Z968) along with a 6” diameter metal hose was used to continuously blow air across the engine to keep it cool during operation.

After testing in this setup, it was discovered that there was significantly more vibration on the skid pad because the engine no longer had the propeller to damp out vibrations. Additionally, having the crankshaft held in place caused its vibrations to move into the stand that then transferred to the pad. Moreover, vibrations from the dyno were not encountered during propeller testing. This extra amount of vibration caused too much noise in the fuel level height sensor, making its readings unreliable. It was also decided that torque measurements needed a better normalization procedure. Therefore, a system to turn the spark on and off during operation was instituted so that pumping and frictional work could be more accurately measured.

#### 4.1.10. ***Setup Iteration 5e***

The finalized dyno setup is depicted in Figure 4.21 and the labels are described in Table 4.2. To solve vibrational problems from the previous setup and implement a system for normalizing torque readings, the following changes were made:

- The fuel cylinder and liquid level height sensor were taken off the pad and placed on top of stacked press wood, rubber matting, and anti-vibrational padding on the floor next to the pad. The cylinder was kept at the same height relative to the engine to prevent flooding or fuel starvation.
- The fuel line and sensor cables were extended to reach the new distance away from the engine and DAQ box. The fuel line had to be held up by threading it through a hole and

zip tying it to a vertical board to prevent the slack from causing the cylinder to topple over; this can be seen in Figure 4.21.

- The DAQ box had anti-vibrational padding placed under it and the wires were taped to the inside of the box to prevent them from moving around.
- The exhaust had insulation padding placed between itself and the stand to reduce any vibrations. In addition, it was further insulated so that thermal tape protected the thermocouple from the crossflow produced by the blower; hence, providing more consistent readings.
- A Fosmon C-10683 Wireless Remote Control Outdoor Electrical Outlet Switch was placed between the power supply and the wall power cord. This allowed the spark to be safely turned on and off with a remote from outside of the test cell during operation.
- The power supply was replaced with a SoulBay Universal AC/DC Adapter Multi-Voltage Regulated Switching Power Supply. This can supply 3-12 VDC and up to 2 Amps, which is within the requirements of the engine's ignition system. It also included an adaptor to use a light emitting diode (LED) terminal connector, which made connecting it to the ignition system with two jumper wires respectively straightforward. This power supply was needed so that the power could be turned on and off without the requirement of an additional button press that the prior power supply required.

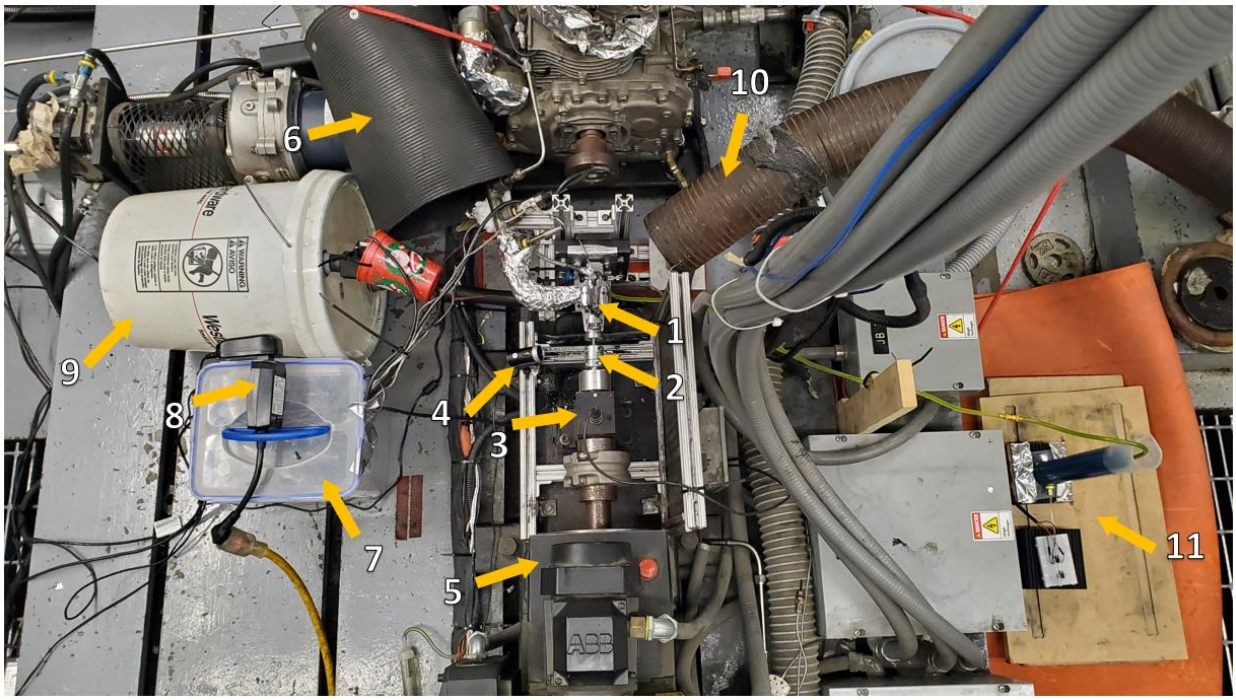


*Figure 4.21: Finalized dyno engine setup*

*Table 4.2: Finalized dyno engine setup label information*

| Label Number | Description |
|---|---|
| 1 | Engine |
| 2 | Coupling |
| 3 | Futek sensor |
| 4 | Monitoring camera |
| 5 | Dyno |
| 6 | Exhaust vent |
| 7 | DAQ box |
| 8 | Spark power switch |
| 9 | Resonating chamber |
| 10 | Cooling blower |
| 11 | Isolated fuel and monitoring |

In this setup, there were two additional connecting rod failures. However, unlike the prior failure, these happened at the crankshaft instead of at the piston. This indicated that temperature

may not be the issue for this setup like it presumably was before the blower was introduced. Instead, it appears that the loading placed on the engine by the respectively larger dyno was at fault. However, all data points needed were collected after replacing the crankshafts prior to testing. In other words, each set of data collected (stock engine, stock cylinder head and AM crankcase, and AM cylinder head with AM crankcase) employed the same connecting rod although it might be a different one than the prior test. Unfortunately, this was unavoidable. This shows that the setup was somewhat successful, but for less detrimental data collection, the engine should be connected to a smaller dyno or one that is more forgiving to shaft vibration.

#### 4.1.11. ***Setup Iteration 6 (Propeller)***

Between setup iteration 5c and 5d, the engine was taken off the dyno and tested with a propeller (Figure 4.22). It should be noted the tape on the propellers in Figure 4.22 was only applied during engine break-in to take optical tachometer measurements for approximate speed. This was accomplished to ensure useable data were collected without risk of failure. Hence:

- The engine stand was moved to the end of the skid to minimize ground effects experienced by the propeller.
- An APC C-2 12 × 6 propeller was installed on the engine along with a spinner cone.
- A plexiglass barrier was included to protect the dyno and existing wires in the test cell.
- The LabVIEW programs were modified to measure engine speed (explained later).
- The DAQ box and intake flow resonating chamber were positioned behind engine stand, and the graduated fuel cylinder placed behind the plexiglass barrier to protect it from the wind generated by the propeller.

- A shield was placed on the intake flow sensor to reduce interference by the propeller wind.

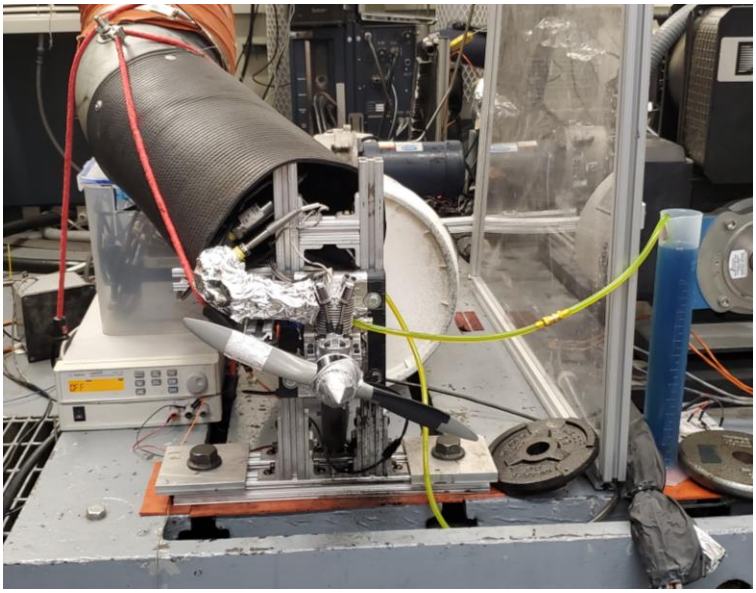

*Figure 4.22: Propeller test setup*

## 4.2 **Data Acquisition - Sensors and Hardware**

To take measurements of parameters during engine operation, multiple data acquisition devices and sensors were used. A wiring diagram of the entire system is provided in Figure 4.23 and every sensor used is discussed along with how it is powered and connected to the acquisition hardware.

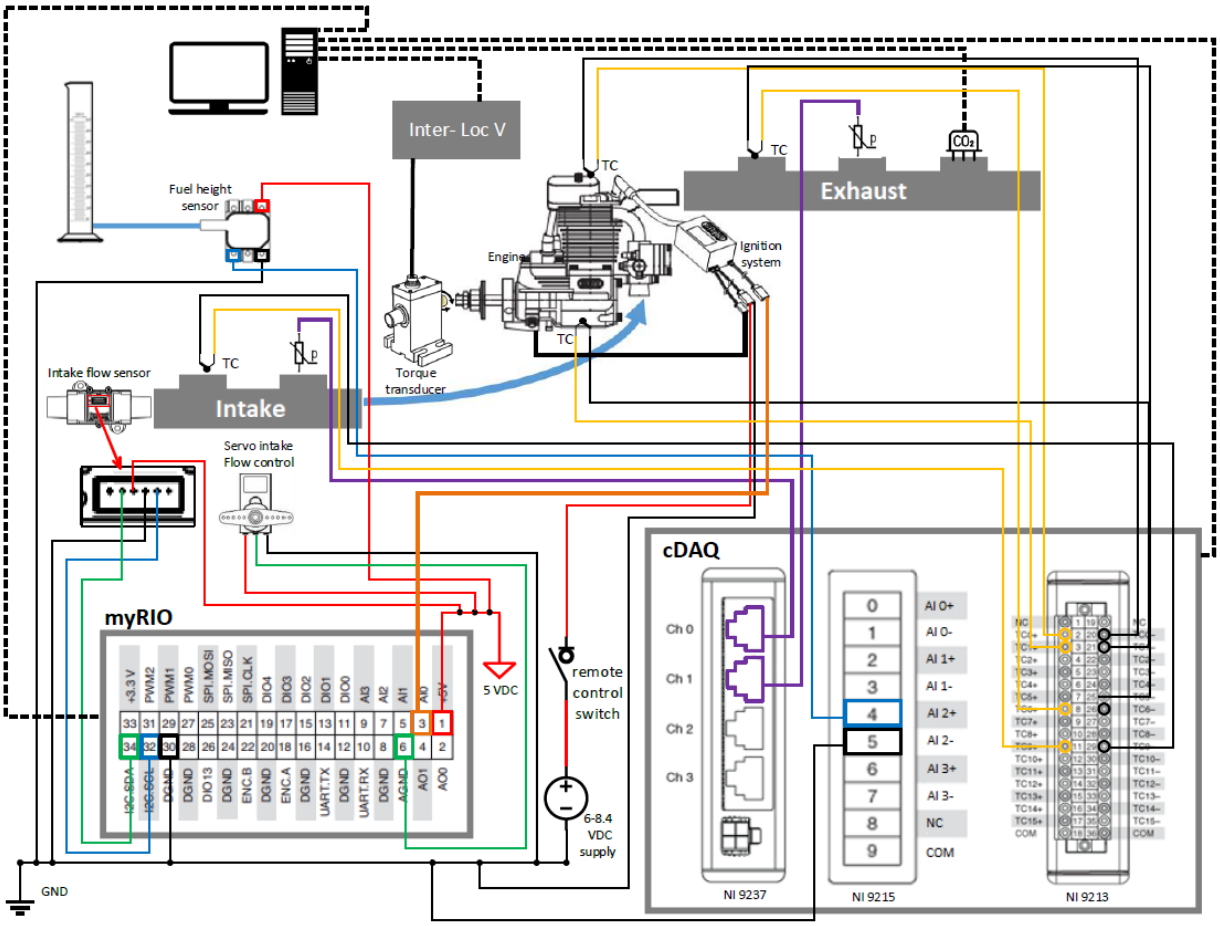


*Figure 4.23: Sensor and data acquisition hardware wiring diagram*

One of the main data acquisition devices used is a 4-slot National Instruments (NI) CompactDAQ (cDAQ-9174) with three modules connected. The first module (NI 9237: AL Bridge) had two stainless steel Omega pressure transducers (PX309-030AV, accuracy ± 0.25% psi) connected to measure the inlet and exhaust pressure. The second module (NI 9213: TC) was used for measuring inlet and outlet temperatures, taken with rugged pipe plug type J thermocouple probes from Omega (TC-J-NPT-G72, accuracy ± 0.75% K) and surface temperatures of the cylinder head and crankcase, taken with type K thermocouple wire from Omega (SAI-K-SRTC, accuracy ± 0.75% K). The placement of these sensors is depicted in

Figure 4.24. Lastly, a third module (NI 9215: Al ± 10 V DIFF SSJ) for voltage inputs was used to measure fuel consumption. The mass flow rate of fuel was found by using a basic board mount pressure sensor from Honeywell (ABPDJJT001PGAA5, accuracy ± 0.25 VDC) to get the liquid level height of the container. To obtain reliable data from this sensor, the top prong must be connected to the liquid container, and the bottom prong left open to the environment. This sensor was calibrated by adding 10 mL of fuel at a time using a Fisherbrand 10 mL graduated cylinder (No: 08-559, accuracy ± 0.1 mL) and taking the average reading of the resulting voltage (VDC) at each step over 10 s with the fuel line in place; i.e., Figure 4.3, Figure 4.5, and Figure 4.7. The calibration curve shown in Figure 4.25 was used later during data analysis to determine how much fuel was consumed based on its changing height.

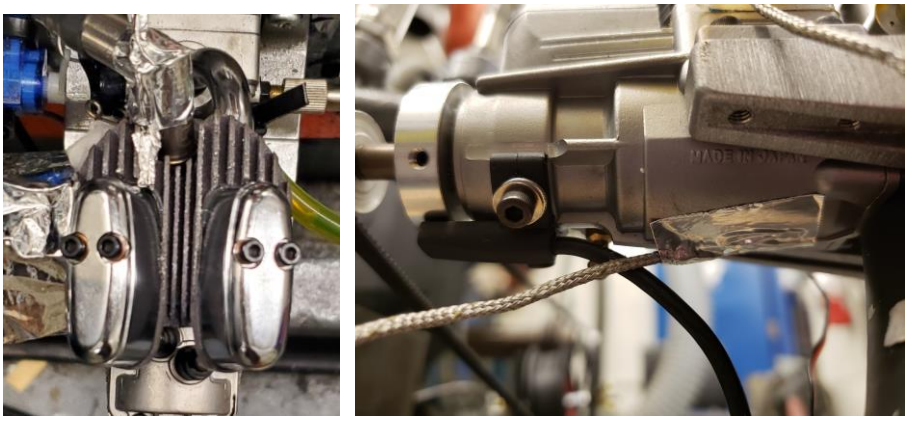

*Figure 4.24: Surface thermocouple placements (left) on cylinder head and (right) on crankcase*

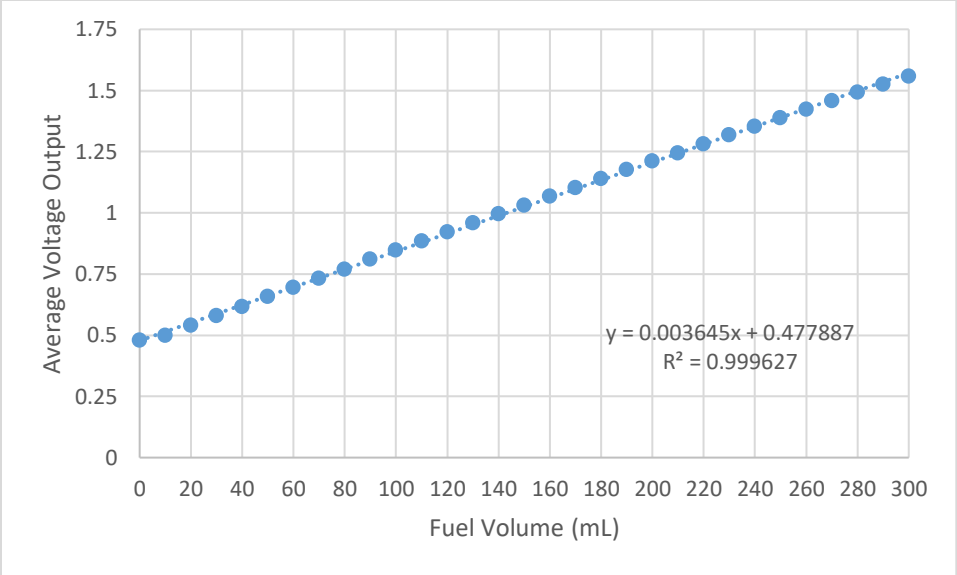


*Figure 4.25: Calibration curve for liquid level height sensor using 20:1 mixture of gasoline and 2-stroke engine oil*

Furthermore, since a digital inter-integrated circuit ($I^2C$) flow sensor from Honeywell (HAFUHH0100L4AXT, accuracy ± 3.5% SLPM) was used to measure the intake flow rate, the setup required the inclusion of a NI myRIO device. This sensor is connected to the serial clock (SCL) and serial data (SDA) inputs on the device and requires a supply voltage of 3-10 VDC. In addition, the myRIO was used for servo motor control (Miuzei SG90), which regulated the air intake opening of the engine. Spark timing and engine speed were also measured with the myRIO by taking voltage readings of the Hall sensor that came with the engine by connecting the orange wire from the electronic ignition system to an analogue input on the myRIO. This signal was measured using the myRIO since it is able to collect data faster than the cDAQ. This sensor reads 5 VDC every time the magnet connected to the crankshaft passes and 0 VDC at all other times. Here, the sampling frequency needs to be roughly 6300 Hz to catch all magnet passes when the engine is at top speed (this calculation is in the Appendix E). Unfortunately, due

to system limitations, the maximum sampling frequency reached was roughly 4000 Hz; hence, not all magnet passes were caught. Therefore, to make up for the missed passes, post-processing of these data were required to obtain engine speed as explained further in the next chapter.

Finally, existing systems present in the test cell were employed for additional engine measurements. For example, the Futek (model #TRS-605, accuracy ± 0.5%) torque transducer already coupled to the dyno and connected to the Dyne Systems Inter-Loc V Multi-loop Dyno Controller was used for torque measurements. Additionally, exhaust $CO_2$ was measured by using one K-33 ICB 30% sensor (capable of monitoring concentration at a rate of 0.5 Hz, accuracy ± 0.5% vol $CO_2$ ± 3% of measured value) and a program called Data Acquisition System (DAS). Further discussion of this sensor's operation can be found in Ragone's thesis [82].

## 4.3 **Data Acquisition - LabVIEW Programing**

### 4.3.1. ***Dyno Testing***

To read and record data while controlling the servomotor, two programs were developed using the LabVIEW 2018 myRIO Toolkit and run simultaneously during testing. The first program will be referred to as the cDAQ and Inter-Loc V (cDLVI) virtual instrument (VI). Its graphical user interface (GUI) along with its block diagram are shown in Figure 4.26 and Figure 4.27, respectively. The second program's GUI and block diagram, shown in Figure 4.28 and Figure 4.29, correspondingly, will be referred to as the myRIO VI. Both programs were constructed in a LabVIEW myRIO project tree and they must be run from within this device to work correctly. There were six main tasks carried out between these two VIs: (1) controlling the

servomotor; (2) reading data from the flow sensor, (3) cDAQ, and (4) Dyne Systems Inter-Loc V; (5) streaming data from the myRIO to the computer; and (6) recording data when prompted.

1. *Controlling the servomotor* - this was accomplished within the myRIO VI (bottom while loop) and was created by referencing code provided by NI [83], with modifications made so that the Pulse Width Modulation (PWM) Express VI could be used instead for further simplification. Additionally, a close intake button was wired for quick shut down of the engine in case of failure, along with indicators for equivalent throttle percentages. In addition, the null offset button was eliminated to further streamline the program.
2. *Reading data from the flow sensor* - this was done in the top of myRIO VI loop. The $I^2C$ Express VI was used, inside which the channel ("either"), mode ("read $I^2C$"), and speed were selected ("default 100 kbps"). The slave address of the sensor ("0x49") and its byte count ("2") were wired into the Express VI on the left side. When running, the bytes read were indexed and the component bytes joined to create an output code. The following transfer function equation was applied to this output [84]:

$$Flow = \text{Full Scale Flow} * [(\text{Output Code}/16384) - 0.1]/0.8 \quad (4)$$

Once transformed, these data should create recognizable values for flow. Finally, a 200 ms wait function was added inside the loop to set the sampling frequency to 5 Hz [84]. Lastly, a waveform graph was added so that the data can be displayed in real-time during testing. Here, these graphs were reset each time the VI was run via a conditional loop inside the top while loop.

3. *Reading data from the cDAQ* - within the middle of loop in the cDLVI, data were read using the DAQ Assistant Express VI to assign sensors to their respective modules and wiring terminals. Inside of this VI, the Acquisition Mode was set to "Continuous Samples" with Samples to Read set to "300", and Rate (Hz) set to "1" to get an approximate sampling frequency of 5 samples per second. Then, these dynamic data were split and converted into floating-point numeric values. Moreover, waveform graphs were used so the information can be viewed in real time during testing. Similar to the myRIO data, the graph was reset each time the VI was run (top conditional loop inside the top while loop in the cDLVI). The temperature plot on the GUI was set so that the *x*-axis would display one minute of data, which made determining steady state easier during the testing process.
4. *Reading data from the Dyne Systems Inter-Loc V* - this was done in the cDLVI (bottom of the loop). The LabVIEW project and VIs provided by Dyne Systems were used as a reference when setting up this serial communication. Deviations from what they provided include having the serial port entered by the user in the GUI and transforming these data from strings to floating point numerical values that could be later saved. To get the cDLVI to connect to the dyno controller after it has just been turned on the Main VI in "LV Semo-ASCII-Serial" project provided by Dyne systems must be ran first to initialize the connection between the computer and the controller.
5. *Streaming data from the myRIO to the computer* - The myRIO effectively acts as its own computer; hence, when data are taken from a connected sensor with this device, they are stored on the myRIO instead of the computer running LabVIEW. To grab these data and put it on the computer instead, a network stream can be used. The process for setting this

up is described in one of NI's white papers [85]. The writer endpoint titled "writer" is placed in the myRIO VI (outside of while loop on left) and the flow data along with the time elapsed are written into the stream via an array inside of the top while loop. To start the stream, the myRIO VI must be run first before the cDLVI. The second half of the stream is inside of the cDLVI (top of while loop under conditional loop). The reader endpoint establishes a connection with the writer endpoint in the myRIO VI by inputting the host uniform resource locator (URL). In this case, the URL is the IP address of the myRIO and the name of the writer endpoint (i.e., //172.22.11.2/writer). It then reads these data from the myRIO and places into the specified location [86].

6. *Record data when prompted* - since the tests could potentially be up to a half hour long, recording data the entire time would make data analysis difficult and it would be an inefficient use of the computers' resources. Moreover, only running the VIs when collecting data is also not ideal because operational conditions, like temperature, would not be able to be monitored actively. Therefore, data were only written to a tab-delimited spreadsheet when a time in seconds for "dataset length" was entered and the "record data" button was pressed. As soon as the button was pressed, the clock was reset to 0 s and the data were recorded until the elapsed time becomes greater than the user inputted "dataset length" (green Boolean in Figure 4.26 shows the user when data recording is live). These data arrays from the cDAQ with the Inter-Loc V and the myRIO were recorded into separate spreadsheets.

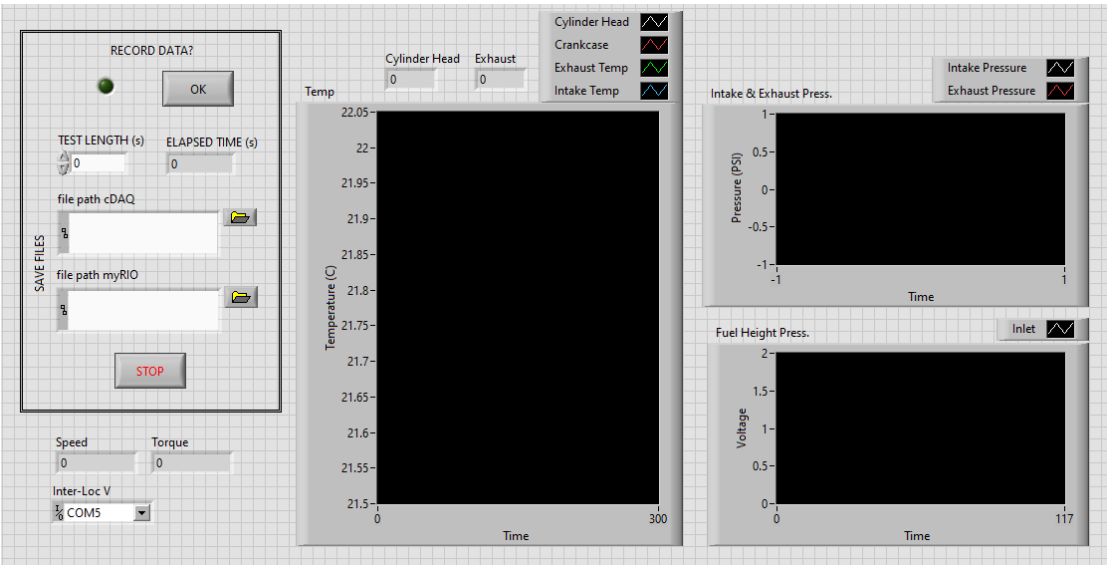


*Figure 4.26: cDAQ and Inter-Loc V with myRIO stream GUI*

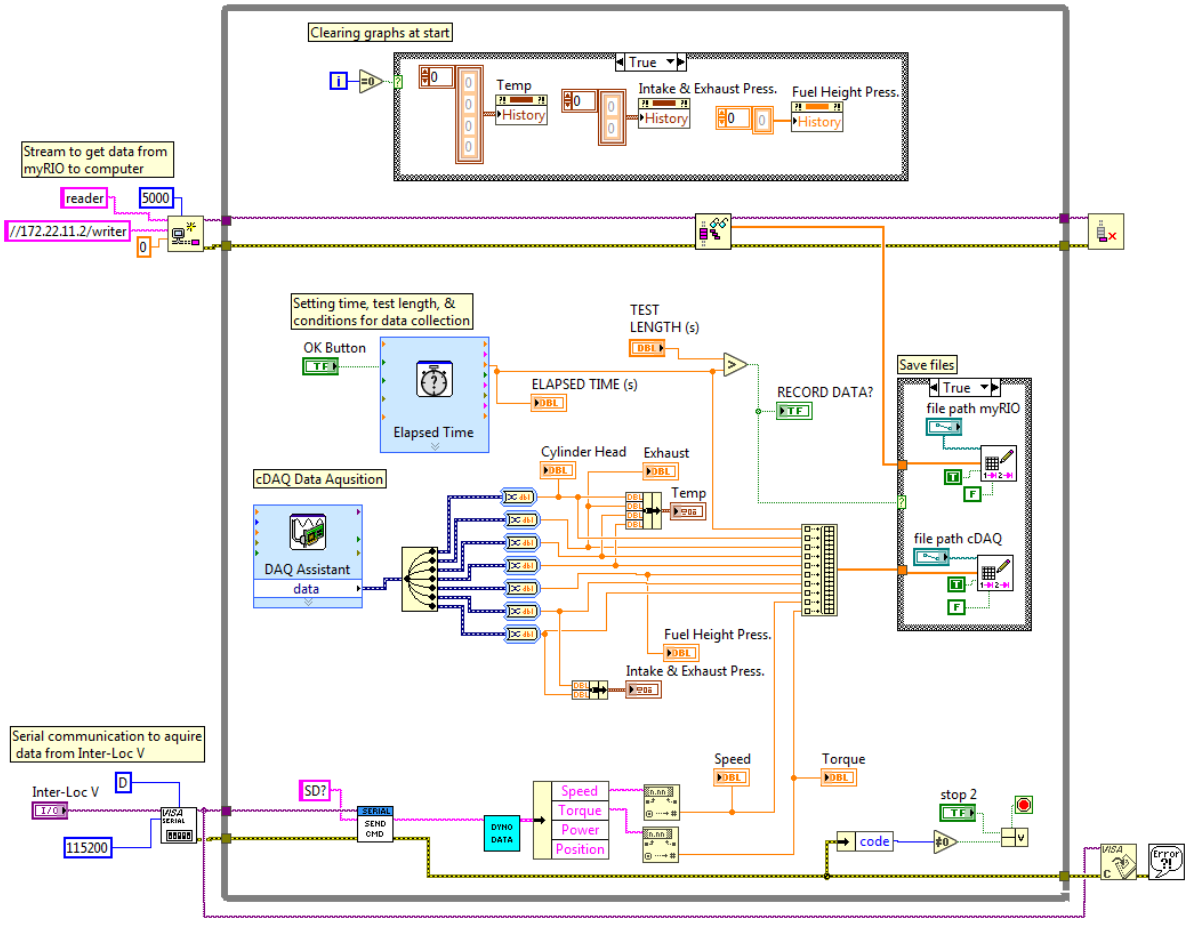


*Figure 4.27: cDAQ and Inter-Loc V with myRIO stream block diagram*

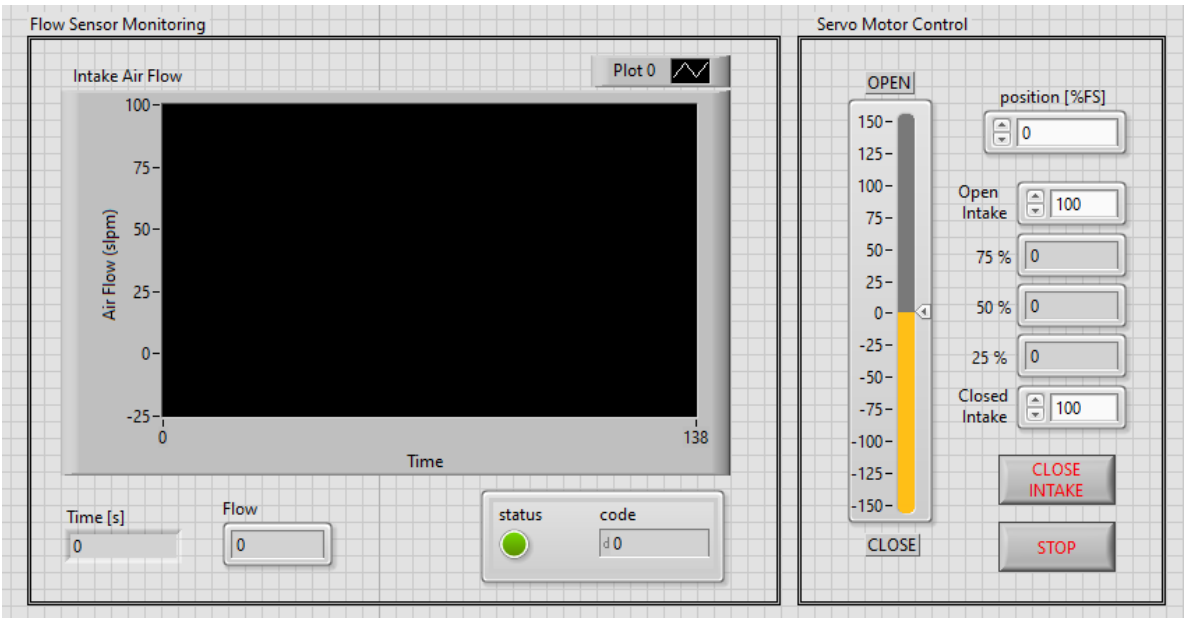


*Figure 4.28: Flow sensor and servo motor with myRIO stream GUI*

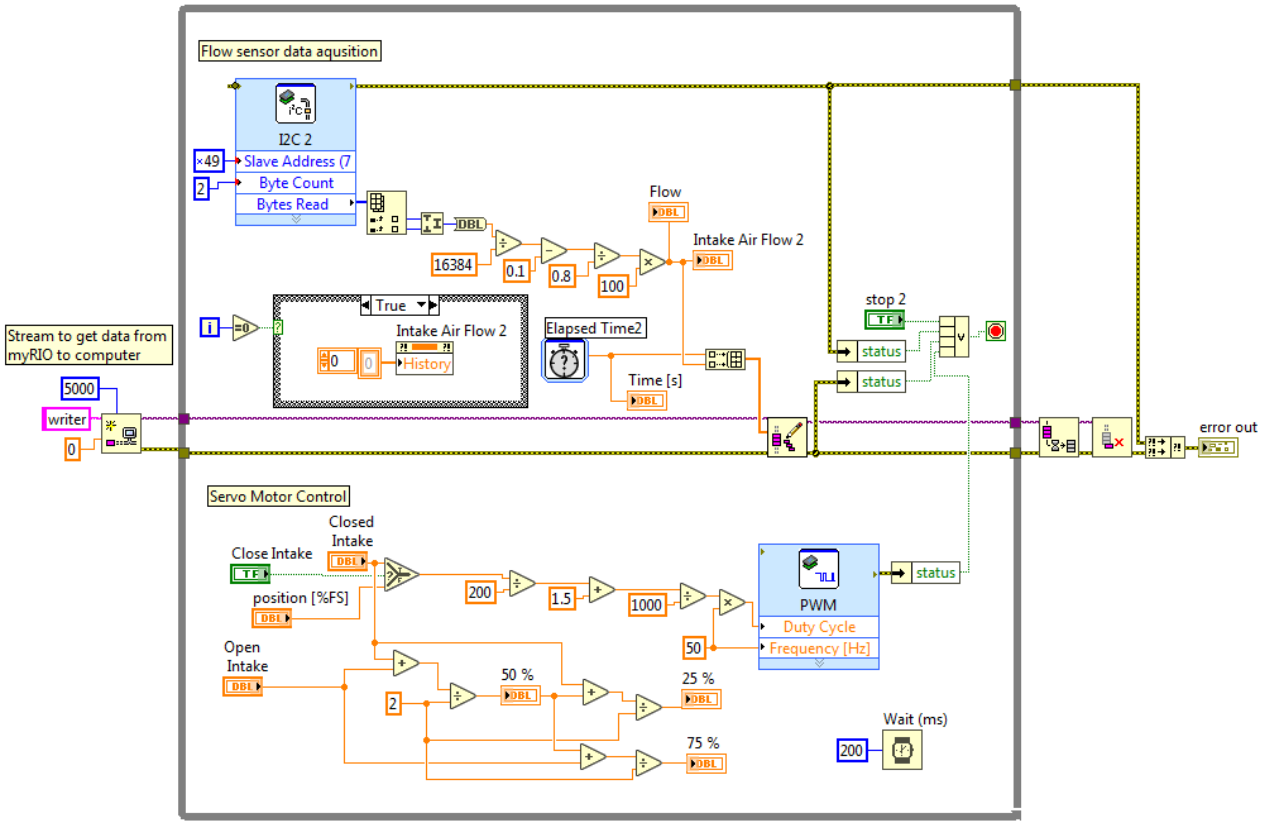


*Figure 4.29: Flow sensor and servo motor with myRIO stream block diagram*

### 4.3.2. *Propeller Testing Modifications*

While propeller testing, there was no longer a direct read output for speed like what the Inter-Loc V provides from the dyno. Because of this, the built-in magnet on the drive flange along with the provided Hall effect sensor were used to measure the magnet passes as the engine rotated. As discussed previously, this sensor required a high sampling frequency to catch as many passes as possible. To accomplish this, the previous LabVIEW programs had to be optimized to take full advantage of the computer's resources. Therefore, the following changes were made to the programs to increase the prior sampling frequency from 1000 samples per second to approximately 4000 samples per second:

- The Inter-Loc V data acquisition at the bottom of the cDLVI was deleted since this system would not be used for the propeller tests.
- The myRIO VI was modified so that the myRIO would only take data from the magnet pass for 20-second intervals after the "Magnet Data" button on the GUI was clicked (true case), during which time it would not collect data from the flow sensor or have control of the servo motor. This was achieved using a case structure as shown in Figure 4.30 and Figure 4.31.
- Error statuses were no longer checked to control whether the loop should continue running or not.

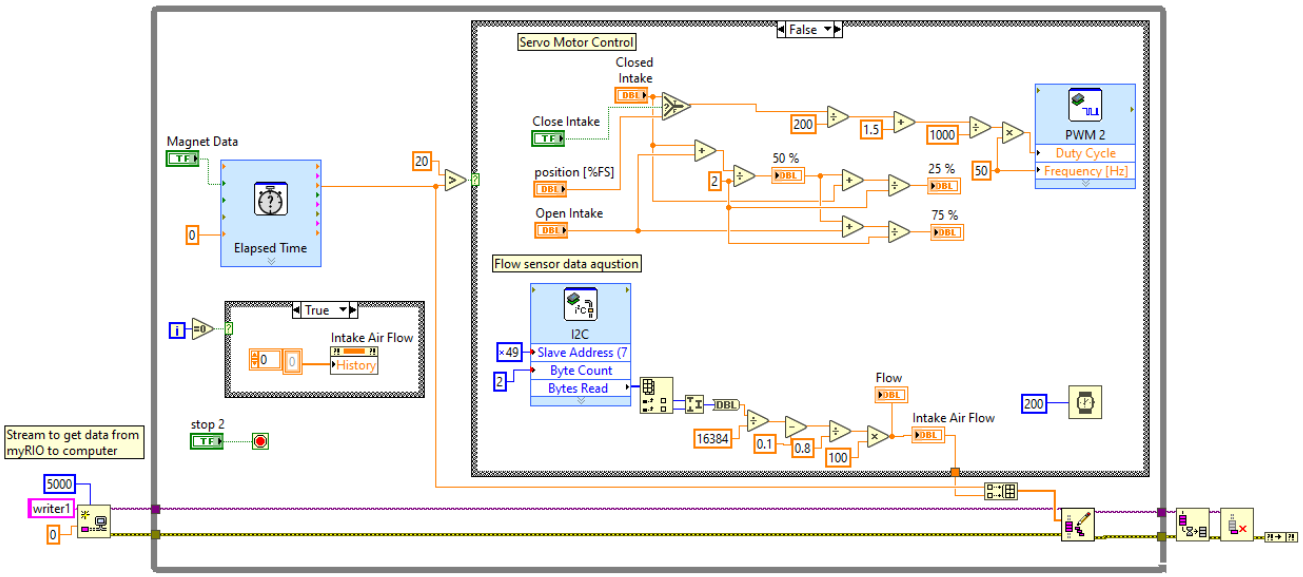


*Figure 4.30: Optimized myRIO VI block diagram with false case structure collecting and displaying data from the flow sensor while also controlling servomotor*

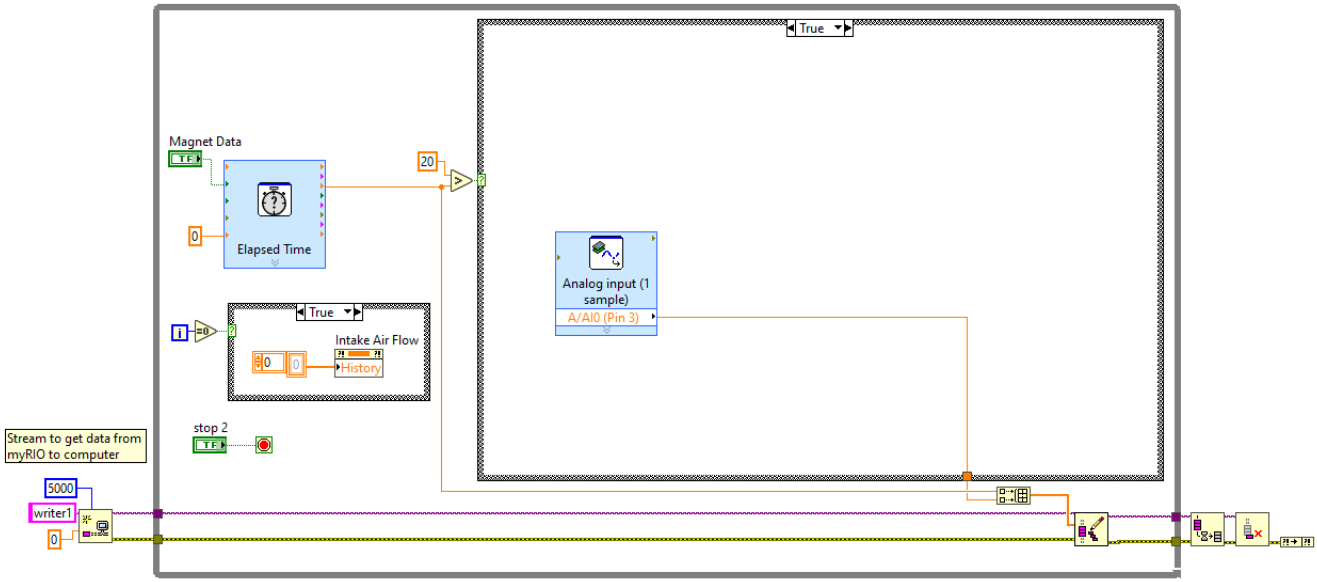


*Figure 4.31: Optimized myRIO VI block diagram with true case structure only collecting data from the Hall effect sensor*

## 4.4 **Conclusions**

While working through the iterations of this experimental setup, significant knowledge was gleaned regarding the operation of the Saito FG-11 engine. Its excessive vibration made using a belt and pulley system unreliable and ineffective. In fact, there were several times during setup testing where the belt snapped. This occurred the most often when the engine was still combusting as the dyno was slowed; hence, making the shutdown process difficult. In addition, the belt rendered using the dyno pointless as it prevented any torque from transferring to the Futek sensor. Furthermore, this process showed that using a test stand made entirely of wood would permit too much movement and vibration. As a result, although the engine still needed to be mounted on wood, more rigid ways of accomplishing this were found. Finally, though this exercise, it was also revealed how important proper cooling of the engine is to prevent a lack of lubrication and ultimately failure.

Fortunately, the trials and tribulations of this iterative process did eventually yield a setup that worked for both propeller and dyno testing. However, the dyno testing specifically required the replacement of the connecting rod between tests due to the harsh nature of the setup causing them to fatigue and fail faster. The propeller testing did not require such replacements, proving it was most likely the dyno that was at fault for the failures, especially since temperatures tended to be lower for the dyno setup after the blower was installed. The specific speeds and throttle positions decided as data set points will be discussed in the next chapter. Overall, the real trial of the engine setup's robustness will come from the extended testing of all three-engine configurations; i.e., stock engine, stock cylinder head and AM crankcase, and AM cylinder head with AM crankcase.

# Chapter 5: Test Procedure, Data Post-Processing and Results

After creating finalized setups for both propeller (prop) and dynamometer (dyno) testing, test procedures were determined to shed light on the differences in performance of engines with AM parts. It is through this comparative data analysis that an overall conclusion regarding the possibility of employing AM in the construction of IC engines is formed. Moreover, due to the nature of these tests, an understanding of the engine's robustness is gained.

## 5.1 **Test procedures**

The three main engine setups that were tested included: the stock engine (SE), AM crankcase with the stock cylinder head (ACS), and the AM crankcase and AM cylinder head (ACAH). When swapping the stock crankcase for the AM version, the front and rear ball bearings, crankshaft, cam gear assembly (cam gear housing, cam gear, cam gear shaft, steal washer set, tappets, lower rubber pushrod seals and cam gear housing screws), and hall sensor were replaced to make swapping the configuration easier. When replacing the cylinder head, the rocker arms, cylinder head gasket, and valve spring assemblies (brass valve guides, valve springs, valve spring holder, retaining rings, and valves) were replaced; again, this was to aid in ease of configuration change. These assemblies are shown in Figure 5.1 and it should be noted that the same spark plug was used between tests. Anytime that a cylinder head was removed or replaced, the tappets were adjusted following the manual's instructions so that the limit gauge cannot be inserted between the valve stems and the rocker arms as shown in Figure 5.2. This ensures that the valves will have their full travel during operation and that they will close fully when necessary.

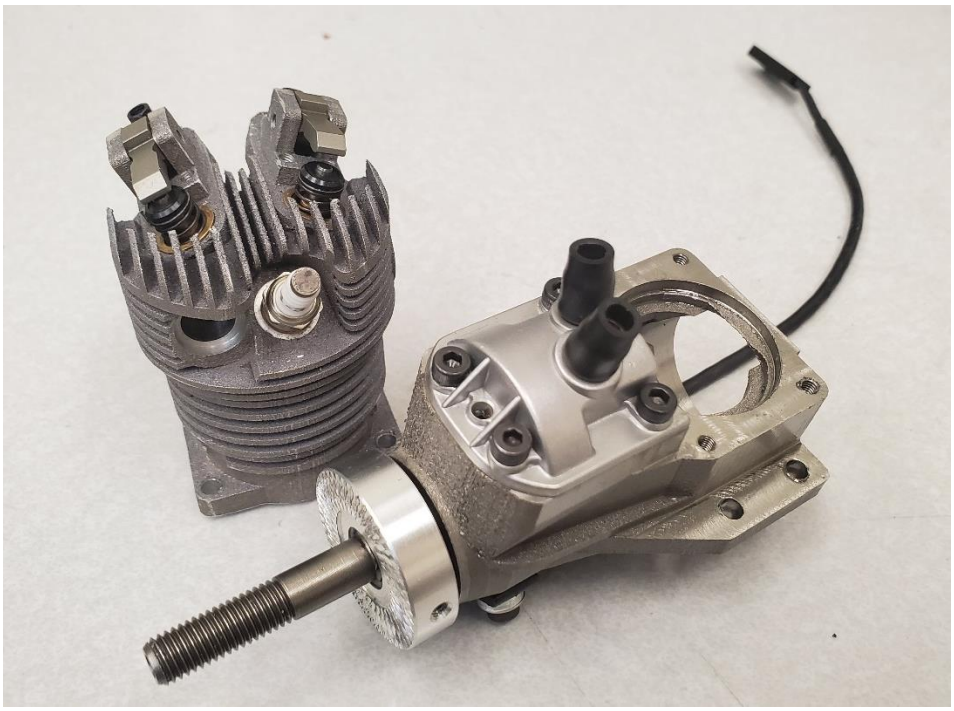

*Figure 5.1: AM cylinder head and crankcase assemblies used during testing*

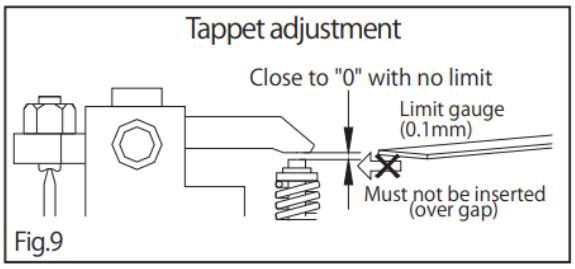


*Figure 5.2: Depiction of tappet adjustment taken from the Saito FG-11 manual [87]*

Here, it is important to highlight the major differences between the additive manufactured parts and the stock versions so that the resulting trends found during testing can be better explained. The most significant difference between the stock and AM crankcase comes from their constructed materials. The stock crankcase is an aluminum alloy and the AM crankcase was manufactured with a less conductive titanium alloy (further discussion of properties in Chapter

3). It should also be noted that the AM crankcase was constructed with a simpler geometry that added more material to the exterior to give better AM results, in turn making it even less conductive; therefore, reducing the level of heat transfer to the ambient. Lastly, the two crankcases could deliver slightly different valve timing through the pushrods. Although efforts were made to keep these consistent, there may still be some slight error during assembly when meshing the cam gear teeth with the crankshaft spline, or in the positioning of the hall effect sensor.

The cylinder walls are the main difference between the two cylinder heads. The stock head included an iron liner; whereas, the AM head relies on the high silicon content in its Al material for its wear resistance. The absence of this liner will allow for more heat transfer to the ambient. However, this could result in more wear occurring over time while possibly increasing the level of friction experienced between the walls and the piston ring. In addition, the construction of the bore as shown in Chapter 3 is slightly different (i.e., the top of cylinder has 0.0010" smaller diameter and the bottom of cylinder has a 0.0005" bigger diameter when compared to the stock head), which could influence performance by having too much friction near Top Dead Center or growing the level of blowby close to Bottom Dead Center. Moreover, this smaller diameter at the top could have caused the piston and ring to self-machine the bore further, which would have changed the surface roughness, effectively eliminating the protective honing procedure to expose the silicon in the material. Furthermore, the AM head had a rougher surface finish on areas that were not post machined. Subsequently, this could reduce the level of flow across the cooling fins. In addition, the top inside surfaces (near the valves) had a coarser finish that could cause more turbulence within the cylinder during combustion; hence, resulting

in a greater turbulent intensity and faster combustion. The subtle differences in this top geometry may also either increase or decrease the compression ratio experienced if the clearance volume changes. Finally, valve lift and timing is disturbed anytime a cylinder head is removed from the crankcase; therefore, each of these engines could possibly have slightly different valve lifts and timing if the tappets are not set correctly according to Figure 5.2.

Before any testing was performed, each engine configuration had the break-in procedure performed as described by the Saito FG-11 manual [87]. Once break-in was completed, the fuel main needle valve was set to one turn for normal engine operation. This is yet another variable that could have changed slightly between engine configurations since the needle did not have clear set positioning; hence, it is possible there could be some respectively small variation each time this was adjusted. The fuel used for this engine was a 20:1 ratio of gasoline (no ethanol) and 2-stroke engine oil. The fuel line also had to be siphoned from the graduated cylinder before attaching to the engine's carburetor to assure sufficient flow at the beginning of testing. To start the engine with the propeller, a spinner cone was installed so that a hand drill and a rubber cone could be used to initiate the combustion process. All bolts were checked and tightened before each series of tests to prevent any additional vibration or hazards. In addition, all sensors were checked to make sure they were functioning properly. For all tests, the two test cell fans are turned on to ensure proper ventilation and, for dyno testing, the blower was also powered on before tests began. The following test procedures are repeated for every test point.

#### 5.1.1. ***Propeller***

For the prop testing, each engine was run at 50, 60, 70, 80, 90, and 100% throttle positions for a total of six datasets per engine. The process for these tests is described as follows:

1. The engine was run for an initial 10-minute period to warm up both the crankcase and cylinder head and then turned off.
2. The fuel height was filled to 250 mL to keep the fuel pressure as consistent as possible through all testing.
3. The data capture length in seconds (180 s for all tests) and the file path for the test with a unique name were entered into the cDAQ and Inter-Loc V (cDLVI) Virtual Instrument (VI) Graphical User Interface (GUI) dialogue boxes where indicated.
4. Once the cylinder head cooled to 70 °C, the engine is spun up with the throttle at 50% using a power drill and then immediately opened to 70% when the engine starts combusting.
5. After the cylinder head reached 100 °C, the engine was then set to the throttle percentage needed for the test point.
6. The engine was left at this set point until it reached steady-state. This point was determined when cylinder head, crankcase, and exhaust temperatures had less than a 3 °C change in one minute.
7. After steady-state was achieved, the “OK” button is pressed on the cDLVI GUI to begin the data collection.
8. As the data are being collected, the “Magnet Data” button was pressed when the “elapsed time” hit 20 s, 80 s, and 140 s. This insures through the three-minute test that there are 20 s of magnet data taken in all three minutes totaling up to a full minute of data.

9. Once the test is over, the engine is immediately turned off by closing the intake, and this process (steps 2-9) is repeated for all test points.

### 5.1.2. ***Dynamometer***

Dyno testing was completed after propeller testing, so there was no need for a break-in process, as it had previously been completed. For these tests, the engines were run at 70, 80, 90, and 100% throttle positions at speeds of 5000 and 6000 rpm. Here, the 50 and 60% throttle positions were unable to sustain combustion; therefore, they were not used as data points. This is likely because the engine is not designed to be spun at these respectively low speeds with this particular fuel setting (e.g., as shown later, the prop testing found that engine speed was largely greater than 6000 rpm). However, the dyno was limited to a speed of 6000 rpm, hence why the test speeds were chosen. The procedure is as follows:

1. Once the dyno is turned on, it is allowed 15 minutes to warm up and then the dyno controller torque measurement is zeroed.
2. The fuel cylinder is filled to 250 mL.
3. The data capture length in seconds (180 s for all tests) and the file path for the test with a unique name were entered into the cDLVI GUI dialogue boxes where indicated.
4. The dyno is spun up to the set speed, and the engine throttle percentage is kept initially at 30%; however, when the speed reaches 4000 rpm the throttle is slowly opened to 70%.
5. The throttle is left at 70% until the temperatures start to level out (<10 °C change in one minute); after which, it is opened to the test set point throttle percentage.

6. Once at the set throttle percentage, the engine is left to run until steady-state is reached when the cylinder head and crankcase temperatures had less than a 3 °C change in one minute. For these tests, the exhaust temperature was more variable due to its positioning in the crossflow of the blower; hence, it was not used as a steady-state indicator.
7. After steady-state is achieved, the "OK" button is pressed on the cDLVI GUI to begin the data collection.
8. Once data collection is over, the spark plug is tuned off for 5 s with the dyno still running and the resulting torque is recorded to determine the torque overcome from frictional and pumping work. Note: this is used to normalize the torque data taken throughout the test.
9. The dyno is then spun down to 100 rpm with the throttle set at 30% while ensuring that the engine is not combusting before turning it off and this entire procedure (steps 2-9) is repeated for each test point.

## 5.2 **Data Post-processing**

A Matlab program was used to streamline the post-processing of all testing data. This program provided four main functions: organizing the myRIO data, finding engine speed based on magnet passes (prop tests only), determining fuel consumption, and calculating all averages, standard deviations (for error bars), and engine performance parameters. Hence, this program kept data analysis consistent through all test points, its code can be found in Appendix F.

As explained in the previous chapter, data was collected by both the myRIO and cDAQ. To accomplish this, a stream had to be used in the LabVIEW program to pull the values off the myRIO and save them to the computer. During prop testing, magnet data were taken at roughly

4000 Hz; however, the cDAQ collects data at approximately 5 Hz. Because these two loops were running at different rates, the data from the myRIO were only being saved five times a second inside the cDLVI. Within that amount of time, ~800 samples were taken by the myRIO. This means, 800 data points went into the stream as a packet and then were saved as a single line in the delimited spreadsheet. However, since the cDAQ data collection step size is not entirely consistent, some lines contained more data points than others. Therefore, a streamlined way to organize this data was required.

As a result, the Matlab program organizes the data while also separating the magnet and flow sensor data. Here in the myRIO VI, these two data components took turns being saved into the same array position to make data collection faster for the Hall sensor because there would only be one data point saved in each loop iteration. The Matlab program goes through each line of the myRIO matrix while taking two values at a time (i.e., time and magnet pass/flow) and placing them into a new two column matrix. This is done until the program has analyzed every row. The data are then separated into the magnet and flow data by investigating the values; i.e., if the value is greater than six, then it is determined to be a flow value. With the dyno testing, this same post-processing was used but without the magnet and flow data sorting.

In addition, the Matlab program was used to determine the engine speed based on the magnet data. Like previously mentioned, because data collection speeds were not completely sufficient, some passes were missed as shown in Figure 5.3. To make up for the missing points, the program took the magnet data and turned all points that were greater than 1 into a value of 1 and all points less than 1 into a zero value to find all peaks. Then, the time between each peak was found and times that were greater than four standard deviations away from the mean were

determined invalid (i.e., missed magnet reading) and removed from the data set. These data points are represented as around 4500 rpm in the histogram that is depicted in Figure 5.4. The average was then recalculated and used to find the engine speed (updated histogram of this is shown in bottom graph of Figure 5.5). This post-processing was not necessary with dyno testing because speed was a direct readout from the dyno controller.

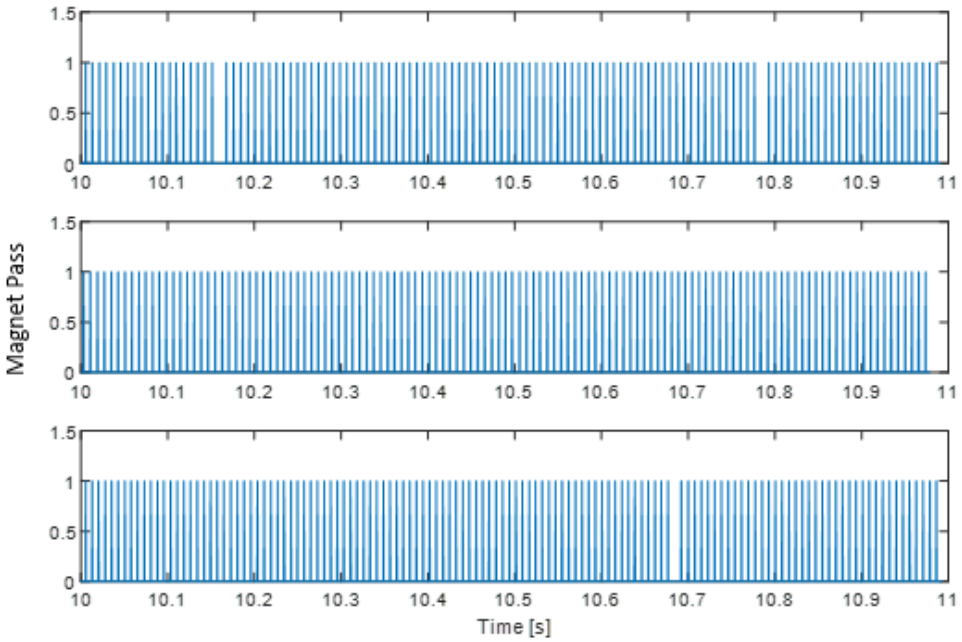


*Figure 5.3: Representation of the magnet pass data; each graph is one second inside each of the 20 s segments taken for one test point*

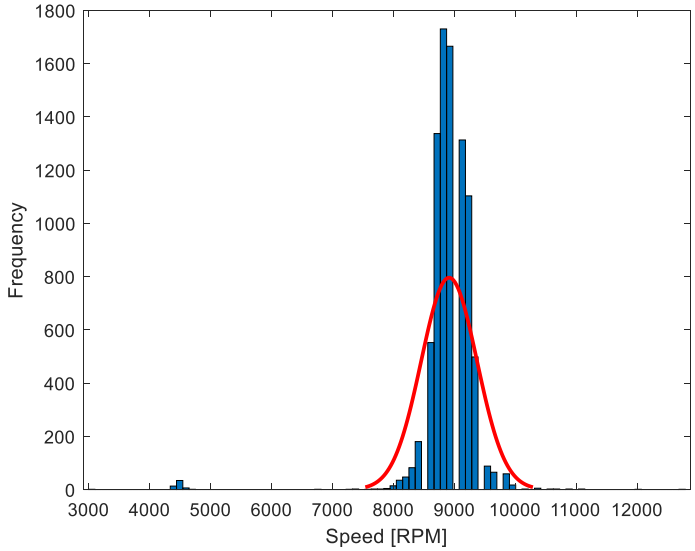


*Figure 5.4: Histogram of the time between magnet passes for one test point with extraneous data with the normal distribution curve displayed (red)*

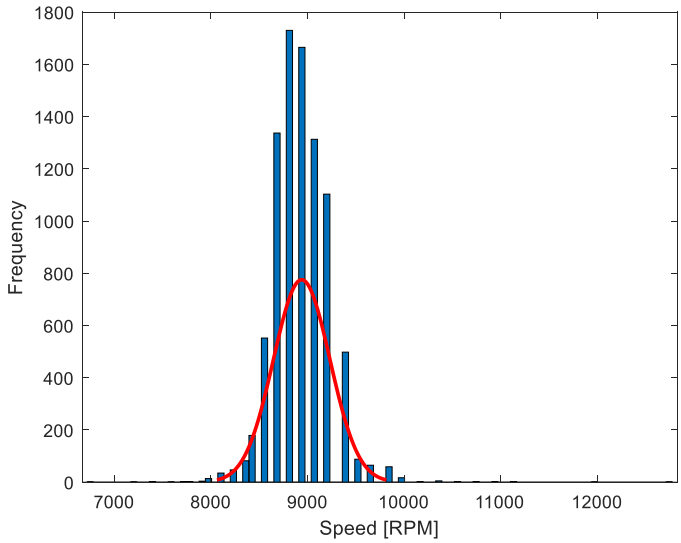


*Figure 5.5: Histogram of the adjusted time between magnet passes for one test point with the normal distribution curve displayed (red)*

In addition, investigating fuel consumption measurement data found that the fuel level height sensor would occasionally give invalid values. Therefore, the Matlab program removed these data points by calculating the average voltage in each minute of the test and eliminating

data that would fall ±0.1 VDC outside of this average. An example of this sensor giving invalid values can be seen in Figure 5.6. Then, the trendline slope of the post-processed data set without the extraneous data was calculated and compared to the calibration curve trendline slope (found in Chapter 4) to determine the fuel consumption. The process for calculating the dataset trendline slope ($\hat{m}$) is:

$$\hat{m} = \frac{n\sum(x*y)-\sum x*\sum y}{n\sum x^2-(\sum x)^2} \tag{5}$$

where $n$ is number of data points, $y$ is voltage (VDC) array, and $x$ is time (for testing) or volume (for calibration) array. The comparison between this trendline and the calibration curve slope to get fuel consumption ($\dot{\mathbb{V}}_{fuel}$) is represented as follows:

$$\dot{\mathbb{V}}_{fuel}\ (mL/min) = \frac{data\ set\ trendline\ slope*60}{calibration\ curve\ slope} \tag{6}$$

Furthermore, the process for calculating the standard deviations of both of these trendline slopes ($s_m$) is shown in Equation (7) where $\bar{x}$ is the mean value of $x$ and $\hat{y}$ is the linear model being fitted ($\hat{y} = \hat{m}x + \hat{b}$):

$$s_m = \sqrt{\frac{\left(\frac{1}{n-2}\right)\sum_{i=1}^{n}(y_i-\hat{y}_i)^2}{\sum_{i=1}^{n}(x_i-\bar{x}_i)^2}} \tag{7}$$

To find this standard deviation, calculating the *y*-intercept ($\hat{b}$) of the linear model is also necessary [88]:

$$\hat{b} = \frac{\sum y-\hat{m}*\sum x}{n} \tag{8}$$

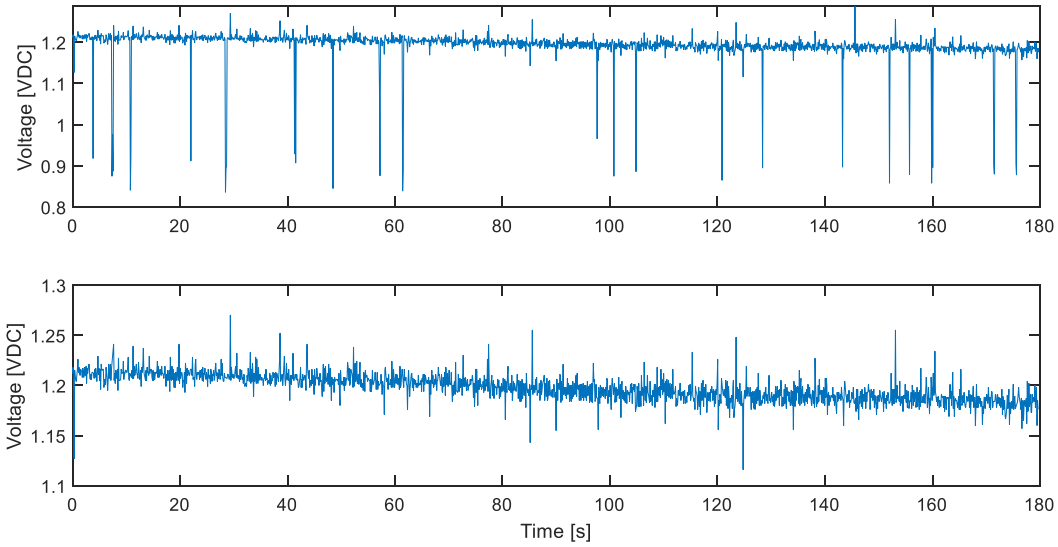


*Figure 5.6: Fuel height senor values (top) and the elimination of the extraneous data (bottom)*

Finally, the Matlab program calculated averages and standard deviations of the other data collected, such as intake flow, temperatures, and pressures. These values are used to find engine performance parameters including volumetric efficiency ($\eta_v$), air fuel ratio ($AF$), and equivalence ratio ($\phi$), respectively:

$$\eta_v = \frac{n_R * \dot{\mathbb{V}}_{air}}{\mathbb{V}_{disp} * N} \tag{9}$$

$$AF = \frac{\dot{m}_{air}}{\dot{m}_{fuel}} = \frac{\dot{\mathbb{V}}_{air} * \rho_{amb}}{\dot{\mathbb{V}}_{fuel} * \rho_{fuel}} \tag{10}$$

$$\phi = \frac{AF_s}{AF} \tag{11}$$

For volumetric efficiency, $n_R$ is the number of crank revolutions per engine cycle (2 for four-stroke engines), $\dot{\mathbb{V}}_{air}$ is the average air intake flow rate, $\mathbb{V}_{disp}$ is the engine displacement

(10.9 cc), and finally *N* is the engine speed. For the air fuel ratio, $\rho_{amb}$ and $\rho_{fuel}$ are the densities of the air and fuel respectively, and the $\dot{\mathbb{V}}_{fuel}$ is the average rate of fuel consumption. Finally, equivalence ratio uses the previous air fuel ratio calculated and compares it to the stoichiometric air fuel ratio ($AF_s$) and the calculation for this value by Dr. Depcik can be found in Appendix G. Error approximations made for these calculated values are also included in the Matlab code using propagation of error and sequential perturbation techniques [89]. These both returned the same result for every value, providing consistency to the error calculations.

## 5.3 **Results**

### 5.3.1. ***Propeller***

Before comparisons between the engines are made, it is important to first discuss the trends that are expected from this testing setup and strategy. For these tests, the independent variable chosen to investigate was the throttle percentage. When increasing the throttle percentage, a direct boost in air flow rate is anticipated due to a growth in the intake cross sectional area (i.e., less flow restriction). With this increase in air flow rate, fuel flow rate is also predicted to rise because the venturi effect inside the carburetor pulls in fuel at a rate determined by the pressure drop produced by the passing air. As the flow rates of air and fuel grow, a greater energy release will raise in-cylinder engine temperatures. Through the ideal gas law, this will subsequently grow the pressure and exert a greater force upon the piston; hence, the engine should spin faster. After in-cylinder temperatures rise, the exhaust temperature will grow followed by the cylinder head and finally the crankcase temperatures through thermal conductivity (note: temperature sensors for the cylinder head and exhaust are on the exterior of

the engine). However, somewhat buffering this increase in temperature is the increase in engine and propeller speed, resulting in a larger cooling effect on the engine as the throttle opens. Hence, the temperature should still grow with throttle percentage, but perhaps at a reduced extent with temperatures potentially leveling off. Overall, in Figure 5.7 through Figure 5.12, these trends are mostly seen as a function of throttle position. The choice of $2^{nd}$ order curve-fits is based on an assumed balance between prop cooling and a greater extent of combustion as the throttle opens and helps to identify these trends while comparing the engines.

From these figures, the following estimated relationships occur between the engine configurations:

- Air flow rate (Figure 5.7): ACS ≥ SE > ACAH
- Fuel flow rate (Figure 5.8): SE ≈ ACS > ACAH
- Engine speed (Figure 5.9): ACS > SE > ACAH
- Exhaust temperature (Figure 5.10): ACS ≥ SE > ACAH
- Cylinder head temperature (Figure 5.11): ACS > SE > ACAH
- Crankcase temperature (Figure 5.12): ACS > SE ≥ ACAH

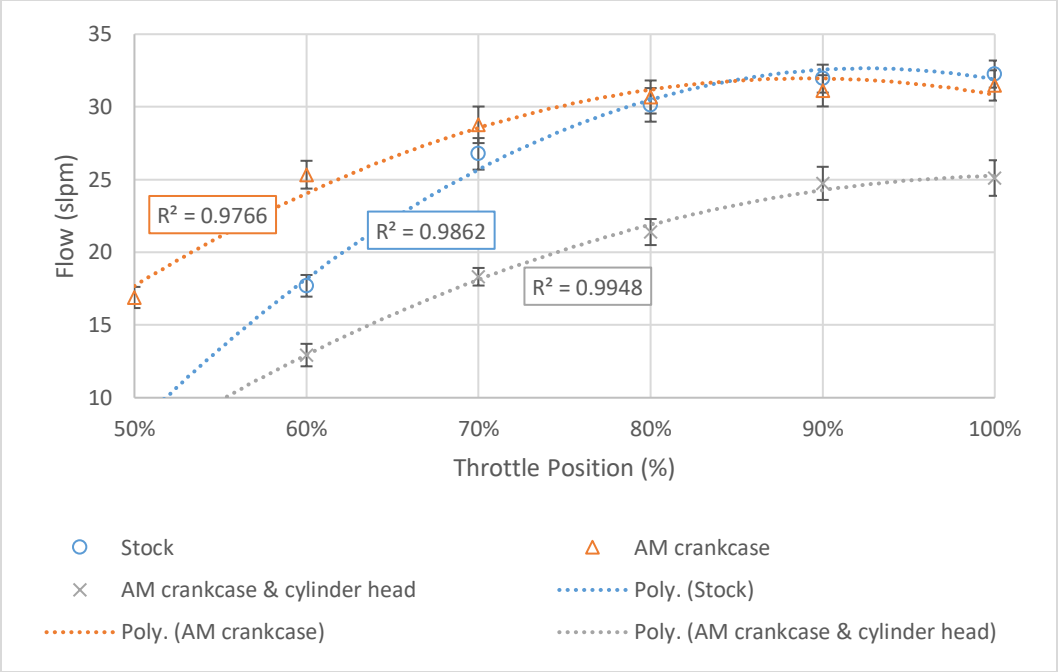


*Figure 5.7: Intake air flow rate results during prop testing*

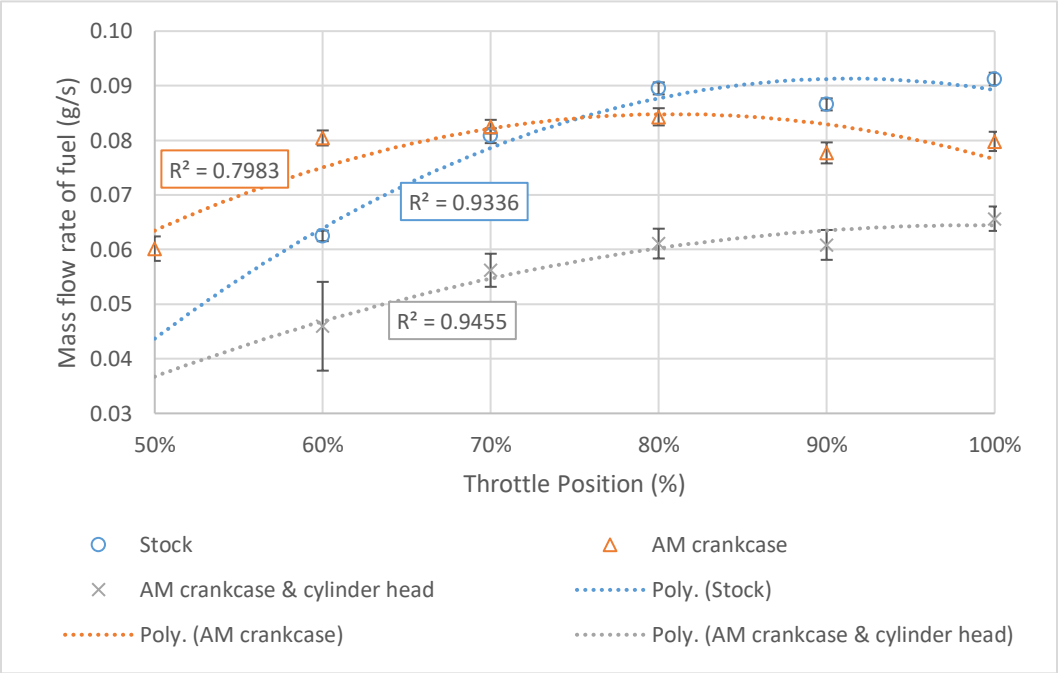


*Figure 5.8: Fuel consumption results during prop testing*

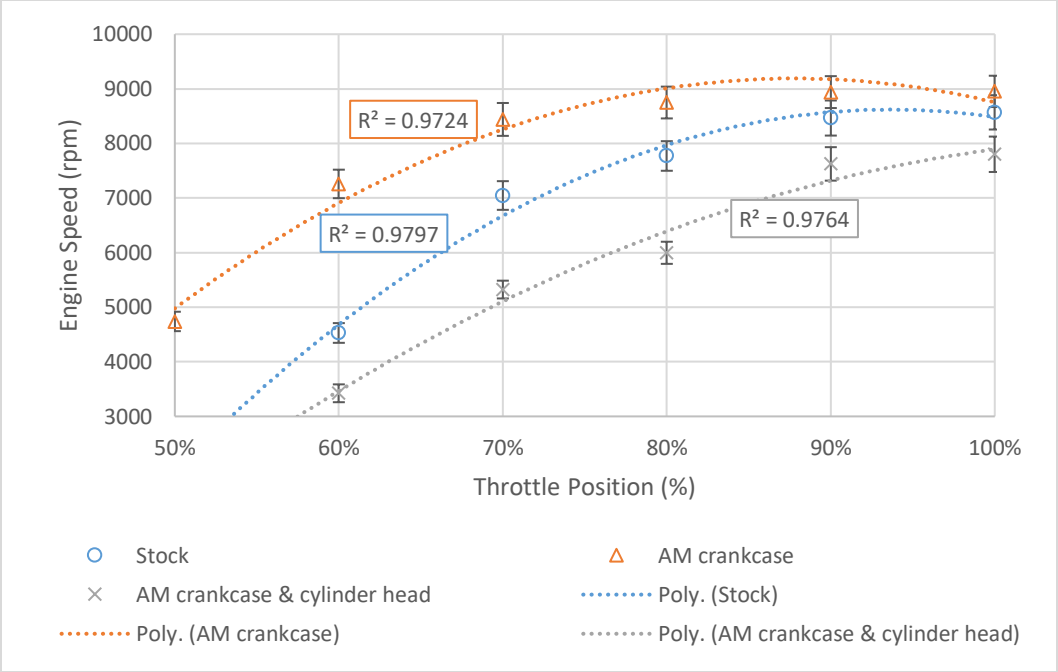


*Figure 5.9: Engine speed results during prop testing*

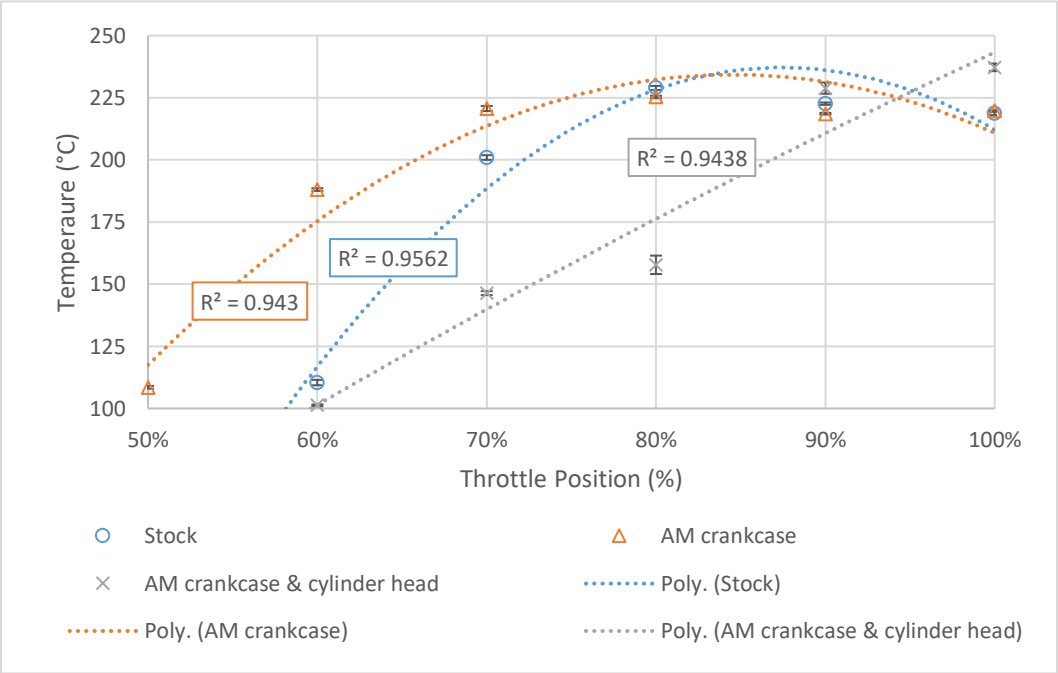


*Figure 5.10: Exhaust temperature results during prop testing*

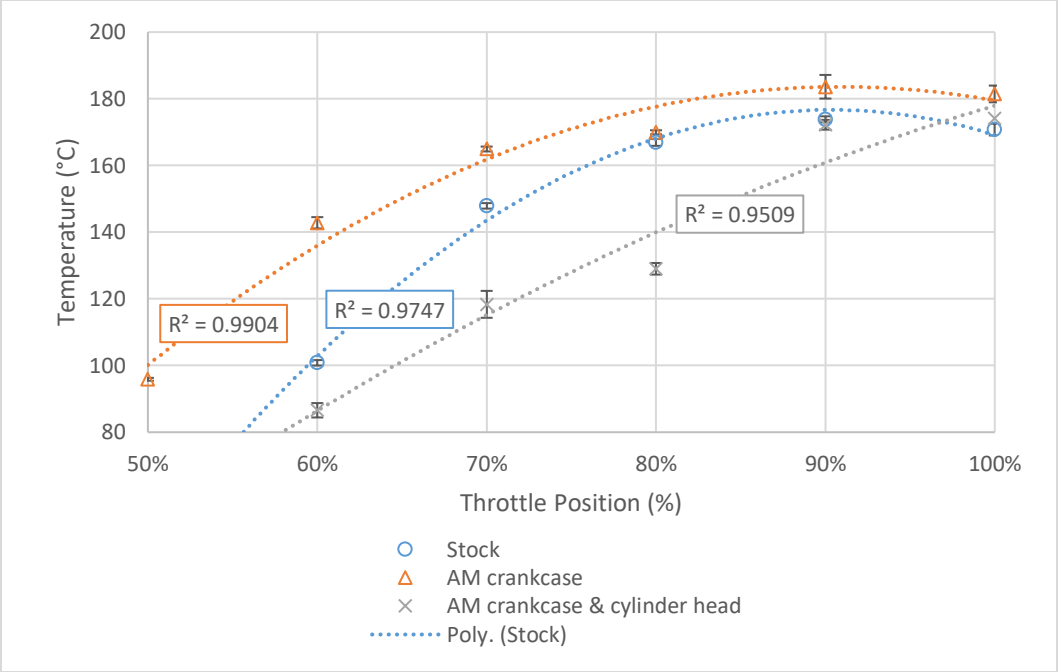


*Figure 5.11: Cylinder head temperature results during prop testing*

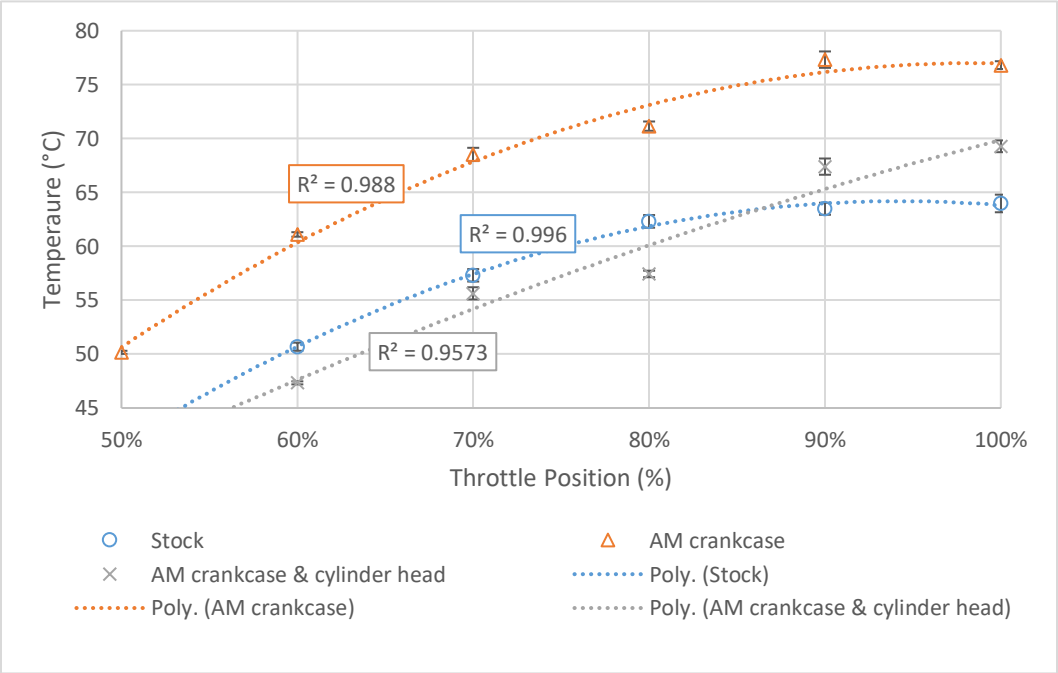


*Figure 5.12: Crankcase temperature results during prop testing*

During testing it was discovered that ACS was the only engine that was able to sustain combustion at 50% throttle. It is suspected that because it was the least thermally conductive engine (titanium crankcase with stock iron lined cylinder head) it can reach higher temperatures, allowing it to maintain combustion more readily. Interestingly, the inlet air flow rate of ACS was generally higher than all engines (Figure 5.7). This is counter to the fact that its assumed hotter cylinder would reduce the inlet air density and air mass flow rate due to a reduction in volumetric efficiency. Now, this decrease in volumetric efficiency is indeed found via the calculations presented in Table 5.1. Furthermore, when comparing engines at similar speeds, Figure 7 highlights that ACS does have a lower air flow rate than SE with ACAH having the lowest air flow rate (Table 5.2 and Table 5.3).

*Table 5.1: Comparison of engine performance parameters during prop testing*

| | STOCK (SE) | | | AM CRANKCASE (ACS) | | | AM CRANKCASE & CYLINDER HEAD (ACAH) | | |
|---|---|---|---|---|---|---|---|---|---|
| | $\eta_v$ | $AF$ | $\Phi$ | $\eta_v$ | $AF$ | $\Phi$ | $\eta_v$ | $AF$ | $\Phi$ |
| **50%** | - | - | - | 0.654 ±0.037 | 5.64 ±0.32 | 2.58 ±0.15 | - | - | - |
| **60%** | 0.717 ±0.042 | 5.68 ±0.26 | 2.56 ±0.12 | 0.641 ±0.033 | 6.32 ±0.26 | 2.30 ±0.10 | 0.693 ±0.053 | 5.65 ±1.06 | 2.57 ±0.49 |
| **70%** | 0.697 ±0.038 | 6.65 ±0.29 | 2.19 ±0.10 | 0.626 ±0.035 | 7.00 ±0.32 | 2.08 ±0.10 | 0.632 ±0.028 | 6.54 ±0.41 | 2.22 ±0.14 |
| **80%** | 0.712 ±0.037 | 6.76 ±0.27 | 2.15 ±0.09 | 0.644 ±0.032 | 7.30 ±0.30 | 1.99 ±0.08 | 0.655 ±0.035 | 7.03 ±0.43 | 2.07 ±0.13 |
| **90%** | 0.692 ±0.034 | 7.40 ±0.24 | 1.96 ±0.06 | 0.638 ±0.030 | 8.03 ±0.34 | 1.81 ±0.08 | 0.595 ±0.036 | 8.16 ±0.53 | 1.78 ±0.12 |
| **100%** | 0.691 ±0.032 | 7.10 ±0.22 | 2.05 ±0.06 | 0.645 ±0.030 | 7.92 ±0.32 | 1.84 ±0.07 | 0.591 ±0.038 | 7.68 ±0.46 | 1.89 ±0.11 |
| **Average** | 0.702 ±0.037 | 6.72 ±0.26 | 2.18 ±0.09 | 0.639 ±0.033 | 7.31 ±0.31 | 2.00 ±0.10 | 0.633 ±0.038 | 7.01 ±0.58 | 2.11 ±0.20 |

*Table 5.2: Comparison of engines at approximately 5000 rpm during propeller testing*

| | SE | ACS | ACAH |
|---|---|---|---|
| Speed [rpm] | 4528.3 | 4739.3 | 5323.1 |
| Throttle Position | 60% | 50% | 70% |
| Air Flow [slpm] | 17.70 | 16.89 | 18.32 |
| Mass Flow Rate of Fuel [g/s] | 0.0625 | 0.0602 | 0.0562 |
| Exhaust Temperature [°C] | 110.41 | 108.51 | 146.39 |
| Cylinder Head Temperature [°C] | 100.82 | 95.87 | 118.36 |
| Crankcase Temperature [°C] | 50.68 | 50.16 | 55.64 |

*Table 5.3: Comparison of engines at approximately 7000 rpm during propeller testing*

| | SE | ACS | ACAH |
|---|---|---|---|
| Speed [rpm] | 7045.9 | 7257.9 | 7624.9 |
| Throttle Position | 70% | 60% | 90% |
| Air Flow [slpm] | 26.77 | 25.34 | 24.74 |
| Mass Flow Rate of Fuel [g/s] | 0.0809 | 0.0804 | 0.0657 |
| Exhaust Temperature [°C] | 200.97 | 188.06 | 228.87 |
| Cylinder Head Temperature [°C] | 147.89 | 142.81 | 172.21 |
| Crankcase Temperature [°C] | 57.31 | 61.10 | 67.39 |

With respect to ACAH, since it has the same crankcase as ACS this promotes higher temperatures ($\eta_v\downarrow$). However, its cylinder head does not have a liner which results in more heat transfer to the ambient ($\eta_v\uparrow$ due to a cooler temperature). In addition, significant lapping of the valve seat was accomplished to create a proper seal for combustion to occur. Therefore, it is possible that there could be a lower effective compression ratio as some air exits back through the intake valve if the lapping was not sufficient ($\eta_v\downarrow$). Additionally, between each engine change the tappets were adjusted so this may have affected valve timing and lift and thereby

influencing volumetric efficiency. Furthermore, as stated prior, the slightly larger bore towards the bottom of the cylinder might lead to a greater extent of blowby ($\eta_v\downarrow$); whereas, a smaller bore at the top of the cylinder might reduce blowby ($\eta_v\uparrow$). Investigating the data Table 5.1 in finds that the negative influences on volumetric efficiency for ACAH overwhelm the reduction in heat transfer due to the omission of a liner; therefore, explaining its lower air flow rate at the same engine speed (Table 5.3). Moreover, this resulted in ACAH having the lowest overall air flow rate as a function of throttle percentage.

Here, it is important to discuss how these engines operate. In specific, since the lubricating oil enters the engine along with the fuel, it is critical to run the engine rich. This is evident through the equivalence ratio calculations in Table 5.1; i.e., all values are significantly greater than one. During testing it was noticed that significant fuel exited the exhaust and the crankcase overflow as an inky black liquid substance, lending credence to the equivalence ratio values. Moreover, since this is a carbureted engine, the quantity of fuel entering is not held consistent to the air flow rate (i.e., a constant equivalence ratio) like what would occur with a fuel injected engine. Overall, as the air flow rate increases with throttle percentage, the fuel flow rate does generally increase in Figure 5.8. However, neither the ACS nor ACAH experience as dramatic an increase as the SE. This could be because the needle setting on the carburetor might have changed slightly between engine setups as each engine required a break-in procedure under higher fuel flow rates (i.e., the needle was adjusted to be rich and then back to the recommended settings before prop testing). As a result, both ACS and ACAH ran closer to stoichiometric combustion ($\Phi$ =1) and the maximum adiabatic flame temperature ($\Phi$=1.1). This would raise combustion temperatures that, subsequently, boosts combustion pressures. In turn, this would

create more work on the piston and grow the engine speed. This phenomenon is seen in Figure 5.9 with ACS having the highest engine speed. Even though ACAH ran closer to stoichiometry, its significantly reduced air flow rate resulted in a greatly diminished fuel flow rate and a lower extent of combustion. In addition, as discussed prior, the ACAH cylinder might encounter more friction due to the absence of a liner (i.e., greater amount of wear leads to rougher surface) and a slightly smaller bore at the top of the cylinder. Since friction grows as a function of engine speed squared [90], this effect is heightened for ACAH and might also indicate why a polynomial trendline is appropriate for all engines. As a result, ACAH would generate the least amount of brake work and have the lowest engine speed, which is seen in Figure 5.9.

In regard to the exhaust temperature, the following phenomenon are occurring:

- A titanium crankcase promotes higher in-cylinder temperatures through a lower level of heat transfer (i.e., less thermally conductive): $T_{ACS} \approx T_{ACAH} > T_{SE}$
- The ACAH cylinder head does not have a linear; hence, a greater level of ambient heat transfer is possible: $T_{SE} \approx T_{ACS} > T_{ACAH}$
- An increased level of friction might result in a greater heat generation as the piston ring moves against the cylinder walls: $T_{ACAH} > T_{SE} \approx T_{ACS}$
- As the engine spins faster, the turbulent intensity increases; hence, more convective heat transfer: $T_{ACAH} > T_{SE} > T_{ACS}$
- An increase in turbulent intensity results in a faster combustion process and more constant volume combustion: $T_{ACS} > T_{SE} > T_{ACAH}$

- A greater engine speed results in the propeller spinning faster resulting in more cooling: $T_{ACAH} > T_{SE} > T_{ACS}$.
- Higher equivalence ratios have a greater level of fuel cooling and lower adiabatic flame temperatures: $T_{ACS} > T_{ACAH} > T_{SE}$
- The surface finish of the top inside surface of the AM cylinder head (near the valves) might result in a greater level of turbulence and more heat transfer: $T_{SE} \approx T_{ACS} > T_{ACAH}$
- The outside surface finish of the AM cylinder head was rougher and therefore it could have increased the level of cooling due to a greater surface area or hindered it due to worse flow past the fins.

Investigating the trends in Figure 5.10 at the roughly the same engine speed (Table 5.2 and Table 5.3) finds that ACAH has the highest exhaust temperature, followed by SE and then ACS. Here, a reduced fuel cooling effect and greater adiabatic flame temperature appears to dominate (equivalence ratios at same engine speed: ACAH (1.78) < SE (2.19) < ACS (2.30)) along with an increased level of friction that is augmented by the decreased amount of fuel lubrication. This appears to overcome material effects on heat transfer. Once the varied engine speeds at specific throttle percentages are factored into the situation, its effect on heat transfer via convective heat transfer (turbulent intensity and propeller cooling) results in lower exhaust temperatures with the trend reversing even though combustion might be more vigorous; i.e., ACS has the highest exhaust temperature, followed by SE and then ACAH with its lack of cylinder liner also influencing the outcome.

Reviewing the cylinder head temperature plots in Figure 11 finds that at the same engine speed (Table 5.2 and Table 5.3), ACAH is greater than SE followed by ACS; hence, mirroring

the findings of exhaust temperature. Here, the effects of material properties for the AM parts should be more prevalent and play a role in this trend. However, the reduced amount of heat transfer due to a titanium crankcase might somewhat balance the increased level of heat transfer for ACAH not having a cylinder liner. Again, when considering engine speed, the same exact trend as the exhaust temperature is encountered.

Finally, investigating crankcase temperatures in Figure 12 at the same engine speed (Table 5.3) sees that ACAH has the greatest crankcase temperature now followed by ACS and then SE. Here, material properties now play a more significant role due to the titanium crankcase having a reduced heat transfer rate. Once engine speed is considered, the same trend as exhaust and cylinder head temperatures is seen; however, with a reduced difference between ACS and SE because of the dissimilar crankcase materials.

### 5.3.2. ***Dynamometer***

After propeller testing was completed, the engine was connected to the dyno for the final rounds of experimentation. Similar to the prop tests, the overall trends experienced as a result of increasing the throttle percentage are important to identify. Unlike the prop tests, these engines are held at a constant speed, and the engine is not allowed to freely self-regulate based on other factors. As a result, even when the throttle percentage is increased, the air flow to the engine in Figure 5.13 remains mostly constant because the engine displacement rate also remains constant (constant speed). However, the opening of the throttle decreases the pressure drop experienced inside of the carburetor (less restriction); therefore, less fuel enters as seen in Figure 5.14 due to the venturi effect. In addition, since the fuel flow rate decreases with throttle position, less space

is taken up and there is more room for air which will lead to an increase in volumetric efficiency with throttle percentage. Although there is less fuel and a lower amount of potential energy entering, the measured temperatures increase (Figure 5.15 through Figure 5.17). As stated in the propeller testing section, these engines run rich of stoichiometry; hence, when less fuel is added, the engine operates with reduced cooling and closer to stoichiometry with higher adiabatic flame temperatures. The trends for this are reflected in Table 5.4 and Table 5.5 via the equivalence ratios. Ignoring the 70% throttle position readings in Figure 5.18 due to potentially unstable combustion, even though combustion is becoming more energetic as the equivalence ratio decreases, the torque readings remain relatively constant. Here, there is a general plateau of power generated running rich after stoichiometry where the added fuel no longer influences the power output and only aids in further cooling the engine. This can be seen by the fuel flow rate decreasing while the adiabatic flame temperature increases; i.e., an effectively constant energy output and similar torque values.

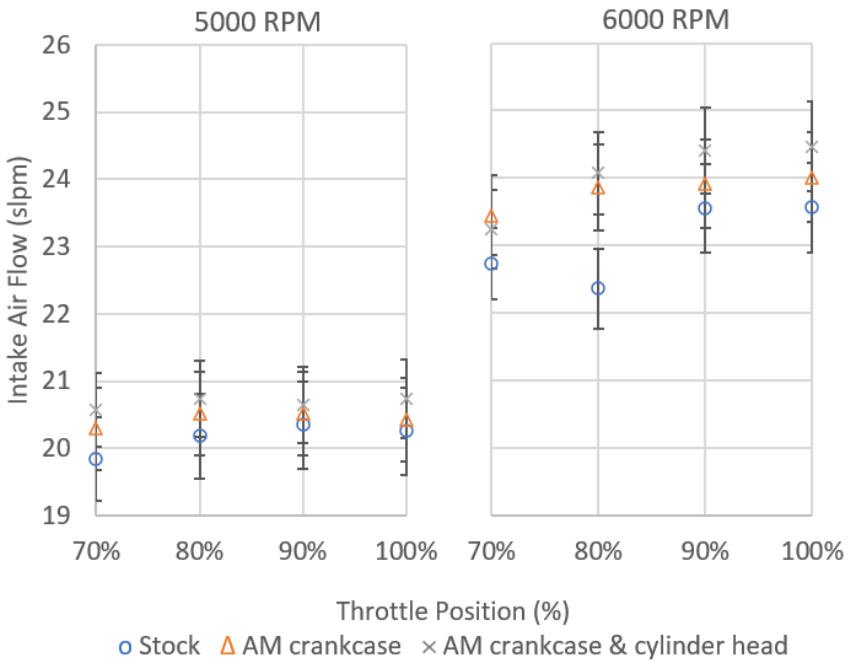


*Figure 5.13: Air intake flow rates results during dyno testing*

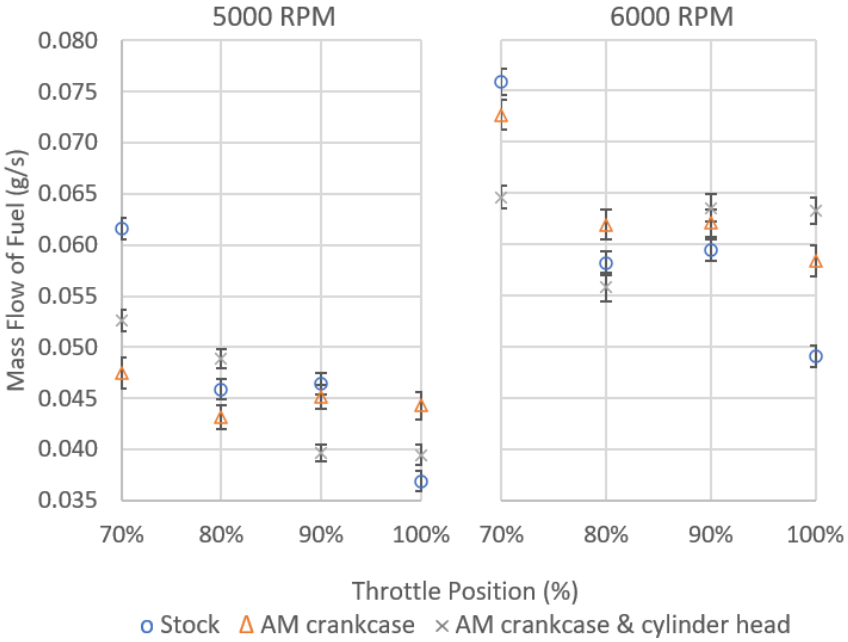


*Figure 5.14: Fuel consumption results during dyno testing*

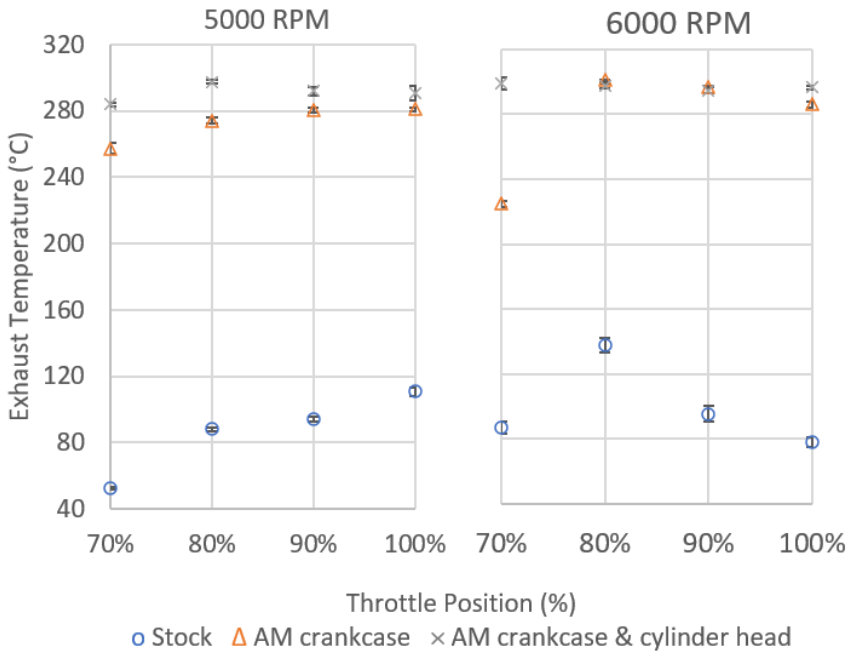


*Figure 5.15: Exhaust temperatures results during dyno testing*

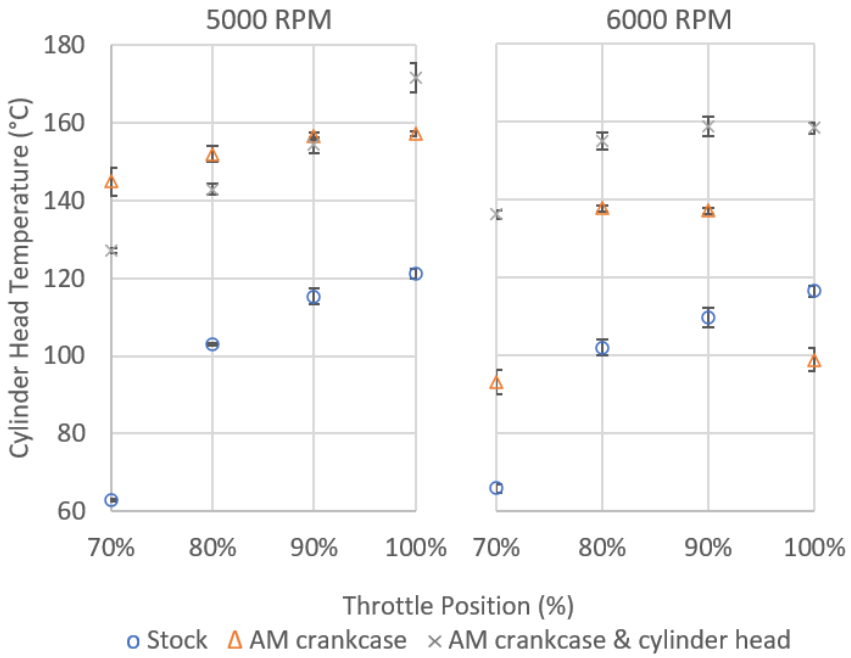


*Figure 5.16: Cylinder head temperatures results during dyno testing*

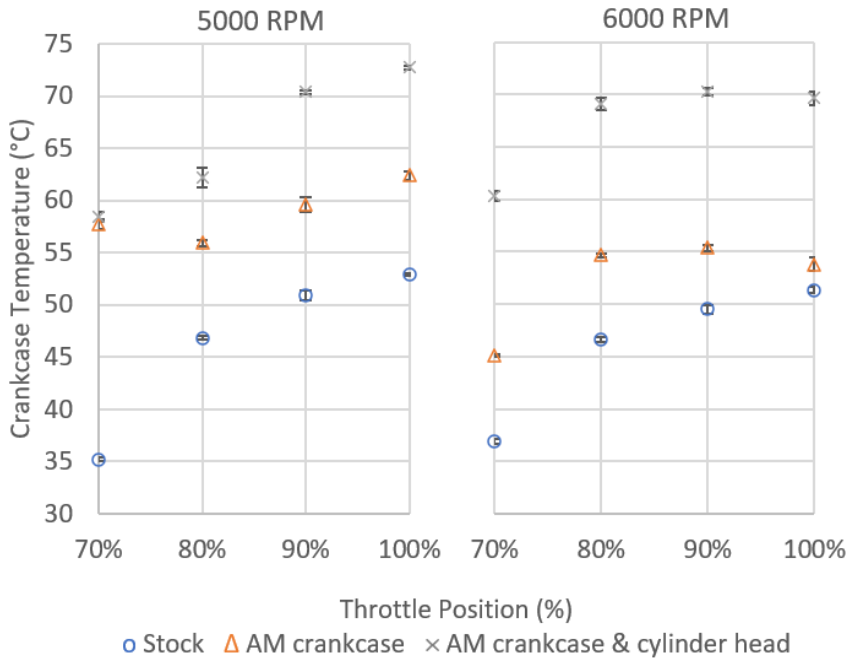


*Figure 5.17: Crankcase temperatures results during dyno testing*

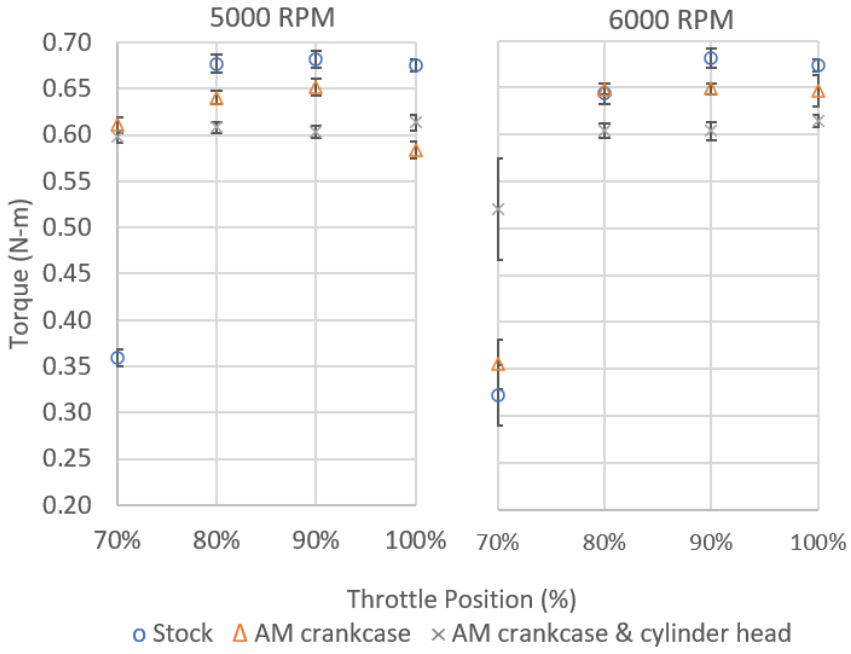


*Figure 5.18: Engine torques produced results during dyno testing*

*Table 5.4: Comparison of engine performance parameters at 5000 rpm during dyno testing*

| | Stock | | | AM Crankcase | | | AM Crankcase & Cylinder Head | | |
|---|---|---|---|---|---|---|---|---|---|
| | $\eta_v$ | *AF* | *Φ* | $\eta_v$ | *AF* | *Φ* | $\eta_v$ | *AF* | *Φ* |
| **70%** | 0.728 ±0.023 | 6.46 ±0.23 | 2.25 ±0.08 | 0.745 ±0.022 | 8.58 ±0.38 | 1.69 ±0.07 | 0.755 ±0.020 | 7.84 ±0.26 | 1.86 ±0.06 |
| **80%** | 0.741 ±0.023 | 8.82 ±0.34 | 1.65 ±0.06 | 0.753 ±0.023 | 9.54 ±0.39 | 1.53 ±0.06 | 0.761 ±0.021 | 8.52 ±0.29 | 1.71 ±0.06 |
| **90%** | 0.747 ±0.024 | 8.79 ±0.34 | 1.65 ±0.06 | 0.753 ±0.023 | 9.12 ±0.37 | 1.60 ±0.06 | 0.758 ±0.021 | 10.44 ±0.36 | 1.39 ±0.05 |
| **100%** | 0.743 ±0.024 | 11.01 ±0.46 | 1.32 ±0.06 | 0.750 ±0.023 | 9.26 ±0.40 | 1.57 ±0.07 | 0.761 ±0.021 | 10.55 ±0.40 | 1.38 ±0.05 |
| **Average** | 0.740 ±0.024 | 8.77 ±0.34 | 1.72 ±0.07 | 0.750 ±0.023 | 9.13 ±0.39 | 1.60 ±0.07 | 0.759 ±0.021 | 9.34 ±0.33 | 1.59 ±0.06 |

*Table 5.5: Comparison of engine performance parameters at 6000 rpm during dyno testing*

| | Stock | | | AM Crankcase | | | AM Crankcase & Cylinder Head | | |
|---|---|---|---|---|---|---|---|---|---|
| | $\eta_v$ | *AF* | *Φ* | $\eta_v$ | *AF* | *Φ* | $\eta_v$ | *AF* | *Φ* |
| **70%** | 0.695 ±0.016 | 6.01 ±0.18 | 2.42 ±0.07 | 0.717 ±0.018 | 6.48 ±0.21 | 2.25 ±0.07 | 0.711 ±0.018 | 7.22 ±0.22 | 2.01 ±0.06 |
| **80%** | 0.684 ±0.018 | 7.71 ±0.25 | 1.89 ±0.06 | 0.730 ±0.019 | 7.73 ±0.27 | 1.88 ±0.07 | 0.736 ±0.018 | 8.65 ±0.31 | 1.68 ±0.06 |
| **90%** | 0.720 ±0.020 | 7.95 ±0.26 | 1.83 ±0.06 | 0.731 ±0.020 | 7.73 ±0.27 | 1.88 ±0.07 | 0.746 ±0.019 | 7.70 ±0.26 | 1.89 ±0.06 |
| **100%** | 0.721 ±0.020 | 7.95 ±0.34 | 1.83 ±0.06 | 0.734 ±0.020 | 8.25 ±0.31 | 1.76 ±0.07 | 0.748 ±0.020 | 7.76 ±0.27 | 1.87 ±0.06 |
| **Average** | 0.705 ±0.019 | 7.41 ±0.26 | 1.99 ±0.06 | 0.728 ±0.019 | 7.55 ±0.27 | 1.94 ±0.07 | 0.735 ±0.019 | 7.83 ±0.27 | 1.86 ±0.06 |

It should be noted that the connecting rod broke between the SE and ACS testing, and again immediately after the ACS testing finished (following 100% throttle at the 6000 rpm data point). In both scenarios, it was replaced with the corresponding original manufacturer's

specified part. In addition, the cylinder head's thermocouple came loose before the last data point (100% throttle at 6000 rpm) and was repositioned back in place before the test started. Both events potentially explain the lower temperature shown for this test point as the connecting rod could have been damaged before this test and the thermocouple might not have been connected to the engine in exactly the same manner.

From these figures, the following estimated relationships occur between the engine configurations:

- Air flow rate (Figure 5.13): ACAH > ACS > SE
- Fuel flow rate (Figure 5.14): ACAH ≈ ACS ≈ SE
- Exhaust temperature (Figure 5.15): ACAH > ACS > SE
- Cylinder head temperature (Figure 5.16): ACAH > ACS > SE
- Crankcase temperature (Figure 5.17): ACAH > ACS > SE
- Torque (Figure 5.18): SE > ACS > ACAH

A notable difference from prop testing is seen here: the ACAH had the highest air flow rate when previously it had the lowest. This trend is reflected in the volumetric efficiencies measured during dyno testing (Table 5.4 and Table 5.5) despite its respectively greater temperatures, which would negatively influence volumetric efficiency ($\eta_v\downarrow$). It could be possible that a potential change in valve timing and lift between each of the engines might be favorable for ACAH and was sufficient enough to overcome all negative factors on volumetric efficiency as previously described in the propeller section. Furthermore, the smaller bore geometry towards the top of the cylinder could have a greater influence than the larger bore geometry on the

bottom, subsequently reducing blowby over the entire engine cycle. In addition, it is possible that the needle settings were slightly different and the ACAH engine ran less rich (see averages in Table 4 and Table 5); hence, less space was taken up by fuel in the intake. Overall, when the engine is running itself during prop testing, bringing air in is a function of the combustion process. Here, because the dyno is oversized for this engine (i.e., it can handle up to 28.6 N-m of torque) the piston is pulled harder and more consistently during the intake stroke than throughout prop testing. This trend is directly demonstrated in air flow rates at 5000 rpm in Figure 5.13 versus Table 5.2, where the air flow during dyno testing about 3 slpm higher across the engines. Overall, this results in less variability during the intake process and, as a result, dyno results provide a better indicator of volumetric efficiency.

With dyno testing, there is not a noticeable trend in fuel flow rate between the engines (Figure 5.14). This is most likely because the speed was held constant by the dyno. As stated previously, this engine is carbureted; hence, fuel flow rate can be highly variable. Moreover, the carbureted fuel flow rate relies on a pressure drop caused by a venturi effect inside of the system. When considering the ideal gas law ($pV = mRT$), it can be assumed that the fuel flow's two major measurable influencers are air flow and temperature. Here, air flow and temperatures did show a clear trend (ACAH > ACS > SE) and these would work to offset each other leaving the pressure to remain relatively constant across the engines resulting in a respectively similar fuel flow for each.

Investigating exhaust temperatures in Figure 5.15 and in Table 5.2 finds that the values for SE are similar to the prop testing. However, ACS and ACAH exhaust temperature values are significantly greater. Temperatures this high suggest a later combustion phase more towards the

Exhaust Valve Opening (EVO) event. Recalling an earlier discussion, these engines on the dyno had a respectively harder time maintaining combustion and required a throttle opening of at least 70%; whereas, for prop testing, combustion was readily achieved at a 60% opening level. Moreover, reviewing Figure 5.9 finds that when these engines self-regulate via prop testing, they readily achieve speeds greater than 7000 rpm. As the throttle opens and engine speed increases, so does the inlet air density and turbulent intensity within the engine while the Taylor microscale shrinks helping to promote a faster and more complete combustion event. In general, relatively small internal combustion engines with reduced length scales have a more difficult time achieving combustion without a significant level of turbulence [91]. Furthermore, as stated prior, it is possible that the amount of valve lift for each engine changed slightly as the tappets had to be adjusted each time. In addition, these engines have two spark timings with one at Top Dead Center and one afterwards. Given the respectively high exhaust temperatures of ACS and ACAH, the following was assumed to have occurred:

- The valve lifts were slightly different for ACS and ACAH versus SE; hence, this will change the intake process and influence the level of turbulence.
- At the dyno speeds tested, the level of turbulence is relatively low making it more difficult for combustion to complete.
- Hence, the second spark event was needed for ACS and ACAH to ensure more complete combustion; i.e., the second spark burned a greater portion of the mixture.
- This occurred closer to EVO resulting in higher exhaust temperatures for ACS and ACAH.

- Even though significant care was taken, the hall effect sensor on the AM crankcase might have been positioned slightly different between prop and dyno testing causing an earlier spark. This earlier spark may not have been igniting the fuel completely during the compression stroke. Instead, operation would have relied more on the second spark more towards EVO.

Unfortunately, without in-cylinder pressure traces it is difficult to confirm these assumptions. Future work is targeting the inclusion of a dual in-cylinder pressure transducer and spark plug to better understand the combustion process. In addition, the exhaust temperatures were influenced by volumetric efficiency and the fuel flow rate that resulted in lower equivalence ratios and less cooling for the ACS and ACAH engines.

The trend of ACAH running hotter than ACS is most likely due to the higher level of friction occurring caused by piston ring contact with the cylinder wall as discussed previously. Since the dyno tests occurred after full rounds of prop testing it is possible that the ACAH had more wear here than previously. To show whether this was the case, surface profile and diameter measurements were again conducted similarly to Chapter 3. These results were then compared to the post honing data presented in Chapter 3. Table 3.7 shows the surface R-values of the cylinder head after the honing procedure (pre engine testing) and after engine testing. Although the surface roughness values for both are comparable, it is important to note that these are averages of four locations on the cylinder, designated by the red numbering in Figure 3.58. Figure 5.19, and Figure 5.20 help provide more insight into the post engine testing surfaces by graphically representing the profiles. Considering the engine bore was not completely symmetrical, it would be feasible that some areas experienced more wear than others, this could be the case of location

2 in Figure 5.19. When comparing this location with the pre engine testing surface (Figure 3.63), it can be observed that most of the peaks were leveled giving merit to this hypothesis. Looking at the surface finish in location 1 (Figure 5.20), shows that there is less consistency than the pre engine testing surface finish (Figure 3.63). Moreover, many of the peaks here are greater than the recommended 19 µin for silicon protrusion above the surface.

Furthermore, Table 5.7 displays diameter measurements (average of three) taken pre and post engine testing using a telescoping gauge and a 1-2" micrometer to characterize if any material wear or self-machining occurred during engine testing. Shown here is proof that the testing did inflict some wear on the walls with the amount of material removed accumulating to over 0.002" from the diameter in some areas. Considering that the honing process only removes $1/4^{th}$ of this amount (after the roughing step), the severity of the wear is revealed. This amount would have completely taken away the protective surface finish required for oil lubrication during operation, and in turn cause the higher temperatures that were observed.

*Table 5.6: Roughness value comparisons of cylinder head walls for pre and post engine testing*

| Value | Description | Unit | Before Testing ("After Silicon Exposure") | After Testing |
|---|---|---|---|---|
| **Ra** | Roughness Average | µin | 9.12 | 9.51 |
| **Rq** | RMS Roughness | µin | 12.99 | 13.24 |
| **Rz** | Average Max. Height of the Profile | µin | 92.04 | 84.28 |
| **Rp** | Maximum Profile Peak Height | µin | 21.47 | 25.55 |
| **Rv** | Maximum Profile Valley Depth | µin | 70.57 | 58.74 |
| **Rsk** | Skewness (Profile Asymmetry) | | -1.66 | -1.38 |
| **Rkµ** | Kurtosis (Profile Peakedness) | | 8.20 | 11.60 |
| **Rt** | Maximum Height of the Profile | µin | 129.31 | 174.00 |
| **Rk** | Core Roughness | µin | 22.21 | 18.82 |
| **Rpk** | Reduced Peak Height | µin | 10.16 | 20.31 |
| **Rvk** | Reduced Valley Depth | µin | 28.57 | 33.8 |
| **Mr1** | Peak Material Ratio | % | 8.47 | 13.44 |
| **Mr2** | Valley Material Ratio | % | 83.46 | 83.55 |

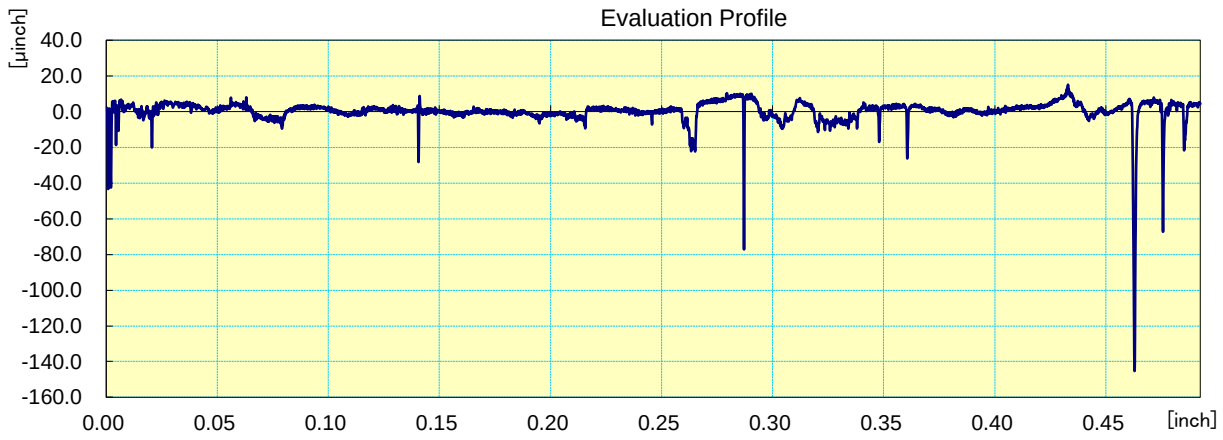


*Figure 5.19: Surface profile of AM cylinder head after engine testing (location 2)*

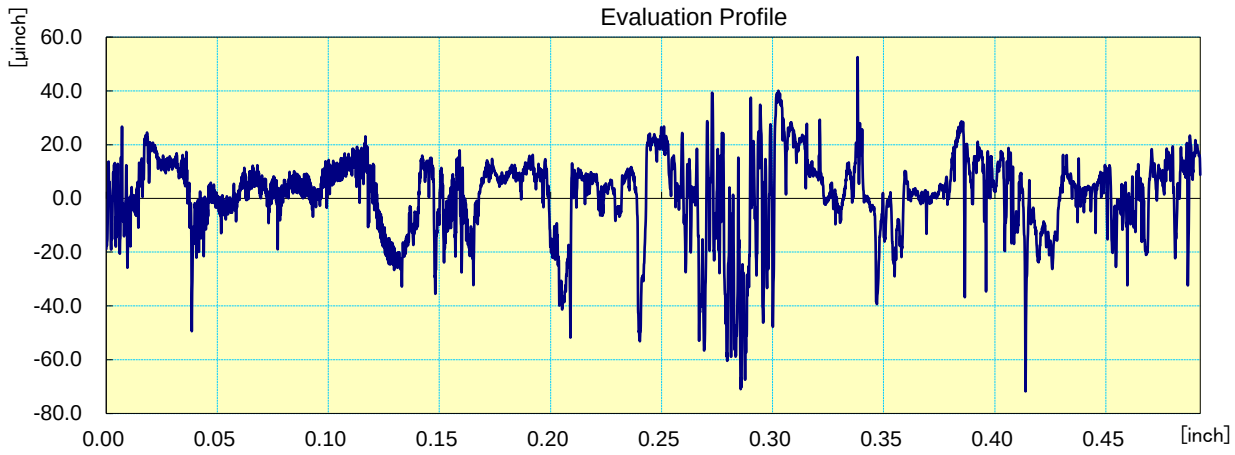


*Figure 5.20: Surface profile of AM cylinder head after engine testing (location 1)*

*Table 5.7: Cylinder head diameter data in mm for pre and post engine testing*

| | Before Testing | After Testing | Material Removed |
|---|---|---|---|
| **1 Top** | 1.0619 | 1.0641 | 0.0022 |
| **2 Top** | 1.0617 | 1.0641 | 0.0024 |
| **1 Middle** | 1.0635 | 1.0651 | 0.0016 |
| **2 Middle** | 1.0633 | 1.0647 | 0.0014 |
| **1 Bottom** | 1.0639 | 1.0640 | 0.0001 |
| **2 Bottom** | 1.0635 | 1.0644 | 0.0009 |

Figure 5.16 displays the cylinder head temperatures, with the general trend between the two speeds tested finding ACAH > ACS > SE. Here, the temperature measured is influenced by conduction; hence, the differences in conductivity between the cylinder heads will play a role. Since ACAH lacks an iron liner, it should dissipate heat more readily that would result in lower temperatures. This is balanced by an assumed greater level of late combustion in the dynamometer experiments that occurs closer to EVO; i.e., less time for heat transfer. In addition, the ACAH engine (mostly) experienced the lowest equivalence ratios that would result in the highest adiabatic flame temperatures. Furthermore, as discussed prior, the ACAH engine is

presumed to encounter more rubbing friction that would additionally increase cylinder head temperatures. As a result, multiple factors play a role in generating the indicated trend.

Crankcase temperatures follow a trend akin to the other temperatures, but again with less variation between the engines (Figure 5.17). This smaller variation is because the physical temperature measurement is further away from the combustion process and relies solely on conduction from the inside cylinder head to outside of the crankcase. To reiterate from earlier, when ranking the conductivity of these engines based on material composition: ACS would be the least conductive and the SE and ACAH would be relatively comparable since the absence of a liner in the ACAH would slightly offset its titanium crankcase. This aligns with the results of the SE since it experienced the lowest temperatures and it has the most conductive crankcase which is where the measurement is taken. In addition, the results show that ACAH experienced the highest temperatures, most likely due to the balance of factors discussed in the previous paragraph. Moreover, when comparing the temperatures here to the prop data at similar speeds in Table 5.2, the dyno results are all within 10 °C of their propeller counterparts (at 80% throttle) providing some consistency in the results between tests.

Finally, torque in Figure 5.18 provides an opposite trend from everything else with SE producing the highest torque followed by ACS and ACAH giving the smallest readings. Interestingly, the equivalence ratios for these engines had the same trend (Table 5.4 and Table 5.5) with ACAH having the lowest ratio and SE having the highest. This result is counter to engine trends typically found; i.e., smaller equivalence ratios that are closer to the adiabatic flame temperature (1.1) provide less fuel for cooling subsequently taking less energy away from the cylinder that results in higher torques. However, the late combustion hypothesis does align

with the results provided in Figure 18. With more energy going towards combustion in the exhaust, ACS and ACAH engines would have less energy respectively released inside of the cylinder. Therefore, with a smaller energy release, less torque would be produced. Moreover, even if the same amount of energy (or more) was released within the ACS and ACAH cylinders, it would have occurred at less-optimum crank angles (more towards EVO), which would also result in the lower torques produced. Finally, the lower torque found in the ACAH compared to the ACS is most likely a result of more energy going towards moving the piston against a larger frictional force.

## 5.4 **Conclusions**

Given that the goal of this endeavor was to prove that an additively manufactured engine could perform similarly to the OEM version, these results are promising. With better command of spark timing, valve lift, and valve timing adjustments, a more accurate representation of these engines could have been gathered and more readily compared. Moreover, with the added difficulty of having a carbureted engine, control of all variables was not achievable. When considering the additional variables introduced from reverse engineering, differing material compositions, and post machining, there is not enough evidence to point to the AM process specifically as the reason for differences in engine performance. It may even be the case that if a cylinder liner was used in AM head, the engines could have operated more similarly. Even so, the fully AM engine ran without failure (note: the stock connecting rod failures were presumed to be a function of the oversized dyno) for over 3.5 hours during all testing performed. Future work includes providing better methods for engine setup between part swaps, the inclusion of an in-cylinder pressure transducer, and an appropriately sized dyno.

# Chapter 6: Conclusion

## 6.1 **Summary of Work**

Currently, prototyping and tooling are the main focus of AM for IC engines applications in industry. However, within research, motorsport, and luxury vehicle applications, a larger percentage of actual parts are being manufactured, tested, and employed. With further development of the technology and improvement of design optimization methods, AM can continue to become a more economical and applicable technique for consumer applications. Hence, research in this area is critically important for advancement to persist. Therefore, this thesis strived to demonstrate the successful implementation of AM for an internal combustion engine. Thus, the importance of researching metal AM for IC engines has been demonstrated throughout this thesis. Not only can it help improve fuel economy in the consumer market by reducing weight, but its ability to manufacture at the point of need also makes it valuable for military applications. The primary goal of this work was to prove the ability of AM in producing major IC engine components and have them perform similarly to parts made using traditional methods. To achieve this overarching goal, five major objectives were identified within each chapter of this thesis. In the first chapter, the motivation behind these efforts are detailed, followed by full review of the literature and the current state of technology within industry/motorsport in the second. Chapter 3 presented a complete understanding of the engine, its manufacturing requirements, and the entire AM process that facilitated its production, including design, manufacture, and post processes. Building on this, Chapter 4 detailed the creation of the physical engine testing setup, along with sensor choices, and the development of

the data collection interface. This then allowed an analysis of both the traditional and AM engine testing results in Chapter 5, including comparisons of how they performed against each other.

For this research, a four-stroke Saito FG-11 engine was chosen due to its smaller, more cost-effective size, while maintaining mechanical similarities to a larger gasoline automotive engine. Thus, the cylinder head and crankcase, which comprise most of the weight of the engine, are targeted for AM using LPBF. The first step in the process was to reverse engineer the engine and identify its critical tolerance areas. After which, the subsequent models were tailored for the AM process by adding material for later machining, reducing stress concentrations, such as corners, and removing unnecessary geometry. Moreover, optimal part orientation for AM was determined by considering later support removal and unsupported overhanging areas that may cause poor surface finishes or distortions. Consequently, supports were then designed for areas with greater than 45° overhang, and the build layout established in order to produce a consistent powder distribution. After successful completion of the AM process, the parts were qualitatively analyzed for cracking, delamination, and surface roughness. Subsequently, CT analysis was performed to determine porosity and identify any potential defects before investing time and resources into post processing. Once quality was confirmed, post processing methods including heat treatments, machining, and honing procedures were executed. Finally, an additional set of CT scans were gathered to establish geometric similarities between the AM parts and their original counterparts.

Following the engine manufacturing process, a testing setup was created to obtain performance data which would allow for direct comparisons to be made. Due to difficulties encountered while connecting the engine and dyno, a propeller setup was used intermediately to

ensure some usable data was collected before risking further engine failures. After 11 iterations (including the propeller setup), a successful dyno setup was found, incorporating added cooling, vibrational damping, and a direct connection with a hytrel spider. When running on the dyno, a servomotor controlled the engine's intake, and a remote-control switch was used to turn the spark on and off. Additionally, temperatures (intake, exhaust, crankcase, and cylinder head), pressures (intake and exhaust), engine speed, mass flow rate of fuel, airflow, torque (dyno), and major parameters of interest were all measured during testing. Moreover, to control the engine and record sensor data, two LabVIEW programs were developed and ran concurrently. While developing the physical engine test setup, an understanding of how to readily achieve stable combustion was formed, and a safe and effective testing procedure was established. Additionally, a Matlab program was developed to streamline the post processing of the collected data.

Consequently, the test results revealed that the AM engine did not perform as well as the stock engine, with propeller testing results indicating lower overall engine speed, and dyno testing revealing lower torques produced. Looking at all the data collected, primarily temperatures, it was postulated that the lower performance was caused by increased internal frictions between the piston ring and the AM cylinder wall. Later measurements of the AM cylinder wall surface and diameter confirmed this hypothesis, demonstrating that engine self-clearanced during operation and removed the protective/lubricating honed surface. Other factors potentially influencing the differences in engine performances include slight variations of valve timing, valve lift, and spark timing. Although the AM engine experienced diminished performance when compared to the OEM, the main goal was to prove that AM can be used

successfully for major IC engine components, which was accomplished. In fact, the fully AM engine ran for over 3.5 hours through all the testing performed, indicating the resilience/effectiveness of the engine and thus further validating the worth of this work.

## 6.2 **Future Work**

The most immediate goal in continuing this research is the development of three-dimensional simulations to verify the engine's performance against theoretical calculations. These simulations will then be used to guide the exploration of design modifications, including the implementation of topology optimization, and part reductions to better demonstrate the unique designs that AM can facilitate. With such design improvements, better post processing is also achievable given that the entire process was documented within this thesis, allowing for the avoidance of the problems encountered. Furthermore, based on the experimental difficulty encountered in this work, care should be taken to improve future comparative testing; specifically, the development of strict procedures for part swaps to limit variation. Lastly, there are two major objectives moving forward regarding the testing setup and data collection. These include the development of an appropriately sized dyno and the inclusion of an in-cylinder pressure transducer, providing data for better analysis of engine performance, and ultimately, more concrete conclusions. Thus, the work presented in this thesis provides a foundation to further the advancement of research for AM in IC engines.

## References


1. *Use of Energy in the United States Explained*. Energy Use for Transportation 2018; Available from: https://www.eia.gov/energyexplained/?page=us_energy_transportation.

2. Davis, S.C., S.W. Diegel, and R.G. Boundy, *Transportation energy data book.* 2009.

3. Pagerit, S., P. Sharer, and A. Rousseau, *Fuel Economy Sensitivity to Vehicle Mass for Advanced Vehicle Powertrains*. 2006, SAE International.

4. Anrico Casadei, R.B., *Impact of Vehicle Weight Reduction on Fuel Economy for Various Vehicle Architectures*. 2007, Ricardo: The Aluminum Association.

5. *Technologies and Approaches to Reducing the Fuel Consumption of Medium- and Heavy-Duty Vehicles (2010)*, ed. N.R. Council. 2010, Washington, DC: The National Academies Press.

6. *Volkswagen AG*. in *Proceedings on the International Conference on Innovative Developments for Lightweight Vehicle Structures*. 2009. Wolfsburg, Germany.

7. Beste, F., W. Schoffmann, and R. Marquard, *Lightweight design~A challenge for modern passenger car engines*. 2000, Society of Automotive Engineers of Korea.

8. Tharumarajah, A. and P. Koltun, *Is there an environmental advantage of using magnesium components for light-weighting cars?* Journal of Cleaner Production, 2007. **15**(11): p. 1007-1013.

9. Luo, A.A., *Magnesium: Current and potential automotive applications.* JOM, 2002. **54**(2): p. 42-48.

10. Gibson, I., D.W. Rosen, and B. Stucker, *Additive manufacturing technologies*. Vol. 17. 2014: Springer.

11. *Additive Manufacturing Opportunities In Automotive - 2018*. 2018, SmarTech Analysis.

12. *Compressing the Design Cycle at Ducati*. 2016, Stratasys.

13. Goldsberry, C. *Ford 3D-printed auto parts save millions, boost quality*. 2014 2014-02-14 5/25/18]; Available from: https://www.plasticstoday.com/content/ford-3d-printed-auto-parts-save-millions-boost-quality/97214356120060.

14. Haba, S.A. and G. Oancea, *Digital manufacturing of air-cooled single-cylinder engine block.* The International Journal of Advanced Manufacturing Technology, 2015. **80**(5): p. 747-759.

15. Guarato, A.Z., E.M. Ticona, and S.L. Braga, *Development of a flex-fuel rotary engine with variable compression ratio*. 2016, SAE International.

16. Han, T., H. Zhen, and G. Mainelis, *Evaluation of Electrostatic Screen Battery for Emissions Control (ESBEC) with Diesel Emissions*. 2016, SAE International.

17. Agarwal, A., et al., *Design and Development of a Restricted Intake Manifold for a Naturally Aspirated Four Cylinder SI Engine*. 2018, SAE International.

18. Moura, T.M., M.R. Cavaglieri, and R.G. Santos, *Pressure Drop on Rapid Prototyping and Final Product Intake Manifolds*. 2009, SAE International.

19. Müller, B., et al. *Laser Beam Melting for Tooling Applications – New Perspectives for Resource-Efficient Metal Forming and Die Casting Processes*. 2013. Berlin, Heidelberg: Springer Berlin Heidelberg.

20. Maki, C., et al., *MMLV: Aluminum Cylinder Block with Bulkhead Inserts and Aluminum Alloy Connecting Rod*. 2015, SAE International.

21. Rochussen, J., et al., *Development of a Research-Oriented Cylinder Head with Modular Injector Mounting and Access for Multiple In-Cylinder Diagnostics*. 2017, SAE International.

22. Conner, B.P., et al., *Making sense of 3-D printing: Creating a map of additive manufacturing products and services.* Additive Manufacturing, 2014. **1-4**: p. 64-76.

23. Agapovichev, A., A. Balaykin, and V.G. Smelov, *Production Technology of the Internal Combustion Engine Crankcase Using Additive Technologies.* Modern Applied Science, 2015. **9**.

24. Gebhardt, A., *Rapid Prototyping–Rapid Tooling–Rapid Manufacturing.* Carl Hanser, München, 2007.

25. A. Rosochowski, A.M., *Rapid tooling: the state of the art.* Journal of Materials Processing Technology 2000. **106**: p. 191-198.

26. Bassoli, E., et al., *3D printing technique applied to rapid casting.* Rapid Prototyping Journal, 2007. **13**(3): p. 148-155.

27. Papyrin, A., et al., *Cold spray technology*. 2006: Elsevier.

28. Ford, S. and M. Despeisse, *Additive manufacturing and sustainability: an exploratory study of the advantages and challenges.* Journal of Cleaner Production, 2016. **137**: p. 1573-1587.

29. Wilson, J.M., et al., *Remanufacturing of turbine blades by laser direct deposition with its energy and environmental impact analysis.* Journal of Cleaner Production, 2014. **80**: p. 170-178.

30. Patki, A.A., *Design for Remanufacturing: The Requirement for Today and Tomorrow*. 2016, SAE International.

31. Suzuki, K., *A homogenization method for shape and topology optimization.* Computer Methods in Applied Mechanics and Engineering. **93**(3): p. 291-318.

32. Marchesi, T.R., et al., *Topologically Optimized Diesel Engine Support Manufactured with Additive Manufacturing.* IFAC-PapersOnLine, 2015. **48**(3): p. 2333-2338.

33. Barbieri, S.G., et al., *Design of an Additive Manufactured Steel Piston for a High Performance Engine: Developing of a Numerical Methodology Based on Topology Optimization Techniques*. 2018, SAE International.

34. Reyes Belmonte, M.A., et al., *Improving Heat Transfer and Reducing Mass in a Gasoline Piston Using Additive Manufacturing*. 2015, SAE International.

35. Hopf, A., et al., *CFD Topology and Shape Optimization for Port Development of Integrated Exhaust Manifolds*. 2017, SAE International.

36. Myriam Orquéra, S.C., Dominique Millet, *Design for additive manufacturingmethodfora mechanicalsystem downsizing.* Elsevier: Procedia CIRP, 2017. **60**: p. 223-228.

37. Ilardo, R. and C.B. Williams, *Design and manufacture of a Formula SAE intake system using fused deposition modeling and fiber-reinforced composite materials.* Rapid Prototyping Journal, 2010. **16**(3): p. 174-179.

38. Johnson, M.V. and S. Scott Goldsborough, *A Small-Scale Flow Rig for Swirl Studies of a Single-Valve, Reverse Uniflow 2S Engine*. 2008, SAE International.

39. Schlier, L., et al., *Macro-Cellular Silicon carbide Reactors for Nonstationary Combustion Under Piston Engine-Like Conditions.* International Journal of Applied Ceramic Technology, 2011. **8**(5): p. 1237-1245.

40. Giorgio Baudana, S.B., Burghardt Klöden, *Electron Beam Melting of Ti-48Al-2Nb-0.7Cr-0.3Si: Feasibility investigation.* Intermatiallics, 2016. **73**: p. 43-49.

41. Kass, M.D., et al., *Experimental Evaluation of a 4-cc Glow-Ignition Single-Cylinder Two-Stroke Engine*. 2014, SAE International.

42. Cooper, D., et al., *Design and manufacture of high performance hollow engine valves by Additive Layer Manufacturing.* Materials & Design, 2015. **69**: p. 44-55.

43. Corporate, R.T., *Renault Trucks Corporate - Press releases : Metal 3D printing: technology of the future for lighter and more compact engines*. 2017, Renault Trucks Corporate.

44. *Fully functional AM automotive cylinder block produced for Volkswagen*. 2016 2016-10-18 [cited 2018; Available from: http://www.metal-am.com/fully-functional-additively-manufactured-automotive-cylinder-block-produced-volkswagen/.

45. *Volkswagen identifies key areas for metal Additive Manufacturing in automotive applications*. 2018 2018-01-09 [cited 2018; Available from: http://www.metal-am.com/volkswagen-identifies-key-areas-metal-additive-manufacturing-automotive-applications/.

46. Fuges, C.M., *Roush Uses Engine Cylinder Head to Prove Out Additive Manufacturing*, in *Additive Manufacturing*. 2018, Gardner Business Media, Inc. : https://www.additivemanufacturing.media.

47. *Koenigsegg One:1 World's First Mega Car*. 2019 [cited 2019.

48. *Studio System™ for rapid prototyping: Virginia-based startup finds opportunity to reduce product development timeline by 25%.* in *Studio System™ Case study*. 2018, Lumenium & Desktop Metal.

49. *Fast! Direct components in vehicle construction.* 2017, ConceptLaser a GE Additive Company: www.concept-laser.de.

50. Defense, D.o., *DEPARTMENT OF DEFENSE HANDBOOK MIL-HDBK-5*, in *METALLIC MATERIALS AND ELEMENTS FOR AEROSPACE VEHICLE STRUCTURES*. 2003.

51. Wu, G.Q., et al., *Effect of microstructure on the fatigue properties of Ti–6Al–4V titanium alloys.* Materials & Design, 2013. **46**: p. 668-674.

52. Management, M.G.M.a.S.C., *Alloy Data: Aluminum Die Casting Alloys*. http://www.mesinc.net/wp-content/uploads/2015/05/Die-Casting-Aluminum-Selection-Guide.pdf.

53. Stockman, T., et al. *In-Space Manufacturing Baseline Property Development*. in *TMS 2016 145th Annual Meeting & Exhibition*. 2016. Springer.

54. William D. Callister, J.a.D.G.R., *Materials Science and Engineering An Introduction*. 9 ed. 2014: Wiley.

55. ToolBox, E., *Thin Circular Ring - Temperature and Expanding Radius*. 2010: EngineeringToolBox.com.

56. Carley, L., *Cylinder Bore Surface Finishes*, in *Engine Builder*. 2000, Babcox.

57. Company, F.M., *Engine Design: Cylinder Block, Heads, and Gaskets (ED 207)* in *EEC-IV Technical Education*. 1990, Ford Motor Company.

58. Depcik, C., *ME 636 Course notes, University of Kansas*.

59. Systems, D., *Direct Metal Printers Specification Sheet*. 2018.

60. Carley, L., *Align Yourself*, in *Engine Builder*. 2003, Babcox.

61. Neale, M.J., *Bearings a Tribology Handbook*. 1993: Society of Automotive Engineers, Inc.

62. Technical, A.E., *Service Engineering Bulletin: Interferance Fit of Valve Guides*, A.E. Technical, Editor.

63. SAE, *Surface Vehicle Information Report*, in *Valve Guide Information Report*. 2017.

64. Carver, A., *Getting A "Good Seat" : The Growth In The Valve Seat Insert Market*, in *Engine Builder*. 1997, Babcox.

65. Prashanth, K.G., et al., *Is the energy density a reliable parameter for materials synthesis by selective laser melting?* Materials Research Letters, 2017. **5**(6): p. 386-390.

66. Scipioni Bertoli, U., et al., *On the limitations of Volumetric Energy Density as a design parameter for Selective Laser Melting.* Materials & Design, 2017. **113**: p. 331-340.

67. Zaeh, M.F. and G. Branner, *Investigations on residual stresses and deformations in selective laser melting.* Production Engineering, 2010. **4**(1): p. 35-45.

68. Schey, J.A., *Introduction to Manufacturing Processes*. 3 ed. 2000: McGraw-Hill.

69. Sietins, J.M., *X-ray Computed Tomography Quantitative Analysis: An Introductory Software Guide for DataViewer and CTAn*. 2018, US Army Research Lab: US Army Research Lab.

70. Mayer, H., et al., *Influence of porosity on the fatigue limit of die cast magnesium and aluminium alloys.* International Journal of Fatigue, 2003. **25**(3): p. 245-256.

71. Major, J., *Porosity control and fatigue behavior in A356-T61 aluminum alloy.* Transactions-American Foundrymens Society, 1998: p. 901-906.

72. Edwards, P., A. O'Conner, and M. Ramulu, *Electron Beam Additive Manufacturing of Titanium Components: Properties and Performance.* Journal of Manufacturing Science and Engineering, 2013. **135**(6): p. 061016-061016-7.

73. Hibbeler, R.C., *Mechanics of Materials*. 9 ed. 2014, Pearson Prentice Hall.

74. Nunes, R.M., *ASM Handbook*. Vol. Volume 4 Heat Treating. 1991.

75. Favor, R.A.W.R.J., *Titanium Alloy Handbook*. Report MCIC-HB-02 ed. 1972, Columbus: Battelle Memorial Institute.

76. Zhou, L., *Microstructure and tensile property of a novel AlZnMgScZr alloy additively manufactured by gas atomization and laser powder bed fusion.* Elsevier, 2018.

77. Pepi, M., *Towards replacement of failed parts on the battlefield via metal casting in 3D printed desert sand molds*, in *Society For Machinery Failure Prevention Conference*. 2019, Army Research Lab: King of Prussia, PA.

78. *Precision Honing Supplies*, Sunnen, Editor. 2012. p. 2.66, 12.3 & 12.4.

79. Saito, *Saito FG-11 4-Stroke Gasoline Single Engine Opperating Instructions*, Saito, Editor.: https://www.horizonhobby.com/pdf/SAIEG11-Manual.pdf.

80. Langness, C., M. Mangus, and C. Depcik, *Construction, Instrumentation, and Implementation of a Low Cost, Single-Cylinder Compression Ignition Engine Test Cell*. 2014, SAE International.

81. Lee, J.A., *Cast aluminum alloy for high temperature applications.* 2003.

82. Ragone, J.C., *Emission Reduction and Assisted Combustion Strategies for Compression Ignition Engines with Subsequent Testing on a Single-Cylinder Engine* in *Mechanical Engineering*. 2012, University of Kansas.

83. Press, N.T.a.S., *NI myRIO: "Servo demo" LabVIEW project*. 2014, National Instraments.

84. *Honeywell ZephyrTM Digital Airflow Sensors*. 2018: Honeywell

85. *Lossless Communication with Network Streams: Components, Architecture, and Performance*, in *White Papers*. 2019, National Instruments.

86. *Lossless Communication with Network Streams: Components, Architecture, and Performance*. 2019, National Instraments.

87. Saito, *Saito FG-11 4-Stroke Gasoline Single Engine Opperating Instructions*, Saito, Editor.: https://www.horizonhobby.com/pdf/SAIEG11-Manual.pdf.

88. Morrison, F.A., *Obtaining Uncertainty Measures on Slope and Intercept of a Least Squares Fit with Excel's LINEST*. Michigan Technological University: Houghton, MI 39931.

89. Beasley, R.S.F.D.E., *Theory and Design for Mechanical Measurements*. 2011: John Wiley & Sons, Inc.

90. Sandoval, D. and J.B. Heywood, *An Improved Friction Model for Spark-Ignition Engines*. 2003, SAE International.

91. Ju, Y. and K. Maruta, *Microscale combustion: technology development and fundamental research.* Progress in energy and combustion science, 2011. **37**(6): p. 669-715.

92. Bridgeport, *Intallation, Operation, Matenance and Parts List* Bridgeport, Editor.: http://www.truetex.com/bridgeport-manual.pdf.

93. in *CHEMICAL AND PHYSICAL INFORMATION FOR GASOLINE*. 1989, Center for Disease Control: Agency for Toxic Substances and Disease Registry.

94. ALLAN, T., F. KIRKPATRICK, and R. COLIN, *Internal combustion engines: applied thermosciences*. 2000: JOHN WILEY.

95. James N. Carroll, I.A.K., Lawrence R. Smith, Eric Fujita, and Barbara Zielinska, *Collaborative Lubricating Oil Study on Emissions* 2011, National Renewable Energy Laboratory. p. 13.

96. Pivsa-Art, N.P.a.S., *Prototype Co-Pyrolysis of Used Lubricant Oil and Mixed Plastic Waste to Produce a Diesel-Like Fuel.* Energies, 2018. **2973**

# Appendices

## Appendix A: Engine Information

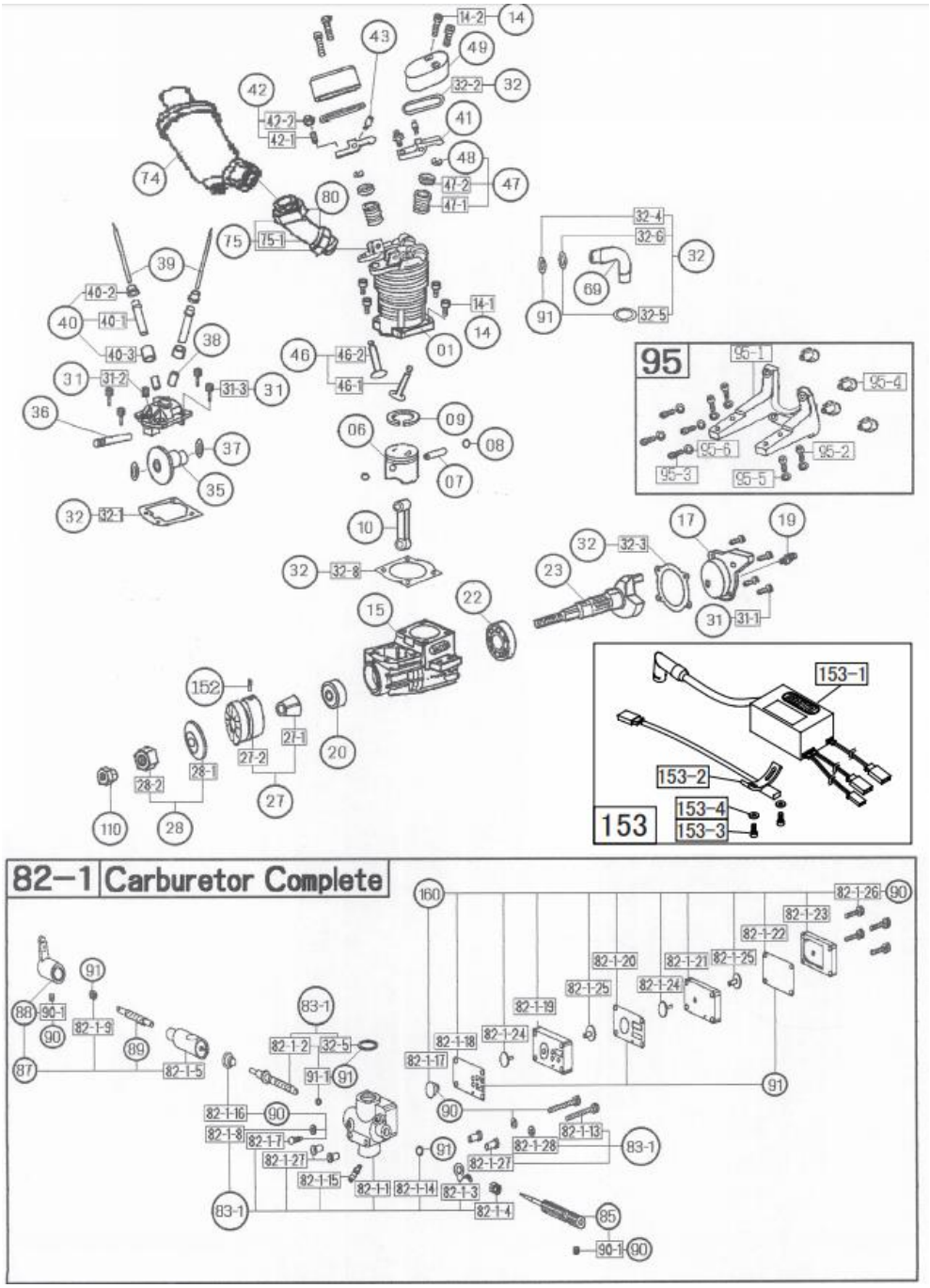


*Figure A.1: Exploded view of Saito FG-11 engine [87]*

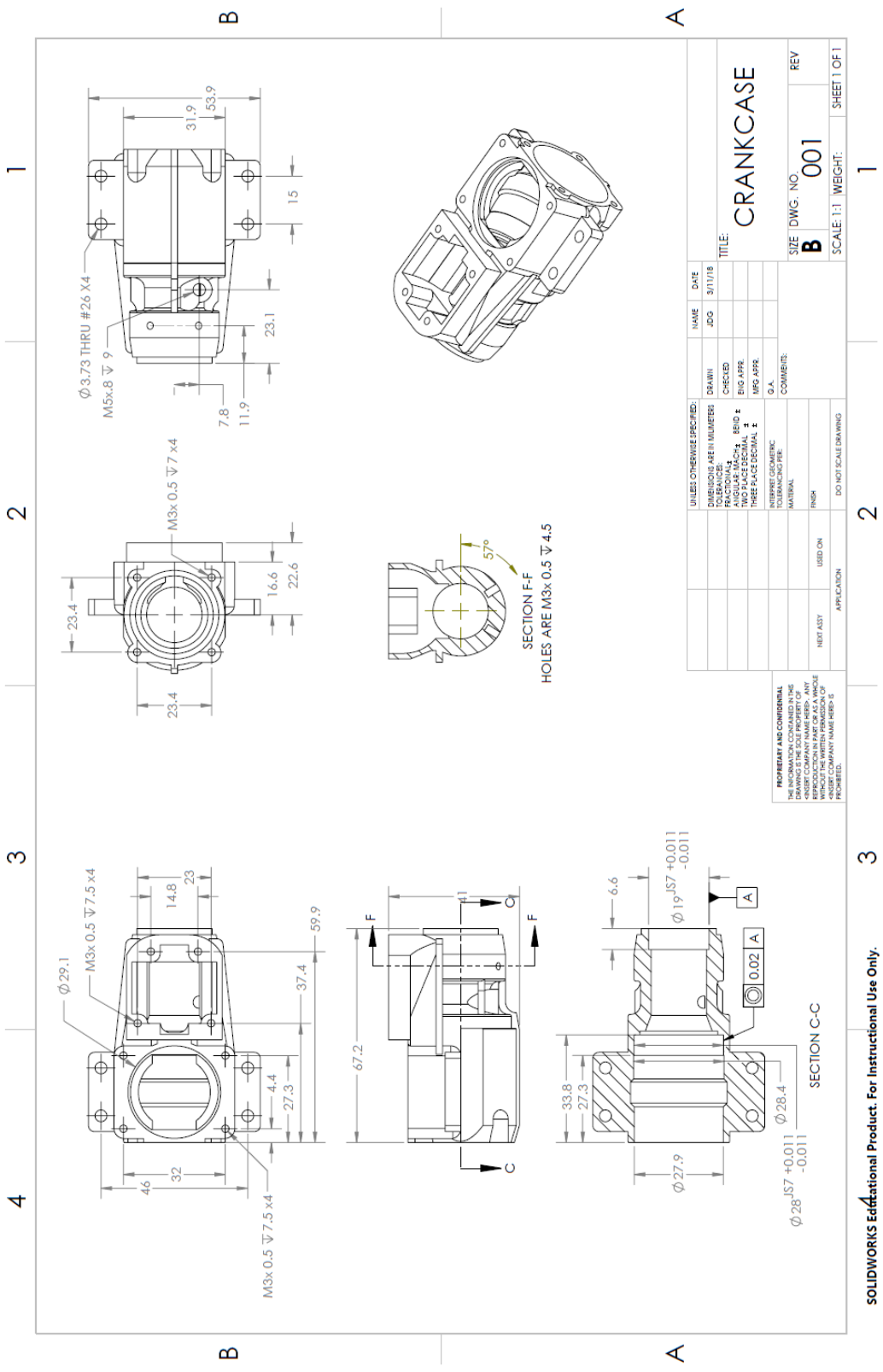


*Figure A.2: Solidworks drawing of crankcase*

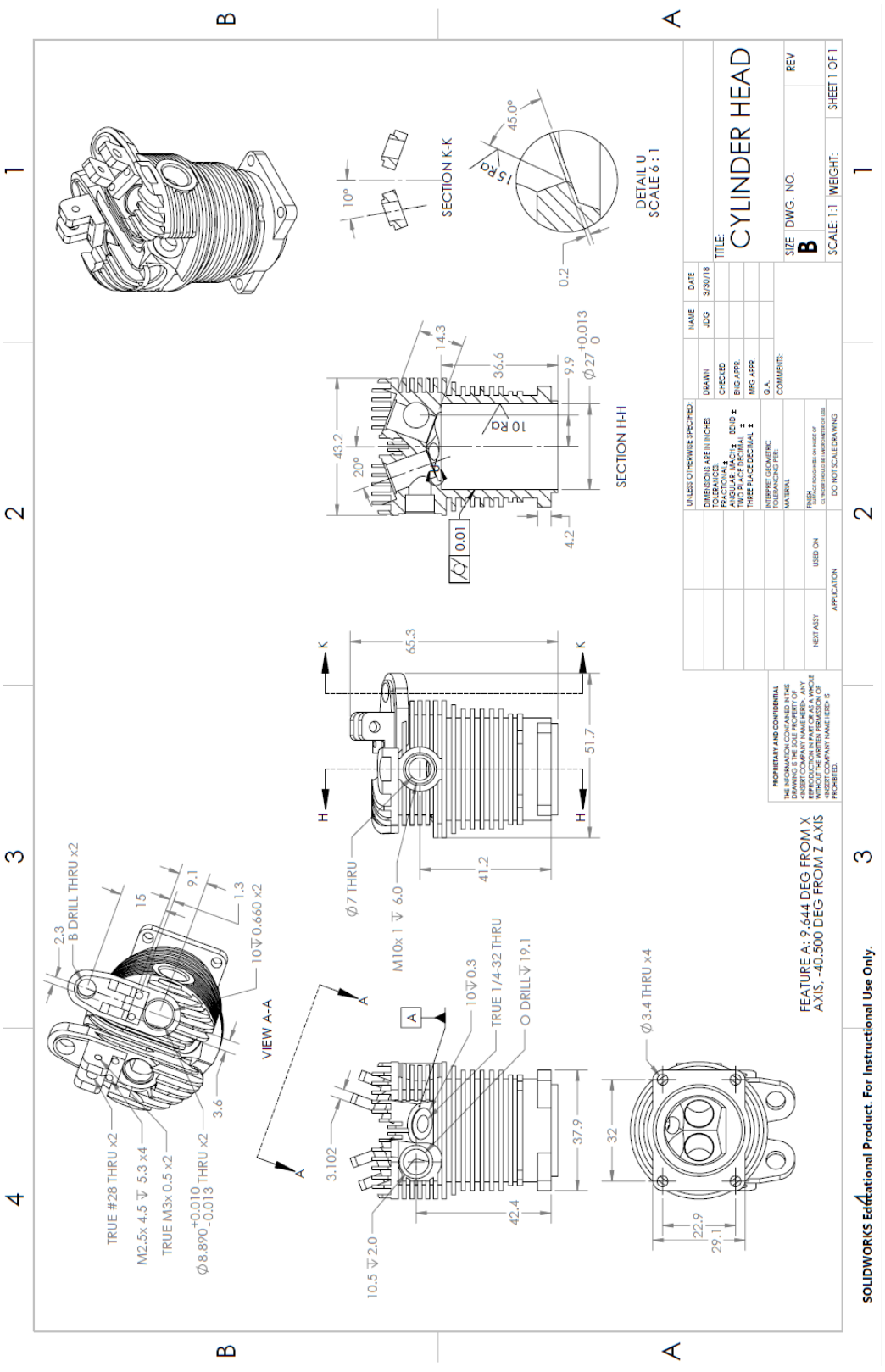


*Figure A.3: Solidworks drawing of cylinder head*

*Table A.1: Additive manufacturing vs. die casting*

| | Additive Manufacturing | Die Casting (Al) |
|---|---|---|
| **Costs** | •Upfront: The machine<br>•Continuous: Powder, maintenance<br>•**<u>Less expensive & faster</u> than die casting when part quantity is low** | •Upfront: purchasing die casting machine, creating the dies<br>•Continuous: cost of metal, storage for dies |
| **Limitations** | •Technology in development<br>•Can require heat treatment, & post machining<br>•Not able to produce high volumes quickly<br>•Some materials are difficult to AM | •Cooling parts uniformly is more difficult<br>•Can require heat treatment, & post machining<br>•Some materials are difficult to die cast |
| **Advantages** | •Room for improvement→ reduced costs in future<br>•Better control of heat & material structure<br>•More room for material development<br>•Less design constraints | •High repeatability<br>•Cheaper for a large production scale<br>•Fully established manufacturing process<br>•More materials readily available<br>•Smoother & more consistent finishes |
| **Tolerances** | ProX 320 & 300: ± 0.1-0.2% with ± 0.002” minimum [59] | Basic: ± 0.010” [74]<br>Critical: ± 0.004” |
| **Build Volume** | ProX 320: 9.84 × 9.84 × 12.01 in<br>ProX 300: 10.82 × 10.82 × 14.96 in [59] | **Flexible to application** |
| **Min. Wall Thickness** | ProX 300 & 320: 0.004” × 0.004” × 0.001” [59] | 0.32”- 0.70” depending on size [74] |

## Appendix B: Surface Roughness and Hardness Data

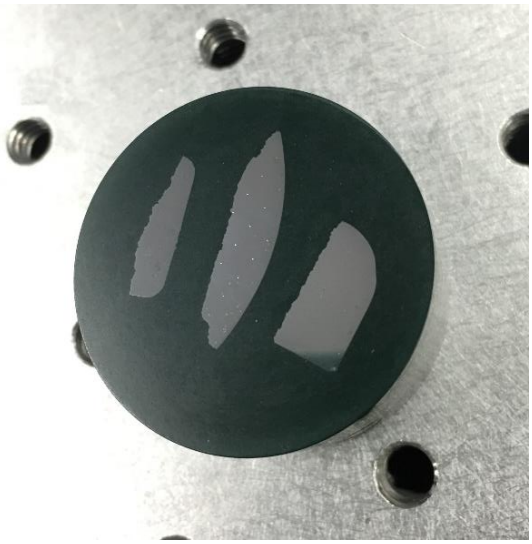

*Figure B.1: Cylinder head broken fins used as a test specimen, polished to 1 µm*

Date: 16-07-2018
Tester: Operator
Program: JKTS_Hardness Mapping
Job: Test job # 33

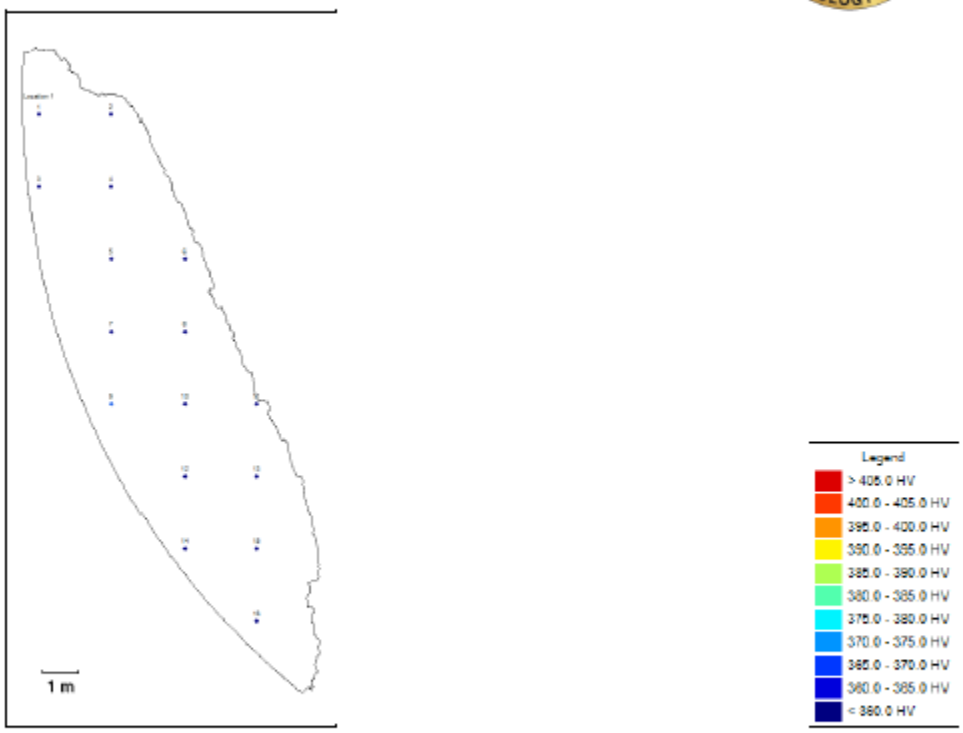


Location 1

| Mean | Mean - minimum | Mean - maximum | Mean - (min/max) | Minimum |
|---|---|---|---|---|
| 105.1 | 105.9 | 104.3 | 105.0 | 96.0 |
| **Maximum** | **Range** | **Std. deviation** | | |
| 117.3 | 22.3 | 5.9 | | |

*Figure B.2: Vickers hardness test result - printout page 1*

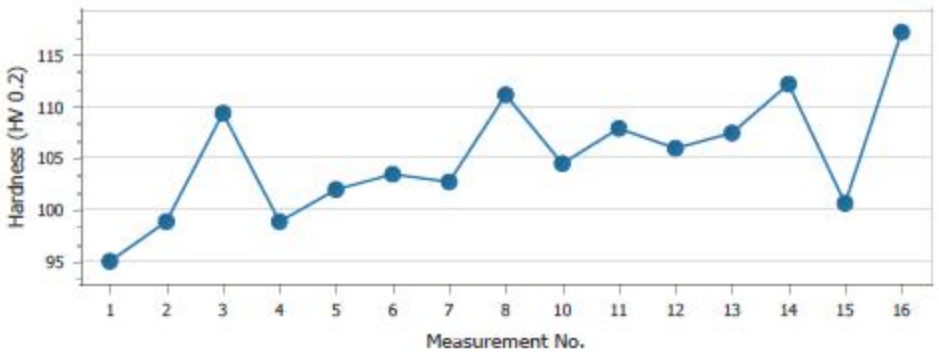


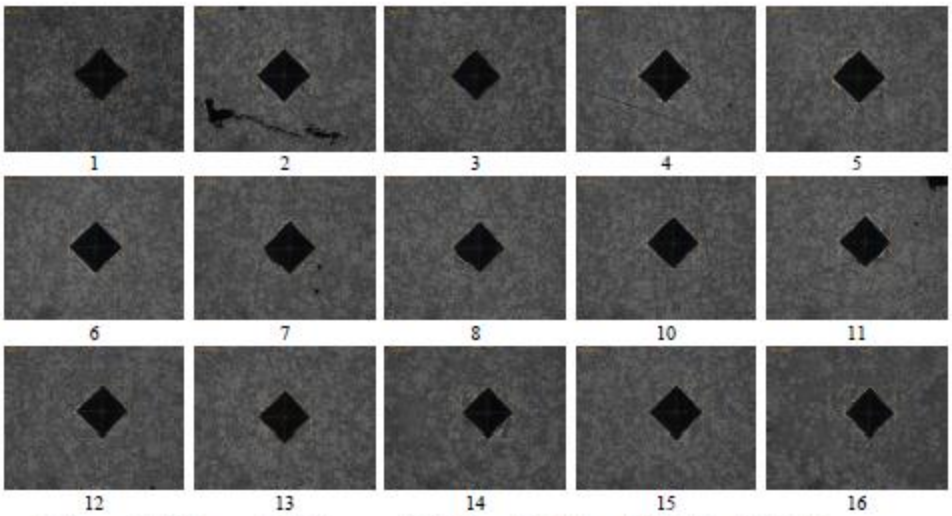


| Point | Distance | Hardness | Converted | Diagonal X | Diagonal Y | Comments |
|---|---|---|---|---|---|---|
| 1 | - | 95.0 HV 0.2 | - | 63.2 µm | 61.8 µm | |
| 2 | - | 98.9 HV 0.2 | - | 61.6 µm | 61.0 µm | |
| 3 | - | 109.4 HV 0.2 | - | 58.0 µm | 58.6 µm | |
| 4 | - | 98.9 HV 0.2 | - | 60.9 µm | 61.6 µm | |
| 5 | - | 102.0 HV 0.2 | - | 60.6 µm | 60.2 µm | |
| 6 | - | 103.4 HV 0.2 | - | 60.2 µm | 59.6 µm | |
| 7 | - | 102.6 HV 0.2 | - | 60.1 µm | 60.1 µm | |
| 8 | - | 111.1 HV 0.2 | - | 57.8 µm | 57.7 µm | |
| 9 | - | Deleted | - | - | - | |
| 10 | - | 104.6 HV 0.2 | - | 59.8 µm | 59.3 µm | |
| 11 | - | 107.9 HV 0.2 | - | 58.8 µm | 58.6 µm | |
| 12 | - | 106.0 HV 0.2 | - | 59.2 µm | 59.1 µm | |
| 13 | - | 107.6 HV 0.2 | - | 59.0 µm | 58.6 µm | |
| 14 | - | 112.2 HV 0.2 | - | 58.2 µm | 56.8 µm | |
| 15 | - | 100.6 HV 0.2 | - | 60.7 µm | 60.8 µm | |
| 16 | - | 117.3 HV 0.2 | - | 56.6 µm | 56.0 µm | |

PROPRIETARY RIGHTS NOTICE This document and information that it contains are the property of Buehler. Rights to duplicate or otherwise copy this document and rights to disclose the document and such information to others and the right to use the information contained threin may be acquired by written permission signed by a duly authorized officer of Buehler.

*Figure B.3: Vickers hardness test result - printout page 2*

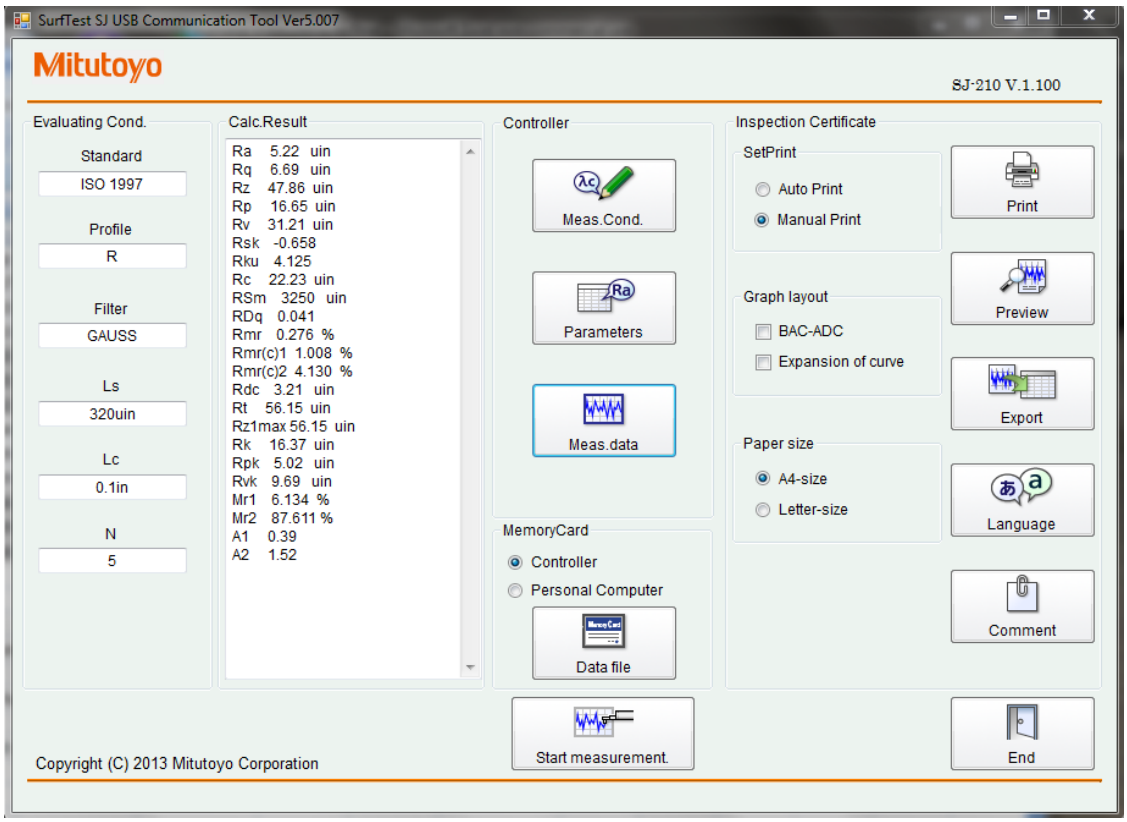


*Figure B.4: SurfTest SJ USB Communication Tool Ver5.007 GUI*

*Table B.1: Roughness value comparisons of un-machined die cast and AM materials*

| Value | Description | Unit | Die Cast | AM Ti64 | AM AlSi12 |
|---|---|---|---|---|---|
| **Ra** | Roughness Average | µin | 86.62 | 294.02 | 876.62 |
| **Rq** | RMS Roughness | µin | 109.12 | 363.05 | 1088.55 |
| **Rz** | Average Maximum Height of the Profile | µin | 572.54 | 1737.70 | 4934.08 |
| **Rp** | Maximum Profile Peak Height | µin | 257.35 | 912.32 | 2562.18 |
| **Rv** | Maximum Profile Valley Depth | µin | 315.18 | 825.41 | 2371.88 |
| **Rsk** | Skewness (Asymetry of Profile) | | -0.17 | 0.20 | 0.18 |
| **Rkµ** | Kurtosis (Peakedness of Profile) | | 3.12 | 2.76 | 2.77 |
| **Rt** | Maximum Height of the Profile | µin | 749.13 | 2296.00 | 6541.98 |
| **Rk** | Core Roughness | µin | 276.39 | 962.68 | 2812.73 |
| **Rpk** | Reduced Peak Height | µin | 95.16 | 429.70 | 1425.33 |
| **Rvk** | Reduced Valley Depth | µin | 139.76 | 280.37 | 848.12 |
| **Mr1** | Peak Material Ratio | % | 8.98 | 12.02 | 11.31 |
| **Mr2** | Valley Material Ratio | % | 89.29 | 92.51 | 92.60 |

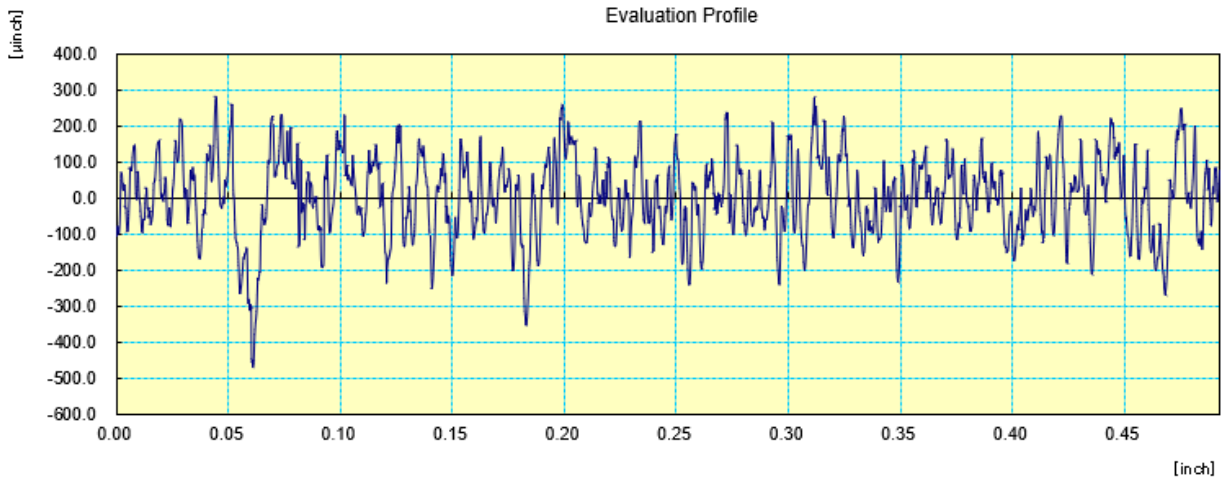


*Figure B.5: Surface profile of un-machined die cast material*

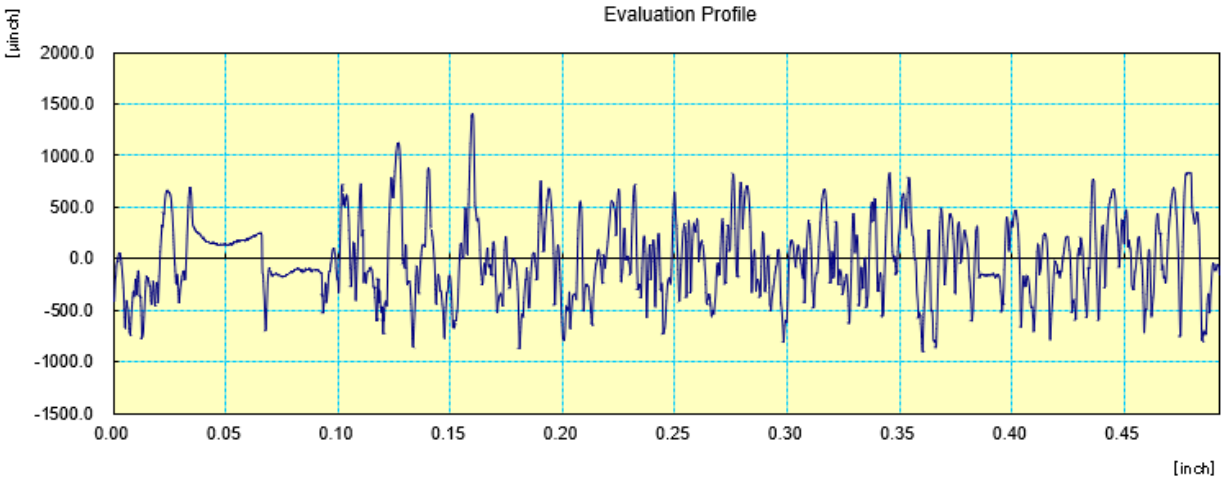


*Figure B.6: Surface profile of un-machined AM Ti64 (crankcase)*

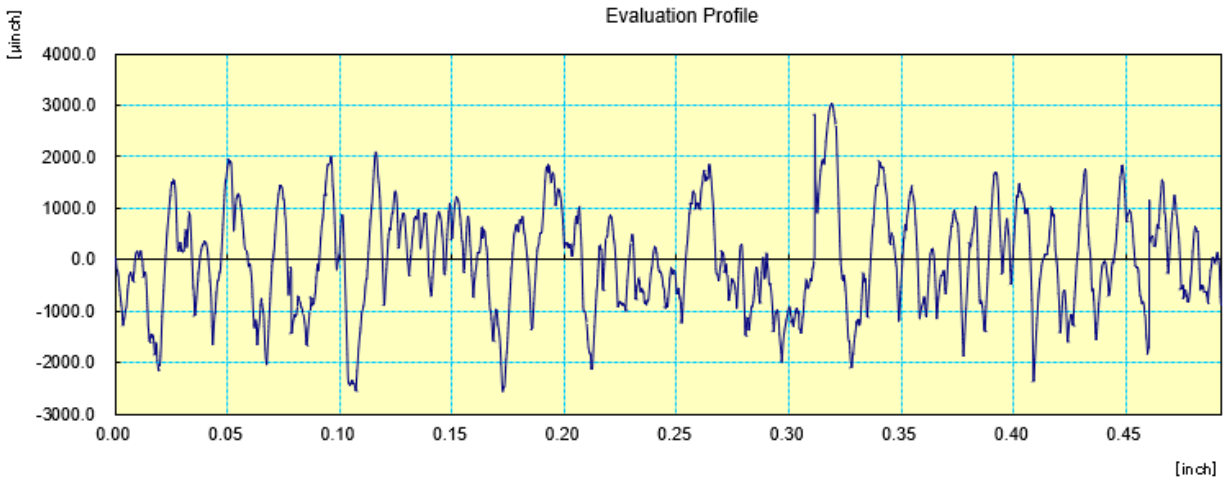


*Figure B.7: Surface profile of un-machined AM AlSi12 (cylinder head)*

## Appendix C: Porosity Data

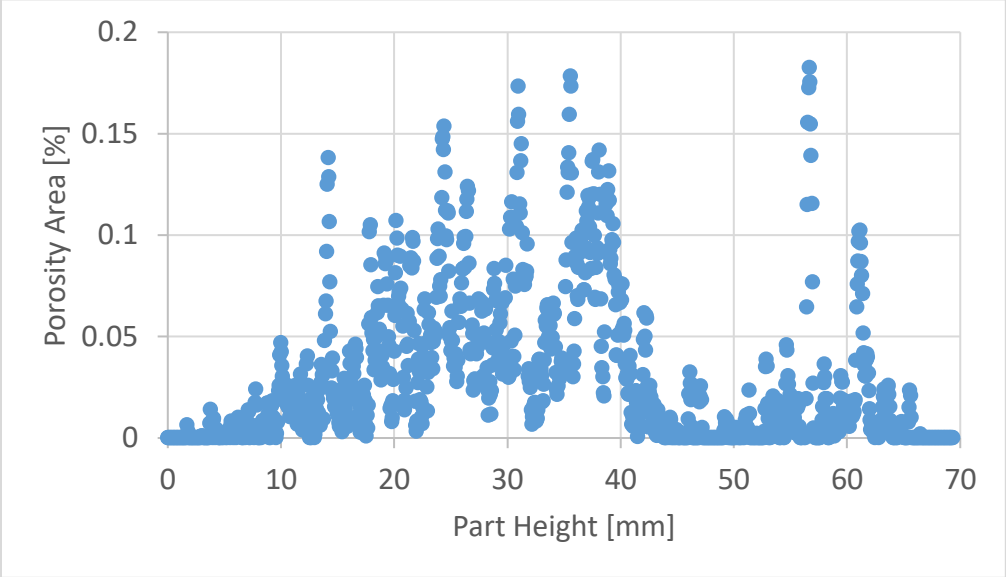


*Figure C.1: Porosity area percentage with height of die cast crankcase*

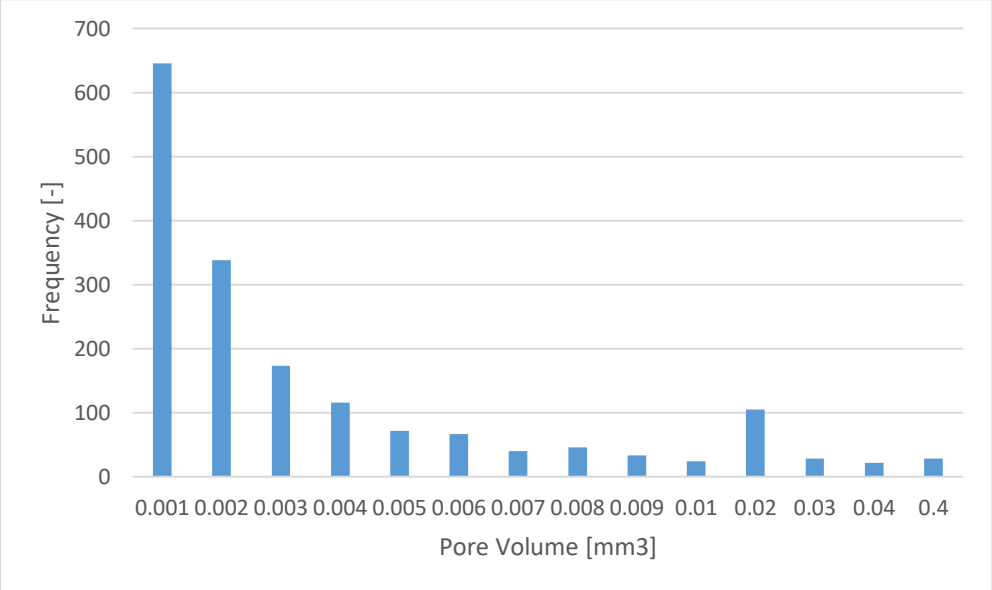


*Figure C.2: Pore size and frequency of die cast crankcase*

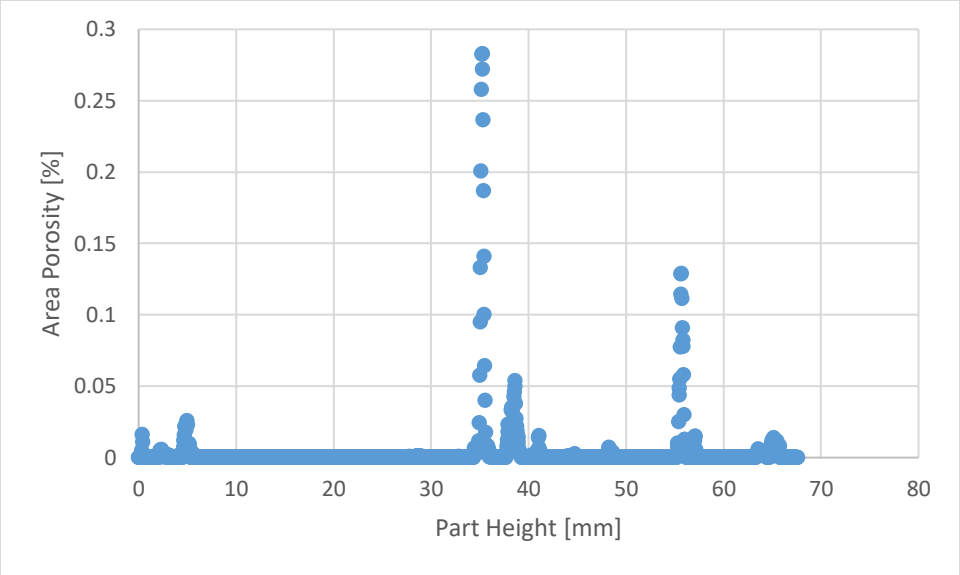


*Figure C.3: Porosity area percentage with height of AM crankcase 1 (original design)*

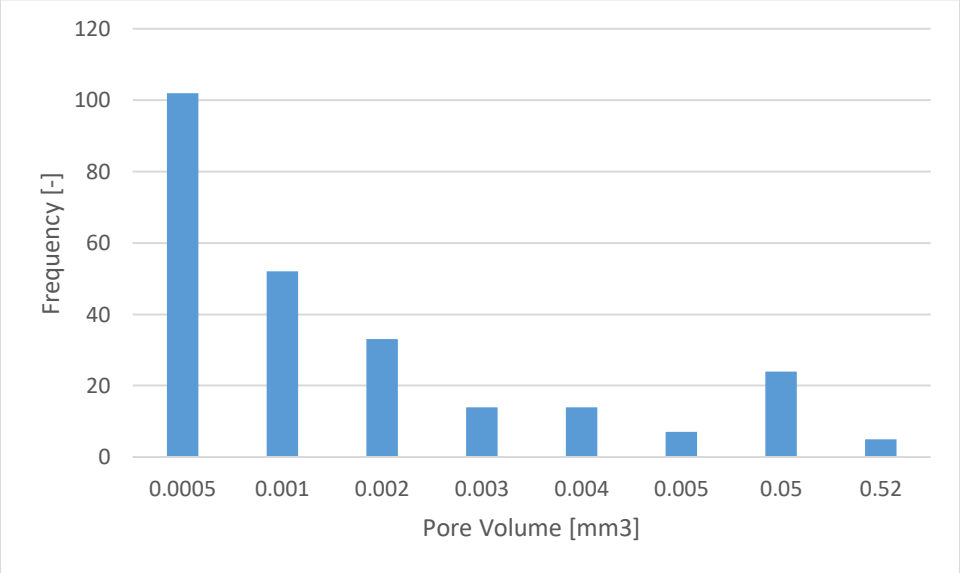


*Figure C.4: Pore size and frequency of AM crankcase 1 (original design)*

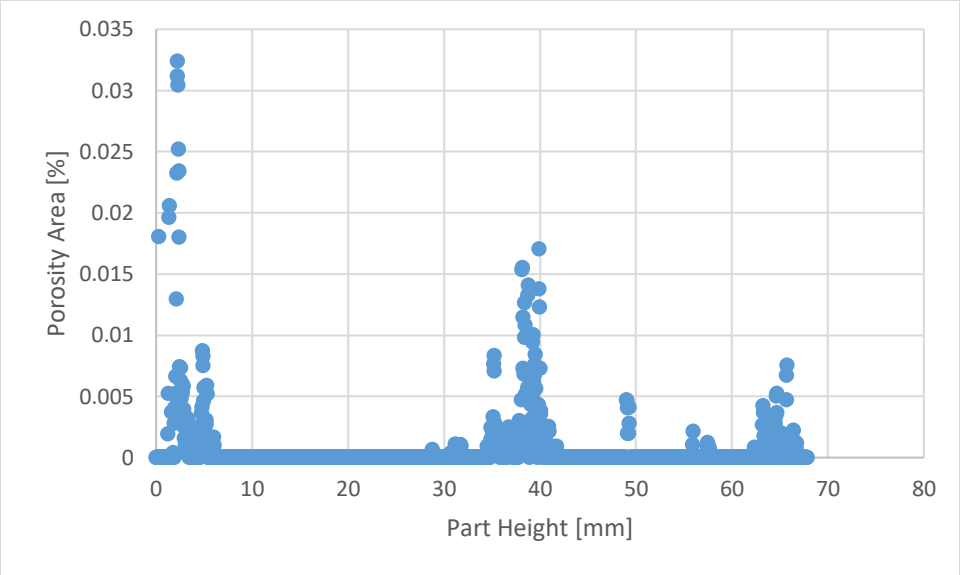


*Figure C.5: Porosity area percentage with height of AM crankcase 4 (original design)*

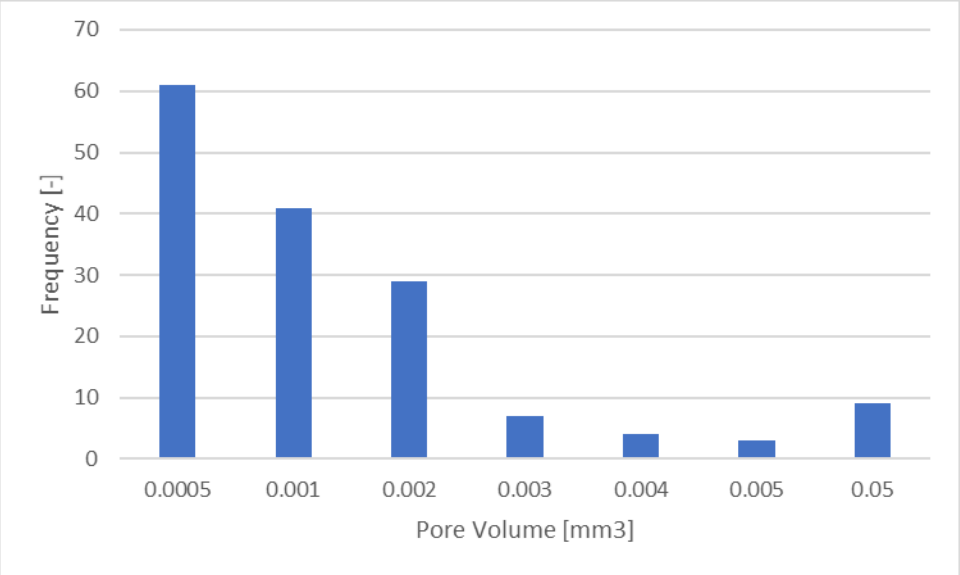


*Figure C.6: Pore size and frequency of AM crankcase 4 (original design)*

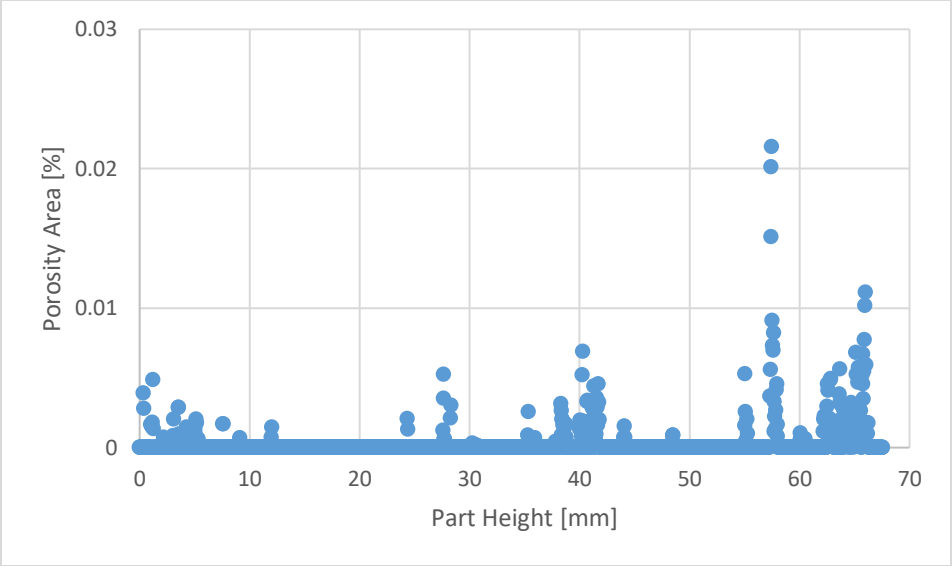


*Figure C.7: Porosity area percentage with height of AM crankcase 2 (modified design)*

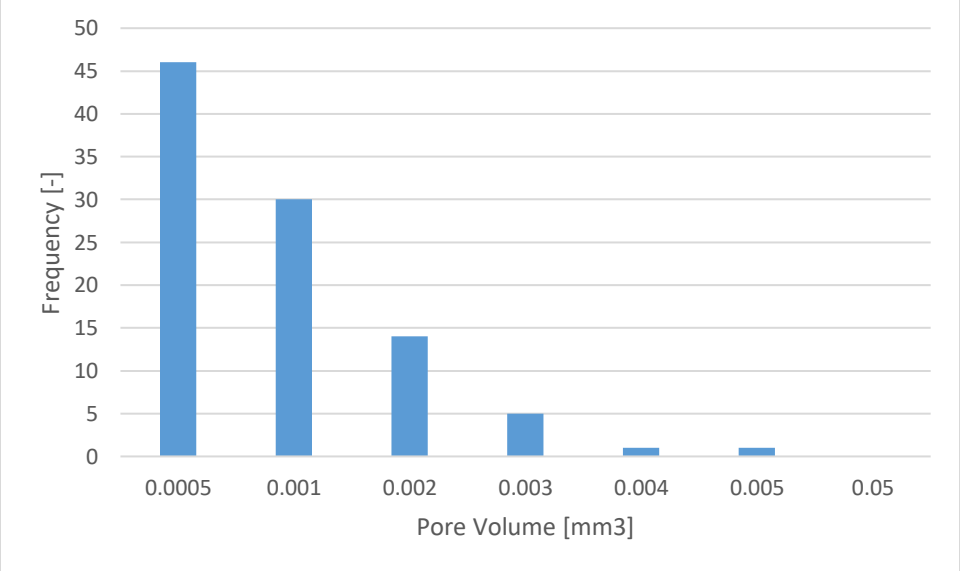


*Figure C.8: Pore size and frequency of AM crankcase 2 (modified design)*

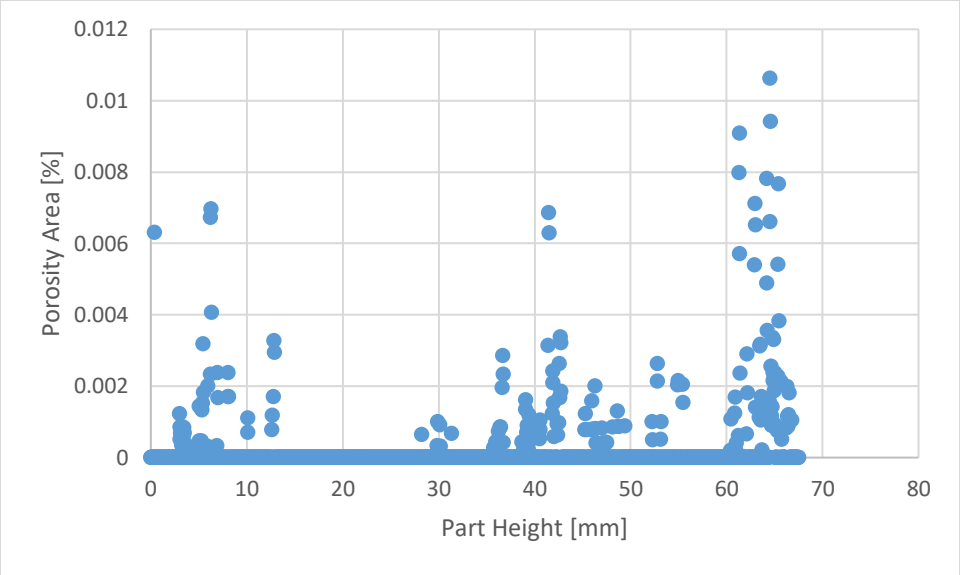


*Figure C.9: Porosity area percentage with height of AM crankcase 3 (modified design)*

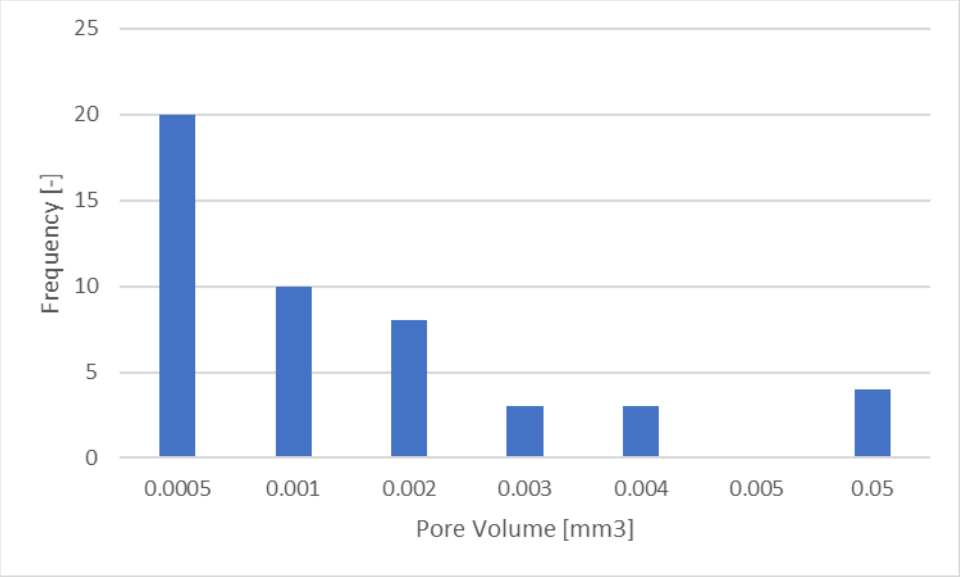


*Figure C.10: Pore size and frequency of AM crankcase 3 (modified design)*

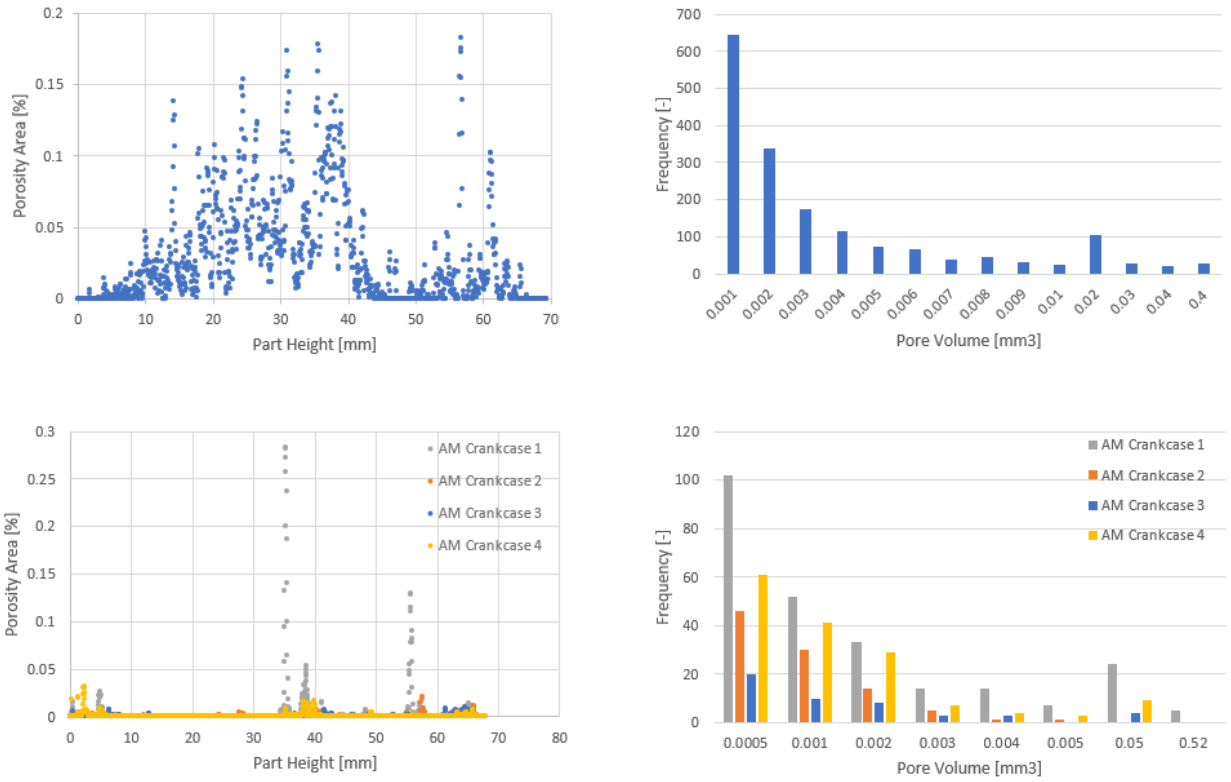


*Figure C.11: Summary of crankcase porosity results, top: original die cast part, bottom: AM parts*

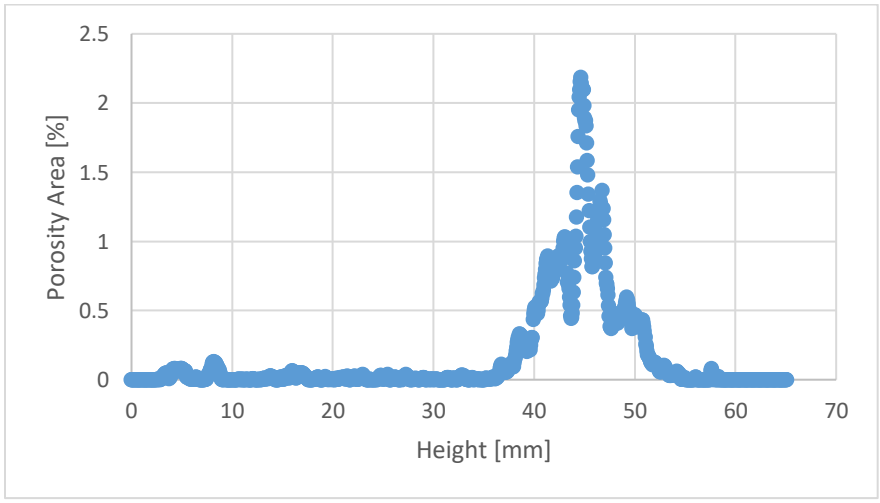


*Figure C.12: Porosity area percentage with height of die cast cylinder head*

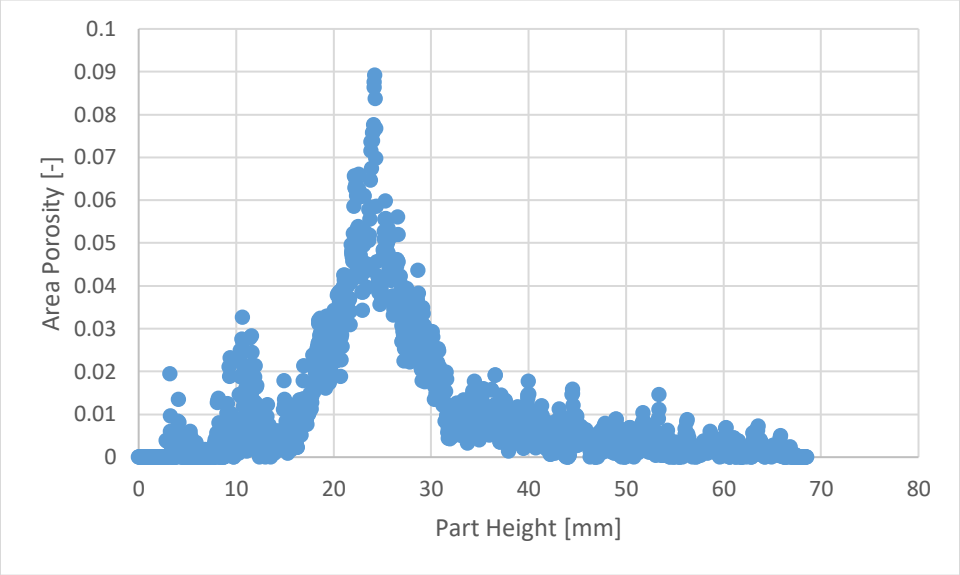


*Figure C.13: Porosity area percentage with height of AM cylinder head 1*

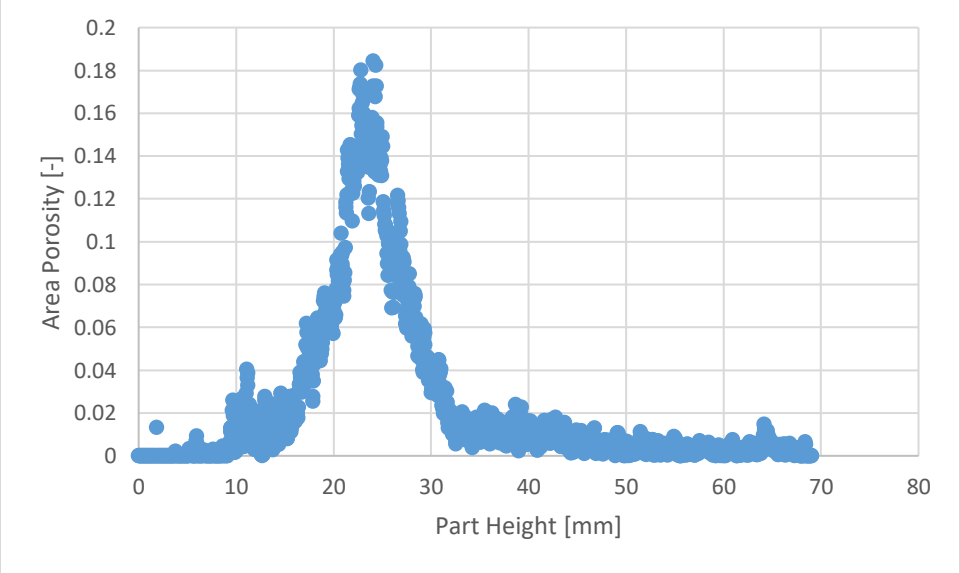


*Figure C.14: Porosity area percentage with height of AM cylinder head 2*

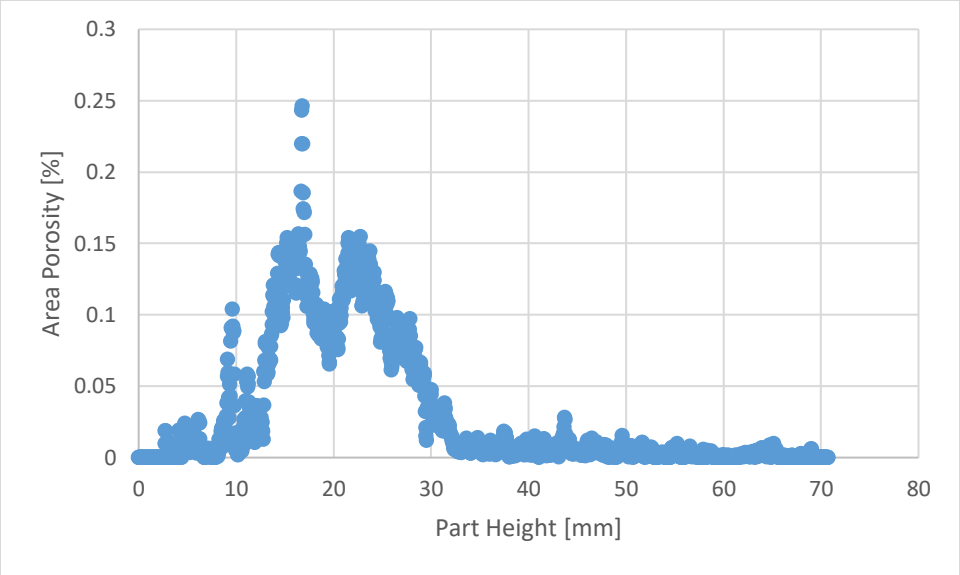


*Figure C.15: Porosity area percentage with height of AM cylinder head 3*

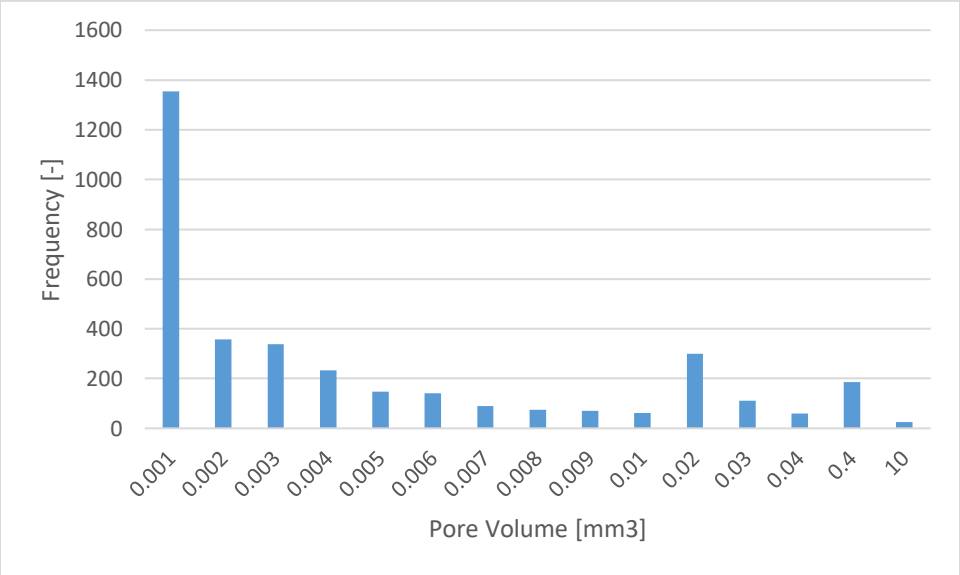


*Figure C.16: Pore size and frequency of die cast cylinder head*

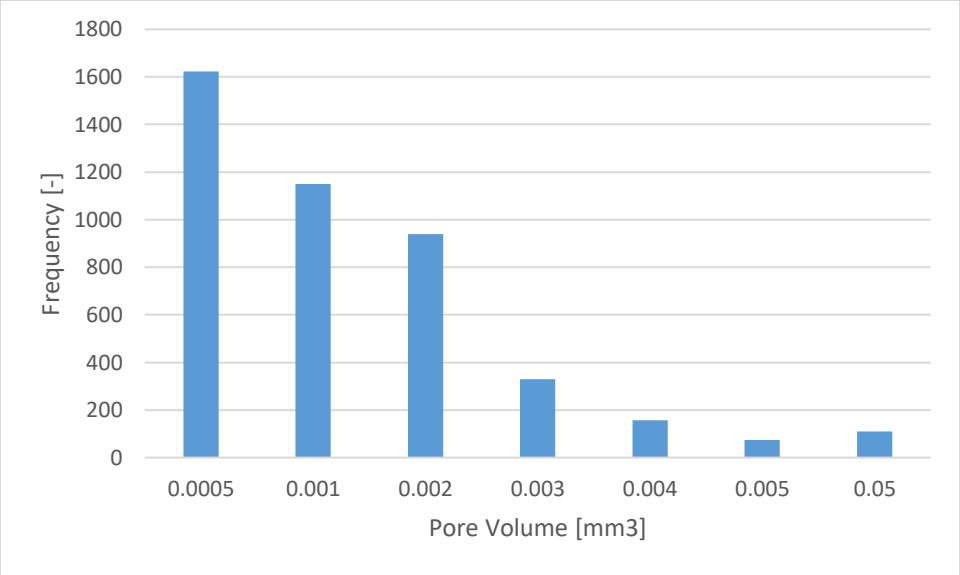


*Figure C.17: Pore size and frequency of AM cylinder head 1*

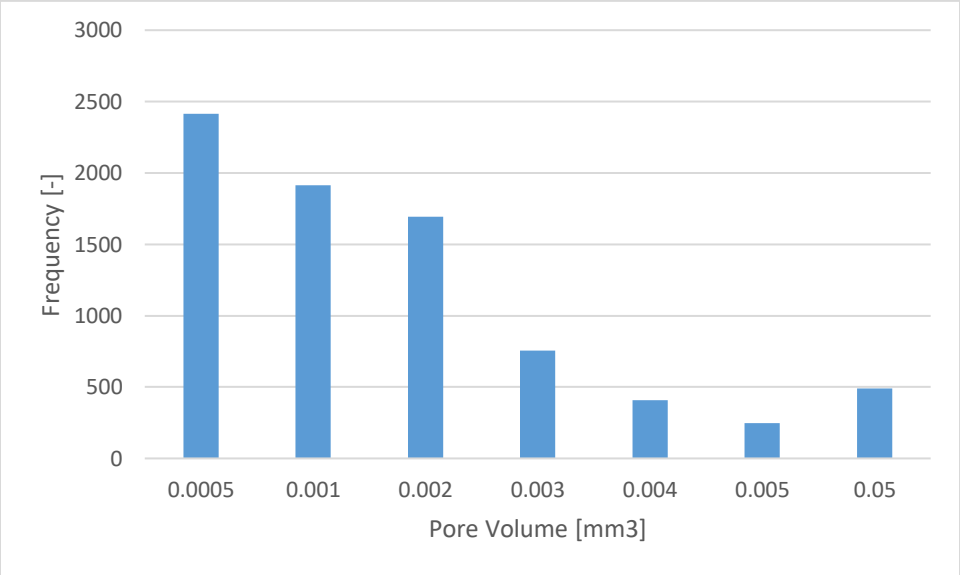


*Figure C.18: Pore size and frequency of AM cylinder head 2*

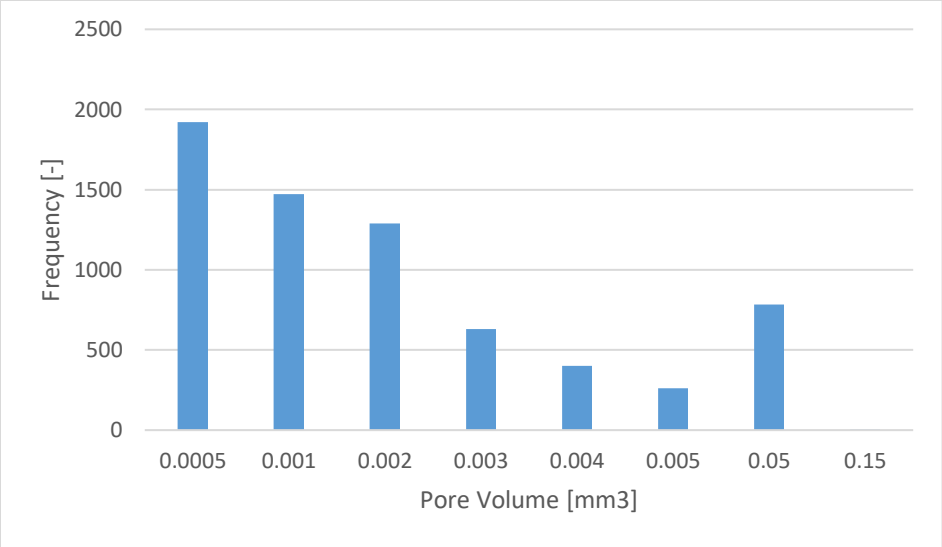


*Figure C.19: Pore size and frequency of AM cylinder head 3*

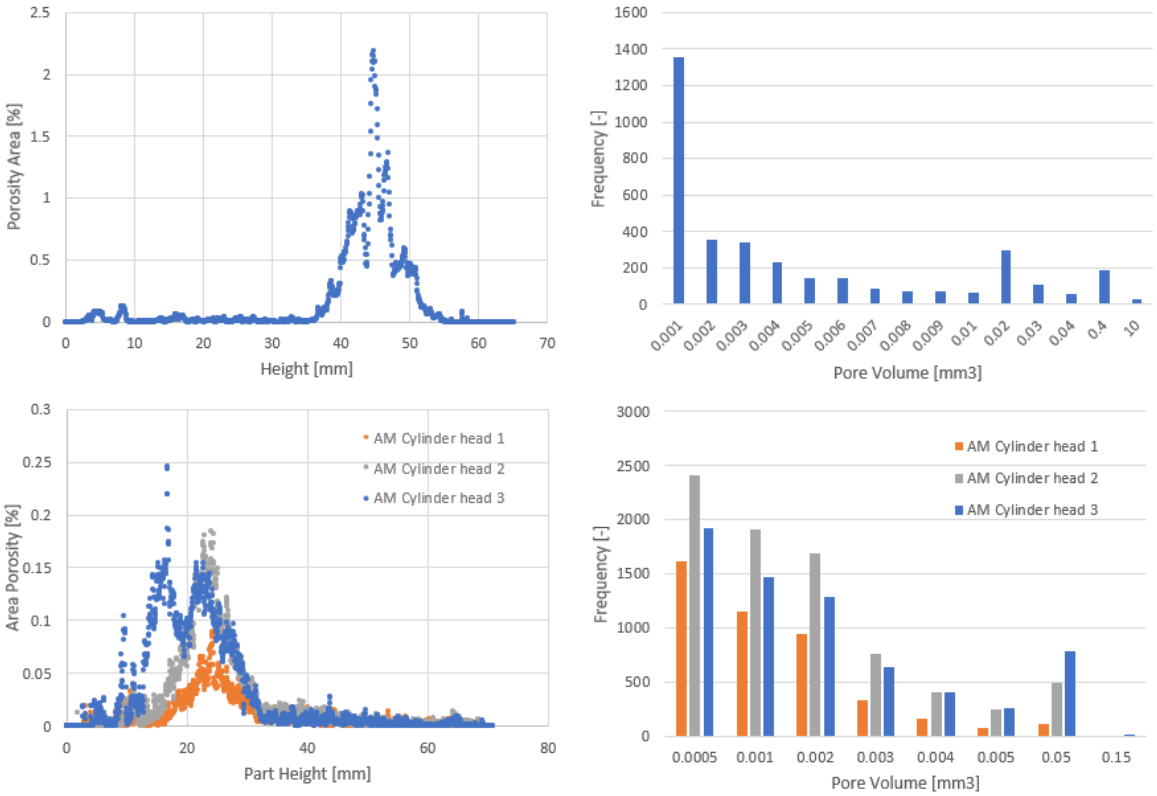


*Figure C.20: Summary of cylinder head porosity results, top: original die cast part, bottom: AM parts*

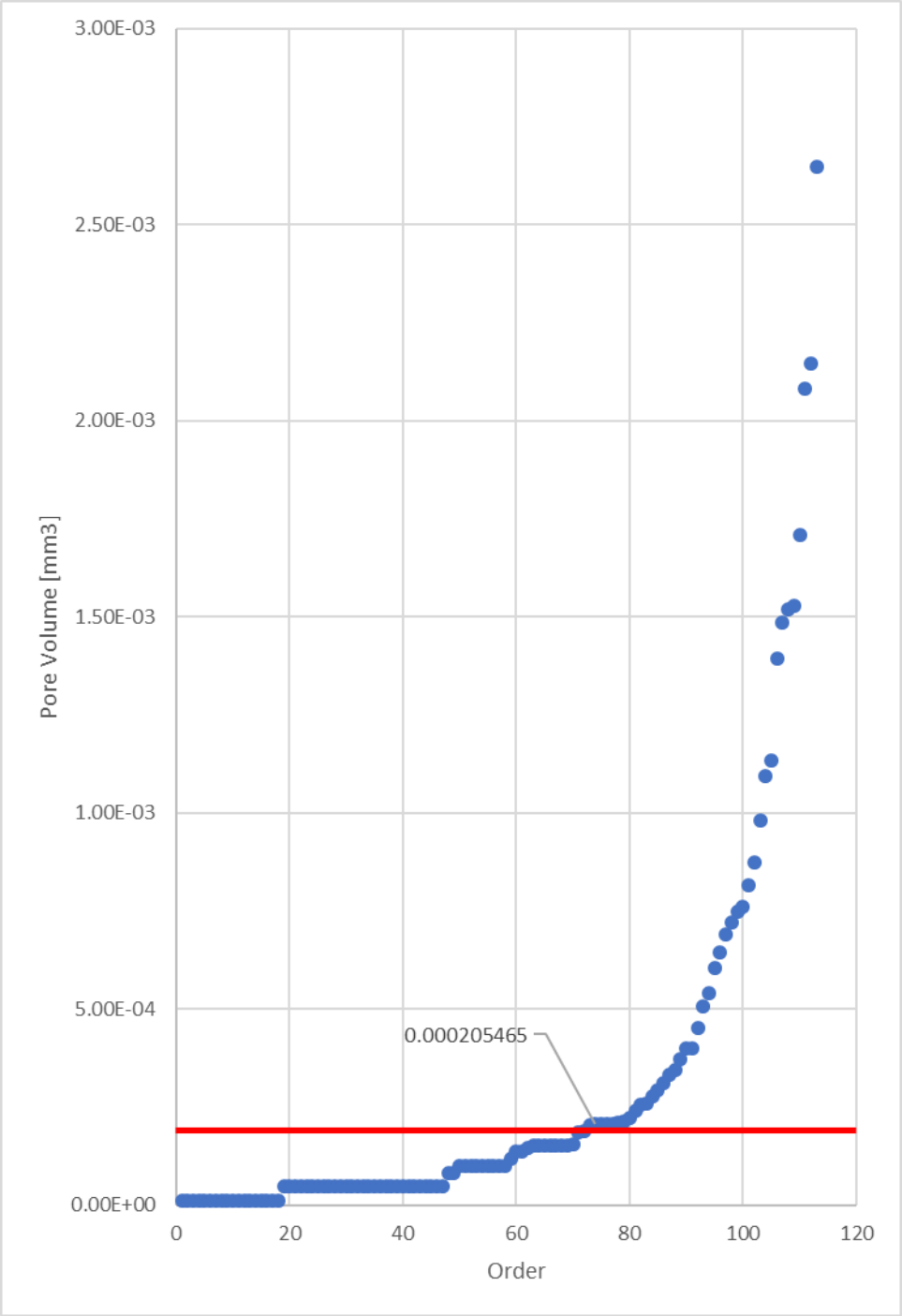


*Figure C.21: Depiction on how the cut off for noise in the CT analysis was found*

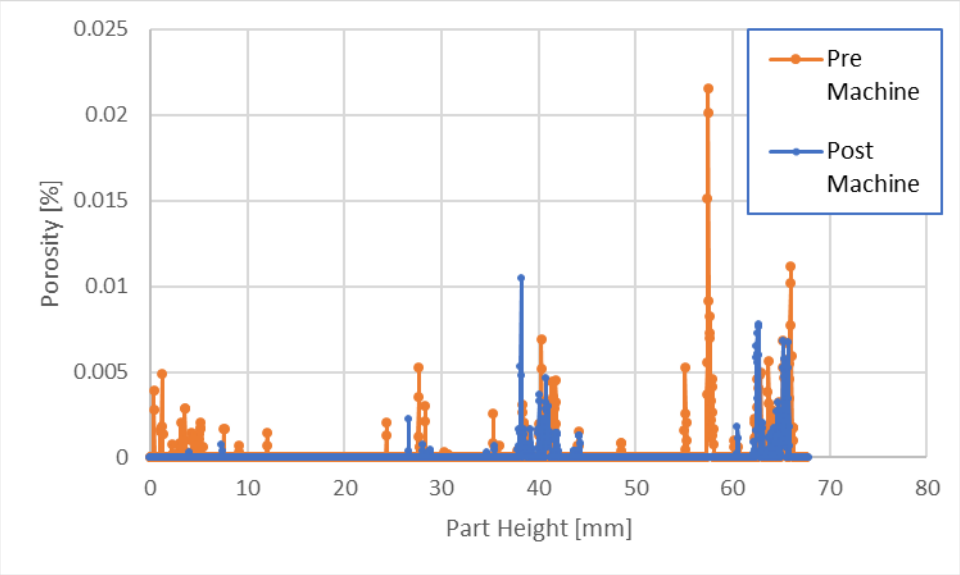


*Figure C.22: Porosity area percentage with height of AM crankcase 2 (modified design) for pre and post machined*

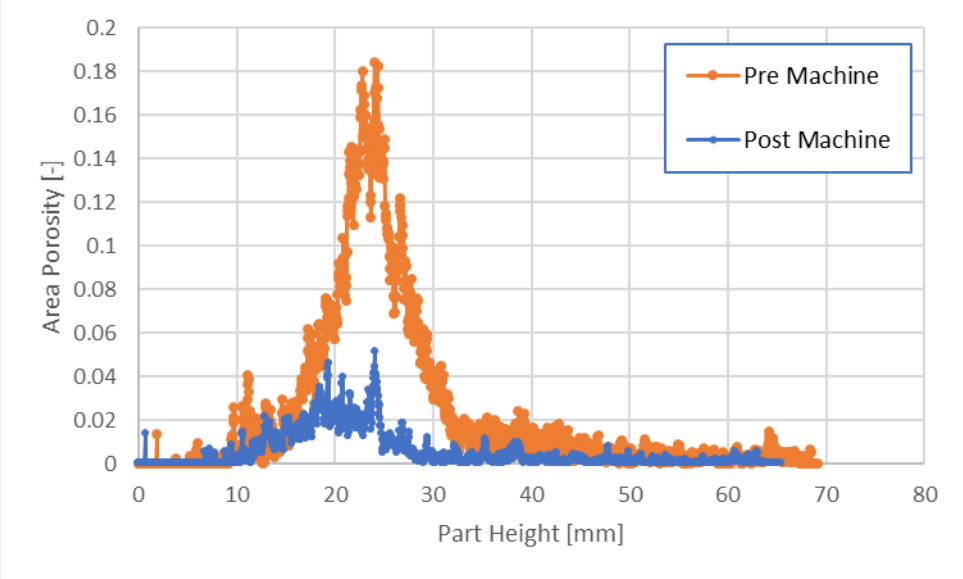


*Figure C.23: Porosity area percentage with height of AM cylinder head 2 for pre and post machined*

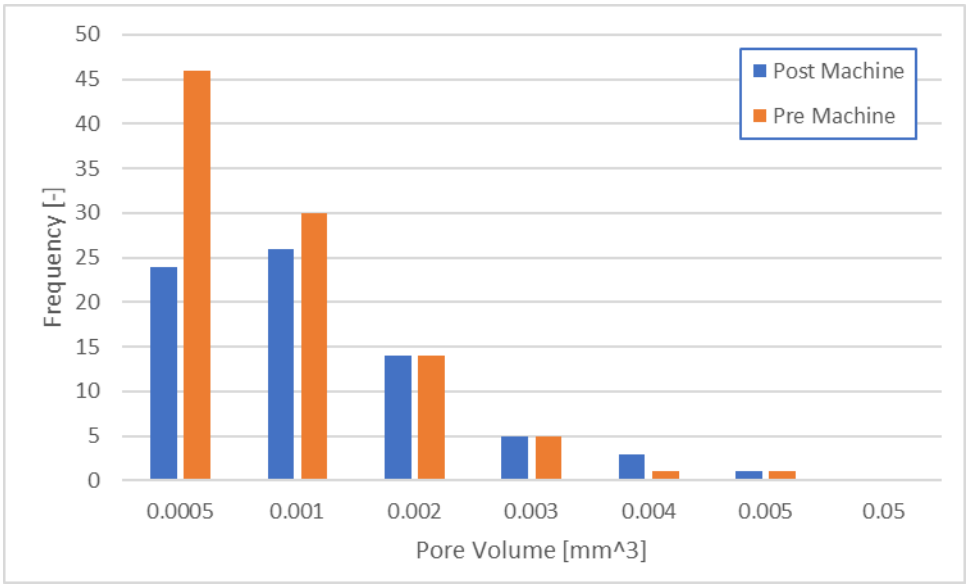


*Figure C.24: Pore size and frequency of AM crankcase 2 (modified design) for pre and post machined*

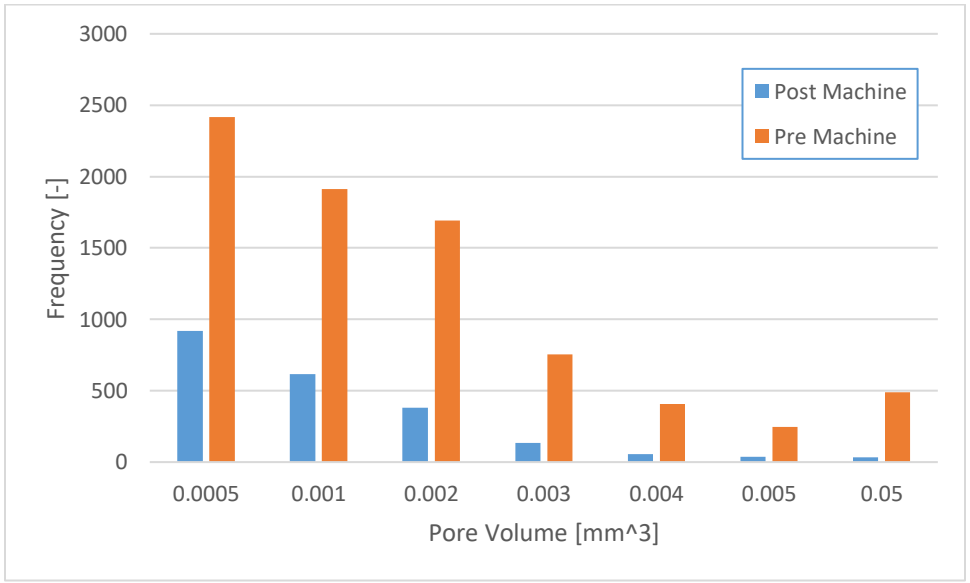


*Figure C.25: Pore size and Frequency of AM cylinder head 2 for pre and post machined*

## Appendix D: Post-processing Information

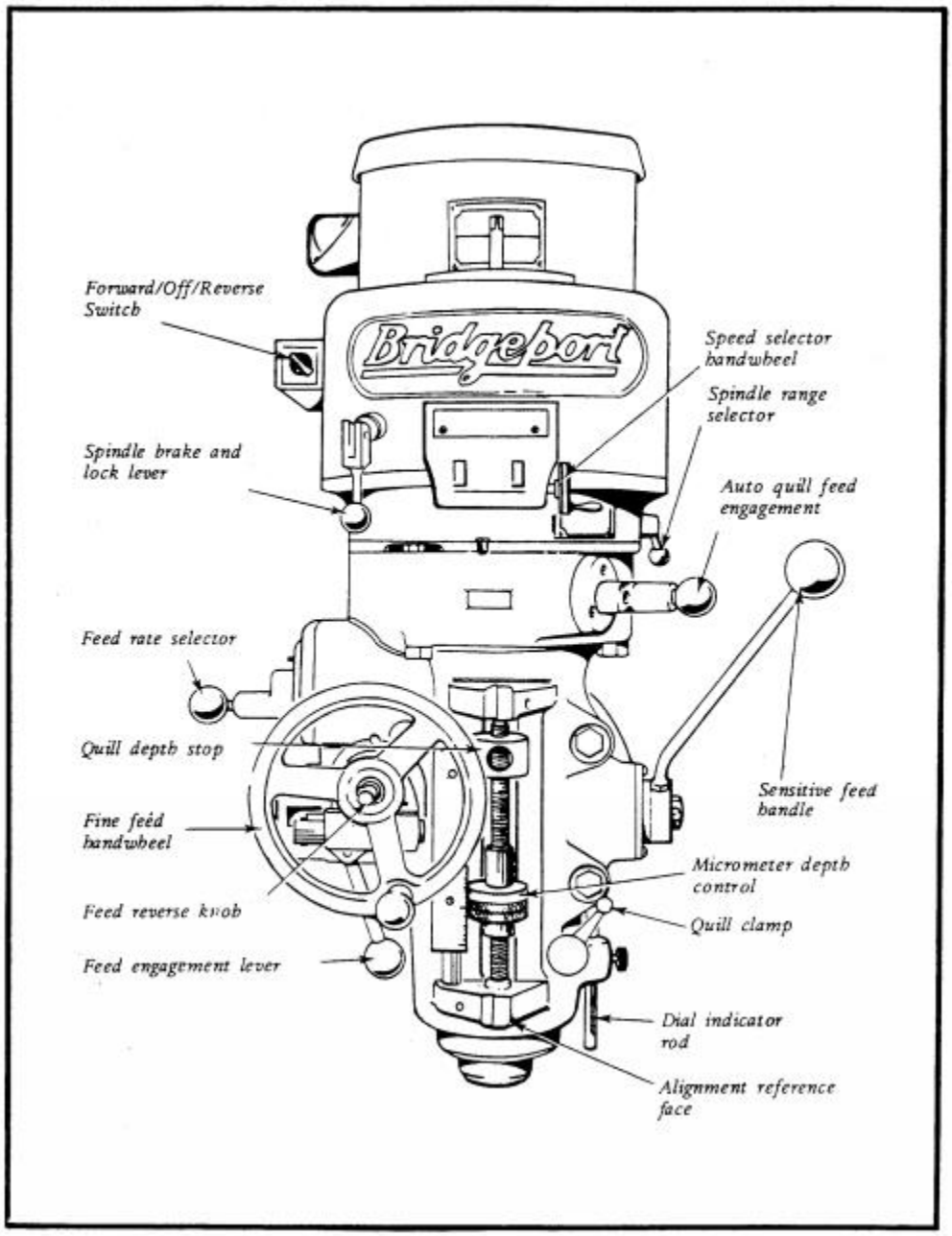


*Figure D.1: Vertical mill head controls with labels [92]*

*Table D.1: Everything needed to machine parts to final form, list does not include drill bits used when stepping up to the final size*

| | Tools | Crankcase | Cylinder head |
|---|---|---|---|
| 1 | 3/8” carbide square-end end mill (TiN/TiAlN coated) | x | x |
| 2 | 3/16” carbide square-end end mill (TiN/TiAlN coated) | x | |
| 3 | ¼” square-end end mill | x | x |
| 4 | 3/32” square-end end mill | x | |
| 5 | 1/8” ball-end end mill | | x |
| 6 | 9 mm square-end end mill | | x |
| 7 | 10 mm square-end end mill | | x |
| 8 | 10.5 mm square-end end mill | | x |
| 9 | 11/16$^{th}$ Reamer | x | |
| 10 | #26 carbide TiN coated drill bit | x | x |
| 11 | #28 drill | | x |
| 12 | #39 carbide TiN coated drill bit | x | x |
| 13 | #19 carbide TiN coated drill bit | x | |
| 14 | #46 drill bit | | x |
| 15 | #58 drill bit | | x |
| 16 | B drill bit | | x |
| 17 | J drill bit | | x |
| 18 | O drill bit | | x |
| 19 | 7/32 drill bit | | x |
| 20 | 11/32 drill bit | | x |
| 21 | 3.4 mm drill bit | | x |
| 22 | ¼-32 tap | | x |
| 23 | M2.5 $\times$ 0.45 tap for blind holes | | x |
| 24 | M3 $\times$ 0.5 tap for blind holes (TiN/CrC/C coated) | x | x |
| 25 | M5 $\times$ 0.8 tap for blind holes (TiN/CrC/C coated) | x | |
| 26 | M10 $\times$ 1 tap for blind holes | | x |
| 27 | Center drill | x | x |
| 28 | 5” sine block | | x |
| 29 | Angle vice | | x |
| 30 | Machinist jack | | x |
| 31 | Machinist probe | | x |
| 32 | 2.5” Sine block | x | x |

| | | | |
|---|---|---|---|
| 33 | Gauge block set | x | x |
| 34 | Drill chuck | x | x |
| 35 | Boring head and bar set | x | x |
| 36 | Carbide cutting tool for boring | x | x |
| 37 | Belt sander | | x |
| 38 | Dial indicator | x | x |
| 39 | Hand tap handle | x | x |
| 40 | Telescoping gage set | x | x |
| 41 | 1 to 2” Micrometer | x | x |
| 42 | 0 to 1” Micrometer | x | |
| 43 | Calipers | x | x |
| 44 | Parallel bar set | x | x |
| 45 | Deburrer | x | x |
| 46 | Brush | x | x |
| 47 | Coolant (WD40) | x | x |
| 48 | Cutting oil | x | |
| 49 | Cutting wax | | x |
| 50 | Mandrel driver (GGN-150) | | x |
| 51 | Honing mandrel 4-13/16 reach length | | x |
| 52 | Mandrel Adapter (Y32A) | | x |
| 53 | PBB bronze guide shoe | | x |
| 54 | Truing Sleeve (S1062) | | x |
| 55 | Silicon Carbide stone 220 Grit | | x |
| 56 | Silicon carbide stone 400 Grit | | x |
| 57 | Felt pads | | x |
| 58 | Honing Oil | | x |
| 59 | Silicon compound (AN30) | | x |
| 60 | Polishing stone (Y32-C03-31) | | x |
| 61 | Lapping compound | | x |

**Appendix E: Tachometer Sampling Frequency Calculation**

$Magnet\ diameter = 0.18"$

$Drive\ flange\ diameter = 1.14"$

$Max\ speed = 9500\ rpm$

$$Magnet\ \% = \frac{Magnet\ diameter}{Drive\ flange\ diameter * \pi}$$

$$Magnet\ pass\ time = \frac{60}{Max\ speed\ (rpm)} * Magnet\ \%$$

$$Sampling\ frequency = \frac{1}{Magnet\ pass\ time} * 2$$

## Appendix F: MATLAB Model for Data Post-processing

```
% ENGINE TEST DATA POST PROCESSER
% JAMEE GRAY
% OCTOBER 8, 2019

clc; clear;

% Loading in data
    cDAQ=importdata('a6.txt'); %cDAQ & Inter-Loc V delimited spreadsheet
    myRIO=importdata('b6.txt'); %myRIO delimited spreadsheet

% % Creating zero matrices to store data
    myRIO_org(:)=zeros; flow_t(:)=zeros; MP_t(:)=zeros;
    MP_count(:,1)=zeros; MP_count_t(:,1)=zeros; MP_time_dif(:,1)=zeros;
    MP_time_dif_adj(:,1)=zeros; flow(:,1)=zeros; MP(:)=zeros;
    torque(:)=zeros; fuel_height_adj(:)=zeros; cDAQ_t_adj(:)=zeros;


% % ORGANIZING MYRIO DATA % %

% creating new organized myRIO data matrix
    myRIO_NAN=~isnan(myRIO); %making NAN values=0 and numerical values=1
    zc = zeros(size(myRIO_NAN,1),1); %creating zero column
    myRIO_NAN = [myRIO_NAN, zc]; %adding zero column to the end

% creating new matrix with organized data
    i=1; k=1;
    while i<length(myRIO(:,1)) %while less than length
    j=1;
        while myRIO_NAN(i,j)==1
        myRIO_org(k,1)=myRIO(i,j); %time column
        myRIO_org(k,2)=myRIO(i,j+1); %magnet and flow data column
        j=j+2;
        k=k+1;
        end
    i=i+1;
    end

% Separating flow and magnet data
    % not needed with dyno testing- propeller only
    i=1; j=1; k=1;
    while i<length(myRIO_org)
        if myRIO_org(i,2)>6
            flow(k,1)=myRIO_org(i,2);
            flow_t(k,1)=myRIO_org(i,1);
            k=k+1;
        else
            MP(j,1)=myRIO_org(i,2);
            MP_t(j,1)=myRIO_org(i,1);
            j=j+1;
        end
        i=i+1;
```

```
    end


% naming variables
    myRIO_t= myRIO_org(:,1)-myRIO_org(1,1);
    cDAQ_t=cDAQ(:,1)-cDAQ(1,1);
    cyl_temp=cDAQ(:,2);
    crank_temp=cDAQ(:,3);
    ehx_temp=cDAQ(:,4);
    int_temp=cDAQ(:,5);
    fuel_height=cDAQ(:,6);
    int_p=cDAQ(:,7);
    exh_p=cDAQ(:,8);
    %speed =cDAQ(:,9); %used with dyno
    %torque=cDAQ(:,10); %used with dyno
    %flow = myRIO(:,2); %used with dyno

% calculating sampling frequencies
    Fs_cDAQ=length(cDAQ)/(cDAQ_t(end)-cDAQ_t(1));
    MP_test_time=60; %propeller only
    Fs_MP= length(MP)/MP_test_time; %propeller only
    Fs_flow= length(flow)/(180-MP_test_time); %propeller only
    %Fs_myRIO= length(myRIO_org)/(myRIO_t(end)-myRIO_t(1)); %dyno only

% % FINDING ENGINE SPEED % %
    % section not needed for dyno testing

% Finding peaks and occurrence time
    i=1; j=1;
    while i<length(MP(:,1))
        if MP(i+1,1)<1
            if MP(i,1)>1
               MP_count(i,1)=1;
               MP_count_t(j,1)=MP_t(i,1);
              j=j+1;
            else
              MP_count(i,1)=0;
            end
        else
            MP_count(i,1)=0;
        end
      i=i+1;
    end

% Plotting 1s of magnet pass data inside each of the 20s segments
    figure
    subplot(3,1,1);
        plot(MP_t(round(Fs_MP*10):round(Fs_MP*11),1),...
                            MP_count(round(Fs_MP*10):round(Fs_MP*11),1))
        axis([10 11 0 1.5])
    subplot(3,1,2);
        plot(MP_t(round(Fs_MP*30):round(Fs_MP*31),1),...
                            MP_count(round(Fs_MP*30):round(Fs_MP*31),1))
        axis([10 11 0 1.5])
```

```
    subplot(3,1,3);
        plot(MP_t(round(Fs_MP*50):round(Fs_MP*51),1),...
                              MP_count(round(Fs_MP*50):round(Fs_MP*51),1))
        axis([10 11 0 1.5])
        xlabel('Time [s]');


% Finding time between peaks
    i=1; j=1;
    while i<length(MP_count_t)-1
        MP_time_dif(j,1)= MP_count_t(i+1,1)-MP_count_t(i,1);
        if MP_time_dif(j,1)>0
            j=j+1;
        end
    i=i+1;
    end

% adjusted average time
     i=1; j=1;
     upperlimit= mean(MP_time_dif)+4*std(MP_time_dif);
     lowerlimit= mean(MP_time_dif)-4*std(MP_time_dif);

       while i< length( MP_time_dif)
        if MP_time_dif(i,1)< upperlimit
            if MP_time_dif(i,1)> lowerlimit
               MP_time_dif_adj(j,1)=MP_time_dif(i,1);
               j=j+1;
            end
        end
        i=i+1;
       end
    speed=60./MP_time_dif_adj;

% Plotting original and adjusted histogram
    figure
    subplot(2,1,1);
        histfit(60./MP_time_dif)
        ylabel('Frequency');
    subplot(2,1,2);
        histfit(speed)
        xlabel('Speed [RPM]');
        ylabel('Frequency');

% % FUEL CONSUMPTION % %

% eliminating extraneous data
    i=1; j=1; k=1;
    min_2_start= length(fuel_height)/3;
    min_3_start= length(fuel_height)*2/3;
    m1_avg= mean(fuel_height(1:round(length(fuel_height)/3)));
    m2_avg= mean(fuel_height(round(length(fuel_height)/3)...
                                    :round(length(fuel_height)*2/3)));
    m3_avg= mean(fuel_height(round(length(fuel_height)*2/3):end));
```

```
    while i<length(fuel_height)-1

        if i< min_2_start %first 1/3 of data
               k= m1_avg;
           elseif i< min_3_start %second 1/3 of data
               k= m2_avg;
           else %last 1/3 of data
               k= m3_avg;
        end

        if fuel_height(i)< k+0.1
            if fuel_height(i)> k-0.1
               fuel_height_adj(j,1)=fuel_height(i);
               cDAQ_t_adj(j,1)=cDAQ_t(i);
               j=j+1;
            end
        end

            i=i+1;
    end

% calculating fuel height trendline slope
    n=length(cDAQ_t_adj);
    x=cDAQ_t_adj;
    y=fuel_height_adj;
    trendline_slope= ((n*sum(x.*y))-(sum(x)*sum(y)))/...
                                          ((n*sum(x.^2))-((sum(x))^2));
    b= (sum(y)-trendline_slope*sum(x))/n;

% stdv of fuel height trendline slope
    yhat=trendline_slope*x+b;
    square_root_variance_y=(1/(n-2))*sum((y-yhat).^2);
    sum_squared_error_xx=sum((x-mean(x)).^2);
    slope_stdv=(square_root_variance_y/sum_squared_error_xx)^0.5;

 % plotting original and adjusted fuel height
    figure
    subplot(2,1,1);
    plot(cDAQ_t,fuel_height)
    ylabel('Voltage [VDC]');
    subplot(2,1,2);
    plot(x,y)
    ylabel('Voltage [VDC]');
    xlabel('Time [s]');


% calculating fuel consumption using calibration curve slope
    cal_curve_slope=0.003645034463353; %calculated seperately
    cal_curve_slope_stdv=4.329686953294337e-07; %calculated seperately
    fuel_cons=-1*trendline_slope*60/cal_curve_slope; %mL/min

        % calculating uncertainty of fuel consumption -Propagation of Error
        x1=cal_curve_slope; %independent variables
        x2=trendline_slope;
```

```
        u1=cal_curve_slope_stdv; %uncertainties
        u2=slope_stdv;
        p1=x2*60/(x1^2); %partial der calibration curve
        p2=-60/x1; %partical derivitive trendline slope
        u_fuel_cons_PE=((p1*u1)^2+(p2*u2)^2)^0.5;

        % calculating uncertainty of fuel cons. -Sequential Perturbation
        R0=fuel_cons;
        R1_pos=-1*x2*60/(x1+u1);
        R1_neg=-1*x2*60/(x1-u1);
        R2_pos=-1*(x2+u2)*60/x1;
        R2_neg=-1*(x2-u2)*60/x1;
        dif_R1_pos= R1_pos-R0;
        dif_R1_neg= R1_neg-R0;
        dif_R2_pos= R2_pos-R0;
        dif_R2_neg= R2_neg-R0;
        dif_R1=(dif_R1_pos-dif_R1_neg)/2;
        dif_R2=(dif_R2_pos-dif_R2_neg)/2;
        u_fuel_cons_SP=(dif_R1^2+dif_R2^2)^0.5;
        %deciding which to use
        u_fuel_cons= max([u_fuel_cons_PE,u_fuel_cons_SP]);


% % DATA ANALYSIS % %
    mass= 74.5; %g
    u_mass= 0.01; % g accuracy of scale
    volume= 100; %mL
    u_vol=1; % mL accuracy of graduated cylinder

    fuel_density= mass/volume; %g/mL
        %uncertainty-Propagation of Error
        x1=mass; %independent variables
        x2=volume;
        u1=u_mass; %uncertainties
        u2=u_vol;
        p1=1/x2; %partial derivative of mass
        p2=-x1/(x2^2); %partial derivative of volume
        u_fuel_density_PE= ((p1*u1)^2+(p2*u2)^2)^0.5;
        %uncertainty-Sequential Perturbation
        R0=fuel_density;
        R1_pos=(x1+u1)/x2;
        R1_neg=(x1-u1)/x2;
        R2_pos=x1/(x2+u2);
        R2_neg=x1/(x2-u2);
        dif_R1_pos= R1_pos-R0;
        dif_R1_neg= R1_neg-R0;
        dif_R2_pos= R2_pos-R0;
        dif_R2_neg= R2_neg-R0;
        dif_R1=(dif_R1_pos-dif_R1_neg)/2;
        dif_R2=(dif_R2_pos-dif_R2_neg)/2;
        u_fuel_density_SP=(dif_R1^2+dif_R2^2)^0.5;
        %deciding which to use
        u_fuel_density= max([u_fuel_density_PE,u_fuel_density_SP]);
```

```
air_density= 1.2041; %kg/m^3 @20C
vol_disp= 10.9/1000; %L
nR=2; % crank revolutions per engine cycle (four-stroke)
AF_stoic=14.543;

fuel_cons_gpers= (fuel_cons/60)*fuel_density; %g/s
    %uncertainty-Propagation of Error
    x1=fuel_cons; %independent variables
    x2=fuel_density;
    u1=u_fuel_cons; %uncertainties
    u2=u_fuel_density;
    p1=x2/60; %partial derivitave of fuel consumption
    p2=x1/60; %partial derivitave of fuel density
    u_fuel_cons_gps_PE= ((p1*u1)^2+(p2*u2)^2)^0.5;
    %uncertainty-Sequential Perturbation
    R0=fuel_cons_gpers;
    R1_pos=(x1+u1)*x2/60;
    R1_neg=(x1-u1)*x2/60;
    R2_pos=x1*(x2+u2)/60;
    R2_neg=x1*(x2-u2)/60;
    dif_R1_pos= R1_pos-R0;
    dif_R1_neg= R1_neg-R0;
    dif_R2_pos= R2_pos-R0;
    dif_R2_neg= R2_neg-R0;
    dif_R1=(dif_R1_pos-dif_R1_neg)/2;
    dif_R2=(dif_R2_pos-dif_R2_neg)/2;
    u_fuel_cons_gps_SP=(dif_R1^2+dif_R2^2)^0.5;
    %deciding which to use
    u_fuel_cons_gps= max([u_fuel_cons_gps_PE,u_fuel_cons_gps_SP]);

vol_eff= nR*mean(flow)/(vol_disp*mean(speed));
    %uncertainty-Propagation of Error
    x1=mean(flow); %independent variables
    x2=mean(speed);
    u1=std(flow); %uncertainties
    u2=std(speed);
    p1=nR/(vol_disp*x2); %partial derivative of flow
    p2=-nR*x1/(vol_disp*(x2^2)); %partial derivative of speed
    u_vol_eff_PE= ((p1*u1)^2+(p2*u2)^2)^0.5;
    %uncertainty-Sequential Perturbation
    R0=vol_eff;
    R1_pos=nR*(x1+u1)/(vol_disp*x2);
    R1_neg=nR*(x1-u1)/(vol_disp*x2);
    R2_pos=nR*x1/(vol_disp*(x2+u2));
    R2_neg=nR*x1/(vol_disp*(x2-u2));
    dif_R1_pos= R1_pos-R0;
    dif_R1_neg= R1_neg-R0;
    dif_R2_pos= R2_pos-R0;
    dif_R2_neg= R2_neg-R0;
    dif_R1=(dif_R1_pos-dif_R1_neg)/2;
    dif_R2=(dif_R2_pos-dif_R2_neg)/2;
    u_vol_eff_SP=(dif_R1^2+dif_R2^2)^0.5;
    %deciding which to use
    u_vol_eff= max([u_vol_eff_PE,u_vol_eff_SP]);
```

```
AF=(mean(flow)/1000*air_density)/((fuel_cons)*(fuel_density)/1000);
        %uncertainty-Propagation of Error
        x1=mean(flow); %independent variables
        x2=fuel_cons;
        x3=fuel_density;
        u1=std(flow); %uncertainties
        u2=u_fuel_cons;
        u3=u_fuel_density;
        p1=(1/1000*air_density)/(x2*x3/1000); %partial derivative of flow
        p2=(-x1/1000*air_density)/(x2^2*x3/1000); %pd of fuel cons.
        p3=(-x1/1000*air_density)/(x2*x3^2/1000); %pd. of fuel dens.
        u_AF_PE= ((p1*u1)^2+(p2*u2)^2+(p3*u3)^2)^0.5;
        %uncertainty-Sequential Perturbation
        R0=AF;
        R1_pos=((x1+u1)/1000*air_density)/(x2*x3/1000);
        R1_neg=((x1-u1)/1000*air_density)/(x2*x3/1000);
        R2_pos=(x1/1000*air_density)/((x2+u2)*x3/1000);
        R2_neg=(x1/1000*air_density)/((x2-u2)*x3/1000);
        R3_pos=(x1/1000*air_density)/(x2*(x3+u3)/1000);
        R3_neg=(x1/1000*air_density)/(x2*(x3-u3)/1000);
        dif_R1_pos= R1_pos-R0;
        dif_R1_neg= R1_neg-R0;
        dif_R2_pos= R2_pos-R0;
        dif_R2_neg= R2_neg-R0;
        dif_R3_pos= R3_pos-R0;
        dif_R3_neg= R3_neg-R0;
        dif_R1=(dif_R1_pos-dif_R1_neg)/2;
        dif_R2=(dif_R2_pos-dif_R2_neg)/2;
        dif_R3=(dif_R3_pos-dif_R3_neg)/2;
        u_AF_SP=(dif_R1^2+dif_R2^2+dif_R3^2)^0.5;
        %deciding which to use
        u_AF= max([u_AF_PE,u_AF_SP]);

    equi_ratio=AF_stoic/AF;
        %uncertainty-Propagation of Error
        x1=AF; %independent variables
        u1=u_AF; %uncertainties
        p1=-AF_stoic/(x1^2); %partial derivative of AF
        u_equi_ratio_PE= ((p1*u1)^2)^0.5;
        %uncertainty-Sequential Perturbation
        R0=equi_ratio;
        R1_pos=AF_stoic/(x1+u1);
        R1_neg=AF_stoic/(x1-u1);
        dif_R1_pos= R1_pos-R0;
        dif_R1_neg= R1_neg-R0;
        dif_R1=(dif_R1_pos-dif_R1_neg)/2;
        u_equi_ratio_SP=(dif_R1^2)^0.5;
        %deciding which to use
        u_equi_ratio= max([u_equi_ratio_PE,u_equi_ratio_SP]);


% CREATING MATRIX WITH ALL RESULTS % %
    Results=[mean(cyl_temp), mean(crank_temp), mean(ehx_temp),...
        mean(int_temp), mean(int_p), mean(exh_p), mean(flow), ...
```

```
        mean(speed), mean(torque), fuel_cons, fuel_cons_gpers,...
        vol_eff, AF, equi_ratio; std(cyl_temp),...
        std(crank_temp), std(ehx_temp), std(int_temp), std(int_p),...
        std(exh_p), std(flow), std(speed), std(torque),u_fuel_cons,...
        u_fuel_cons_gps,u_vol_eff,u_AF,u_equi_ratio];

% UNCERTAINTY CHECK MATRIX % %
      Uncertainties=[ fuel_cons, fuel_cons_gpers,...
        vol_eff, AF, equi_ratio; u_fuel_cons_PE,...
        u_fuel_cons_gps_PE, u_vol_eff_PE, u_AF_PE, u_equi_ratio_PE;...
        u_fuel_cons_SP, u_fuel_cons_gps_SP, u_vol_eff_SP,...
        u_AF_SP, u_equi_ratio_SP];
```

## Appendix G: Depcik $AF_s$ Calculation

Molecular weight of atmospheric air components (g/mol):

$$W_C = 12.0107$$

$$W_H = 1.00784$$

$$W_N = 14.0067$$

$$W_O = 15.999$$

Combining the major components of gasoline according to their percentage compositions gives [93] (This also aligns with Ferguson & Kirkpatrick's estimate [94]):

$$C_{gas} = 7$$

Estimating H/C ratio of gasoline [95]:

$$H_{to}C_{gas} = 1.884$$

$$H_{gas} = C_{gas} * H_{to}C_{gas} = 1.884$$

$$O_{gas} = 0$$

$$N_{gas} = 0$$

$$X_{gas} = \frac{20}{21}$$

Combining the major components of 2-stroke oil according to their percentage compositions gives [28]:

$$C_{oil} = 23.99$$

Estimating H/C ratio of used oil [96]:

$$H_{to}C_{oil} = 1.98$$

$$H_{oil} = C_{oil} * H_{to}C_{oil} = 47.5$$

$$O_{oil} = 0$$

$$N_{oil} = 0$$

$$X_{oil} = \frac{1}{21}$$

Fuel properties calculation:

$$\alpha = X_{gas} * C_{gas} + X_{oil} * C_{oil} = 7.809$$

$$\beta = X_{gas} * H_{gas} + X_{oil} * H_{oil} = 14.822$$

$$\delta = X_{gas} * O_{gas} + X_{oil} * O_{oil} = 0$$

$$\gamma = X_{gas} * N_{gas} + X_{oil} * N_{oil} = 0$$

Balancing the general stoichiometric equation to solve for a, b, c, d:

$$C_{\alpha}H_{\beta}O_{\delta}N_{\gamma} + a * (O_2 + 3.76 * N_2) = b * CO_2 + c * H_2O + d * N_2$$

Using coefficient, a to find $AF_s$:

$$AF_s = \frac{a * (2 * W_O + 3.76 * 2 * W_N)}{\alpha * W_C + \beta * W_H + \delta * W_O + \gamma * W_N} = 14.543$$

## Appendix H: Additional Engine Testing Data

*Table H.1: Stock engine results for propeller testing*

| | 50% | 60% | 70% | 80% | 90% | 100% |
|---|---|---|---|---|---|---|
| Cylinder head temperature (°C) | - | 100.82 ±0.82 | 147.89 ±0.82 | 166.91 ±1.02 | 173.83 ±0.91 | 170.77 ±1.77 |
| Crankcase temperature (°C) | - | 50.68 ±0.38 | 57.31 ±0.58 | 62.31 ±0.59 | 63.48 ±0.56 | 63.97 ± .82 |
| Exhaust temperature (°C) | - | 110.41 ±1.09 | 200.97 ±0.94 | 228.95 ±0.82 | 222.63 ±0.47 | 218.69 ±0.65 |
| Intake temperature (°C) | - | 23.32 ±0.02 | 23.76 ±0.01 | 23.90 ±0.01 | 24.15 ±0.02 | 24.31 ±0.04 |
| Intake pressure (psi) | - | 14.00 ±0.04 | 13.98 ±0.08 | 13.97 ±0.10 | 13.95 ±0.11 | 13.95 ±0.13 |
| Exhaust pressure (psi) | - | 13.93 ±0.40 | 14.00 ±0.73 | 13.98 ±0.76 | 13.98 ±0.80 | 14.00 ±0.83 |
| Air Flow (slpm) | - | 17.70 ±0.74 | 26.77 ±1.09 | 30.14 ±1.16 | 31.95 ±0.96 | 32.26 ±0.93 |
| Fuel consumption (g/s) | - | 0.0625 ±0.0010 | 0.0809 ±0.0014 | 0.0895 ±0.0011 | 0.0866 ±0.0011 | 0.0912 ±0.0012 |
| Speed (rpm) | - | 4528.3 ±180.6 | 7045.9 ±262.6 | 7770.0 ±271.2 | 8464.9 ±321.1 | 8568.8 ±314.4 |

*Table H.2: AM crankcase engine results for propeller testing*

| | 50% | 60% | 70% | 80% | 90% | 100% |
|---|---|---|---|---|---|---|
| Cylinder head temperature (°C) | 95.87 ±0.44 | 142.81 ±1.70 | 164.94 ±0.73 | 169.95 ±0.61 | 183.61 ±3.55 | 181.46 ±2.51 |
| Crankcase temperature (°C) | 50.16 ±0.14 | 61.10 ±0.21 | 68.52 ±0.61 | 71.15 ±0.43 | 77.32 ±0.76 | 76.81 ±0.36 |
| Exhaust temperature (°C) | 108.51 ±0.57 | 188.06 ±0.56 | 220.67 ±1.02 | 225.30 ±0.49 | 218.59 ±0.33 | 219.84 ±0.15 |
| Intake temperature (°C) | 23.49 ±0.01 | 23.84 ±0.01 | 23.97 ±0.02 | 24.15 ±0.03 | 24.32 ±0.01 | 24.37 ±0.01 |
| Intake pressure (psi) | 13.99 ±0.04 | 13.97 ±0.07 | 13.97 ±0.10 | 13.95 ±0.12 | 13.95 ±0.15 | 13.94 ±0.15 |
| Exhaust pressure (psi) | 13.93 ±0.40 | 13.95 ±0.68 | 13.97 ±0.81 | 14.01 ±0.85 | 13.97 ±0.79 | 13.99 ±0.78 |
| Air Flow (slpm) | 16.89 ±0.73 | 25.34 ±0.96 | 28.77 ±1.26 | 30.68 ±1.14 | 31.11 ±1.07 | 31.48 ±1.04 |
| Fuel consumption (g/s) | 0.0602 ±0.0022 | 0.0804 ±0.0014 | 0.0825 ±0.0013 | 0.0843 ±0.0016 | 0.0777 ±0.0019 | 0.0798 ±0.0018 |
| Speed (rpm) | 4739.3 ±177.6 | 7257.9 ±261.2 | 8439.2 ±301.1 | 8748.9 ±291.2 | 8940.0 ±292.1 | 8952.9 ±286.5 |

*Table H.3: AM crankcase and cylinder head engine results for propeller testing*

| | 50% | 60% | 70% | 80% | 90% | 100% |
|---|---|---|---|---|---|---|
| Cylinder head temperature (°C) | - | 86.58 ±0.20 | 118.36 ±2.16 | 129.01 ±4.03 | 172.21 ±1.73 | 174.11 ±1.47 |
| Crankcase temperature (°C) | - | 47.33 ±0.14 | 55.64 ±0.57 | 57.44 ±0.30 | 67.39 ±0.75 | 69.28 ±0.55 |
| Exhaust temperature (°C) | - | 101.27 ±0.36 | 146.39 ±0.78 | 157.79 ±3.70 | 228.87 ±2.26 | 237.25 ±1.55 |
| Intake temperature (°C) | - | 22.47 ±0.01 | 23.65 ±0.03 | 23.84 ±0.03 | 23.81 ±0.02 | 23.88 ±0.02 |
| Intake pressure (psi) | - | 14.00 ±0.03 | 13.99 ±0.06 | 13.98 ±0.09 | 13.97 ±0.13 | 13.97 ±0.13 |
| Exhaust pressure (psi) | - | 13.92 ±0.31 | 13.93 ±0.49 | 13.95 ±0.63 | 13.95 ±0.74 | 13.93 ±0.77 |
| Air Flow (slpm) | - | 12.93 ±0.77 | 18.32 ±0.60 | 21.40 ±0.90 | 24.74 ±1.14 | 25.11 ±1.22 |
| Fuel consumption (g/s) | | 0.0460 ±0.0081 | 0.0562 ±0.0030 | 0.0611 ±0.0027 | 0.0609 ±0.0027 | 0.0657 ±0.0022 |
| Speed (rpm) | - | 3423.2 ±163.4 | 5323.1 ±162.9 | 5996.5 ±202.7 | 7624.9 ±306.5 | 7801.1 ±324.2 |

*Table H.4: Stock engine results for dyno testing*

| | 5000 RPM | | | | 6000 RPM | | | |
|---|---|---|---|---|---|---|---|---|
| | 70% | 80% | 90% | 100% | 70% | 80% | 90% | 100% |
| Cylinder head temperature (°C) | 62.90 ±0.31 | 103.05 ±0.42 | 115.31 ±2.10 | 121.17 ±1.18 | 65.87 ±1.11 | 102.05 ±2.14 | 109.66 ±2.49 | 116.47 ± 1.45 |
| Crankcase temperature (°C) | 35.21 ±0.16 | 46.83 ±0.18 | 50.90 ±0.47 | 52.90 ±0.15 | 36.92 ±0.22 | 46.59 ±0.27 | 49.49 ±0.46 | 51.33 ±0.29 |
| Exhaust temperature (°C) | 52.24 ±0.82 | 88.19 ±1.12 | 94.28 ±1.59 | 110.75 ±2.54 | 87.01 ±3.54 | 137.81 ±4.67 | 95.51 ±4.74 | 77.86 ±3.02 |
| Intake temperature (°C) | 24.10 ±0.06 | 25.25 ±0.03 | 25.66 ±0.03 | 25.88 ±0.02 | 25.23 ±0.03 | 25.75 ±0.05 | 26.27 ±0.03 | 26.44 ±0.03 |
| Intake pressure (psi) | 14.00 ±0.04 | 14.02 ±0.04 | 13.97 ±0.07 | 14.00 ±0.08 | 13.98 ±0.07 | 13.95 ±0.09 | 13.94 ±0.11 | 13.93 ±0.10 |
| Exhaust pressure (psi) | 13.93 ±0.53 | 13.85 ±0.49 | 13.86 ±0.39 | 13.85 ±0.53 | 13.89 ±0.51 | 13.82 ±0.51 | 13.81 ±0.52 | 13.80 ±0.51 |
| Air Flow (slpm) | 19.83 ±0.62 | 20.18 ±0.63 | 20.34 ±0.65 | 20.25 ±0.65 | 22.73 ±0.53 | 22.36 ±0.59 | 23.55 ±0.65 | 23.57 ±0.66 |
| Fuel consumption (g/s) | 0.0616 ±0.0010 | 0.0459 ±0.0010 | 0.0464 ±0.0010 | 0.0369 ±0.0010 | 0.0759 ±0.0013 | 0.0582 ±0.0011 | 0.0595 ±0.0011 | 0.0491 ±0.0011 |
| Normalized torque (N-m) | 0.359 ±0.009 | 0.677 ±0.010 | 0.682 ±0.009 | 0.675 ±0.006 | 0.322 ±0.032 | 0.644 ±0.011 | 0.681 ±0.010 | 0.673 ±0.006 |

*Table H.5: AM crankcase engine results for dyno testing*

| | 5000 RPM | | | | 6000 RPM | | | |
|---|---|---|---|---|---|---|---|---|
| | 70% | 80% | 90% | 100% | 70% | 80% | 90% | 100% |
| Cylinder head temperature (°C) | 144.99 ±3.60 | 152.00 ±1.96 | 156.65 ±0.85 | 157.16 ±0.68 | 93.12 ±3.19 | 137.72 ±0.75 | 137.03 ±0.68 | 98.83 ±2.95 |
| Crankcase temperature (°C) | 57.74 ±0.44 | 55.91 ±0.27 | 59.65 ±0.70 | 62.38 ±0.43 | 45.05 ±0.11 | 54.64 ±0.16 | 55.35 ±0.29 | 53.81 ±0.62 |
| Exhaust temperature (°C) | 257.35 ±3.08 | 274.29 ±2.11 | 280.75 ±1.51 | 280.97 ±1.12 | 224.68 ±2.16 | 300.70 ±0.42 | 296.68 ±0.38 | 285.90 ±1.72 |
| Intake temperature (°C) | 25.45 ±0.08 | 26.08 ±0.03 | 26.31 ±0.04 | 26.38 ±0.03 | 25.95 ±0.01 | 26.40 ±0.02 | 26.33 ±0.03 | 26.31 ±0.04 |
| Intake pressure (psi) | 13.96 ±0.07 | 13.97 ±0.07 | 13.95 ±0.07 | 13.92 ±0.07 | 13.92 ±0.11 | 13.90 ±0.11 | 13.93 ±0.11 | 13.91 ±0.11 |
| Exhaust pressure (psi) | 13.81 ±0.44 | 13.79 ±0.42 | 13.86 ±0.49 | 13.76 ±0.22 | 13.80 ±0.51 | 13.92 ±0.40 | 13.91 ±0.45 | 13.84 ±0.45 |
| Air Flow (slpm) | 20.29 ±0.61 | 20.52 ±0.63 | 20.51 ±0.62 | 20.43 ±0.62 | 23.45 ±0.59 | 23.87 ±0.64 | 23.92 ±0.66 | 24.01 ±0.67 |
| Fuel consumption (g/s) | 0.0474 ±0.0015 | 0.0432 ±0.0012 | 0.0452 ±0.0012 | 0.0443 ±0.0014 | 0.0727 ±0.0015 | 0.0619 ±0.0014 | 0.0621 ±0.0013 | 0.0584 ±0.0015 |
| Normalized torque (N-m) | 0.611 ±0.009 | 0.640 ±0.007 | 0.651 ±0.009 | 0.584 ±0.010 | 0.355 ±0.026 | 0.649 ±0.006 | 0.649 ±0.006 | 0.647 ±0.017 |

*Table H.6: AM crankcase and cylinder head engine results for dyno testing*

| | 5000 RPM | | | | 6000 RPM | | | |
|---|---|---|---|---|---|---|---|---|
| | 70% | 80% | 90% | 100% | 70% | 80% | 90% | 100% |
| Cylinder head temperature (°C) | 127.26 ±0.60 | 142.90 ±1.41 | 154.28 ±2.10 | 171.70 ±3.85 | 136.12 ±3.01 | 154.89 ±1.38 | 158.71 ±1.55 | 158.34 ±4.01 |
| Crankcase temperature (°C) | 58.44 ±0.47 | 62.18 ±0.92 | 70.39 ±0.18 | 72.74 ±0.19 | 60.31 ±0.47 | 69.10 ±0.57 | 70.27 ±0.40 | 69.62 ±0.68 |
| Exhaust temperature (°C) | 283.86 ±0.84 | 297.58 ±0.88 | 292.08 ±2.48 | 290.96 ±4.40 | 299.06 ±3.67 | 297.42 ±1.21 | 294.69 ±1.86 | 296.39 ±1.13 |
| Intake temperature (°C) | 26.13 ±0.18 | 27.37 ±0.35 | 26.86 ±0.08 | 26.97 ±0.10 | 26.96 ±0.12 | 27.06 ±0.03 | 27.25 ±0.08 | 27.16 ±0.11 |
| Intake pressure (psi) | 13.91 ±0.05 | 13.95 ±0.09 | 13.93 ±0.05 | 13.92 ±0.18 | 13.90 ±0.11 | 13.89 ±0.13 | 13.91 ±0.11 | 13.90 ±0.12 |
| Exhaust pressure (psi) | 13.89 ±0.50 | 13.85 ±0.60 | 13.78 ±0.50 | 13.74 ±0.55 | 13.96 ±0.60 | 13.88 ±0.69 | 13.90 ±0.64 | 13.95 ±0.62 |
| Air Flow (slpm) | 20.57 ±0.55 | 20.73 ±0.57 | 20.65 ±0.57 | 20.73 ±0.58 | 23.25 ±0.58 | 24.07 ±0.60 | 24.41 ±0.63 | 24.47 ±0.67 |
| Fuel consumption (g/s) | 0.0527 ±0.0010 | 0.0489 ±0.0010 | 0.0397 ±0.0008 | 0.0394 ±0.0010 | 0.0646 ±0.0011 | 0.0559 ±0.0014 | 0.0636 ±0.0014 | 0.0633 ±0.0013 |
| Normalized torque (N-m) | 0.598 ±0.007 | 0.608 ±0.006 | 0.603 ±0.006 | 0.613 ±0.009 | 0.520 ±0.054 | 0.604 ±0.008 | 0.603 ±0.010 | 0.614 ±0.007 |